EFFECTS OF CONTROLLED DISORDER ON THE VORTEX PHASES OF HIGH-TEMPERATURE SUPERCONDUCTORS

Thesis by

Wen Jiang

In Partial Fulfillment of the Requirements

for the Degree of

Doctor of Philosophy

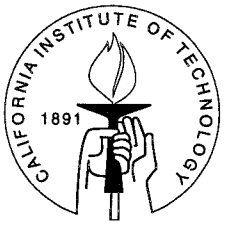

California Institute of Technology

Pasadena, California

1995

(Submitted May 15, 1995)

Acknowledgements

With my deepest appreciation, I thank my thesis advisor, Professor Nai-Chang Yeh, for her invaluable assistance, guidance and high standards during my research and preparation of this thesis. Without her perceptive understanding of physics and her dedication to research, today's achievements of our group, including that of this thesis, would not have been the same. I want to acknowledge Professors Michael Cross, Michael Roukes, and Thomas Tombrello for serving on my thesis committee. I also greatly appreciate the help and friendship of my fellow graduate students of/from our group Daniel Reed, Ushma Kriplani, David Beam and Andy Fu, in particular, the effort of Daniel Reed in automating our measurement systems; the technical assistance of Nils Asplund who constructed the sample probes used in this work, helped in maintaining all of our vacuum systems and kept the cryogenic systems functioning; and Alan Rice who performed the proton irradiations with his exceptional skills and efficiency. I also appreciate the help of Amit Mehra, Ruth Brain and Eric Daniel in part of this work.

For their contributions to this work, I would like to thank all our collaborators, in particular, Professor Thomas Tombrello who helped design the experiments for this work and provided the beam time for the proton irradiation and lots of stimulating discussions; Dr. Fred Holtzberg at IBM Thomas J. Watson Research Center, who supplied all the $YBa_2Cu_3O_7$ crystals used in this work; Dr. Marcin Konczykowski at Ecole Polytechnique in Palaiseau, France, who performed the heavy-ion irradiation; and Alan Rice who performed the proton irradiation. I would also like to thank Professor Michael Cross at Caltech and Dr. Valerii Vinokur at Argonne National Laboratory for their stimulating discussions.

I gratefully acknowledge the financial support from the David and Lucile Packard Foundation, the National Science Foundation, the Office of Naval Research, and NASA/OACT.

For the enjoyable environment over the years and for the support during the difficult times I had, I thank all the condensed matter group members; in particular, Pat Stevens and Andrea Aguirre who were always willing to help, and Dr. Eugenia Kuo for her friendship since I first stepped into Sloan Annex. I also thank Professors Xiangdong Ji and Steven Koonin who first introduced me to this wonderful and exciting institute, Caltech.

Finally, and above all others, I wish to express my gratitute to my parents and my sister for their constant love and encouragement; my eternal gratitude to my husband Alex Zhi Qiang Zheng, who has been most supportive and understanding, and has provided help in my experiments and in preparing this thesis in addition to all his work including writing his own Ph.D. thesis. This thesis is dedicated to our beloved daughter, Stephanie Jin-Yu Zheng, who had once brought so much joy to our life, and who is always in our hearts.

Abstract

The high transition temperature, short coherence length and long penetration depth of high-temperature superconductors result in novel vortex properties associated with the large thermal and disorder fluctuations. This thesis presents systematic experimental invetigations on the vortex phases of $YBa_2Cu_3O_7$ single crystals with different types of controlled disorder. Measurements of dc current-voltage characteristics and ac impedance as a function of frequency are carried out on dilutely twinned $YBa_2Cu_3O_7$ single crystals irradiated with 3.0 MeV protons. It is found that the moderately increased vortex pinning caused by the increasing density of controlled point defects does not change the nature of the second-order vortex-glass transitions in $YBa_2Cu_3O_7$ single crystals with dilute twin boundaries, as manifested by the universal critical exponents and scaling functions for samples with different densities of point defects. In $YBa_2Cu_3O_7$ single crystals with c-axis correlated columnar defects created by 0.9 GeV Pb-ion irradiation, a Bose-glass to "superfluid" transition is demonstrated by the universal critical scaling behavior of the ac impedance versus frequency isotherms. The static and dynamic critical exponents and the universal scaling functions are determined from our self-consistent critical scaling analyses. The Bose-glass transition temperature is found to decrease with the increasing angle between the applied magnetic field and the column orientation, in contrast to the angular dependence of the vortex-glass transition temperature which increases monotonically with the increasing angle due to the intrinsic sample anisotropy.

The interplay of vortex pinning and thermodynamic vortex phase transitions is further studied in the weak pinning limit by investigating the vortex transport properties of a nearly defect-free, untwinned $YBa_2Cu_3O_7$ single crystal. Two novel phenomena are observed and studied quantitatively. The resistive hysteresis near the vortex-solid melting transition is ascribed to a current-induced non-eqilibrium effect; the resistive "peak effect" below the vortex-solid transition is found to be a general phenomenon

existing in extreme type-II superconductors, and is associated with the softening of the vortex-solid before the thermodynamic melting transition. It is therefore concluded that the current-induced effects are of particular importance in determining the vortex properties of extreme type-II superconductors with weak pinning.

Contents

Chapter 1 Introduction

The discovery of superconductivity at 30K in the Ba-La-Cu-O system by Bednorz and Müller at IBM Zurich Research Laboratory in 1986 (Bednorz & Muller, 1986) has brought superconductivity research into a new era. Superconductors with transition temperatures (T_c's) of 93 K in $YBa_2Cu_3O_7$ (Wu *et al.*, 1987) and 120 K in $Bi_2Sr_2Ca_2Cu_3O_8$ (Subramanian *et al.*, 1988) were found soon afterwards. To date, the highest T_c has reached 135 K in $HgBa_2Ca_2Cu_3O_{8+\delta}$ ($0 < \delta < 1$) (Tsuei *et al.*, 1994). These discoveries have led to numerous applications of these high-temperature superconductors(HTS's) without the expensive liquid helium environment required for conventional superconductors. However, the brittle nature and chemical reactivity of these high-temperature superconducting materials have limited the major development in the applications to thin film devices, such as high-temperature SQUIDS (Gupta *et al.*, 1994), superconducting microwave filters (Chew *et al.*, 1991) and high speed electronics (Raider, 1988). In addition to a wide range of applications, HTS's have also opened new opportunities for studying novel phenomena that are associated with the fundamental physics in high-temperature superconductivity. One issue that has received considerable attention is the novel vortex properties due to the large thermal and disorder fluctuations in HTS's. In fact, not only that the superconducting to normal state transition becomes significantly broadened in HTS's, but also that a dissipative new vortex phase is found between the nondissipative superconducting vortex phase and the normal state. Understanding when and how the superconducting phase becomes dissipative is very important since it is the nondissipative nature of superconductors that is desired in their applications. It is the goal of this thesis to investigate these issue.

1.1 Motivation

1.1.1 Novel Vortex Phases in High-Temperature Superconductors

The copper oxide based high-temperature superconductors(HTS's) share three most unusual fundamental properties:

i. high superconducting transition temperature (T_c);

ii. large electronic mass anisotropy;

iii. short coherence length (ξ_s) and long penetration depth (λ).

The large anisotropy reflects the layered crystalline structure of HTS's. The high T_c and short ξ_s result in large thermal fluctuations. The short ξ_s and long λ result in a large Ginzberg-Landau parameter $\kappa \equiv \lambda/\xi_s$ and therefore a soft vortex lattice. Together with the large anisotropy, the vortex system of HTS's are very sensitive to disorder fluctuations. One major consequence of the large thermal and disorder fluctuations in HTS's is the novel vortex phase diagram as compared with that of conventional superconductors shown in Fig. 1.1. A brief description of these phase diagrams is given below. More theoretical background will be provided in Chapter 2.

Superconductors are generally categorized into two types according to their magnetic properties; type-I superconductors with $\xi_s > \sqrt{2}\lambda$ and type-II superconductors with $\xi_s < \sqrt{2}\lambda$. In type-I superconductors, the normal-metal state is recovered by increasing the external magnetic field to above the thermodynamic critical field $H_c(T)$ (see Fig.1.1(a)). In conventional type-II superconductors, two critical fields are found which separate three thermal equilibrium phases (see Fig.1.1(b)). A Meissner state exists in a very low magnetic field below the lower critical field $H_{c1}(T)$. With an increasing external field, the magnetic field begins to penetrate the sample in the form of "quantized" flux lines in the Abrikosov vortex-lattice state, each of the flux lines encloses one flux quantum ($\Phi_0 = 2.07 \times 10^{-15}$ Tesla-m^2). At the upper critical field

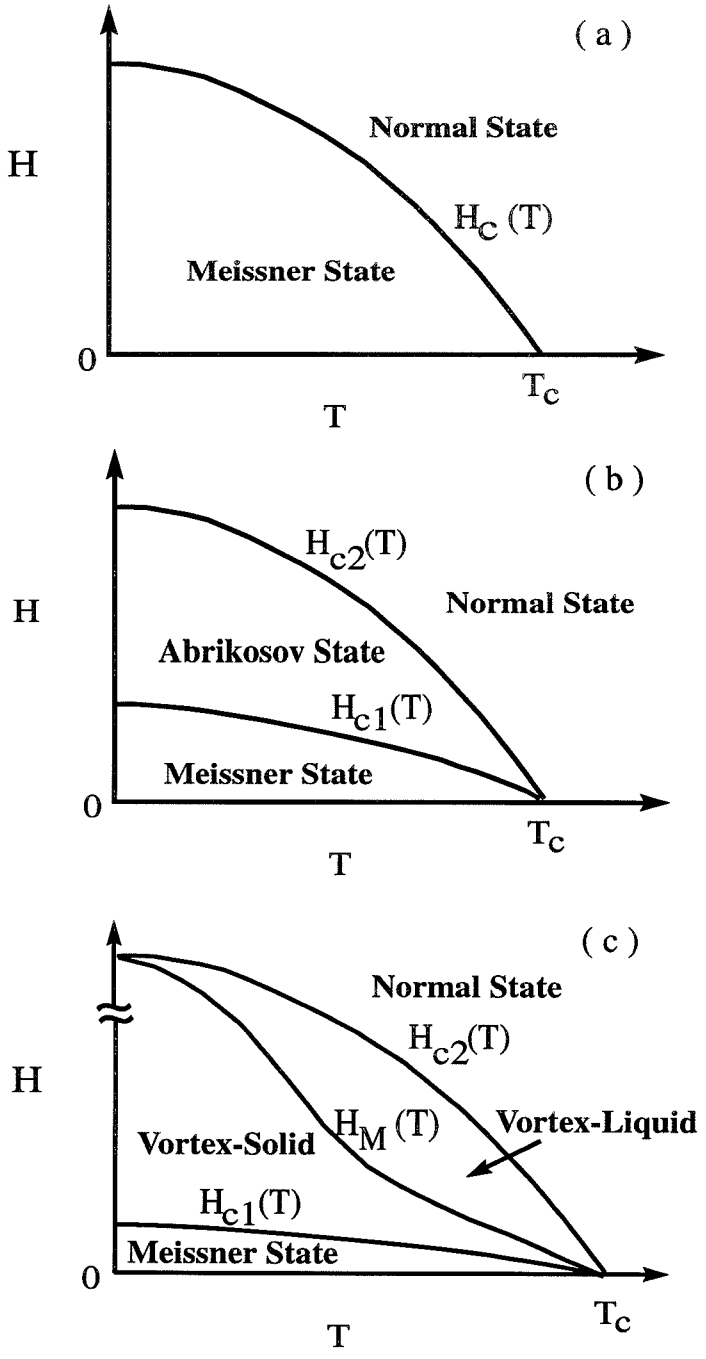

Figure 1.1: The vortex phase diagrams of (a) type-I superconductors, (b) conventional type-II superconductors, and (c) high-temperature superconductors.

$H_{c2}(T)$, a normal state is recovered. High-temperature superconductors are extreme type-II superconductors with $\kappa \sim 100$. The vortex dissipation in HTS's begins before $H_{c2}(T)$ is reached, suggesting the existence of a new vortex phase, the vortex-liquid phase (see Fig.1.1(c)). The vortex-solid phase at lower temperatures is also different from the Abrikosov state, the latter being characterized by a regular vortex lattice in conventional type-II superconductors. Because of the large penetration depth in HTS's, the magnetic fields associated with the vortices are usually so strongly overlapped that there is no longer a well-defined discrete flux line lattice, even though the vortex positions can still be identified. The line separating the vortex-solid phase and the vortex-liquid phase in the magnetic field (H) versus temperature (T) phase diagram is called the melting line. The focus of this thesis is to explore the nature of the melting line in the presence of different types of static disorder.

1.1.2 Vortex Dissipation and Pinning

To study the vortex-solid melting, we need to first understand the origin of vortex dissipation and the effects of static disorder on the vortex properties. In the presence of an applied current, if the vortex lattice is not pinned by either material defects or impurities, vortices will move with a finite velocity v transverse to the current under the Lorentz force $\boldsymbol{F}_L = \mathbf{J} \times \mathbf{\Phi_0}$, and $v \propto F_L$. Here, $\mathbf{\Phi_0}$ is parallel to the external filed $\mathbf{B}$. This vortex motion results in an electric field $\mathbf{E} \propto (\mathbf{B} \times \boldsymbol{v})$ which is the origin of the vortex dissipation. In any real material, however, there are always structural defects, or sometimes referred to as *static disorder* in this thesis, which provide energetically preferred positions for the flux lines and thus inhibit their motion. This inhibition of vortex motion is called "pinning". The vortex pinning force provided by defects is due to the weakening or absence of superconductivity in the local defect regions, so that the energy cost of locating a flux line (which has a normal core with a free energy higher than the superconducting region) in the defect position is reduced. The reduced energy is therefore the pinning energy for vortices, and can be estimated as $U_p = \epsilon(H_c^2/8\pi)V_v$, where ϵ is the fractional depression of superconductivity in the

defect, H_c is the thermodynamic critical field, and V_v is the volume of the vortex core that is pinned. Apparently, ϵ and V_v depend on the nature of the defect and the vortex-defect interaction. In addition to the defects in as-grown superconductors, one can create control densities and types of defects by means of ion irradiation.

1.1.3 Vortex Phase Transitions

Our experimental investigations of the vortex phase transitions in extreme type-II superconductors with different types of static disorder were initially inspired by various theoretical work (Nelson & Seung, 1989; Marchetti & Nelson, 1990; Fisher *et al.*, 1991; Nelson & Vinokur, 1992). In particular, the proposal of a vortex-glass phase transition (Fisher *et al.*, 1991) for a vortex system with weak random point defects, and that of a Bose-glass transition (Nelson & Vinokur, 1992) for a system with correlated vortex pinning provided by parallel columnar defects, have had the most important impaction on the experimental studies of vortex phase transitions in HTS's.

In addition to possible new universality classes of second-order vortex phase transitions in samples with different types of static disorder, another very important issue, regarding the nature of the vortex-solid melting transition in very "clean" HTS's, has also received intense attention (Brezin *et al.*, 1985). Since direct theoretical calculations of vortex-pin interaction are very difficult, systematic experimental investigations on HTS samples of different dominating pinning mechanisms are of particular importance for providing crucial information for the interplay of the thermal fluctuations and disorder effects near the vortex-solid melting.

1.2 Previous Work

High-temperature superconductivity research has been a very competitive area since the beginning of the field. Although most of the research topics in our group were uniquely designed, it is unavoidable that some of our experimental work still overlapped that of other research groups. In the following, a brief summary is given

for the work by other groups that is related to this thesis. More technical discussions will be referred to in later chapters.

As stated in the previous section, the vortex-glass model has inspired various experimental studies of the vortex-properties in HTS's. Although several publications on the DC transport measurements (Koch *et al.*, 1989; Gammel *et al.*, 1991) and one paper on the low-field AC transport measurements (Olsson *et al.*, 1991) had been suggestive of a second-order vortex-glass transition prior to our work, there were two common flaws which hindered a convincing experimental proof for a second-order vortex phase transition below H_{c2}. One is the large error bars involved in the "critical exponents" determined by other research groups (Koch *et al.*, 1989; Gammel *et al.*, 1991; Olsson *et al.*, 1991); the supposedly "universal" exponents for a second-order phase transition in fact vary by a few hundred percents with varying the applied magnetic field, the sample, and the experimental technique. The other serious flaw is to do with the absence of a reasonable critical regime near the supposedly second-order critical temperature in those reports (Koch *et al.*, 1989; Gammel *et al.*, 1991; Olsson *et al.*, 1991). For instance, in Ref. (Koch *et al.*, 1989) the critical analysis was applied to the current-voltage isotherms over a temperature interval of 11.8K around the "vortex-glass" temperature T_G for $H = 40$ kOe. This temperature interval is not only much broader than what is allowed by the Ginzberg criterion, but also overlaps the upper critical field line H_{c2} for the same field. In other words, the "vortex-glass" transition quoted in Ref. (Koch *et al.*, 1989) is essentially not distinguishable from the upper critical field $H_{c2}(T)$, rendering serious doubts for the correctness of the critical exponents and phase transition temperature, as well as for the entire issue of a true vortex-glass transition.

On the other hand, in an effort to determine whether first-order vortex-solid melting transitions exist in samples nearly free of static disorder, electrical transport measurements were attempted in untwinned $YBa_2Cu_3O_7$ single crystals (Safar *et al.*, 1992a; Kwok *et al.*, 1994a; Charalambous *et al.*, 1993). Resistive hysteresis was observed in the vortex state and was initially viewed as the experimental evidence for the first-order transition. However, as the issue was further scrutinized, it becomes

questionable whether a non-thermodynamic quantity such as the resistivity should follow the same hysteretic behavior as the internal energy.

Although the effects of controlled disorder had been studied via electrical transport (Vichery *et al.*, 1989), magnetization (van Dover *et al.*, 1989; Civale *et al.*, 1990; Civale *et al.*, 1991; Konczykowski *et al.*, 1991), AC susceptibility measurements (Civale *et al.*, 1990; Civale *et al.*, 1991), and AC transmittivity and transmissivity (Konczykowski, 1991; Konczykowski *et al.*, 1991), most experimental work only focuses on the effects of disorder on the linear resistivity, the critical current density, and the irriversibility line (Muller *et al.*, 1987; Yeshurun & Malozemoff, 1988). No attempts had been made prior to our work to investigate of the vortex-solid to liquid transition with controlled disorder.

1.3 Our Experimental Approach

In this thesis, the interplay between the thermal and disorder fluctuations in HTS's is investigated by studying the vortex properties near the vortex-solid to liquid transitions in $YBa_2Cu_3O_7$ single crystals systematically with different types of static disorder.

1.3.1 Controlled Static Disorder

Most as-grown $YBa_2Cu_3O_7$ single crystals contain two types of defects: twin boundaries which are planar defects extending through the entire sample thickness, and the random point defects associated with oxygen vacancies. To study the effects of static disorder in a controlled manner, we use the ion irradiation technique. This technique allows the flexibility of varying the species, fluences and energies of the irradiating ions to alter the types and densities of the defects created in the sample. The use of ion irradiation technique to modify material properties was first employed in semiconductor research as early as in the 1950s. In the 1970s, the applications of ion irradiation technique on conventional type-II superconductors were mostly on implanting ions into superconducting films to form new metastable alloys which have

better superconducting properties such as higher transition temperatures or higher critical currents (see Ref. (Richard, 1980) and references therein). Shortly after the discovery of HTS's, the ion irradiation technique was carried out to create structural defects without adding foreign species in the HTS samples (van Dover *et al.*, 1989; Vichery *et al.*, 1989; Civale *et al.*, 1990). In our work, two types of ion irradiation were employed to create defects of different nature: 3 MeV protons irradiation and 0.9 GeV Pb-ion irradiation. By using the 3 MeV proton irradiation, we are able to vary the density of randomly distributed point defects. By using the 0.9 GeV Pb-ion irradiation, a unique type of defects, the columnar defects, were created. The columnar defects had an average diameter comparable to the vortex core size at low temperatures. In addition, these parallel defects extend through the entire thickness of the sample, providing a long pinning length and giving rise to very different vortex dynamics from that incurred by random point defect pinning.

1.3.2 Experimental Approach to Studies of Phase Transitions

In order to study the nature of the vortex-solid to liquid transition experimentally, we need to review the basic concepts of critical phenomena near a phase transition[1].

When a system is sufficiently close to the critical point (T_C) of a phase transition, anomalies occur in a variety of static properties such as the magnetization or specific heat, and in dynamic properties such as the transport coefficients and relaxation times. According to the critical scaling hypothesis, long range correlations give rise to the singular behavior near T_c. In other words, the critical anomalies may be asymptotically expressed in terms of the average size of critical fluctuations, the correlation length ξ. For a system with isotropic critical fluctuations, the correlation

[1]For a more comprehensive description of the theory of critical phenomena, see for example Ma, Shang-Keng, *Modern Theory of Critical Phenomena* (W. A. Benjamin, Inc., Advanced Book Program, Massachusetts, 1977) and the review article: Hohenberg and Halperin, Rev. Mod. Phys. **49**, 435 (1977).

length diverges as the temperature (T) approaches the transition temperature (T_c),

$$\xi \sim \left|1 - \frac{T}{T_c}\right|^{-\nu}, \tag{1.1}$$

where ν is the static critical exponent. The dynamic properties are related to the relaxation time τ of thermal fluctuations, which is the time needed to approach thermal equilibrium after a disturbance. As $T \to T_c$, it takes longer and longer to equilibrate the system. This phenomenon is known as the *critical slowing down.* As ξ diverges, the relaxation time also diverges with the relation

$$\tau \sim \xi^z, \tag{1.2}$$

where z is the dynamic critical exponent.

With the development of the renormalization group theory, the idea of scaling hypothesis is linked to an important concept — *universality.* Since the study of critical phenomena concerns the behavior of a system whose correlation length ξ is very large compared to the interatomic spacing, it is natural to suppose that many details of the microscopic Hamiltonian become irrelevant for critical behavior. It follows that systems showing critical phenomena can be divided into groups known as *universal classes*, such that all members of a given class have "identical" critical exponents.

Based on these concepts, second-order phase transitions can be studied experimentally via different physical quantities and using different techniques. Although this thesis emphasizes the electrical transport properties near the vortex phase transitions, other related work conducted in our group has also unambiguously manifested universal critical quantities such as the AC magnetic susceptibility and the third-harmonic transimissivity (Reed *et al.*, 1994; Reed *et al.*, 1995). Since the electrical transport experiment does not measure thermodynamic quantities directly, systematic and self-consistent studies have to be carried out in order to interpret the experimental results properly. The advantage of measuring electrical transport properties is

that it provides a more effective way of investigating vortex motion and dissipation in high-temperature superconductors, as supposed to the specific heat and magnetization measurements which yield very small vortex contributions to a large electric and phonon background.

The electrical transport properties under investigation include the measurements of DC resistivity as a function of the temperature and current in different magnetic fields, and the AC impedance as a function of frequency and temperature in different magnetic fields. The relevant critical exponents are the static critical exponent ν and the dynamic critical exponent z. The critical scaling relations for these physical quantities near the vortex-solid melting temperatures can be obtained based on the critical scaling hypothesis and the symmetry consideration of disorder fluctuations, and will be described in details in Chapters 4 and 5.

1.4 Thesis Overview

The thesis is organized as follows. An introductory theoretical background for the magnetic properties of superconductors is first given in Chapter 2. The basic concepts of superconductivity, the Ginzberg-Landau theory for conventional type-II superconductors near H_{c2}, the consequences of the high transition temperature, short coherence length and long penetration depth in HTS's are discussed. In addition, the elastic properties of the vortex lattice are briefly described. After reviewing the conventional concepts of vortex dissipation due to flux-flow and flux-creep, a recently developed collective flux-creep theory is introduced, and the vortex dissipation in the presence of pinning is considered in the context of vortex bundle hopping and vortex elasticity. Once the existence of a truly nondissipative vortex-solid phase is justified based on the flux-creep model, the theoretical models for the vortex-solid to liquid phase transitions in the presence of different static disorder are introduced.

Chapter 3 describes the basic experimental techniques used for carrying out the investigations in the thesis, including details of the sample preparation and general techniques used for cryogenic measurements. In the sample preparation section, the

ion irradiation techniques are also described, with the point defect creation process detailed in Appendix A. A summary of the sample information for six $YBa_2Cu_3O_7$ single crystals studied in this thesis is also provided in this Chapter.

The main experimental results are presented in Chapters 4 to 6. Chapter 4 focuses on the universality of second-order vortex-glass transitions among various $YBa_2Cu_3O_7$ twinned single crystals with different densities of point defects. Chapter 5 demonstrates the experimental evidence for a second-order Bose-glass transition in $YBa_2Cu_3O_7$ single crystals with parallel columnar defects by showing *universal* critical scaling of frequency-dependent AC resistivity data from 10^2 to 2×10^6 Hz. The signature of the transition, that the Bose-glass transition temperature T_{BG} *decreases* with the increasing angle (θ) between the applied magnetic field and the c-axis, has been confirmed and is in sharp contrast to the smooth *increase* of the vortex-glass temperature (T_M) with increasing θ. Chapter 6 studies two current-induced phenomena in nearly defect-free, untwinned $YBa_2Cu_3O_7$ single crystals. The physical origin of the resistive hysteresis near the vortex-solid melting transition, as well as the nonlinear resistive "peak effect" below the thermodynamic melting transition, are investigated extensively. Finally, Chapter 7 summarizes the contributions of this work.

Chapter 2 Magnetic Properties of Type-II Superconductors

In order to investigate the novel vortex properties of high-temperature superconductors (HTS's), it is necessary to review the magnetic properties of conventional superconductors, particularly the vortex properties of type-II superconductors. This chapter serves as an introduction of the basic concepts and terminology that are required to describe the research presented in later chapters[1]. In addition, the consequences of the high transition temperature, short coherence length and long penetration depth of HTS's will be discussed to illustrate the importance of both thermal and disorder fluctuations on the vortex phase transitions presented in this thesis.

2.1 Meissner Effect and Superconductivity

One of the key signatures of superconductivity is the disappearance of the electrical resistance in certain materials as they are cooled below certain critical temperatures, the superconducting transition temperatures (T_c) (See Fig. 2.1). However, a superconductor is more than a perfect conductor. The expulsion of magnetic flux, the Meissner effect, which is best demonstrated in type-I superconductors as shown in Fig. 2.2, represents an important aspect of superconductivity in addition to the infinite electrical conductivity. However, Meissner effect does not occur exactly everywhere in the superconductor. The magnetic field actually penetrates a rather small but finite distance into the superconducting material. This distance is called the *penetration depth* (λ), within which the shielding supercurrents are flowing. It

[1]For a more comprehensive description of the theory of critical phenomena, see for example Ma, Shang-Keng, *Modern Theory of Critical Phenomena* (W. A. Benjamin, Inc., Advanced Book Program, Massachusetts, 1977) and the review article: Hohenberg and Halperin, Rev. Mod. Phys. **49**, 435 (1977).

is this Meissner effect which makes the superconducting state a thermal equilibrium state. Superconductivity can be destroyed by increasing the magnetic field above the thermodynamic critical field (H_c) which is related to the condensation energy of the superconducting state that differentiates the free energies between the normal and superconducting states. In terms of the energy densities for the normal state $f_n(T)$ and the superconducting state $f_s(T)$, we have (in the cgs units)

$$f_n(T) - f_s(T) = \frac{H_c^2(T)}{8\pi}, \quad T < T_c \tag{2.1}$$

Note that $f_s(T) < f_n(T)$ for $T < T_c$, and $H_c(T) = 0$ for $T > T_c$.

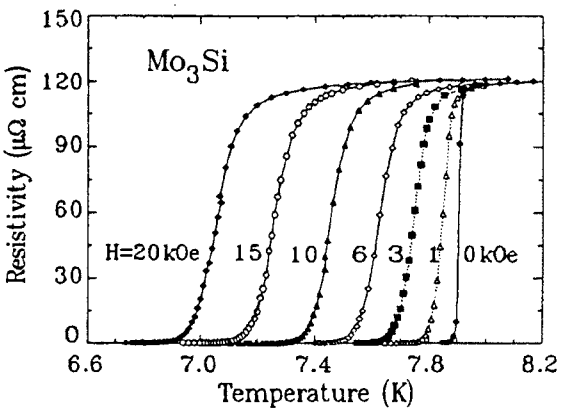

Figure 2.1: Resistance versus temperature curves a conventional superconductor Mo_3Si in different magnetic fields.

2.2 Microscopic Properties of Superconductivity

The microscopic properties of superconductivity for many conventional superconductors in the absence of magnetic field has been well described by the BCS theory (Bardeen *et al.*, 1957). According to this theory, the carriers responsible for superconductivity form the Cooper pairs, which are paired electrons bound by a weak attractive force through the electron-phonon interaction. The Cooper pairs condense into the ground state below the superconducting transition temperature, resulting in an infinite conductivity. The binding energy of the electron pairs is 2Δ, where Δ is

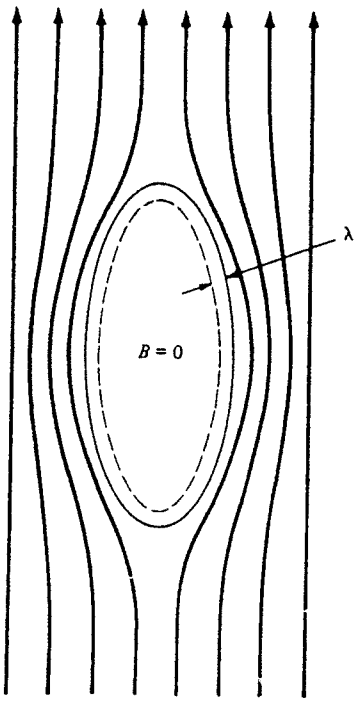

Figure 2.2: Schematic diagram showing the exclusion of magnetic flux from the interior of a superconductor. Here λ is the penetration depth.

called the superconducting gap energy.

2.3 The London Theory

In the presence of an applied magnetic field, the Meissner effect can be phenomenologically explained by the London theory. Since the ground state momentum of the superconductor is zero, i.e., $\mathbf{P} = m^* < \mathbf{v}_s > + e^*\mathbf{A}/c = 0$, where $m^*(= 2m$ for weak-coupling systems, where m is the rest mass of a free electron.) and e^* $(= 2e)$ are the effective electronic mass and charge, respectively, of the Cooper pairs, $\mathbf{v}_s$ is the superfluid velocity and $\mathbf{A}$ is the vector potential. Therefore, the superfluid velocity is given by

$$< \mathbf{v}_s >= -\frac{e^*\mathbf{A}}{m^*c}, \tag{2.2}$$

which is related to the superconducting screening current density $\mathbf{J}_s$ by the expression

$$\mathbf{J}_s = n_s^* e^* < \mathbf{v}_s >= -\frac{n_s^*(e^*)^2\mathbf{A}}{m^* c}. \tag{2.3}$$

From the Maxwell equation

$$\nabla \times \mathbf{h} = \frac{4\pi \mathbf{J}_s}{c}, \tag{2.4}$$

and the magnetic field $\mathbf{h} = \nabla \times \mathbf{A}$, one obtains

$$\nabla^2 \mathbf{h} = \frac{4\pi n_s^*(e^*)^2}{m^* c^2}\mathbf{h} = \frac{1}{\lambda_L^2}\mathbf{h}, \quad \lambda_L^2 = \frac{m^* c^2}{4\pi n_s (e^*)^2} \tag{2.5}$$

which has the solution

$$\mathbf{h} = \mathbf{h}_0 e^{-r/\lambda_L}. \tag{2.6}$$

Here, λ_L is called the London penetration depth.

The London theory is valid when $\mathbf{v}(\mathbf{r})$ and $\mathbf{J}_s(\mathbf{r})$ vary slowly in space. More specifically, since $\mathbf{h}$, $\mathbf{J}_s$ and $\mathbf{v}$ all vary on the scale of λ_L, the London equation holds when $\lambda_L >> \xi_0$, ξ_0 is the superconducting coherence length. One can estimate ξ_0 from the uncertainty principle by considering the relevant momentum space for electrons:

$$E_F - \Delta < \frac{p^2}{2m} < E_F + \Delta, \tag{2.7}$$

where E_F is the Fermi level. Therefore, $\frac{p\delta p}{m} \approx v_F \delta p \approx 2\Delta$, and the coherence length is given by

$$\xi_0 \approx \frac{\hbar}{\delta p} \approx \frac{\hbar}{2\Delta/v_F} = \frac{\hbar v_F}{2\Delta}. \tag{2.8}$$

From Eq.(2.2), one can see that if the magnetic field becomes so large that the kinetic energy of the Cooper pairs exceeds the gap energy, all pairs may break and the sample becomes normal.

2.4 Type-I and Type-II superconductors

Among all superconductors, only cylindrical type-I superconductors have simply

two thermal equilibrium phases in an applied magnetic field: the Meissner phase with complete field expulsion, and the normal phase. The superconductor goes to the normal state through a first-order phase transition at the thermodynamic critical field $H_c(T)$. In a type-I superconductor of an arbitrary shape, due to the demagnetization factor of the sample, there is generally an intermediate state when magnetic field can enter the superconductor as discrete normal domains, as shown in Fig. 2.3, each containing many flux quanta. The real magnetic field distribution pattern can be very complicated and has been beautifully illustrated in the work of Huebener (Huebener, 1979).

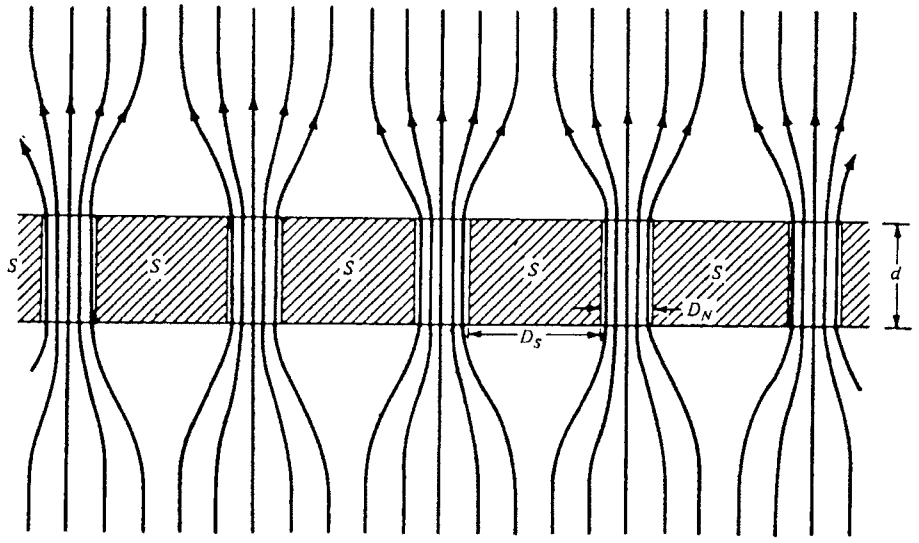

Figure 2.3: Schematic diagram showing magnetic flux channeling through the normal region in the intermediate state of type-I superconductors.

In type-II superconductors, the Meissner state occurs only at fields below the lower critical field H_{c1}(see Fig. 1.1(b)). In higher fields, the magnetic field penetrates the sample in the form of quantized fluxoids enclosed by vortices of shielding currents (see Fig. 2.4). Each vortex contains one flux quantum, $\Phi_0 = 2.07 \times 10^{-7}$ Gauss cm^2. This state is called the mixed state, or the vortex state. Because each vortex contains exactly one flux quantum, the density of vortices must increase with increasing applied field until the upper critical field H_{c2} is reached, at which the entire sample becomes normal.

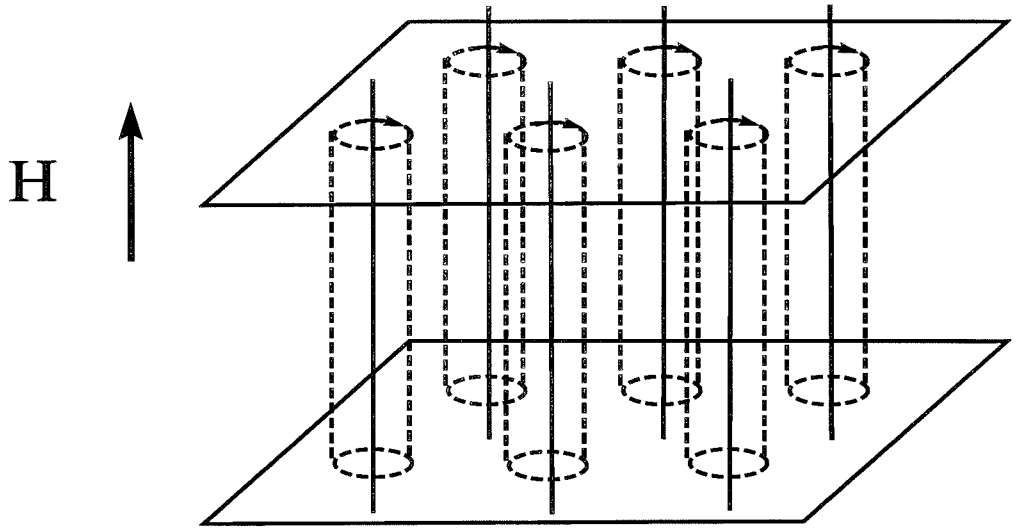

Figure 2.4: Schematic diagram of a vortex lattice of a type-II superconductor in an applied magnetic field **H**.

2.5 The Ginzburg-Landau Theory

To understand the difference between type-I and type-II superconductors, we need to introduce the Ginzburg-Landau theory. The Ginzburg-Landau (GL) theory (Ginzburg & Landau, 1950) is based on purely phenomenological concepts. However, Gor'kov has shown (Gor'kov, 1958; Gor'kov, 1959) that, for both very pure and very dirty superconductors, the GL theory follows rigorously from the BCS theory near $H_{c2}(T)$, provided that the spatial variations of both the order parameter and of the magnetic field are slow.

The starting point of GL theory is to express the free-energy density in terms of the *superconducting order parameter* $\psi = |\psi|e^{i\varphi}$ as follows,

$$f = f_n + \alpha(T)|\psi|^2 + \frac{\beta(T)}{2}|\psi|^4 + \frac{1}{2m^*}\left|\left(\frac{\hbar}{i}\nabla - \frac{e^*}{c}\mathbf{A}\right)\psi\right|^2 + \frac{h^2}{8\pi}, \qquad (2.9)$$

where h is the local magnetic field. For $\psi = 0$, we have $f = f_n + h^2/(8\pi)$, i.e., the free-energy density of the normal state. The meaning of the order parameter becomes clear from its relation with the density of the Cooper pairs n_s given by $n_s(\mathbf{r}) = |\psi(\mathbf{r})|^2$.

Following a standard variational procedure, one finds two *GL differential equa-*

tions,

$$\alpha\psi + \beta|\psi|^2\psi + \frac{1}{2m^*}\left(\frac{\hbar}{i}\nabla - \frac{e^*}{c}\mathbf{A}\right)^2\psi = 0 \tag{2.10}$$

and

$$\mathbf{J_s} = \frac{e^*h}{2m^*i}(\psi^*\nabla\psi - \psi\nabla\psi^*) - \frac{e^{*2}}{m^*c}\psi^*\psi\mathbf{A}, \tag{2.11}$$

and the boundary condition for a superconductor-insulator surface satisfies

$$\left(\frac{h}{i}\nabla - \frac{e^*}{c}\mathbf{A}\right)|_n\psi = 0, \tag{2.12}$$

where the subscript n denotes the component normal to the surface.

These equations yield the *coherence length*

$$\xi_s(T) = \sqrt{\frac{\hbar^2}{2m^*|\alpha(T)|}}, \tag{2.13}$$

which represents the natural length scale for spatial variations of the superconducting order parameter ψ, and the magnetic field *penetration depth*

$$\lambda(T) = \left[\frac{m^*c^2}{4\pi e^{*2}\psi_0^2(T)}\right]^{1/2}, \tag{2.14}$$

where $\psi_0^2 = -\alpha/\beta$. Since $\lambda(T)$ and $\xi_s(T)$ have the same temperature dependence of $\xi_s(T) \sim \lambda(T) \sim |T - T_c|^{-1/2}$ near T_c, it is useful to introduce the ratio of these two length scales

$$\kappa = \frac{\lambda}{\xi_s}, \tag{2.15}$$

which is nearly constant, at least near T_c. This ratio κ is called the Ginzburg-Landau parameter and its value determines whether a superconductor is of type-I or type-II.

As shown in Fig. 2.5, near the boundary from a superconducting state material to a normal state material in an external magnetic field, neither the superconducting parameter nor the magnetic field can vanish abruptly at the boundary. Instead, the order parameter drops off over a characteristic length scale ξ_s, and the magnetic field drops off over another length scale λ. As a consequence, we encounter an increase of

free energy due to the loss of negative condensation energy in the superconducting region as the result of the increasing normal region near the interface. The increase of free energy per unit area is approximately $\xi_s H_c^2/(8\pi)$. On the other hand, the penetration of magnetic fields into the superconducting phase results in a reduction of the magnetic energy which is about $\lambda H_c^2/(8\pi)$ per unit area of the interface. Therefore, the domain-wall energy per unit area of the interface becomes

$$\gamma = \frac{H_c^2}{8\pi}(\xi_s - \lambda). \tag{2.16}$$

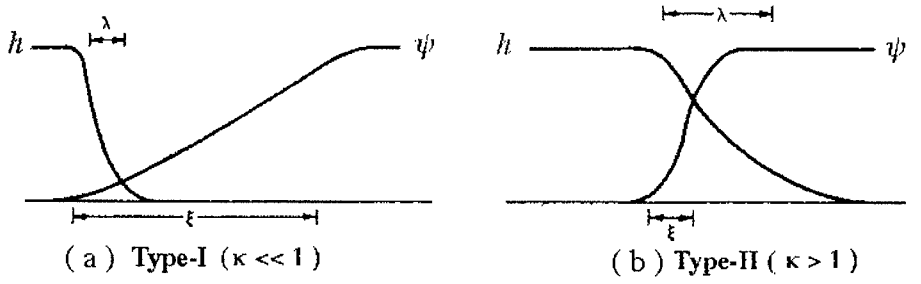

Figure 2.5: Schematic superconductor-normal material interface in the case of (a) type-I ($\kappa << 1$), and (b) type-II ($\kappa > 1$) superconductors. Here h is the magnetic field and ψ is the superconductiong order parameter.

It is found that for type-I superconductors ($\xi_s >> \lambda$ or $\kappa << 1$), the domain wall energy is positive and for type-II superconductors ($\xi_s < \lambda$ or $\kappa > 1$), the domain wall energy becomes negative, and therefore the latter case favors flux penetration. Figure 2.5 demonstrates a superconducting-normal metal interface for both type-I and type-II superconductors. Note that Eq. 2.16 is only a simple estimate. Following Ginzburg-Landau theory, the exact crossover from positive to negative wall energy is found to occur at $\kappa = 1/\sqrt{2}$. Subsequently, Abrikosov showed that (Abrikosov, 1957) the negative wall energy in type-II superconductors causes the flux-bearing (normal) regions to subdivide until a quantum limit is reached, in which each quantum of flux Φ_0 passes through the sample as a distinct flux tube at low temperatures. The diameter of each tube is about the superconducting coherence length ξ_s. With the increasing temperature, the vortex diameter ξ_s grows until the entire sample

becomes normal beyond a temperature T_{c2} determined by $H_{c2}(T) = \Phi_0/(2\pi\xi_s(T))$. On the other hand, for a given temperature, the density of vortices increases with the increasing magnetic field until $H_{c2}(T)$ when the entire sample becomes normal.

The high-temperature superconductors are extreme type-II superconductors with $\kappa \sim 100$. The coherence length ξ_s of HTS's is very small compared to that of the conventional type-II superconductors. For example, the anisotropic coherence lengths of $YBa_2Cu_3O_7$ are $\xi_s^{ab} \approx 12$ to 18Å and $\xi_s^c \approx 2$ to 3Å in the *ab*-plane and along the *c*-axis, respectively (Welp *et al.*, 1989a), both values much smaller than that of the conventional superconductor Nb which is $\xi_s \approx 380$Å. Large T_c and short ξ_s result in large thermal fluctuations near T_c. The size of the critical regime, $Gi \equiv |1 - T_f/T_c|$, within which the thermal fluctuations are important and therefore mean-field theory is no longer applicable, can be estimated from the Ginzburg-Landau theory. Using the Ginzburg criterion, T_f is the "fluctuation" temperature when $|\delta\psi/\psi|^2(T_f) = 1$ is satisfied, where $\delta\psi$ denotes the critical fluctuation of the superconducting order parameter.This criterion yields (Ginzburg, 1950; Lobb, 1987)

$$Gi \approx \frac{1}{2}\left(\frac{k_B T_c}{H_c^2(0)\xi_s^3(0)}\right)^2 = \frac{16\pi^3\kappa^4}{\Phi_0^3}\frac{k_B T_c^2}{H_{c2}(0)}, \tag{2.17}$$

where in the second step we have used the relation $H_c(T) = H_{c2}(T)/(\sqrt{2}\kappa)$ for type-II superconductors. For anisotropic HTS's, the superconducting coherent volume ξ_s^3 becomes $(\xi_s^{ab})^2\xi_s^c$. With an anisotropy factor ε defined as the square root of the ratio of the effective mass in the ab-plane to that along the c-axis, $\varepsilon = \sqrt{m/M} = \xi_s^c/\xi_s^{ab}$, where Eq. 2.13 for the relation between ξ_s and the effective mass has been used. Therefore, Eq. 2.17 yields

$$Gi \approx \frac{1}{2}\left(\frac{k_B T_c}{H_c^2(0)\varepsilon(\xi_s^{ab})^3(0)}\right)^2 = \frac{16\pi^3\kappa^4}{\Phi_0^3}\frac{k_B T_c^2}{\varepsilon^2 H_{c2}^{ab}(0)}. \tag{2.18}$$

For HTS's such as $YBa_2Cu_3O_7$ superconductors, $T_c \approx 93$ K, $H_{c2}^{ab}(0) \approx 5 \times 10^5$ G, $\kappa \approx 80$ and $\varepsilon \sim 1/7$, resulting a Gi of the order of 10^{-3} K, much larger than that of conventional superconductors which is typically less than 10^{-6}. That is why fluctua-

tion effects in most type-II superconductors are only important when the temperature is very close to the critical temperature. Therefore, the discovery of HTS's opens up new experimental opportunities for studying the thermal fluctuation effects in superconductors. In addition, we note that the superconducting transition temperature T_c in Eq.2.18 can be generalized to a critical temperature of a second-order vortex phase transition, with the critical field adjusted correspondingly.

Various novel vortex properties in HTS's can be attributed to the large Ginzburg-Landau parameter, $\kappa \equiv \lambda/\xi_s$, in addition to the large fluctuation effects. With a small coherence length, the vortices in HTS's are very sensitive to the effects of sample disorder. With a large penetration depth compared to the average vortex lattice constant, the magnetic fields of the vortices strongly overlap each other, even though the vortex positions can still be identified from the zero points of the superconducting order parameter. Therefore there is no well-defined, discrete flux line lattice in HTS's. Overall, the large κ results in a "soft" vortex lattice in HTS's with a small elastic deformation energy. To understand the softening of the vortex lattice, we introduce key concepts about vortex interactions and vortex lattice elasticity in the following section.

2.6 Vortex Interactions and Vortex Lattice Elasticity

The simplest approach to understanding vortex interactions is to start with the line energy of a single flux line and the interaction of two parallel flux lines.

2.6.1 Vortex Line Energy and Interaction Between Two Parallel Flux Lines

The line energy per unit length (the line tension ϵ_l) of an isolated vortex line can be obtained by considering the magnetic and kinetic energies associated with the

vortex (excluding the core):

$$\epsilon_l = \int_{(r>\xi_s)} d\mathbf{r}\frac{1}{8\pi}[\mathbf{h}^2 + \lambda^2(\nabla \times \mathbf{h})^2], \tag{2.19}$$

in the limit $\lambda >> \xi_s$. Minimizing ϵ_l relative to gives

$$\mathbf{h} + \lambda^2 \nabla \times \nabla \mathbf{h} = 0 \qquad |r| > \xi_s. \tag{2.20}$$

Since the vortex core size ξ_s is small, the core contribution to the line tension can be expressed as a two-dimensional delta function and rewritten into

$$\mathbf{h} + \lambda^2 \nabla \times \nabla \mathbf{h} = \Phi_0 \delta_2(r), \tag{2.21}$$

where $\Phi_0 = \Phi_0 \hat{n}$ and $\hat{n}$ is a vector along the line direction. The solution of Eq.(2.21) together with the Maxwell equation $\nabla \cdot \mathbf{h} = 0$ gives

$$h = \frac{\Phi_0}{2\pi\lambda^2} K_0\left(\frac{r}{\lambda}\right), \tag{2.22}$$

where K_0 is the zero-order modified Bessel function. The line tension is then

$$\epsilon_l = \left(\frac{\Phi_0}{4\pi\lambda}\right)^2 \ln\left(\frac{\lambda}{\xi_s}\right). \tag{2.23}$$

Next we consider two parallel flux lines directed along the z axis with positions $\mathbf{r}_1 = (x_1, y_1)$, $\mathbf{r}_2 = (x_2, y_2)$. The magnetic field distribution is determined by the equation

$$\mathbf{h} + \lambda^2 \nabla \times \nabla \mathbf{h} = \Phi_0[\delta(\mathbf{r} - \mathbf{r}_1) + \delta(\mathbf{r} - \mathbf{r}_2)]. \tag{2.24}$$

The solution $\mathbf{h}$ is the superposition of the field $\mathbf{h}_1$ and $\mathbf{h}_2$ due to the flux lines 1 and 2:

$$h(r) = h_1(r) + h_2(r) \tag{2.25}$$

$$h_i = \frac{\Phi_0}{2\pi\lambda^2} K_0\left(\frac{(r_1 - r_2)}{\lambda}\right), \qquad i = 1, 2. \tag{2.26}$$

The energy of the system is therefore

$$\epsilon_l = \int d\mathbf{r} \frac{1}{8\pi}[\mathbf{h}^2 + \lambda^2(\nabla \times \mathbf{h})^2] = 2\epsilon_l + U_{12}, \tag{2.27}$$

where U_{12} represents the interaction between the two flux lines

$$U_{12} = \frac{\Phi_0 h_{12}}{4\pi}, \qquad h_{12} = h_1 = h_2. \tag{2.28}$$

This is a repulsive energy which decreases as $(1/\sqrt{r_{12}})e^{-r_{12}/\lambda}$ at large distances, and diverges as $\ln(|\lambda/r_{12}|)$ at short distances.

2.6.2 Lower Limit for Flux Penetration and H_{c1}

For a vortex lattice, the Gibbs free energy density can be written as:

$$G = n_L \epsilon_l + \sum_{ij} U_{ij} - \frac{BH}{4\pi}, \tag{2.29}$$

where the first term represents the individual energies of the lines, n_L is the real density of flux lines which is related to the induction B by

$$B = n_L \Phi_0; \tag{2.30}$$

the second term in Eq.(2.29) describes the interaction between vortices; and the last term gives the magnetic energy density which favors large values of B.

At very low line densities (low B), the interaction term is small and can be neglected. From

$$G \approx B\left(\frac{\epsilon_l}{\Phi_0} - \frac{H}{4\pi}\right), \tag{2.31}$$

we can see that for $H > 4\pi\epsilon_l/\Phi_0$, G can be lowered by choosing $B \neq 0$ so that there is some flux penetration. Therefore, the first penetration field, the lower critical field H_{c1}, is given by

$$H_{c1} = \frac{4\pi\epsilon_l}{\Phi_0} = \frac{\Phi_0}{4\pi\lambda^2} \ln \frac{\lambda}{\xi_s}. \tag{2.32}$$

2.6.3 Abrikosov Lattice and Upper Critical Field H_{c2}

In large magnetic fields, the superconducting order parameter becomes small so that the GL differential equation (Eq.(2.10)) can be linearized by neglecting the higher order terms in $|\psi|$:

$$\frac{1}{2m}\left(-i\hbar\nabla - \frac{2e\mathbf{A}}{c}\right)^2 \psi = -\alpha\psi. \tag{2.33}$$

Consider the case of an infinite medium in the xy plane with $\mathbf{H}$ along z-axis. Equation (2.33) together with the London gauge $\nabla \cdot \mathbf{A} = 0$ describes a particle of mass m^* moving in a circle in the xy plane with the frequency

$$\omega_c = \frac{2eH}{m^*c} \tag{2.34}$$

and a constant velocity v_z along the field. The eigenvalues are the Landau levels

$$\epsilon_n = (n + 1/2)\hbar\omega_c + (1/2)m^*v_z^2. \tag{2.35}$$

The lowest level and therefore the highest field (H_{c2}) at which superconductivity can nucleate in the interior of a large sample corresponds to $n = 0$, $v_z = 0$. This leads to

$$\frac{1}{2}\hbar\omega_c = -\alpha = \frac{\hbar^2}{2m^*\xi_s^2}, \tag{2.36}$$

which gives

$$H_{c2} = \frac{\Phi_0}{2\pi\xi_s^2}. \tag{2.37}$$

In addition, from the following equations,

$$\frac{H_c^2}{8\pi} = \frac{\alpha^2}{2\beta}, \tag{2.38}$$

$$H_{c2} = \sqrt{2}\kappa H_c, \tag{2.39}$$

we find that, if $\kappa > 1/\sqrt{2}$ ($H_c < H_{c2}$), a condensed phase will appear in the bulk of the sample for fields $H < H_{c2}$. This phase cannot correspond to a complete exclusion of

the magnetic flux, since a complete Meissner effect is energetically unfavorable at fields $H > H_c$. When the external magnetic field is very close to H_{c2}, Abrikosov demonstrated that there exists close packed flux lines forming a triangular or square vortex lattice, with each flux line containing one flux quantum (Abrikosov, 1957). Such a vortex lattice structure has been verified experimentally. On the other hand, when $\kappa < 1/\sqrt{2}$ ($H_{c2} < H_c$), a complete Meissner effect takes place when H is decreased below H_c. In this case, the superconductor is therefore a type-I superconductor.

2.6.4 Elastic Properties of the Flux Line Lattice (FLL)

In general, the vortex lattice is not in its equilibrium configuration but rather in some distorted state. The elasticity of a vortex lattice describes how the lattice respond s to elastic distortions such as thermal fluctuations or static disorder. The nonlocal elastic theory of a vortex lattice in an isotropic superconductor has been worked out by Brandt (Brandt, 1977) using the GL description at high inductions $B > 0.6H_{c2}$ and the London theory for small fields $B < 0.2H_{c2}$.

Define the displacement field of an elastically deformed flux line lattice as $\mathbf{u}_\nu(z)$,

$$\mathbf{u}_\nu(z) = \mathbf{r}_\nu(z) - \mathbf{R}_\nu, \tag{2.40}$$

where $\mathbf{r}_\nu(z) = (x_\nu(z); y_\nu(z); z)$ and $\mathbf{R}_\nu = (X_\nu; Y_\nu; z)$ are the displaced and regular lattice positions of the νth flux line, respectively. Note that $\mathbf{u}_\nu(z) = (u_\nu^x(z); u_\nu^y(z); 0)$ is a two-dimensional vector. Its Fourier transform is

$$\mathbf{u}(\mathbf{k}) = \sum_\nu \int dz e^{-i\mathbf{k}\cdot\mathbf{R}_\nu} \mathbf{u}_\nu(z). \tag{2.41}$$

The corresponding inverse Fourier transform is

$$\mathbf{u}_\nu(z) = \int_{BZ} \frac{d^3k}{(2\pi)^3} e^{i\mathbf{k}\cdot\mathbf{R}_\nu} \mathbf{u}(\mathbf{k}), \tag{2.42}$$

where the integration is over the two-dimensional Brillouin zone (BZ) of the vortex

lattice. Within local elastic theory, the energy of such a distorted state is given by (Brandt, 1977; Blatter *et al.*, 1994)

$$\begin{aligned}\mathcal{F}[\mathbf{u}_\nu(z)] &= \mathcal{F}[\mathbf{r}_\nu(z)] - \mathcal{F}[\mathbf{R}_\nu(z)] \\ &= \frac{1}{2}\left[\sum_\mu \sum_\nu \int dz \int dz' \Phi_{\mu\nu}(\mathbf{r}-\mathbf{r}') u_\nu(\mathbf{r}) u_\mu(\mathbf{r}') \right. \\ &\quad \left. - \sum_\nu \int dz f_\nu(z) u_\nu(z)\right]\end{aligned} \tag{2.43}$$

where $\Phi(\mathbf{r})$ is the elastic matrix of the vortex lattice, and $f_\nu(z)$ is the force field which generates the distortion $\mathbf{u}_\nu(z)$. Here, the harmonic approximation has been used. While expressing $\mathcal{F}$ in term of $\mathbf{u}(\mathbf{k})$, we have

$$\mathcal{F}[\mathbf{u}] = \frac{1}{2}\int_{BZ} \frac{d^3k}{(2\pi)^3}\left[u_\alpha(k)\Phi_{\alpha\beta}(k)u_\beta(-k) - f_\beta(k)u_\beta(-k)\right], \tag{2.44}$$

where $\Phi(k)$ and $f(k)$ are the Fourier transformations of $\Phi(\mathbf{r})$ and $\mathbf{f}_\nu(z)$, respectively. In the low fields with $B <\sim 0.2H_{c2}$ when the vortex cores do not overlap and the London theory is applicable, the elastic matrix can be expressed as (Brandt, 1977; Blatter *et al.*, 1994)

$$\Phi_{\alpha\beta}(\mathbf{k}) = \frac{B^2}{4\pi}\sum_\nu [f_{\alpha\beta}(\mathbf{k}+\mathbf{K}_{\nu'}) - f_{\alpha\beta}(\mathbf{K}_{\nu'})], \tag{2.45}$$

with

$$f_{\alpha\beta}(\mathbf{k}) = (k_\alpha k_\beta + \delta_{\alpha\beta}k_z^2)V^{int}(\mathbf{k}), \tag{2.46}$$

$\mathbf{K}_{\nu'}$ being the two-dimensional reciprocal lattice vector, and $V^{int}(\mathbf{k})$ the interaction potential between two vortex segments. For a regular triangular lattice, both $\mathbf{R}_\nu$ and $\mathbf{K}_{\nu'}$ can be reduced to two-dimensional vectors: $\mathbf{R}_\nu = (n\frac{\sqrt{3}}{2}a_0, \frac{2m+n}{2}a_0, z)$, $\mathbf{K}_\nu = 2\pi(\frac{2n-m}{\sqrt{3}a_0}, \frac{n}{a_0})$, where m and n are two integers. In the nonlocal continuum limit (Brandt, 1977; Blatter *et al.*, 1994),

$$\Phi_{\alpha\beta}(k) = [c_{11}(k) - c_{66}]K_\alpha K_\beta + \delta_{\alpha\beta}[c_{66}K^2 + c_{44}(k)k_z^2], \tag{2.47}$$

with $c_{11}(k)$ and $c_{44}(k)$ denoting the dispersive compression and tilt moduli and c_{66} the non-dispersive shear modulus. Here, $\mathbf{K} = (k_x, k_y)$, and $k^2 = K^2 + k_z^2$. From Eqs. (2.44)-(2.47), the elastic energy can then be expressed in terms of the elastic moduli as

$$\mathcal{F}[\mathbf{u}(\mathbf{k})] = \frac{1}{2}\int \frac{d^3k}{(2\pi)^3}\left\{c_{11}(\mathbf{k})[\mathbf{K}\cdot\mathbf{u}(\mathbf{k})]^2 + c_{66}[\mathbf{K}_\perp\cdot\mathbf{u}(\mathbf{k})]^2 + c_{44}(\mathbf{k})[k_z u(\mathbf{k})]^2 - \mathbf{f}(-\mathbf{k})\cdot\mathbf{u}(\mathrm{k})\right\}, \tag{2.48}$$

with $\mathbf{K}_\perp = (k_y, -k_x)$. Correspondingly, in terms of $\mathbf{u}(\mathbf{r})$,

$$\mathcal{F}[\mathbf{u}] = \frac{1}{2}\int d^3r[(c_{11} - c_{66})(\nabla\cdot\mathbf{u})^2 + c_{66}(\nabla_\perp\cdot\mathbf{u})^2 + c_{44}(\partial_z\mathbf{u})^2]. \tag{2.49}$$

Within the local *isotropic* approximation (corresponding to taking $\mathbf{K}_{\nu'} = 0$ in equation 2.47), the resulting compression and tilt moduli are

$$c_{11}(k) \approx c_{44}(k) \approx \frac{B^2}{4\pi}\frac{1}{1+\lambda^2k^2}, \tag{2.50}$$

and the shear modulus is zero such that this description applies to a vortex liquid phase. The nonlocal terms ($\mathbf{K}_{\nu'} \neq 0$) which correspond to nonlocal interactions add up to produce a finite shear modulus

$$c_{66} \approx \frac{\Phi_0 B}{(8\pi\lambda)^2}, \tag{2.51}$$

which is essentially non-dispersive. The corrections of $\mathbf{K}_{\nu'} \neq 0$ terms to c_{11} and c_{44} are small.

In the high induction limit, GL theory yields an expression for the elastic matrix which is similar to the London results in Eq.(2.47) except for a double sum over two sets of reciprocal lattice vectors $\mathbf{K}_{\nu'}$ and $\mathbf{G}_{\nu'}$ (Brandt, 1977). For a regular triangular lattice, $\mathbf{G}_{\nu'}$ can be expressed as $\mathbf{G}_{m'n'} = m'\mathbf{G}_{10} + n'\mathbf{G}_{11}$, where G_{10} and G_{11} are the Brillouin zone boundary vectors. Also, the reduction in the order parameter at large fields renormalizes the length scales λ and ξ_s to $\lambda' = \lambda/(1-b)^{1/2}$ and $\xi_s' = \xi_s/(1-b)^{1/2}$, with the reduced field $b \equiv B/H_{c2}$ (Brandt, 1977; Brandt, 1986; Brandt, 1991).

It is the dispersive behavior and the renormalization of the penetration depth in the compression and tilt moduli $c_{11}(k)$ and $c_{44}(k)$ shown in Eq.(2.50) that leads to a considerable softening of the vortex lattice. Near the BZ boundary $K_{BZ} \approx \sqrt{4\pi}/a_0$ a suppression factor $(\lambda K_{BZ})^2 \approx B \ln(\kappa/H_{c1})$ is obtained with respect to the value at $k = 0$ describing a uniform distortion. In the HTS's, κ is of the order of 100, and the lower critical field H_{c1} is small due to a larger λ (see Eq.(2.32)). Thus the softening of the lattice is an important effect in the high field limit. In addition, in HTS's the shear modulus c_{66} goes to zero before H_{c2} is reached, resulting in a novel vortex phase, the vortex-liquid phase, between the normal phase and the vortex-solid phase.

2.7 Vortex Dissipation

So far, the vortex motion in superconductors has not been discussed. Let us now consider the effects of vortex motion. It is known that the presence of an applied current can give rise to vortex dissipation. However, such dissipation is generally negligible in conventional superconductors so that various type-II superconductors can be used to make superconducting solenoids which can supply steady fields of over 100 kOe without noticeable dissipation of energy. The ability of making superconducting magnets with these type-II superconductors is one of their most important applications, and the issue of vortex dissipation under the influence of a finite applied current is undoubtedly of both fundamental and applied concern.

To consider the vortex dissipation due to finite applied currents, consider the Lorentz force on a fluxoid:

$$\mathbf{F}_L = \mathbf{J} \times \mathbf{\Phi}_0. \tag{2.52}$$

Because of this force, flux lines tend to move transverse to the current, provided that the Hall angle is small. If vortices respond to the force by moving with a velocity $\mathbf{v}$ along the direction of $\mathbf{F}_L$, an electric field $\mathbf{E} \parallel \mathbf{J}$ is induced, since

$$\mathbf{E} = \mathbf{B} \times \mathbf{v}. \tag{2.53}$$

The existence of a finite electric field **E** under a finite current density **J** corresponds to a finite resistivity and therefore dissipation in the superconductor. Therefore, a type-II superconductor in a magnetic field $H > H_{c1}$ will show resistance and will be unable to sustain a persistent current unless some mechanism exists which prevents the Lorentz force from moving the vortices. Such a mechanism is called a "pinning" force.

2.7.1 Theory of Flux Flow

Flux flow occurs when pinning is negligible, so that the vortex motion is only retarted by the viscous drag, i.e.,

$$J\Phi_0 = \eta v, \tag{2.54}$$

with η the viscosity per flux line length. This vortex motion gives rise to a flux-flow resistivity,

$$\rho_f = \frac{E}{J} = \frac{vB}{J} = \frac{vB}{\eta v/\Phi_0} = \frac{B\Phi_0}{\eta}. \tag{2.55}$$

According to the Bardeen-Stephen model (Bardeen & Stephen, 1965), each vortex contains a normal core with a diameter of ξ_s, the superconducting coherence length. In the flux-flow limit, the total dissipation is a fraction of the normal resistivity:

$$\rho_f \approx \rho_n \frac{\xi_s^2}{a_0^2} \approx \rho_n \frac{B}{H_{c2}(T)}. \tag{2.56}$$

Comparing Eqs. (2.55) and (2.56), the Bardeen-Stephen viscosity is therefore given by

$$\eta = \frac{H_{c2}(T)}{\rho_n \Phi_0}. \tag{2.57}$$

Since the flux-flow resistivity is current independent as shown in Eq.(2.55), the current-voltage characteristic in the limit of flux-flow is linear.

2.7.2 Conventional Flux-Creep Theory

The first theoretical model for the vortex dissipation in the presence of pinning is the Anderson-Kim theory (Anderson, 1962; Anderson & Kim, 1964) of flux creep. In this theory, vortex bundles are effectively modeled as a single, approximately independent, zero-dimensional "particle" moving in a random pinning potential U_p. Vortex bundles can hop from one local pinning well to another due to thermal fluctuations and Lorentz force. As shown in Fig. 2.6, in the absence of a transverse current, the probability is the same for hopping along any direction. With a transverse current, it becomes easier for the flux bundle to hop along the direction of the Lorentz force exerted by the current. In this case, the hopping rate is determined by the following relation:

$$\nu_{hop} = \nu_0[e^{-(U_p-\Delta W)/(k_BT)} - e^{-(U_p+\Delta W)/(k_BT)}], \tag{2.58}$$

where ν_0 is the attempt frequency, ΔW is the work done by the Lorentz force (Anderson & Kim, 1964). Defining a hopping distance w and a coherent volume of the flux bundle V_c, U_p and ΔW can be expressed as

$$U_p = (J_c B r_p)V_c, \tag{2.59}$$

$$\Delta W = (JBw)V_c, \tag{2.60}$$

where r_p is the pinning range, J is the applied current and B is the magnetic field inductance.

The hopping rate gives rise to a net flux-creep velocity $v = \nu_{hop} w$. The vortex dissipation is therefore

$$\rho = \frac{E}{J} = \frac{|v \times B|}{J} = \frac{2\nu_0 wB}{J} \sinh\left(\frac{\Delta W}{k_BT}\right) e^{-U_p/(k_BT)}. \tag{2.61}$$

In conventional superconductors the pinning potential U_p is large, the temperature is

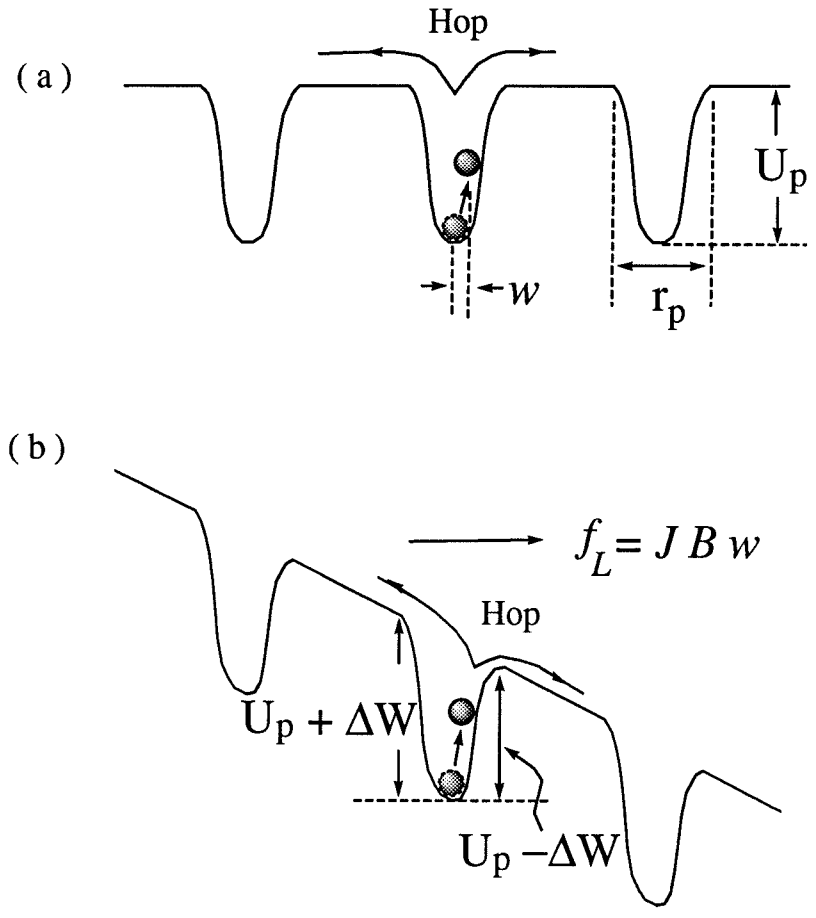

Figure 2.6: Schematic diagram of vortex bundles hopping due to thermal fluctuations (a) in the absence of an applied current when the probability is the same for hopping towards left and right, and (b) in the presence of an applied current when it is easier for the vortex bundles to hop towards right due to an effectively smaller energy barrier. Here f_L is the Lorentz force density. See the text for the definition of other quantities.

low, and therefore the creep is weak if $J << J_c$, and

$$\rho \rightarrow \left[\frac{\nu_0 w^2 B^2 V_c}{k_B T}\right] e^{-U_p/(k_B T)}. \tag{2.62}$$

In the limit of $(J_c - J)/J_c << 1$, i.e., when the current density is very close to the critical current density, since $\sinh(\Delta W/(k_B T)) \approx \frac{1}{2} e^{\Delta W/(k_B T)}$,

$$\rho \approx \frac{\nu_0 w B}{J} e^{-(U_p - \Delta W)/(k_B T)}. \tag{2.63}$$

This theory established the concept the hopping conductivity of vortex bundles. However, the pinning potential U_p in Eq.(2.59) remains finite even as $J << J_c$, which means a nonzero flux creep resistivity $\rho \sim e^{-U/(k_B T)}$ at any finite temperature.

Since vortex lines are extended one-dimensional objects, the consideration of elasticity and collective interactions of vortices is in fact essential. A recently developed theory, the collective flux creep theory (Feigel'man *et al.*, 1989), has taken this more rigorous approach, (in contrast to the single vortex pinning model by Anderson & Kim), which leads to a diverging energy barrier at low temperatures as $J \to 0$.

2.7.3 Collective Flux-Creep Theory

The starting point of collective pinning theory (Feigel'man *et al.*, 1989) is the elastic free energy (see Eq.(2.49)) in the presence of weak pinning,

$$\mathcal{F}[\mathbf{u}] = \int d^3\mathbf{r} \left[\frac{(c_{11} - c_{66})}{2} (\nabla \cdot \mathbf{u})^2 + \frac{c_{66}}{2} (\nabla_\perp \cdot \mathbf{u})^2 + \frac{c_{44}}{2} (\partial_z \mathbf{u})^2 + U_{pin}(\mathbf{r}, \mathbf{u}) \right]. \quad (2.64)$$

Here, the two-dimensional vector $\mathbf{u}(\mathbf{r})$ is the displacement field of the flux-line lattice in the continuum limit; c_{11}, c_{44} and c_{66} are bulk, tilt, and shear elastic moduli, respectively, and $U_{pin}(\mathbf{r}, \mathbf{u})$ is the random potential describing the lattice interaction with the static defects. The random potential leads to the destruction of long-range translational order in the vortex lattice. It has been shown in the collective pinning theory by Larkin and Ovchinnikov (Larkin & Ovchinnikov, 1979) that a new set of correlation lengths, R_c and L_c for the transverse and longitudinal correlation lengths (relative to the $\mathbf{B}$ direction) for vortices, can be used to describe the elastic response of the vortex lattice to the presence of pinning disorder. Defining W as the mean-square value of random force produced by defects, Larkin and Ovchinnikov (Larkin & Ovchinnikov, 1979) find that

$$L_c \simeq R_c (c_{44}/c_{66})^{1/2}, \qquad R_c \simeq c_{44}^{1/2} c_{66}^{3/2} \xi_s^2 / W. \quad (2.65)$$

In addition, the critical current density J_c is given by (Larkin & Ovchinnikov, 1979):

$$J_c \simeq (W/V_c)^{1/2} B^{-1} \simeq c_{66}\xi_s/(R_c^2 B), \tag{2.66}$$

where $V_c \approx R_c^2 L_c$ is the vortex correlation volume.

In the case of collective pinning, the flux bundle activation barrier $U(J)$ is comparable to the elastic energy of the hopping flux bundle. In the presence of a current, the flux bundle hopping distance (u_{hop}) can be estimated from the relation (Feigel'man *et al.*, 1989)

$$JBu_{hop}(J) \sim c_{66}u_{hop}^2(J)/R_\perp^2(J), \tag{2.67}$$

where $R_\perp$ is the size of the bundle in the direction of the vector $\mathbf{B} \times \mathbf{u}_{hop}$ where the correlation volume $V_c = R_\perp R_\parallel L_c$, and $R_\parallel \approx \left(\frac{C_{11}}{C_{66}}\right)^{\frac{1}{2}} R_\perp$. The first term in Eq.(2.67) corresponds to the work done by the current per unit volume and the second term describes the elastic energy density due to $u_{hop} > 0$. It has been shown (Feigel'man *et al.*, 1989) that the relation between the hopping distance (u_{hop}) and the bundle size ($R_\perp$) follows that of the displacement field (u) at the distance R

$$u(R) = < |\mathbf{u}(\mathbf{r}) - \mathbf{u}(\mathbf{r}+\mathbf{R})|^2 >^{1/2} \propto R^\zeta, \tag{2.68}$$

where $\zeta > 0$. Using the relation $U(J) \sim JBV_c u_{hop}(J) \sim JR_\parallel R_\perp^{(d-1)} u_{hop}(J)$, and substituting Eq.(2.68) into (2.67), one obtains

$$U(J) \sim J^{-\mu} \tag{2.69}$$

where $\mu = (d-2+2\zeta)/(2-\zeta)$, and d is the dimensionality of the elastic lattice. It has been found that $\mu > 0$ at low temperatures (Feigel'man *et al.*, 1989) so that the corresponding resistivity becomes:

$$E/J \sim exp\left[-\frac{U(J)}{k_B T}\right] \sim exp\left[-\left(\frac{J_0(T)}{J}\right)^\mu\right], \tag{2.70}$$

which goes to zero as $J \to 0$ for $J_0(T) > 0$, and therefore defines a true superconduct-

ing vortex-solid phase. As shown later in our experimental results, such a nonlinear resistivity described by Eq.(2.70) is indeed observed.

Generally speaking, the value of μ depends on the vortex bundle size and the dimension of vortex system. As shown in Blatter, et al (Blatter *et al.*, 1994), two representative values for $d = 3$ are

$$\mu = \begin{cases} 5/2, & \text{large vortex bundles;} \\ 7/9, & \text{small vortex bundles.} \end{cases}$$

2.8 Vortex Pinning and Vortex Phases in HTS's

The high transition temperature, short coherence length and long penetration depth of HTS's have opened up new opportunities for studying the effects of thermal and disorder fluctuations on the vortex properties. The mere inspection of the resistivity versus temperature curve of HTS's in an applied magnetic field near T_c has led to unequivocal realization that the transition from the normal state to the superconducting state is much broader in HTS's than that in conventional superconductors. Another important consequence of the large thermal fluctuations and disorder fluctuations in HTS's is that the critical regimes in the phase and the amplitude of the superconducting order parameter become separated, with the former associated with the vortex-solid to vortex-liquid transition, and the latter with the vortex-liquid to normal state transition. In contrast, for most conventional superconductors, with moderate Ginzburg-Landau parameters, the thermal fluctuations of the order parameter are only important very close to $H_{c2}(T)$. The main thrust of this thesis is to investigate the vortex-solid to vortex-liquid phase transition in HTS's, with special emphasis on the effects of static disorder. These experimental studies were inspired by various recent theoretical investigations. In the following, we briefly introduce the theoretical concepts which are related to the research topics presented in later chapters. More details and discussions are left to chapters 4 to 6.

The concept of dislocation-mediated melting was first applied to the two-dimensional

melting by Nelson and Halprin (Nelson & Halperin, 1978). It was argued by Marchetti and Nelson (Marchetti & Nelson, 1990) that "vortex loops" due to correlated vortex dislocations may be the underlying mechanism for the melting of a vortex lattice into a fluid phase. (Examples for such dislocation-mediated "vortex loops" are given later in sections 4.1 and 5.2.)

More specifically, in the case of randomly distributed weak pinning sites, Fisher, Fisher, and Huse (Fisher *et al.*, 1991) have proposed that the long-range correlation in the vortex lattice is replaced by a new "vortex-glass" phase that has a spin-glass like off-diagonal long-range ordering and is truly superconducting. It is argued that in this phase there exist thermally activated vortex dislocation loops. The energy barrier $U(J)$ for the vortex loop excitations diverges with the decreasing J with a functional form $U(J) \sim J^{-\mu}$, and $\mu \leq 1$. Therefore, thermally activated vortex loops lead to nonlinear vortex dissipation as shown in the electric field $E \sim exp[-(J_T/J)^{\mu}]$, where J_T is a characteristic current density. Therefore resistivity $\rho = E/J$ approaches zero in the limit of $J \rightarrow 0$. With the increasing temperature, the vortex system goes through a continuous phase transition from the vortex-glass phase to the vortex-liquid phase. Although the collective flux creep theory described by Feigel'man et al. (1989) and Section 2.7.3 does provide indirect theoretical evidence for the existence of a vortex-solid state with a diverging energy barrier for vortex motion, it is still an open question whether rigorous theoretical evidence can be found for such a vortex-glass phase in 3D system (Fisher *et al.*, 1991; Blatter *et al.*, 1994).

In the case of correlated strong pinning, provided by parallel columnar defects of diameter comparable to the superconducting coherence length and extending through the entire sample, the vortex system is found (Nelson & Vinokur, 1992; Nelson & Vinokur, 1993) to be isomorphic to a two-dimensional dirty boson system (Fisher *et al.*, 1989). In real samples, this kind of correlated disorder is recently realized by means of high-energy heavy ion irradiation (Civale *et al.*, 1991; Konczykowski *et al.*, 1991; Hardy *et al.*, 1991). The vortex-solid to vortex-liquid transition associated with such correlated pinning in superconductors is described as a Bose-glass to a "superfluid" transition (Nelson & Vinokur, 1992; Nelson & Vinokur, 1993). The

isomorphic mapping between the system of two-dimensional bosons and that of three-dimensional vortices in the presence of one-dimensional correlated disorder, as well as the signatures of Bose-glass transitions, will be described in more details later in Chapter 5.

Finally, we note that rigorous theoretical calculations involving both thermal fluctuations and disorder fluctuations are very difficult and still lacking. Therefore, experimental investigations of the vortex phases in the presence of different static disorder are particularly important in shedding light onto these complicated issues. For instance, there have not been theoretical calculations of the critical exponents that are associated with various universality classes of the proposed vortex phase transitions. Experimental determination of the critical exponents and vortex phase diagrams will naturally play a crucial role in unraveling many important physics issues.

The static disorder investigated in this thesis involves random point defects, twin boundaries, and correlated columnar defects in $YBa_2Cu_3O_7$ single crystals. The physical quantity studied is the resistivity as a function of the temperature, current, frequency (of the applied AC current), and the applied magnetic field. As shown later, near a vortex phase transition, various physical quantities can be scaled with the diverging vortex correlation length and the relaxation time of thermal fluctuations. The critical scaling analysis derived in our recent work (Yeh *et al.*, 1993a; Yeh *et al.*, 1992a; Reed *et al.*, 1993; Reed *et al.*, 1992; Yeh *et al.*, 1993b; Yeh *et al.*, 1994; Jiang *et al.*, 1994), which is based on general critical scaling hypothesis and symmetry consideration, has yielded both static and dynamic critical exponents and universal functions for different vortex phase transitions. Similar experimental investigations based on the same critical scaling analysis has been proven applicable to various other physical quantities such as AC susceptibility and the third harmonic transmissivity (Reed *et al.*, 1994; Reed *et al.*, 1995).

Chapter 3 Experimental: Samples, Experimental Apparatus and Techniques

This thesis consists of experimental investigations of six $YBa_2Cu_3O_7$ single crystals. Two of them were as-grown samples and the other four had been modified by ion irradiation. In this chapter, general structural properties of the as-grown single crystals are given. In addition, the procedures of sample preparations for electrical transport measurements, the techniques for sample modifications, and the experimental apparatus for the electrical transport measurements are also described in detail. Since most of the transport measurements require a high magnetic field and a temperature stability better than ± 0.01 K in the range of 70 to $\sim$ 95 K, this chapter also discusses the design of the cryogenic dewar for measurements in magnetic fields and the general temperature control techniques. Additional refinements for high-sensitivity resistivity measurements using lock-in techniques and precision temperature control to ± 1 mK stability will be left to Chapter 6 where these improved techniques are applied to measurements of an untwinned single crystal.

3.1 $YBa_2Cu_3O_7$ Single Crystals

The $YBa_2Cu_3O_7$ single crystals studied in this thesis have been provided by Dr. F. Holtzberg at IBM Thomas J. Watson Research Center. A mixture of YBa_2Cu_3O, $BaCuO_2$ and CuO are pressed into a pellet which is placed in a solid gold crucible and heated to 975°C for 1.5 hours. The mixture is then cooled slowly at a rate of 5°C per hour to allow the growth of the crystals. After the melt cools, the crystals are carefully removed from the remaining melt. The crystals are found to be oxygen deficient so that they have to be annealed in pure O_2 (1 atm) at 420°C for a month or longer to ensure that oxygen fully diffuses into the interior of the crystal (Kaiser

et al., 1987).

The resulting chemical composition is $YBa_2Cu_{2.98}Au_{0.02}O_{6.97\pm0.02}$ with orthorhombic structure and lattice constants $a = 3.8177(1)$ Å, $b = 3.8889(1)$ Å, and $c = 11.7136(4)$ Å. Shown in Fig. 3.1 is the unit cell structure of $YBa_2Cu_3O_7$, with Cu(2), O(2) and O(3) atoms in the so-called CuO_2 planes and Cu(1) and O(4) atoms along the CuO chains (Beno *et al.*, 1987). It has been established that the CuO_2 planes are the most important building blocks for the high-temperature superconducting cuprates, and the CuO chains in $YBa_2Cu_3O_x$ provide charge transfer to the CuO_2 planes. The crystalline axes of the $YBa_2Cu_3O_x$ system are defined as the c-axis perpendicular to the CuO_2 planes, the a-axis perpendicular to the CuO chains, and the b-axis parallel to the CuO chains. The absence of oxygen atoms at O(5) sites results in an orthorhombic instead of tetragonal structure. In real samples, there are random oxygen vacancies within the layers of the CuO chains. Because the samples are grown in a gold crucible, a small amount of Au atoms (Au^{3+}) are found to have substituted Cu(1) atoms (Cu^{2+}) in the crystals. The presence of Au^{3+} has an effect of increasing the oxygen content (~ 0.015 of extra oxygen for each 1 atomic percent of Au^{3+}), and therefore helps to increase T_c. Since this thesis is not concerned with the small effect incurred by the Au atoms, all samples will be referred to $YBa_2Cu_3O_7$ single crystals for simplicity.

The typical dimensions of the crystals are generally smaller than 1mm × 1mm × 25μm, with the smallest dimension along the c-axis. The preparation procedures for electrical transport measurements are considerably difficult because of the small size as well as the brittle nature of these crystals.

3.1.1 Anisotropic Superconductors

As shown in Fig. 3.1, the crystalline structure of $YBa_2Cu_3O_7$ system consists of layers of CuO_2 which are most responsible for the electrical conduction. This structural anisotropy gives rise to anisotropic conduction such that the conduction in the *ab*-plane is much better than that along the c-axis. The anisotropic effective

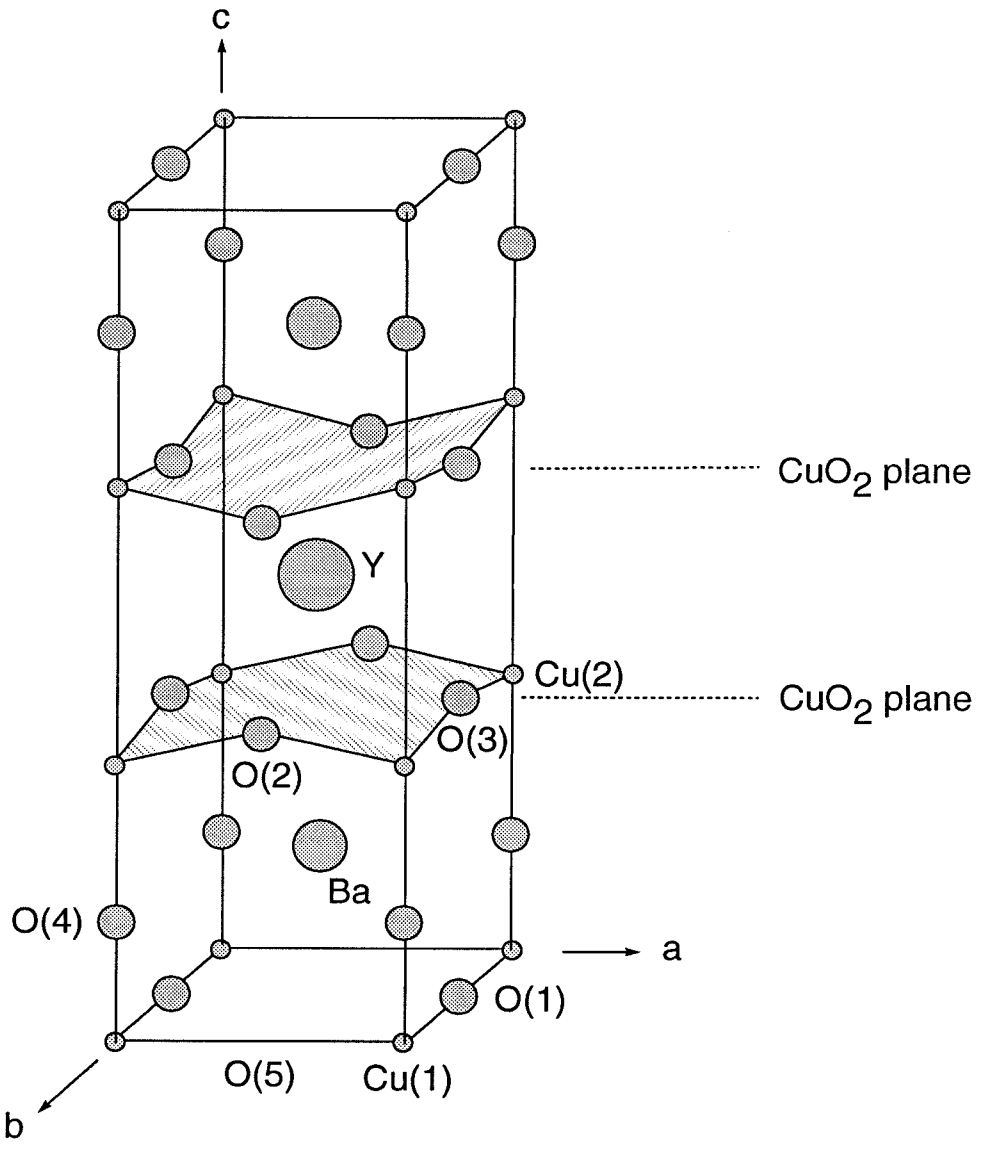

Figure 3.1: Unit cell of $YBa_2Cu_3O_7$ crystal

mass tensor of the carrier, with the coordinate axes coinciding the crystalline axes, can be expressed as

$$\mathbf{M} = \begin{pmatrix} m^*_{aa} & 0 & 0 \\ 0 & m^*_{bb} & 0 \\ 0 & 0 & m^*_{cc} \end{pmatrix} \approx \begin{pmatrix} m & 0 & 0 \\ 0 & m & 0 \\ 0 & 0 & M \end{pmatrix}. \tag{3.1}$$

Among the high-temperature superconducting cuprates, the moderately anisotropic system $YBa_2Cu_3O_7$ has a mass anisotropy ratio $\varepsilon^{-2} \equiv M/m \approx 60$. For comparison, the highly anisotropic system $Bi_2Sr_2CaCu_2O_8$ has a mass ratio as large as $\varepsilon^{-2} \approx 10^4$ (Martin *et al.*, 1988). In the literature, an anisotropic factor γ is often used to represent the quantity $\gamma = \sqrt{M/m} = \varepsilon^{-1}$.

3.1.2 Twinned Microstructure

Most of the as-grown $YBa_2Cu_3O_7$ single crystals have twinned microstructures which are formed during the crystal growth when the structure changes from tetragonal to orthorhombic upon cooling. The a-axis and b-axis rotate by 90° next to a "twin plane" which extends along the <110> direction (see Fig. 3.2(a)). The region within which the crystalline structure is distorted due to the presence of the twin plane is called a twin boundary, the width of which is typically 30-50 Å. These twin boundaries generally extend throughout the entire thickness of the sample. The distribution and density of the twin boundaries in a sample can be observed with polarized light optical microscopy (PLM). This technique relies on the small difference in the phase of the reflected light when it is polarized along the a and b axes. For an incident polarization intermediate to a and b directions this leads to reflected light which is elliptically polarized. It has a different direction of rotation (i.e. clockwise or anti-clockwise) for the two twins, resulting dark and light regions in a PLM picture (see Fig. 3.2(b)). The twin boundaries are aligned either in parallel or in perpendicular to each other, and the twin density is found to be very sensitive to the post-annealing

conditions. A lower temperature (< 500°C) longer time annealing in oxygen generally yields lower twin densities. The twin separation in our samples varies from 2 to 10 μ m. The larger twin separation (lower twin density) in our crystals compared with that in the samples used by most other research groups is consistent with our slow post-annealing processes.

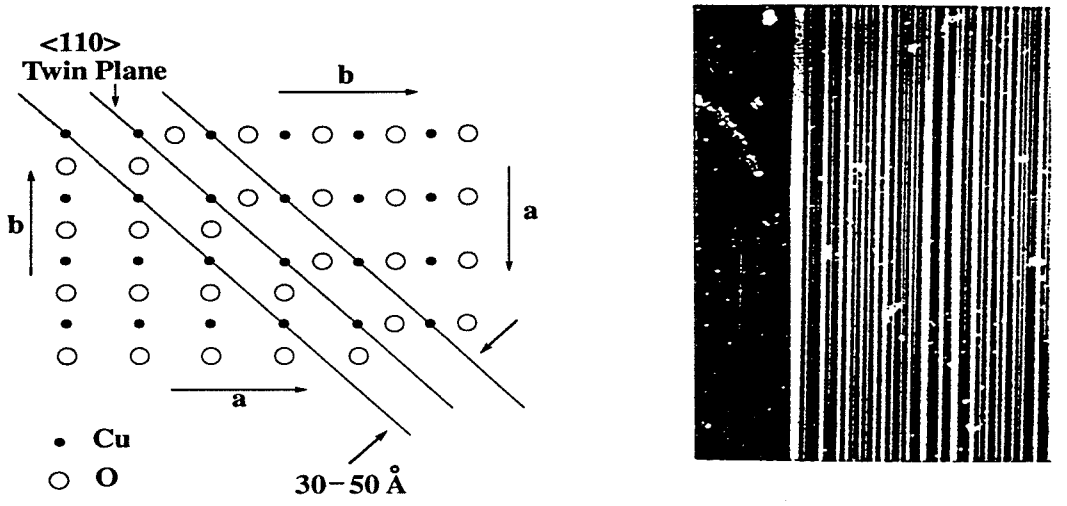

Figure 3.2: Twin boundaries in $YBa_2Cu_3O_7$: (a) Atomic structure; (b) Polarized light microscope picture: Twin boundary distribution.

3.1.3 Untwinned Crystals

Recently, it has become possible to produce crystals without (110) twinning by quenching the melt during growth and post annealing the crystals in a stress-free environment (Rice & Ginzberg, 1991). Twinned crystals can also be detwinned at elevated temperatures by using thermo-mechanical detwinning (Kaiser *et al.*, 1989; Schmid *et al.*, 1989; Giapintzakis *et al.*, 1989; Welp *et al.*, 1989b). Alternatively, since the untwinned configuration has lower total free energy, longer annealing time in oxygen results in less twin boundaries in a sample. Our untwinned sample was found among one batch of samples after being annealed for two months. There are only a couple of twin boundaries at the edge of one corner, which were subsequently

covered by one of the gold contacts during the transport measurements, and therefore do not make significant contribution to our transport studies.

In the following, we denote the two as-grown samples as sample #1 for the twinned crystal and sample #5 for the untwinned crystal.

3.2 Sample Preparation for Electrical Transport Measurements

In order to perform standard four-probe transport measurements, four electrical contacts have to be made on these very small single crystals. This sample preparation procedure includes (i) cleaning the sample surface to remove non-stoichiometric surface layer, (ii) making the contacts on the sample surface, and (iii) making electrical connection between the contacts on the sample surface and the electrodes on the sample probe.

The $YBa_2Cu_3O_7$ single crystals are moderately air sensitive and the sample surface degrades in air by forming a non-stoichiometric surface layer. This has to be removed before good electrical contacts can be made. A chemical etching method has been developed by Dr. R. P. Vasquez at the Jet Propulsion Laboratory. The procedure involves first etching the single crystal in a 1% solution of Br_2 in ethanol for at least 10 minutes to fully remove the deleterious surface layer, and then rinsing the sample twice in pure ethanol. After etching, a clear Fermi edge is observed in x-ray photoelectron-spectroscopy (XPS) studies (Vasquez *et al.*, 1991), indicating the improved sample surface quality.

To make electrical contacts, the sample has to be masked in preparation for evaporating gold pads onto the four corners so that bulk currents can be applied to the sample. To minimize the time during which the sample is exposed to the air, the masking procedure is always carried out before the chemical etching process. In case there is grease on the sample surface, the sample is usually cleaned in toluene for 15 sec and then rinsed in pure ethanol before being masked. As shown in Fig. 3.3, the

sample is masked with gold foil, and the loose ends of the gold foil are held onto a glass slide with silver paint. (The glass slide has been cleaned in acetone(C_3H_6O) and n-propyl alcohol.) The use of gold foils is essential because gold dissolves much slower than most metals in the Br_2 etch, so that the mask remains intact during the 10-minute etching of the YBCO single crystals.

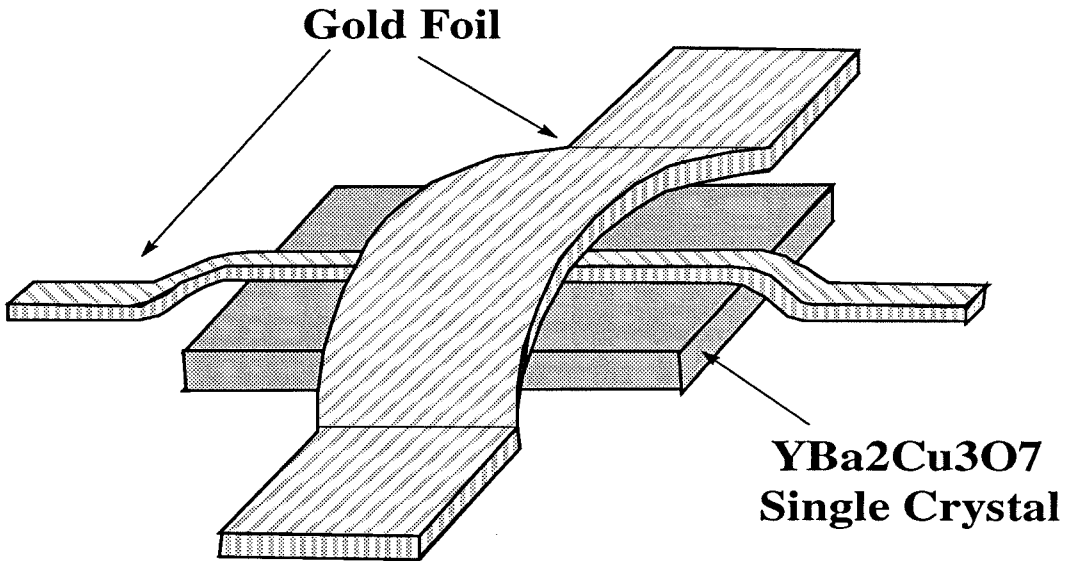

Figure 3.3: $YBa_2Cu_3O_7$ single crystal masked with 0.020" Au foil in preparation of Br_2 etching and deposition of Au contact pads.

Immediately after etching, the sample is transferred to our Perkin-Elmer Ultek ultra-high vacuum chamber which is subsequently pumped down to a vacuum level of $\sim 1.0 \times 10^{-8}$ torr before gold evaporation. After depositing $\sim$ 2500Å of gold contacts, the sample is post annealed in pure O_2 at 300°C to 400°C for up to 24 hrs. Gold sputtering has also been used to make contacts, in which case the sample is transferred to an evaporator with an ion sputtering system. The chamber of the evaporator is pumped down to a pressure lower than $\sim 1.0 \times 10^{-5}$ torr and then filled with pure argon gas to a pressure of $\sim$ 30 mTorr before gold is sputtered onto the sample surface. The contacts made by gold sputtering can be used for the next step

without post annealing.

After the gold contact pads are made, the sample is mounted onto a sapphire substrate of either 0.375 inch or 0.5 inch in diameter with a small amount of N-type Apiezon thermal grease placed between the sample and the sapphire. The sapphire substrate has been cleaned in boiling nitric acid and rinsed in ethanol and then in distilled water. Two methods are used to attach electrical leads between the gold pads on the crystal surface and the substrate. The first method requires gold pads made on the substrate. Gold wires of 0.001 inch in diameter are bonded with an ultrasonic wire bonder onto the gold pads on both the crystal surface and the substrate, as shown in Fig. 3.4(a). Since gold does not diffuse into sapphire, a buffer layer of aluminum of $\sim$ 5000Å thick is first evaporated onto the sapphire substrate. The whole procedure is time consuming and the ultrasonic wire bonding is especially difficult because of the brittle nature of the crystals. In the second method, 0.005 inch indium wires are used in the place of gold wires(see Fig. 3.4(b)). Indium wires cleaned in acetone are very malleable and they stick very well to both gold and bare sapphire surface after being pressed into place using a sharp plastic tip or tooth-pick.

The first method gives typically $\sim 1\Omega$ contact resistance at room temperature. With the second method, the contact resistance can be as small as $\sim 0.05\Omega$.

3.3 Sample Modifications

To investigate the effects of controlled disorder, two types of ion irradiation techniques are applied to the samples under investigations: 3 MeV light ion (proton) irradiations and 0.9 GeV heavy ion (Pb) irradiations. The ion irradiation is usually performed after the gold contacts are made onto the sample for the following reasons. The 3 MeV ion irradiation is usually performed at room temperature. Since high-temperature superconductors are not good conductors at room temperature, gold contacts on the sample can reduce the surface charging effects. In the case of heavy-ion irradiation, the damaged regions become amorphous. Since these regions are susceptible to removal during the surface cleaning procedure employing a 1% Br_2

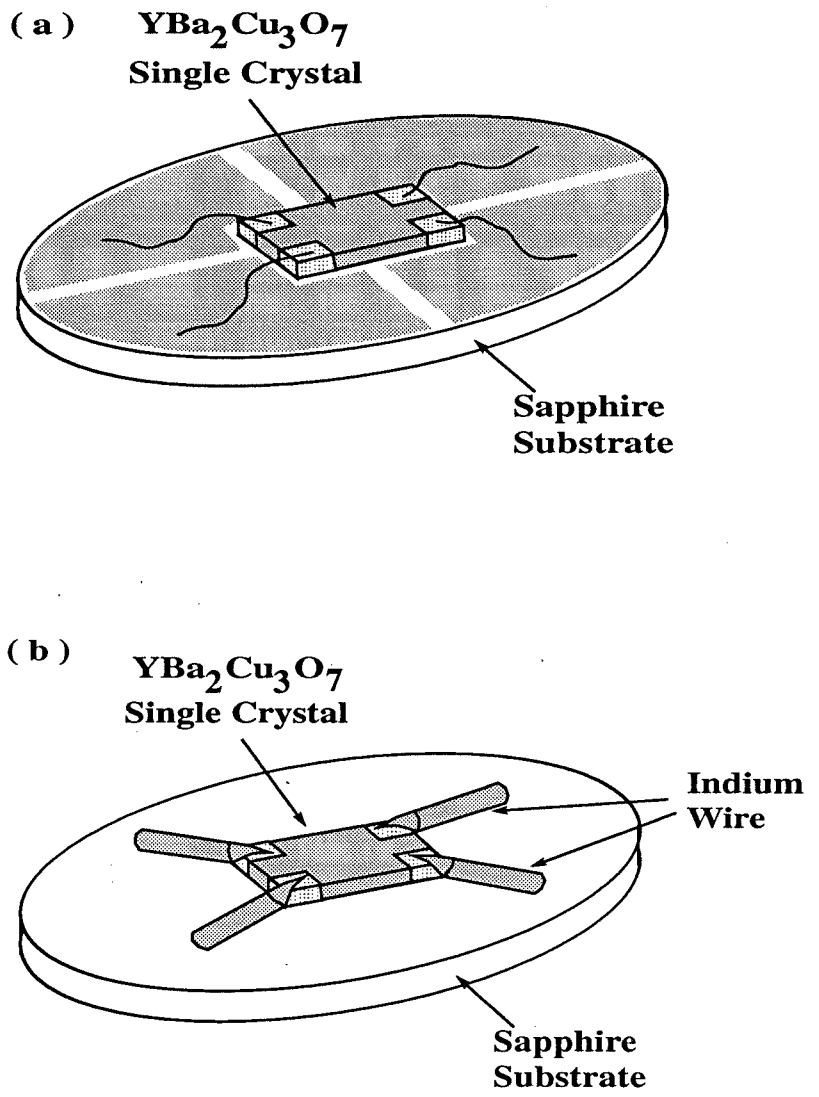

Figure 3.4: (a) $YBa_2Cu_3O_7$ single crystal mounting onto a sapphire substrate with gold pads. Electrical contacts are made with gold wires; (b) $YBa_2Cu_3O_7$ single crystal mounting onto a sapphire substrate. Electrical contacts are made with indium pressed onto the gold contact pads.

solution of ethanol, their etching rate is much larger than that of the rest of the sample surface. Therefore the sample surface will not be smooth if it is etched after the heavy-ion irradiation and the gold contacts can no longer stick to the sample surface.

3.3.1 3 MeV Proton Irradiations

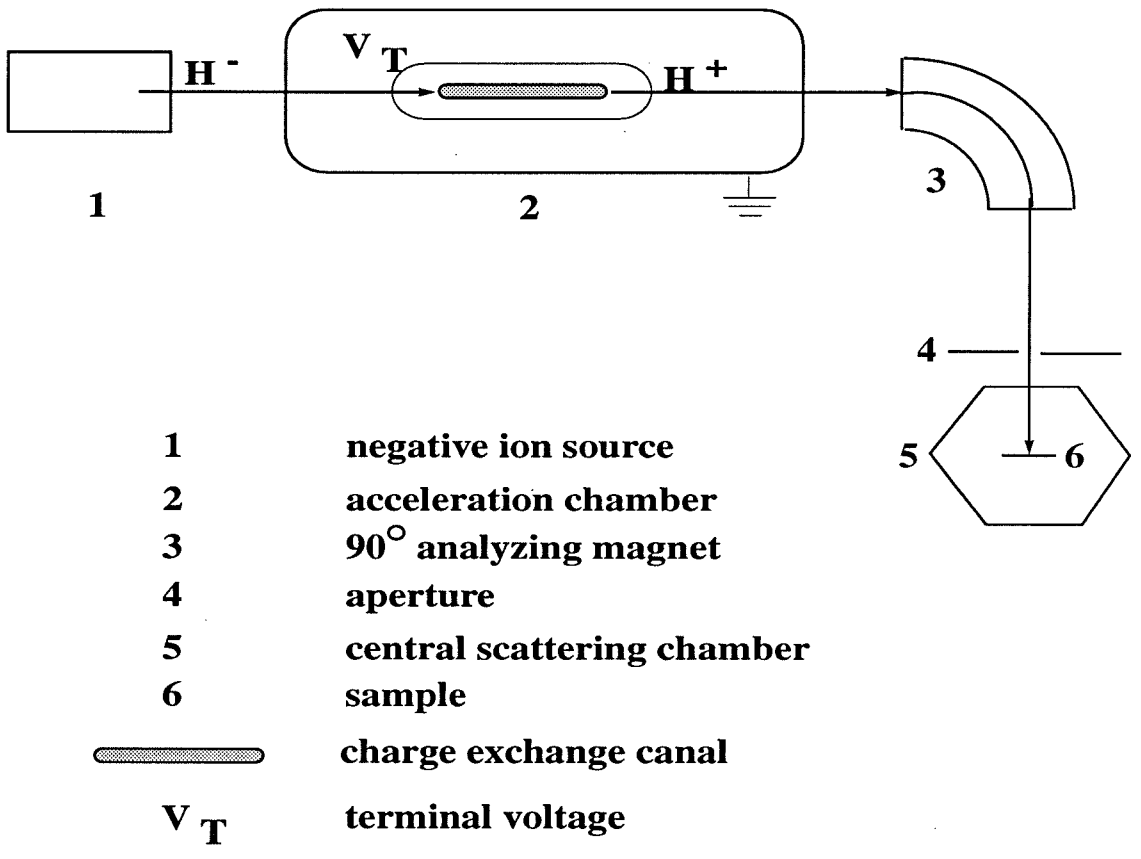

Figure 3.5: Block Diagram of Tandem Van de Graff Accelerator

The 3 MeV proton irradiations are performed using the tandem Van de Graff accelerator at Caltech. The block diagram of the accelerator is shown in Fig. 3.5. Negative hydrogen ions (H^-) with initial kinetic energy of 45 keV are extracted from the duoplasmatron negative ion source and are accelerated under the terminal voltage $V_T = 1.475$ MeV to the gas exchange chamber where the ions lose 2 electrons and become protons (H^+). The protons are then accelerated under the same terminal

voltage and gain a kinetic energy $E = 45keV + 2eV_T \approx 3.0$ MeV at the end of the tandem accelerator. The 3 MeV protons are then selected by the analyzing magnet and focused by a series of electric and magnetic lenses onto the sample through an aperture confined by horizontal and vertical slits. The sample on its sapphire substrate is mounted onto an aluminum sample holder (see Figs. 3.6 and 3.7) in the central scattering chamber with a vacuum level of $\sim 1.0 \times 10^{-6}$ Torr.

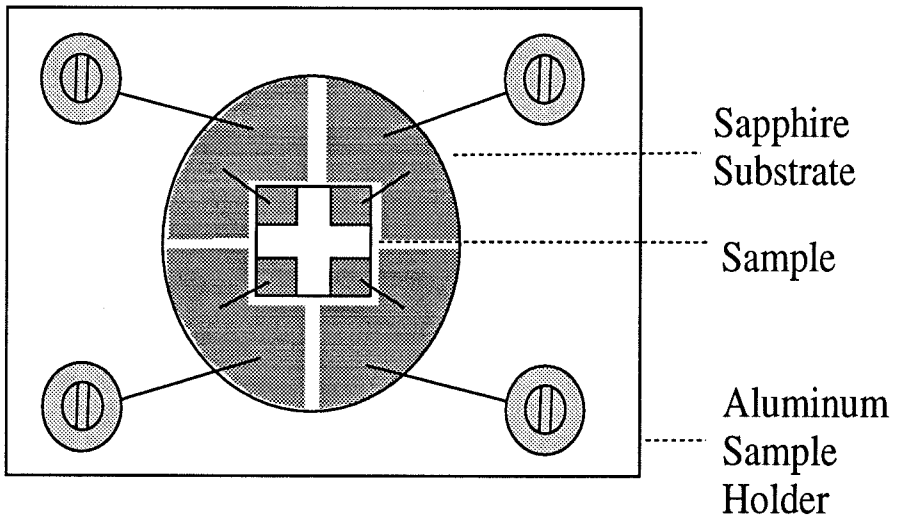

Figure 3.6: Sample arrangement for 3.0 MeV proton irradiations (top view).

The slowing down process of light ions in matter has been well understood, and the traveling range of incident ions in most materials can be calculated numerically using the program TRIM (Biersack & Ziegler, 1989). As shown in Appendix A, the traveling range of a 3 MeV proton in $YBa_2Cu_3O_7$ single crystals is $46.5\mu m$. Since our sample thickness is typically 20 to 30 μm, all the protons pass through the sample and stop in the sapphire substrate. The incident charges go through the conducting paths from the sample to the aluminum sample holder and eventually pass through the integrator to the ground (see Fig. 3.7). For the sample arrangement shown in Fig.

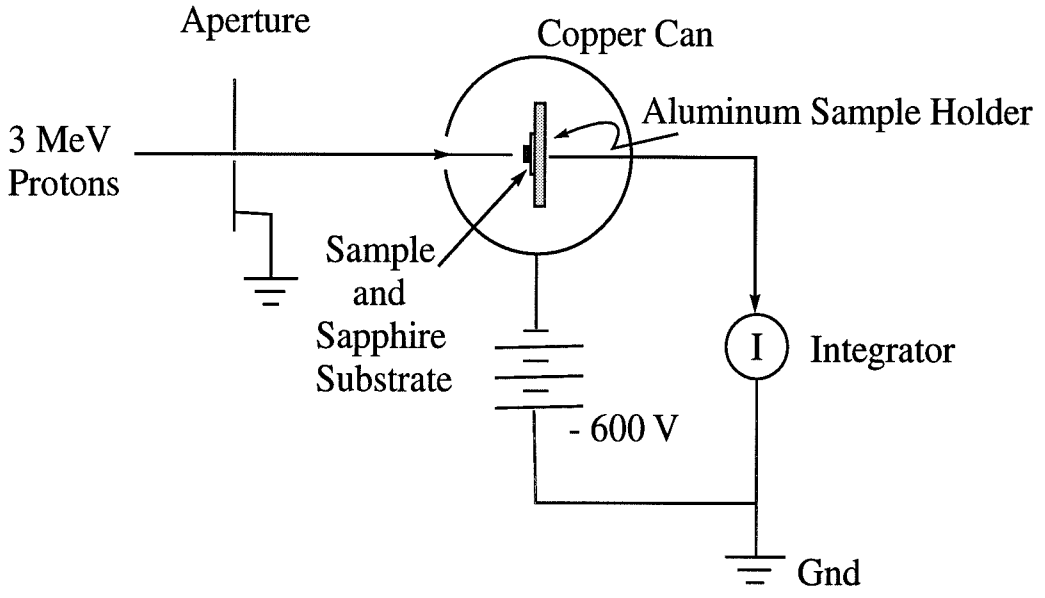

Figure 3.7: Schematic diagram of the ion path and charge collection in the 3 MeV proton irradiation.

3.4(b), an additional aluminum foil is used for masking so that only the sample is exposed to the ion beam, and the electrical charges will go through the aluminum foil and sample holder to the ground to prevent charging effects due to the direct impact of protons onto the insulating sapphire surface. The areal density of the incident protons, which is called the fluence of the irradiation, can be calculated from the total charges passing through the current integrator. To ensure a uniform areal density, the incident ion beam on the sample is an elongated spot slightly larger than our sample size which is typically under 1mm × 1mm. The ion beam is scanned by magnetic deflection through a much larger area (confined by the aperture) with a speed of 1 Hz horizontally and 11 Hz vertically. An averaged current passing through the integrator is measured and correspondent charges are counted with respect to time. The total

counts (C) for a specific fluence (Φ) can be calculated by the following equation:

$$C = \frac{\Phi \times S_{apt} \times Z_{ion}}{I_{max}}, \tag{3.2}$$

where S_{apt} is the aperture area, Z_{ion} is the charge per ion, and I_{max} is the integrator scale. All the experimental parameters are summarized in Table 3.1. along with the defect type as a summary of the sample information.

Table 3.1: **Experimental Parameters for the 3.0 MeV Proton Irradiation**

species	H^+
fluence	5.0×10^{15} ions/cm^2
initial negative ion energy	45 keV
terminal voltage	1.475 MeV
analyzing magnetic field NMR frequency	12.3330 MHz
beam scanning frequency	Horizontal: 11 Hz; Vertical: 1 Hz
scanning averaged current	75 — 90 nA
integrator scale	200 nA
central scattering chamber vacuum	$\sim 1.0 \times 10^{-6}$ torr

To ensure the accuracy in the counting of the total numbers of incident protons, a copper grid at -600 V is placed between the aperture and the target, as shown

schematically in Fig. 3.7, to collect the secondary electrons excited by the ion beam on the surfaces of the aperture and the sample.

One twinned single crystal which is from the same batch as sample #1 is irradiated twice with a fluence of 5×10^{15} protons/cm^2 each. After the first irradiations, the sample is denoted as sample # 2, and after the second, sample #3. The same irradiation is performed on the untwinned crystal sample #5, after which the sample is denoted as sample #6.

3.3.2 GeV Heavy Ion Irradiations

The sample irradiated with 0.9 GeV Pb ions at Grand Accelerateur National d'Ions Lourds (GANIL, Caen, France) is denoted as sample #4. The irradiation is performed at liquid nitrogen temperature with the ion beam along the c-axis of the sample. High resolution transmission electron microscopy (TEM) studies reveal the formation of continuous amorphous tracks of a typical diameter of $\sim$ 70Å, and these tracks extend throughout the entire thickness of the sample (Konczykowski *et al.*, 1991). These columnar defects are randomly distributed in the ab plane of the sample. Since vortices in superconductors also have line structures and the vortex lattice constant (a_0) satisfies $B \approx \Phi_0/a_0^2$, where $B \approx H$ (the applied magnetic field), it is convenient to compare the areal density of vortices and that of the columnar defects by defining a matching field $B_\varphi \equiv \Phi_0/d^2$, with Φ_0 being the flux quantum and d the average separation of columnar defects. For a fluence of $\sim 5 \times 10^{10}$ $ions/cm^2$ used for sample #4, the corresponding matching field is $B_\varphi \approx 10.0$ kOe. The averaged separation of the columns observed by TEM studies is about 490Å, consistent with the vortex lattice constant $a_0 = 489$Å for $H = 10kOe$.

3.3.3 Defects Created by Ion Irradiation

The slowing down of incident ions in a solid is mainly due to two energy loss mechanisms, the *nuclear energy loss* S_n and the *electronic energy loss* S_e. The nuclear energy loss S_n results from energy transfer from the incident ions to target atoms

during elastic collisions, i.e., without excitations of internal degrees of freedom, while S_e originates from ionizations and/or electronic excitations of target atoms. Generally speaking, S_n leads to defect production provided that the energy transferred to a target atom exceeds a material dependent displacement threshold T_d. In contrast, defect production via electronic excitations and/or ionizations requires an additional mechanism to convert the excitation energy into atomic motion. For most materials, there exists an effective electronic energy loss threshold S_{e0}, below which defect production is predominantly due to S_n, and above which the structure becomes progressively sensitive to electronic excitations.

In the 3 MeV proton irradiation, both S_e and S_n are small (see Table 3.2 for the calculated values averaged over all the elements in $YBa_2Cu_3O_7$). The defect production is mainly due to the random events of elastic collisions when the energy transferred to a target atom is larger than T_d. Obviously, oxygen atoms are the easiest to be knocked out of their equilibrium lattice positions because of their light weight. As shown in Appendix A, this process can be well described by the elastic collision theory. The defects created through atomic displacements are mainly atomic-size point defects. For a fluence of 5.0×10^{15} protons/cm^2, the defects density in a sample of thickness 25 μm is approximately 1.1×10^{19} defects/cm^3 (see Appendix A), corresponding to an average separation of defects about 400Å, i.e., about 500 unit cells per defect (*cf*, the total number of unit cells in typical sample of dimensions $1.0mm \times 0.5mm \times 20\mu m$ is $\sim 5 \times 10^{18}$).

If the energy transferred to the target atom is much larger than T_d, secondary displacements or cascade effects could occur and larger clusters may be created. In the TEM studies on a similar irradiated single crystal (Civale *et al.*, 1990), clusters of $\sim$ 30Å in diameter have been observed. The cluster density is found to be about 0.1% of the calculated atomic-size point defect density.

In the case of GeV heavy ion irradiations, the main energy loss is through S_e, i.e., electronic excitations and ionization, as clearly shown in Table 3.2 which the magnitude of S_e is much larger than that of S_n. The electronic energy loss is approximately 46 keV/nm. High-resolution TEM imaging reveals continuous amorphous

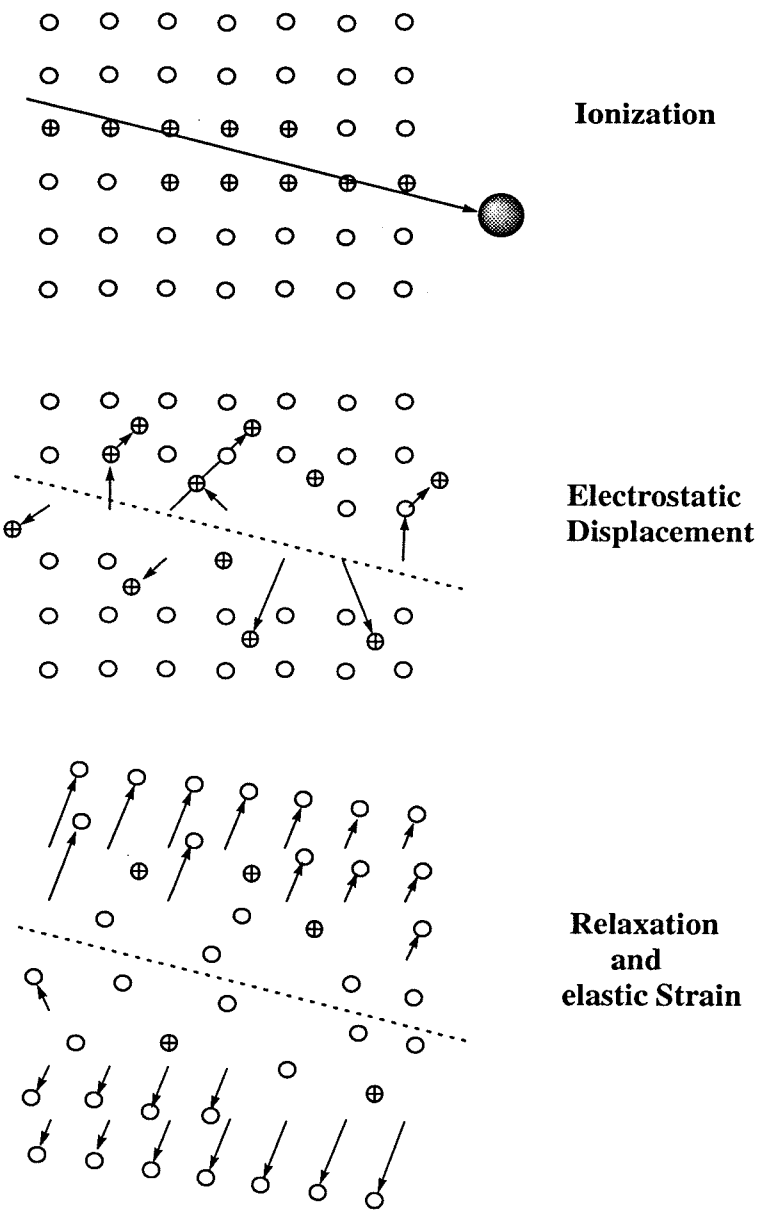

Figure 3.8: The ion explosion spike mechanism for track formation (Fleischer *et al.*, 1975). The original ionization left by a charged particle (*top*) is unstable such that the induced ions are ejected into the solid, creating vacancies and intersitials (*middle*). Later the stressed region relaxes elastically (*bottom*), straining the undamaged matrix.

Table 3.2: **Projected Ranges and Energy Losses S_n and S_e**

(Calculated by TRIM (Biersack & Ziegler, 1989))

Projectile	Energy (MeV)	Projected Range (μm)	S_e (keV/nm)	S_n (keV/nm)
^{1}H	3.0	45.6	0.04	2.34×10^{-5}
^{208}Pb	900	26.4	46.4	0.10

tracks along the ion paths (Hardy *et al.*, 1991; Konczykowski *et al.*, 1991). Although there has been a long history of ion irradiation techniques, the application of such high energy heavy ions in the GeV range has not been unprecedented. Therefore the process of defect production through the electronic excitations and ionizations are not well understood. Recent experimental studies (Hardy *et al.*, 1991) have suggested that the track formation process is similar to the ionization process in inorganic crystals during nuclear fission (Fleischer *et al.*, 1975) (see Fig. 3.8). Following a burst of ionizations along the path of a charged particle, an electrically unstable array or adjacent ions are created, followed by the formation of an array of interstitial ions and vacant lattice sites via the Coulomb interactions between the ions, and then elastic relaxation takes place to reduce the local stresses by spreading the strain more widely. It is the creation of long range strains in this third step that makes possible the continuous tracks in the single crystals.

3.4 Sample Characterization

Before any detailed measurements were performed, the quality of all the as-grown samples were first characterized by measuring the magnetic susceptibility and resis-

tivity in zero magnetic field. The superconducting volume of these samples in zero field is 100%, from the magnetic susceptibility measurements, and the magnetic transition width is about $\sim 0.2\ K$ (Kaiser *et al.*, 1987). The resistive transition width is typically less than $0.1\ K$. The irradiated samples were characterized by the electrical transport measurements. The corresponding zero-field transition temperature (T_c's) are summarized in Table 3.3 along with the defect type and other sample information.

Table 3.3: Sample Information

Sample	As-Grown defects	Controlled Defects				T_c
		Ion Specie	Ion Energy (MeV)	Fluence (ions/cm^2)	Defects Type	(K)
# 1	TB[1] PT[2]	---	---	---	---	92.95
# 2	TB PT	protons	3.0	5×10^{15}	PT	92.25
# 3	TB PT	protons	3.0	1.0×10^{16}	PT	91.62
# 4	TB PT	Pb ions	900.0	5×10^{10}	CL[3]	91.77
# 5	PT	—	—	—	—	93.18
# 6	PT	protons	3.0	5×10^{15}	PT	92.5

[1]Twin Boundaries
[2]Point Defects
[3]Columnar Defects

3.5 Experimental Low Temperature Environment

To investigate vortex phase transitions in $YBa_2Cu_3O_7$ single crystals, stable temperature control and applied magnetic fields larger than H_{c1} are required. The temperature range of interest varies with the strength and the orientation of the applied magnetic field. For the field range available in our lab from $\sim$ 1.0 kOe to 90 kOe (which is well above $H_{c1}(0) \approx 100Oe$), the temperature range is from 75 K to ~95 K. To stabilize the sample temperature to high precisions within this range and to apply large external magnetic fields, one needs proper designs for the cryogenic dewar and the sample probe.

3.5.1 Cryogenic Dewars

Two cryogenic dewars have been used for different magnetic field ranges. The high-field dewar, as shown in Fig. 3.9, contains a superconducting solenoid which can provide a magnetic field up to ~90.0 kOe. Because the magnet is made of conventional superconducting material of NbTi, it is crucial to submerge the entire magnet in liquid helium. During the experiments, the cooling of the sample chamber is provided by a weak thermal link between the helium exchange gas in the chamber and the liquid helium reservoir. For the temperature range of interest, the amount of needed exchange gas is typically about 0.1-0.2 mbar at room temperature. The sample chamber is enclosed by a stainless steel tube which extends to the top of the dewar. A vacuum jacket shown in Figure 3.9 extends $\sim$ 40 cm above the sample to prevent direct thermal contact between the liquid helium bath and the sample chamber. All the vacuum jackets are pumped down to $\sim 10^{-4}$ mbar at room temperature.

For more accurate measurements in magnetic fields below 10 kOe, a low-field electric magnetic dewar is used in order to prevent inaccuracies in the superconducting magnet due to flux trapping. As shown in Fig. 3.10, the dewar used for low-field measurements has a narrow tail which inserts into the gap of an external standard DC electrical copper-coil magnet. The magnet provides a horizontal magnetic field up to 6.3 kOe. The residual field of the DC magnet is about 40 Oe which is negligible

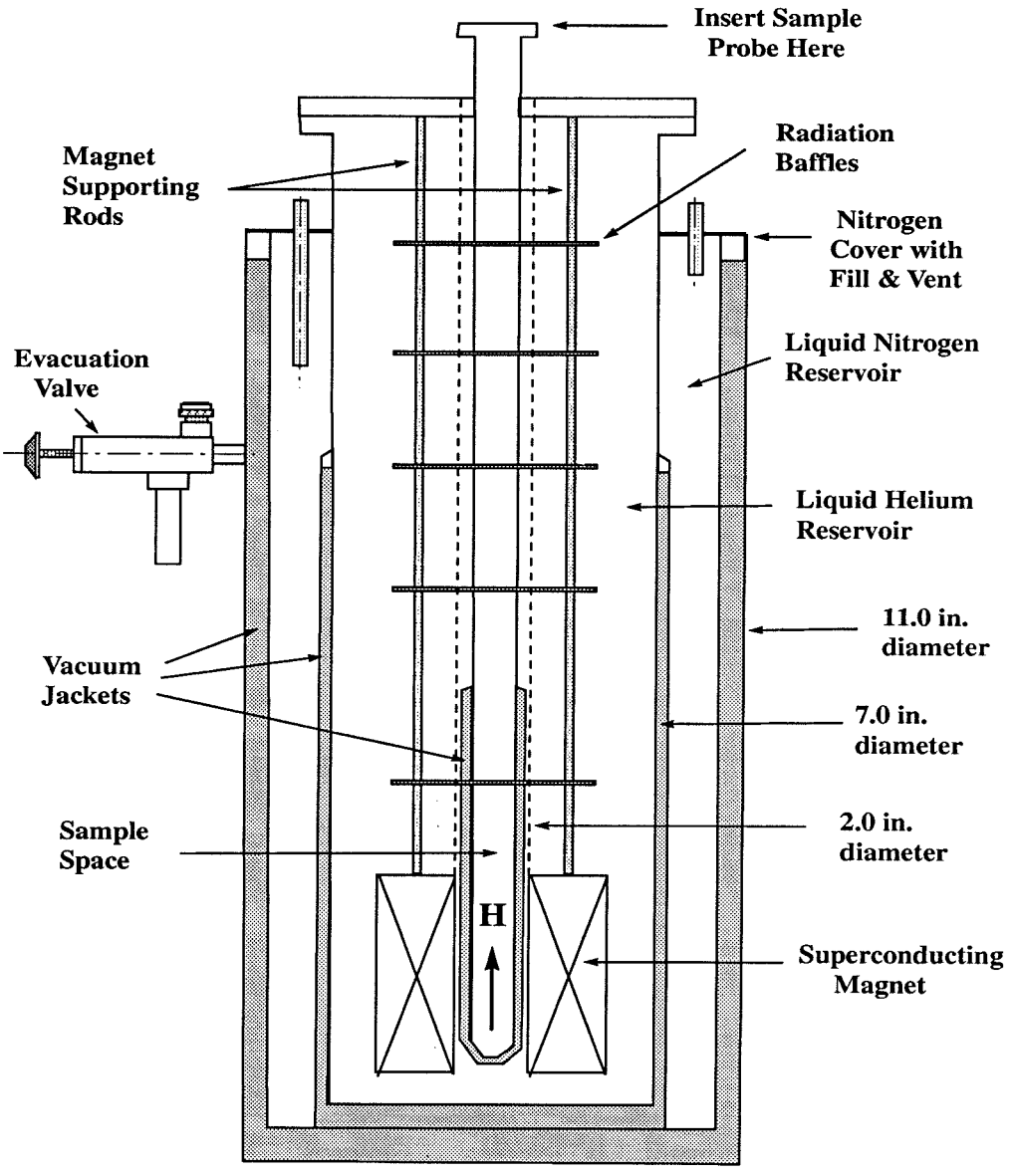

Figure 3.9: Schematic diagram of the high-field dewar (Cross-Section).

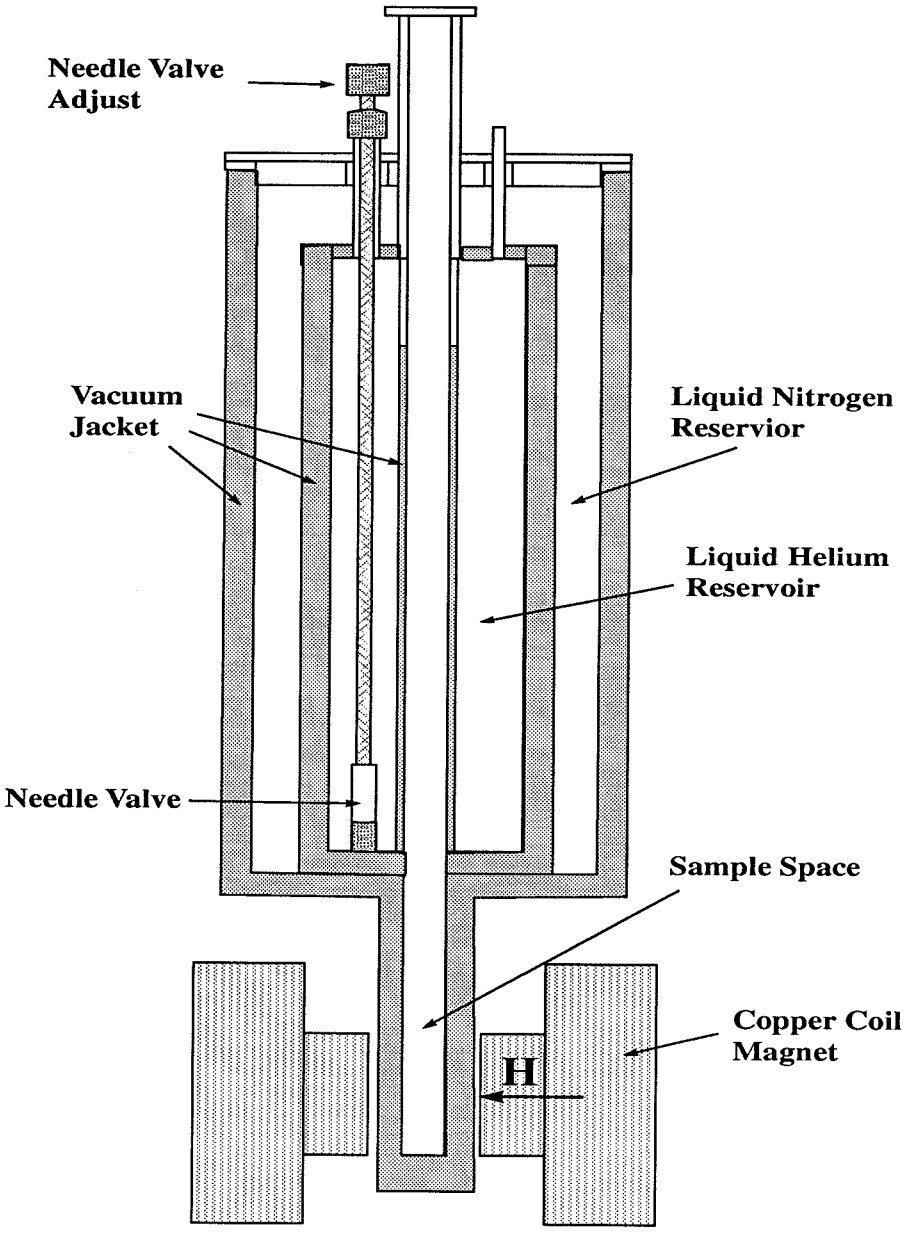

Figure 3.10: Schematic diagram of the low-field Dewar (Cross-Section).

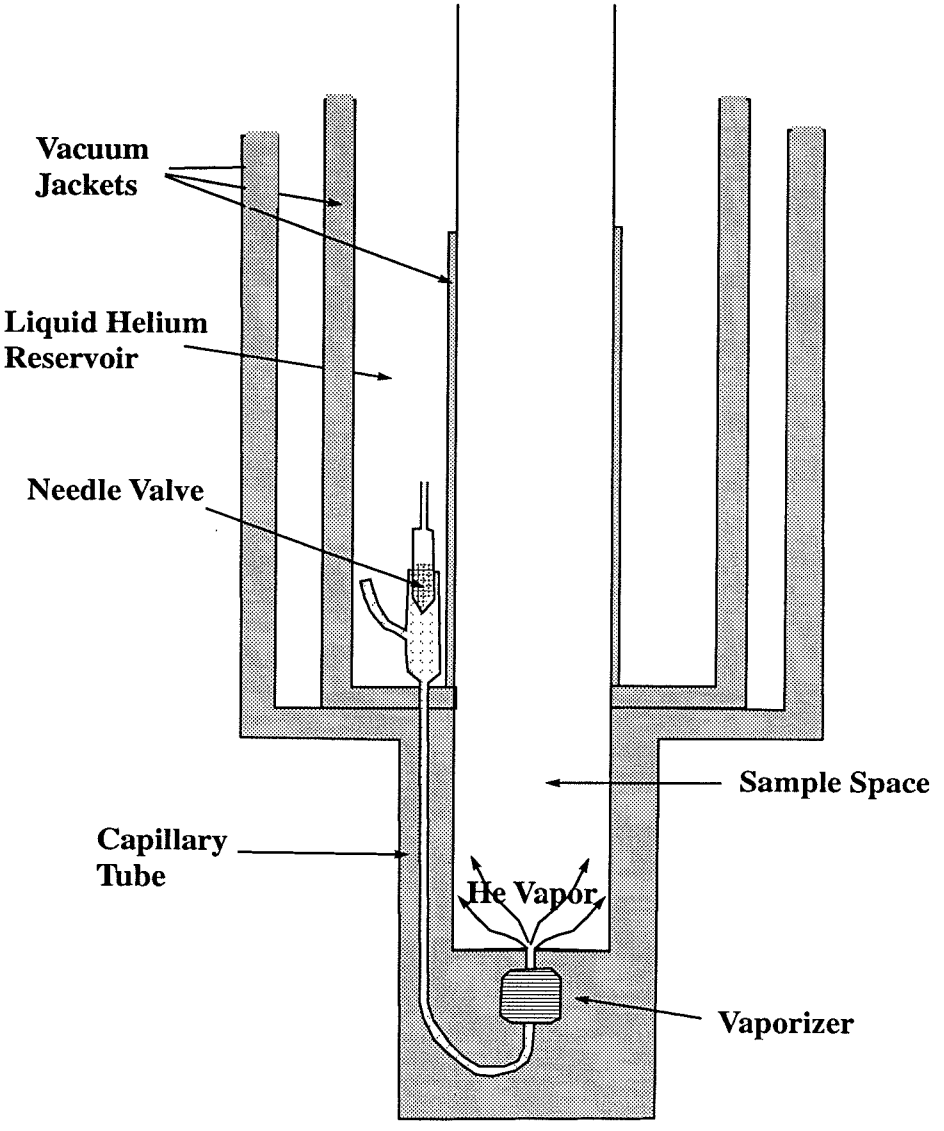

Figure 3.11: Temperature control for the low field dewar.

for our measurements when fields above 0.5 kOe are used. The dewar is equipped with a "SuperVariTemp" system built by Janis Research Co.. As illustrated in Fig. 3.11, a capillary tube carries liquid helium to the bottom of the sample chamber where the liquid helium is vaporized by a DC current heater before entering the sample chamber. The flow of liquid helium is controlled by adjusting a needle valve that is accessible at room temperature. The cold helium vapor provides the cooling power for the temperature control. This technique generally works very well for the temperature range from $\sim$ 5.5K to $\sim$ 20K. However, for the temperature range of interest ($\sim$ 70 K to $\sim$ 90 K) in most of our experiments, the cold helium vapor results in a large temperature gradient between the sample and the thermal shield around the sample. This large temperature gradient makes steady temperature control difficult. In addition, it results in an offset between the temperature sensor reading and the real sample temperature. To resolve these problems, an alternative way of controlling temperature near 90 K is developed by using helium gas instead of liquid helium in the helium reservoir. With the needle valve open, the helium gas, which is cooled by liquid nitrogen to $\sim$ 77K, flows through the capillary tube into the sample chamber. In addition, the helium gas flow rate can be controlled by an external regulator. This modification greatly reduces the temperature gradient between the sample and the cooling source, and with a steady exchange gas flow rate, the temperature stability can be improved from $\pm$0.01K to $\pm 0.003K$. The only disadvantage of this technique is the limited temperature range of its applicability.

3.5.2 Sample Probe

A sample probe is used to transfer samples to the low temperature cryostat and to provide a sample stage where the temperature sensor and heater for temperature control as well as the electrical wiring for measurements can be assembled. For our measurements, the sample probe is usually made of a long stainless steel tube with a sample stage attached at the bottom end. The top section is made of anodized aluminum (which is a good thermal conductor with an electrically-insulating surface

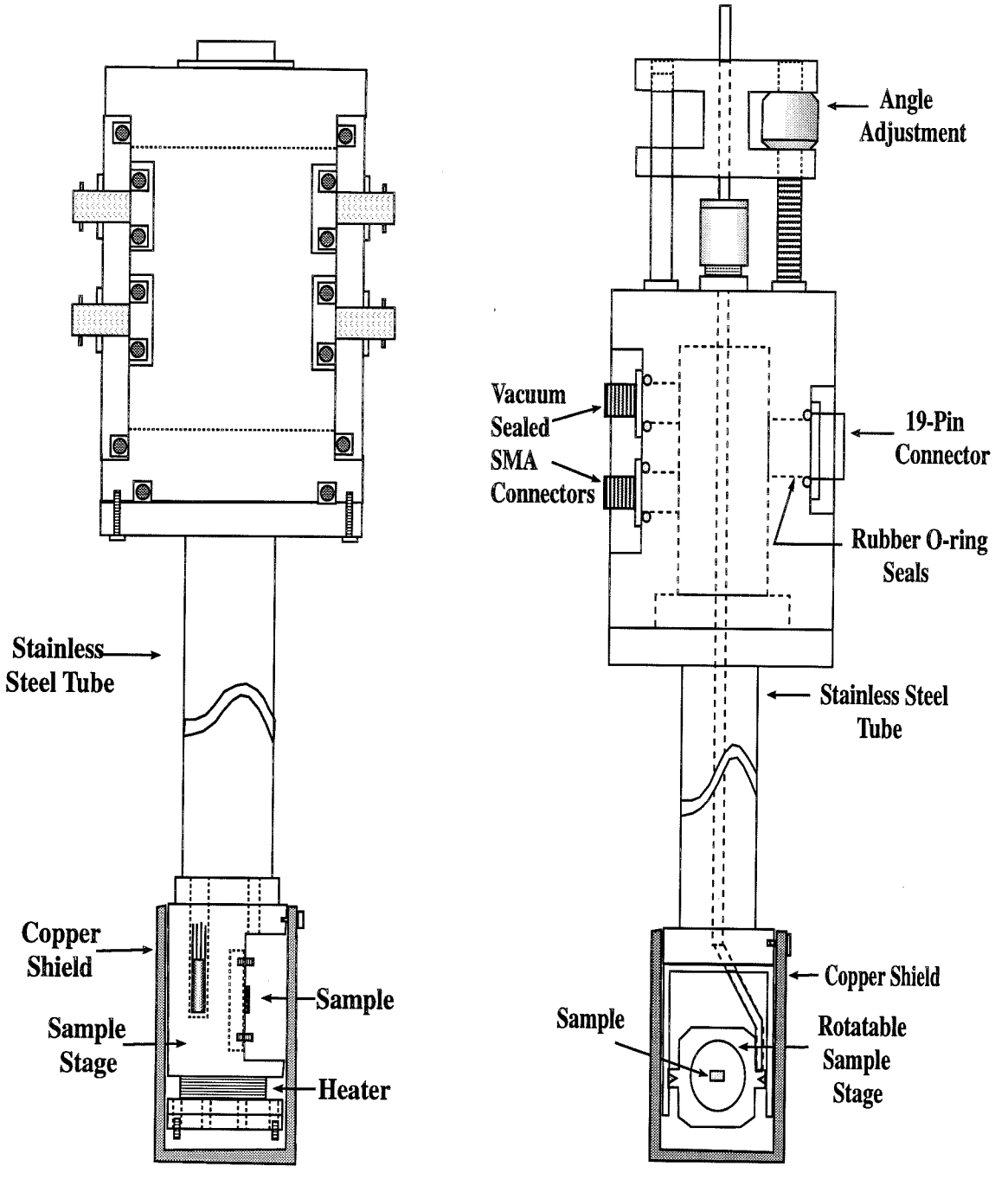

Figure 3.12: Schematic diagrams of the sample probes for both DC and AC transport measurements. Probe (a) is mostly used for low-field measurements. For high-field measurements, probe (b) with a sample stage rotatable along a horizontal axis is usually used.

layer) for mounting the electrical connectors with vacuum seals. Stainless steel tubes are used for the purpose of thermally isolating the sample stage from the room temperature environment. The sample stage is made of copper to minimize temperature fluctuations around the sample. Two commonly used probes are shown schematically in Fig. 3.12.

From Fig. 3.12 it is clear that probe (a) can be easily used in the low-field dewar to study the angular dependence of vortex transport properties to a resolution of 1° to 2° by rotating the probe relative to the vertical axis. In the high-field dewar, however, this probe can only be used for the measurements with $\theta = 0°$ and 90°, where θ is the angle between the magnetic field and the sample c-axis. The ball-shape sample stage on probe (b) is specially designed for varying θ for the high-field measurements. The sample stage can be rotated along a horizontal axis by a stainless steel rod attached to the side of the ball, and the height of the rod is adjustable with the threaded screw at the top of the probe. On both probes, the sample stage is enclosed by a copper can which serves as a thermal shield. Thermofoil heaters are attached to the copper shield of the sample stage in order to reduce the temperature gradient across the sample stage and between the sample and the cold environment outside the copper shield. Both probes can be used for DC and AC transport measurements. The BNC and SMA connectors are used to make electrical connections through coaxial cables to the sample.

3.5.3 Temperature Control

For most of the experiments, a temperature stability of ±10mK at temperatures around 90 K is desirable. The temperature is controlled by commercial LakeShore temperature controllers DRC-91, DRC-93C or DRC-93CA. The sample stage design is crucial for good temperature control. Shown in Fig. 3.13(a) is a typical sample stage in our experimental setup. The sample stage is made of copper because of its large thermal conductivity at low temperatures It is arranged in such a way that the temperature sensor is place right next to the sample and the heater slightly further

from the sample. Cryocon grease is applied between the sensor and the copper to enhance the thermal conduction. Thermofoil heaters are used to provide uniform heating of the entire sample stage. In addition, it is also important to minimize any possible heat flow across the sample stage to ensure the temperature stability, and to minimize the temperature difference between the sample and the temperature sensor to ensure the accuracy of temperature measurements.

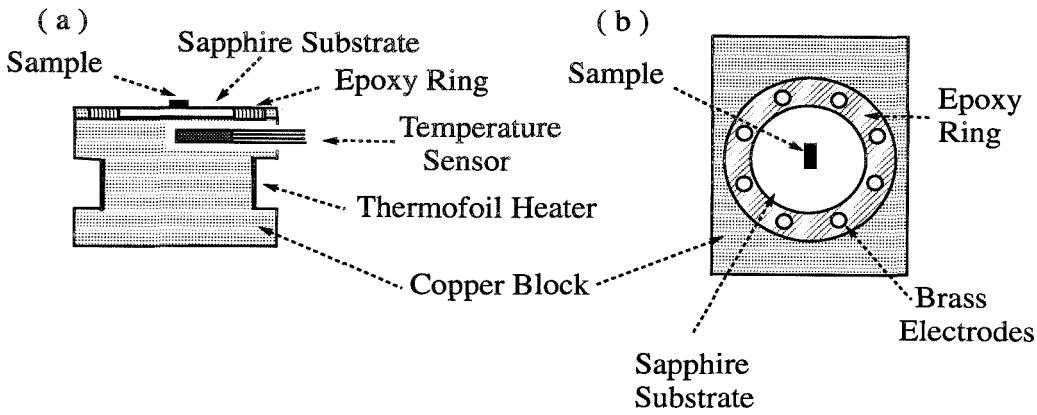

Figure 3.13: Sample stage design for temperature control: (a) cross-section view; (b) top view.

To minimize undesired external heat flow across the sample stage, the electrodes on the sample stage and the electrical leads extending to the room temperature environment should be properly heat-sunk to the copper sample stage before they reach the sample. Meanwhile, the electrodes on the sample stage have to be electrically isolated from each other and from the copper stage. The Stycast 2850KT Blue epoxy is therefore used for this purpose. As shown in Figs. 3.13(a) and (b), brass electrodes are molded in an epoxy ring, so that both good thermal conduction and good electrical insulation can be achieved. To make AC transport measurements up to $\sim 10^7$ Hz, flexible coaxial cables with thin insulation layers are needed for better heat-sinking purposes in a limited sample space. In the case of the specially designed ball-shape sample stage, due to the limited volume and surface area of the ball for heat sinking,

the electrical leads have to be held together first and then heat-sun k to the copper ball by using varnished KimWipes which provides good thermal contact but electrical insulation.

In order to obtain accurate temperature measurements, it is necessary to maintain a uniform temperature across the sample stage in addition to placing the temperature sensor close to the sample. The techniques used for this purpose, such as enclosing the sample stage with a copper thermal shield and reducing the temperature gradient between the desired temperature and the cooling source temperature, have been discussed in the previous two sections.

With the above precautions, we are able to achieve a temperature stability within ± 0.008K.

3.6 Electrical Transport Measurements

As mentioned earlier, two types of routine measurements have been carried out on all the samples: DC current-voltage characteristics and AC impedance as a function of the frequency up to $\leq 10^7$ Hz. Both DC and AC currents ($\mathbf{J}$) are always applied in the direction that ensures $\mathbf{J} \perp \mathbf{H}$ for any angle (θ) between the magnetic field direction and the sample c-axis (see Fig. 3.14). Since the Lorentz force on vortices is $\mathbf{F}_L = \mathbf{J} \times \mathbf{B}$, this arrangement ensures that the vortices are subject to the same $\mathbf{F}_L$ for different θ.

3.6.1 DC Transport Measurements

The block diagram of DC electrical transport measurement is shown in Fig. 3.15. A wide current range from 10^{-7} and 10^{-1} A is provided by a Keithley 220 current source. The DC voltage at each applied current is measured using Keithley 181 or Keithley 182 nanovoltmeters. The four-terminal method eliminates the effects of contact and lead resistances. The DC offset voltages are canceled by reversing the applied current direction so that the sample voltage is given by $V_S = [V(I) - V(-I)])/2$.

To resolve a very small sample voltage signal to an accuracy better than 10 nV,

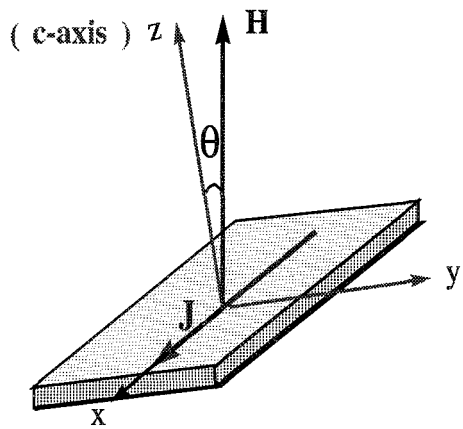

Figure 3.14: Relative orientations of the applied transport current (**J**), the sample c-axis and the applied magnetic field (**H**). Note that the coordinate axes are defined such that the z-axis is parallel to the sample c-axis and $\mathbf{J} \parallel \hat{x}$. When the sample is being rotated, the magnetic field is always in the y-z plane and can be expressed as $\mathbf{H} = Hsin\theta\hat{y} + Hcos\theta\hat{z}$. The condition that $\mathbf{H} \perp \mathbf{J}$ is therefore always satisfied.

precautions have to be taken to minimize possible sources of noise. For instance, as shown in Fig. 3.16, in order to eliminate the noises due to the ground loop currents, the chassis ground of the voltmeter has to be separated from the ground of the power line by a 10Ω resistor. In addition, the chassis grounds of all other equipment have to be shorted together before connecting to the power line ground. RF power line filters are also inserted in the circuit to eliminate AC current noises. Although the thermal EMFs provides a small DC offset voltage, they are often time dependent and therefore may not be completely canceled by reversing the current. To minimize such noise, it is necessary to take measurements within as short time periods as possible. On the other hand, a longer low-pass filter time constant eliminates more RF noise. Consequently, there is a trade-off in selecting the filter mode on the voltmeter. The better way is to take voltage measurements with a relatively short filter time constant so that the thermally induced voltage offset can be mostly canceled, and then to perform external filtering by averaging over several readings at each constant current.

With all these precautions, the noise level is found to be $\leq$ 50 nV. It should be emphasized that good contacts on the sample surface is essential to achieve a low noise level. In high magnetic fields when the Lorentz force may pull the gold or

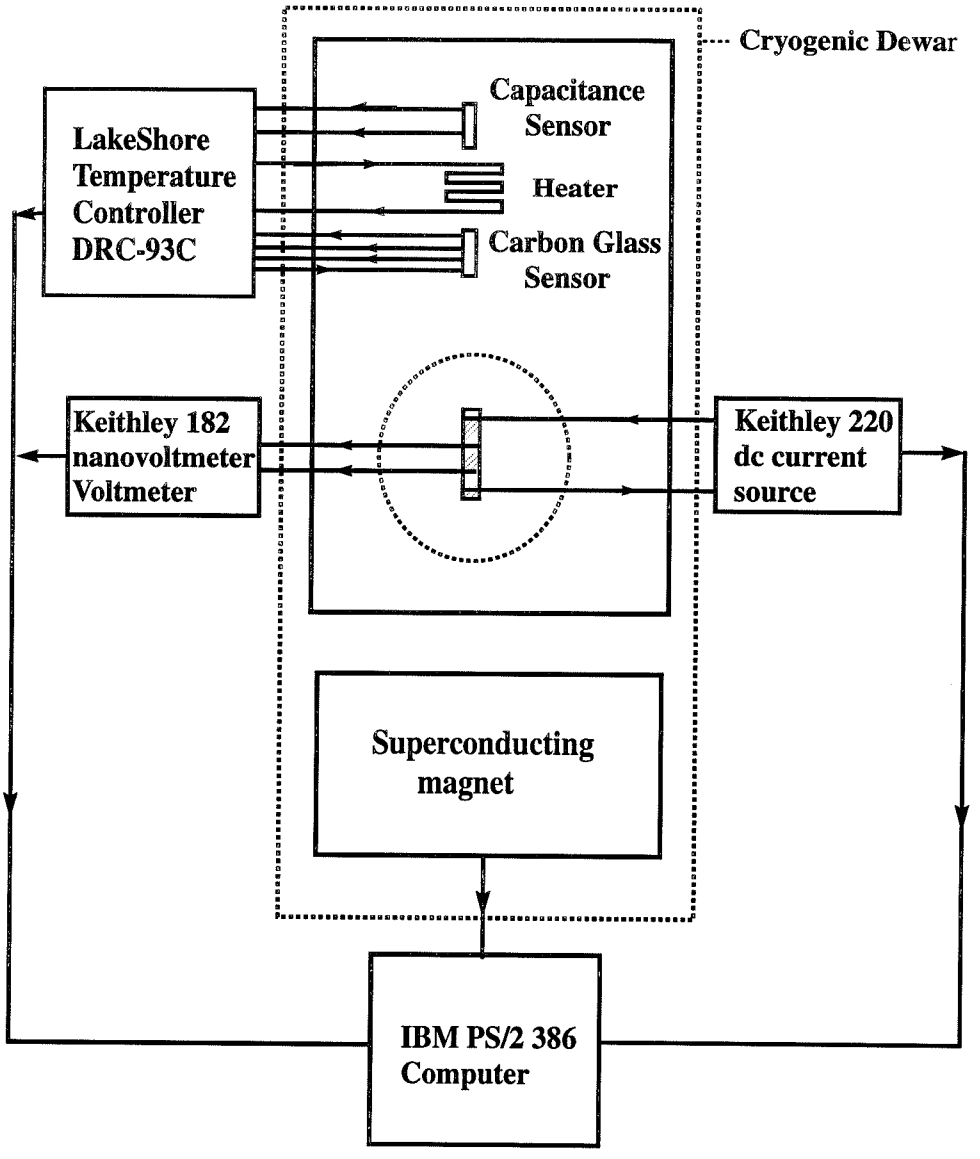

Figure 3.15: Block diagram of the DC transport measurements.

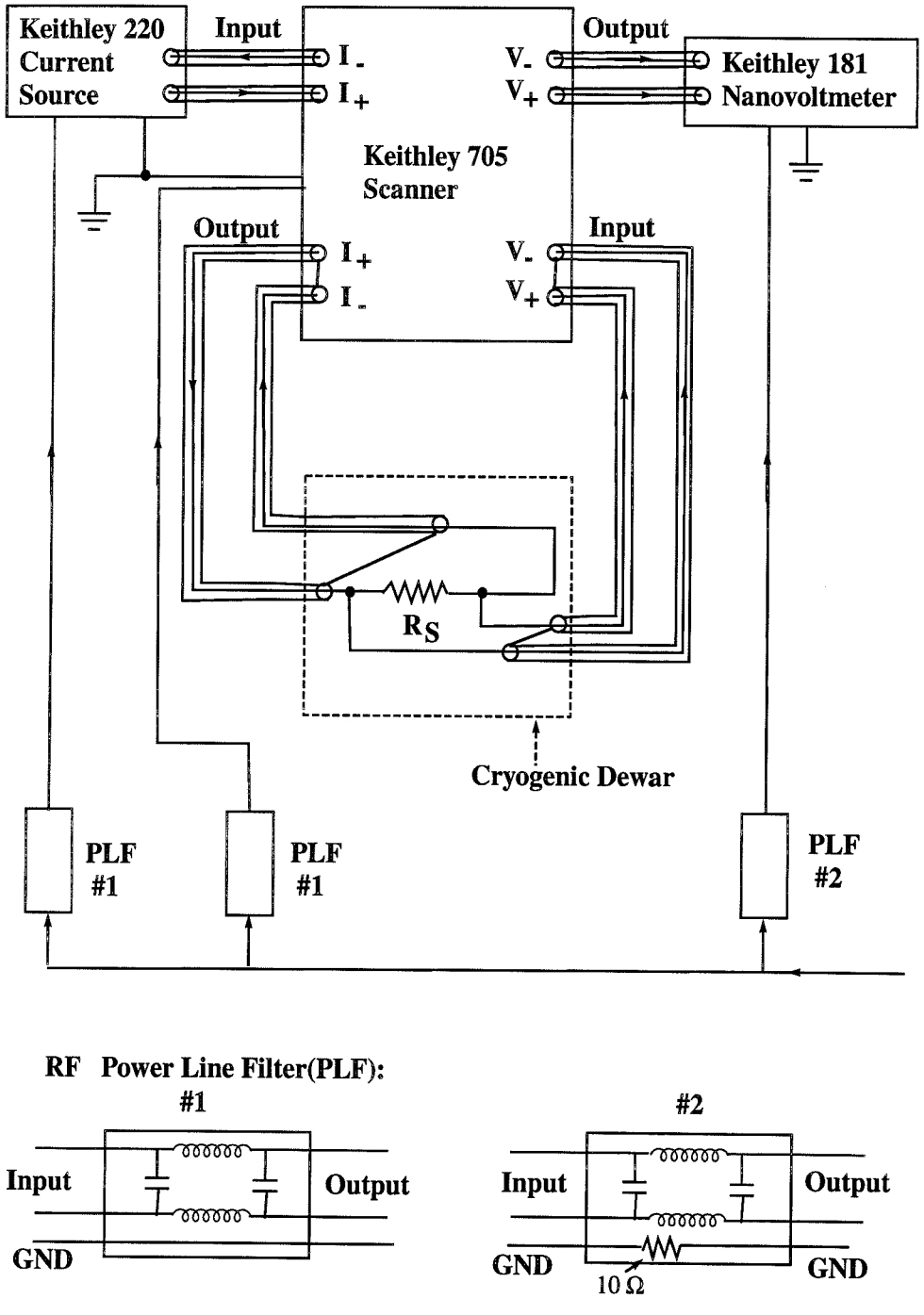

Figure 3.16: Noise reduction in the DC transport measurements.

indium wires on the sample surface, bad electrical contacts may be worsened which cause additional DC offset voltages that cannot be completely canceled by reversing the current. Overall, such noise level is low enough for most analysis of our data. For linear resistance measurements, much improved voltage resolution ($<\sim 10^{-9}$ V) can be obtained by using the low-frequency lock-in techniques. These measurement techniques will be described later in Chapter 6.

3.6.2 AC Transport Measurements

The purpose of AC performing transport measurements is to study the frequency dependence of the linear AC resistivity of $YBa_2Cu_3O_7$ single crystals near the vortex phase transitions, so that the critical scaling behavior at low frequencies can be investigated. The technique developed in our lab (Reed, 1995; Reed *et al.*, 1992; Reed *et al.*, 1993) has proven successful in fulfilling this purpose. An outline of the technique and the calibration procedures are briefly described below. The block diagram of the experimental set-up is shown in Fig. 3.17. Using the standard four-terminal contact arrangement, a sinusoidal AC current is applied through the bulk of the sample in the *ab*-plane. The current is provided by a 0.5 volt oscillator output of an HP4194A impedance analyzer. A noninductive 1 kΩ load resistor is placed at the high current output in series with the sample to ensure a constant current through the sample for the entire frequency range of our measurements. The voltage across the sample is measured by the HP4194A impedance analyzer enhanced with an EG&G PARC 80dB low noise preamplifier. This amplifier limits the maximum frequency to 2 MHz. The sample signals are carried by double shielded low-loss coaxial cables, and all shielding connections are arranged to eliminate ground loops (see Figure 3.17). The HP4194A impedance analyzer uses a lock-in technique to reduce the bandwidth to 10Hz about the applied current frequency, permitting a noise level of 10nV which corresponds to a measurable resistance of 20$\mu\Omega$. For more details of the AC measurement techniques, please see the Ph.D. thesis by D.S. Reed and related publications (Reed *et al.*, 1993; Reed *et al.*, 1992; Reed, 1995).

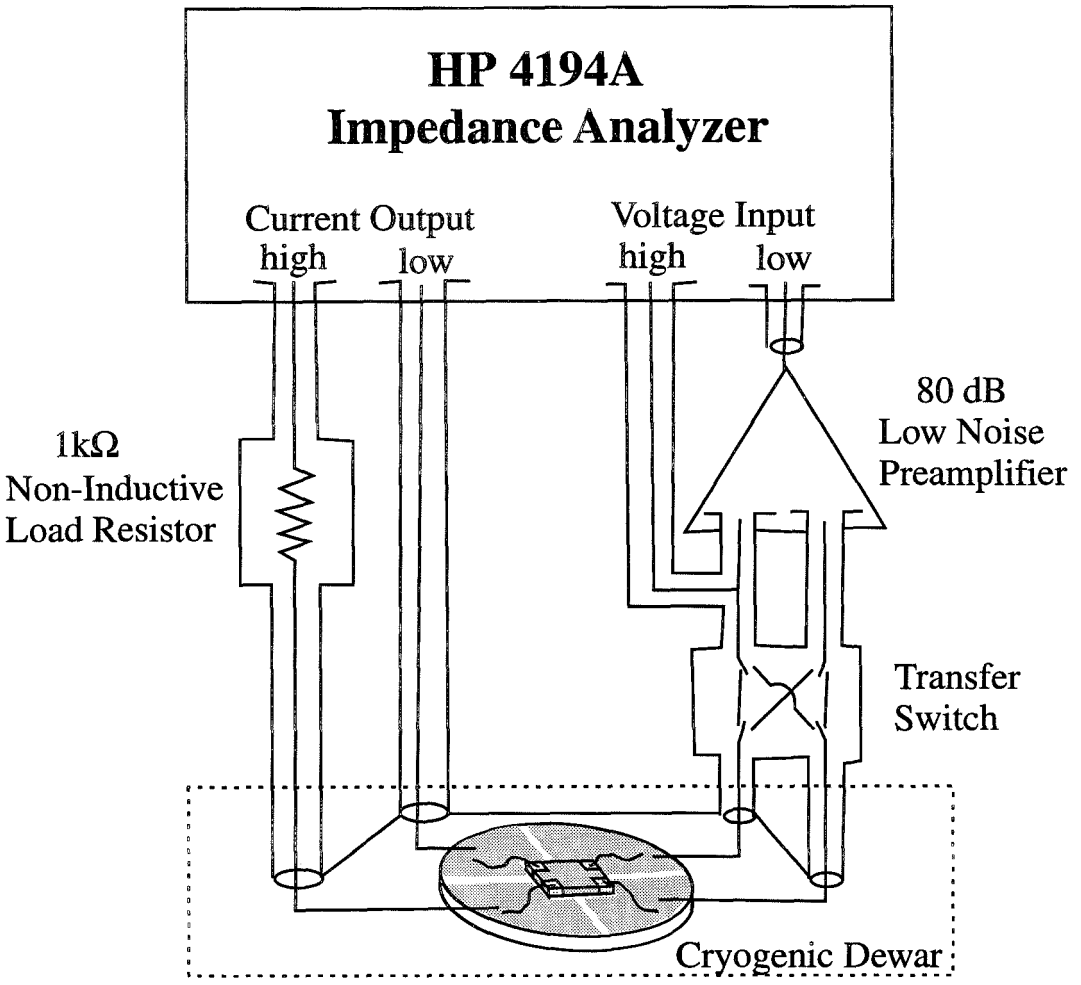

Figure 3.17: Block diagram of the AC impedance measurement system.

In addition to careful electronic arrangements, a detailed frequency-dependent calibration is needed to resolve the real sample signals. A reasonable approach is to consider the measured impedance signal Z_{meas} as a combination of the following contributions:

$$Z_{meas}(\omega) = [Z_{signal}(\omega) + Z_{back}(\omega)]G(\omega)e^{i\theta(\omega)}. \tag{3.3}$$

Here, Z_{signal} is the desired signal from the sample, Z_{back} is some purely imaginary background signal due to the parasitic inductance and capacitance in the circuit components, $G(\omega)$ and $\theta(\omega)$ are the frequency-dependent amplitude and phase of the

preamplifier gain, and $\omega = 2\pi f$ is the angular frequency of the applied AC current. Generally $G(\omega)$ and $\theta(\omega)$ can be found from Z_{meas} at room temperature, because at room temperature we can assume a frequency-independent sample signal for $\omega <$ 2MHz, i.e., $Z_{signal} = Z_{signal}(\omega = 0)$, and a much large sample signal than the parasitic background, $|Z_{signal}| >> |Z_{back}|$. This approximation gives a measured signal with an amplitude $|Z_{meas}(\omega)| = |Z_{signal}(\omega = 0)|G(\omega)$ and a phase which is simply $\theta(\omega)$. One can confirm the accuracy of the calibration for $\theta(\omega)$ by measurements at low temperatures where the sample is completely superconducting so that

$Z_{signal}(\omega)$ becomes purely imaginary. Finally, Z_{back} can found by measuring an ideal short, such as a small piece of gold foil, so that $Z_{signal}(\omega) = 0$, and $Z_{meas}(\omega) = Z_{back}(\omega)G(\omega)e^{i\theta(\omega)}$, where $G(\omega)$ and $\theta(\omega)$ are already known. Best results are obtained if the short has the same geometry and contact configuration as that of the sample.

An additional requirement for the success of this technique is the negligible contact resistance. Bad contact resistance will give an additional background signal which is hard to calibrate due to the complicated frequency and temperature dependence of the effective capacitance incurred by the poor electrical contacts to the sample.

3.7 Data Acquisition

The data acquisition is automated through the GPIB interface using IBM PS2/286 and 386 computers. The computer programs for controlling the data acquisition for all the measurements are described in the Ph.D. thesis by D. S. Reed (Reed, 1995).

Chapter 4 Vortex-Glass Transitions in As-Grown and Proton Irradiated Twinned $YBa_2Cu_3O_7$ Single Crystals

The primary goal of this thesis is to reveal the effects of different types of static disorder on the nature of the vortex-solid to liquid melting transition in high-temperature superconductors. A natural starting point is to investigate the as-grown $YBa_2Cu_3O_7$ single crystals which contain mainly twin boundaries and point defects. Although various reports of DC and at transport measurements by other research groups (Koch *et al.*, 1989; Gammel *et al.*, 1991; Olsson *et al.*, 1991) prior to our work had been suggestive of a second-order vortex-glass transition, the large error bars in the critical exponents and the unjustified broad temperature interval involved in the so-called "critical scaling" analysis about each "critical point" in those reports provided little convincing evidence of a true second-order transition. In addition, as shall be discussed below, various complications arise if one considers DC transport measurements alone. Although presented in this chapter are mostly detailed studies of the DC transport properties near the vortex-solid melting transition, it should be emphasized that this work is only part of our full-scope investigations which involve self-consistent studies of the vortex-solid melting transition. With three different experimental techniques: DC current-voltage characteristics (Yeh *et al.*, 1992b; Yeh *et al.*, 1992a; Yeh *et al.*, 1993a; Jiang *et al.*, 1993), frequency-dependent AC impedance (Reed *et al.*, 1993) , and frequency-dependent AC magnetic susceptibility (Reed *et al.*, 1994), we have found that the application of our rigorous critical scaling analysis to all three independent experiments yields universal critical exponents $\nu \approx 2/3$ and $z \approx 3$ (Yeh *et al.*, 1993a; Reed *et al.*, 1993) and universal scaling functions. The manifestation of universality therefore provides a strong support for a second-order vortex-glass to liquid phase transition in samples with twin boundaries and point defects.

Rather than verifying the universality of vortex-glass transitions with different experimental techniques, this chapter focuses on the universality of such transitions among various $YBa_2Cu_3O_7$ twinned single crystals with different densities of point defects. This approach is accomplished by studying the transport properties of as-grown and 3 MeV proton-irradiated $YBa_2Cu_3O_7$ single crystals. The DC transport measurements are studied in the context of both critical scaling behavior and vortex-pinning related properties. The idea of probing the critical phenomena within certain temperature regime (the "critical regime") and certain applied current range becomes clear with our investigations. It will be shown that the current range within which the critical scaling analysis is applicable is limited by the finite size effect at low currents and the flux-flow crossover at high currents.

4.1 Critical Scaling Analysis

In a vortex state with weak random pinning, thermal fluctuations can excite vortex dislocation loops consider from the originally pinned vortex configuration, as illustrated in Fig. 4.1. Assuming a second-order vortex-solid melting transition driven by isotropic static disorder and thermal fluctuations, the vortex correlation length ξ_v for a constant magnetic field H will diverge as $T \to T_M(H)$:

$$\xi_v(T,H) = \xi_0(H)|1 - T/T_M|^{-\nu}, \tag{4.1}$$

where ξ_0 is the zero-temperature correlation length, T_M is the transition temperature, and ν is the static critical exponent. The critical relaxation rate $\omega_T \propto \tau^{-1}$, with τ being the thermal relaxation time for fluctuating vortices, is related to ξ_v as $\omega_T(T) \sim \xi_v^{-z}$, i.e.,

$$\omega_T(T) = \omega_c|1 - T/T_M|^{\nu z}, \tag{4.2}$$

where ω_c is the zero-temperature relaxation rate, and z is the dynamic exponent. Since $\xi_v \to \infty$ and $\tau(\sim \xi_v^z) \to \infty$ near T_M, we may scale various physical quantities near T_M with ξ_v because ξ_v and tau are the most significant length and time scales.

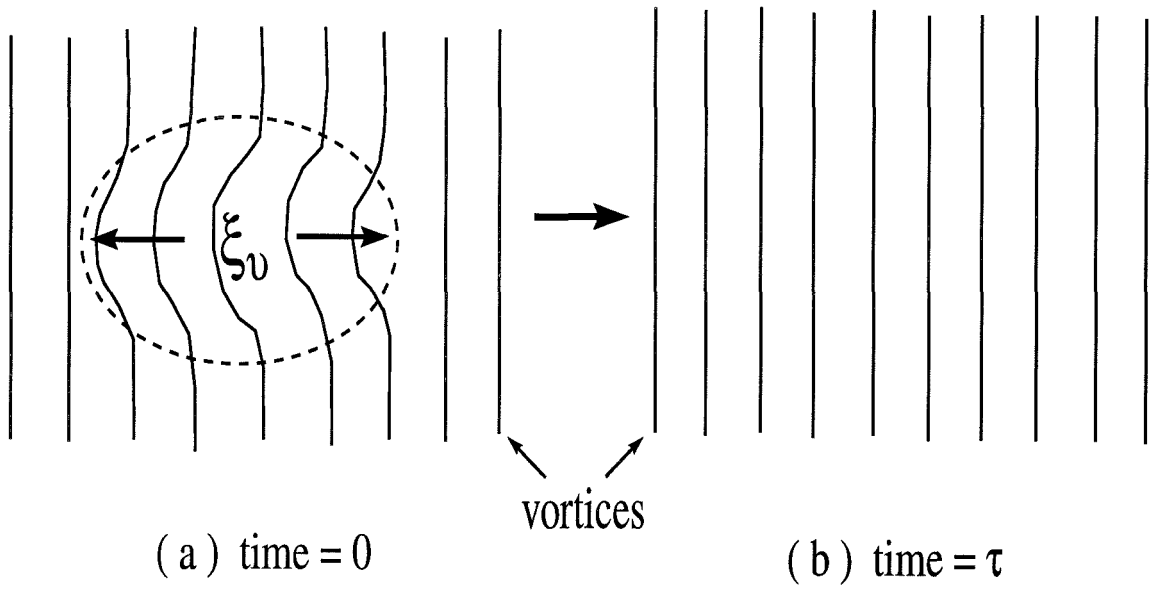

Figure 4.1: Illustration of the vortex dislocation loop caused by thermal fluctuations. After the time τ, the vortices relax back to the ground state.

Consider the sample resistivity ρ as a function of temperature (T), frequency (f), and the applied current density (J). The resistivity is related to an effective "superfluid density" ρ_s by $\rho^{-1} \sim i\rho_s/f$. It should be emphasized that the effective superfluid density ρ_s is not directly related to the superconducting order parameter of the sample. Rather, it is similar to the stiffness of the vortex-solid and is related to the shear modulus. In the critical regime, the superfluid density scales as (Fisher *et al.*, 1973) $\rho_s \sim \xi_v^{2-d}$, where d is the dimensionality of the phase transition. Combining this expression with the frequency scaling, $f = \omega/(2\pi) \sim \xi_v^{-z}$, gives the scaling for the resistivity $\rho \sim \xi_v^{d-2-z}$. The general scaling relation can be expressed as

$$\rho_(\delta; f; J) \sim \xi_v^{d-2-z} \tilde{\rho}_{\pm}(\delta \xi_v^{1/\nu}; f\xi_v^z; J/J_T), \quad \delta \equiv |1 - (T/T_M)|, \tag{4.3}$$

where $\tilde{\rho}_{\pm}$ are the universal functions for temperatures $T > T_M(+)$ and $T < T_M(-)$, respectively, and the characteristic current density J_T is defined by (Fisher *et al.*,

1991)

$$J_T \xi_v^{d-1} \Phi_0 = k_B T, \tag{4.4}$$

as shown in Fig. 4.2 for $d = 3$.

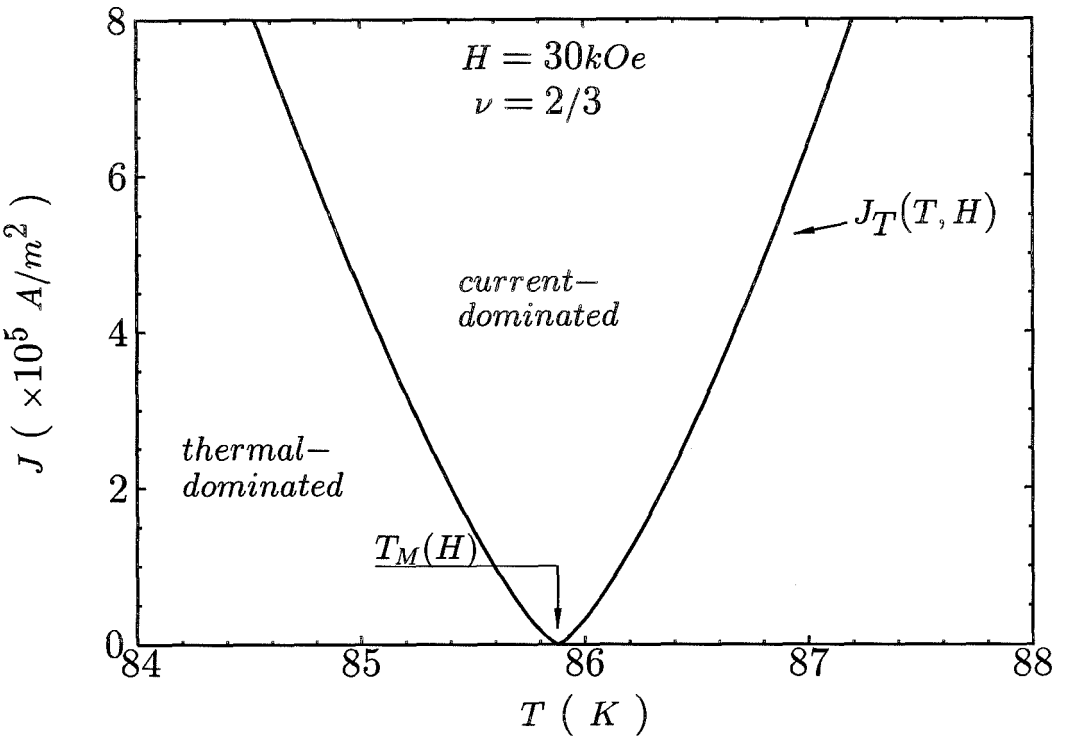

Figure 4.2: The J-vs-T diagram for $H = 30$ kOe showing the characteristic current density $J_T(T, H)$ (the solid line) which separates the current-dominated regime from the thermal-dominated regime.

In the presence of a DC current ($f \to 0$), when the driving force exerted on the vortices by the applied current is smaller than that of the thermal fluctuations, *i.e.*, $J < J_T$, the scaling relation of the resistivity (ρ) can be simplified into:

$$\rho = E/J \sim \xi_v^{d-2-z} \tilde{\rho}_{\pm}(x) \sim \left|1 - \frac{T}{T_M}\right|^{\nu(2+z-d)} \tilde{\rho}_{\pm}(x), \quad x \equiv \frac{J}{J_T(T,H)} = \frac{J \xi_v^{d-1} \Phi_0}{k_B T}, \tag{4.5}$$

where E is the electric field. The forms of the scaling functions $\tilde{\rho}_+$ and $\tilde{\rho}_-$ can be obtained by the following considerations. We expect $\tilde{\rho}_+ \to$ constant as $x \to 0$ because the sample resistance becomes Ohmic in the normal state. On the other hand, for $x \to \infty$($J >> J_T$ or $T \to T_M$), the correlation length becomes limited by the applied

current density J according to Eq. (4.4), such that

$$\xi_v \sim \left(\frac{k_B T}{J\Phi_0}\right)^{1/(d-1)}, \tag{4.6}$$

and

$$\rho \sim \xi_v^{d-2-z} \sim \left(\frac{J\Phi_0}{k_B T_M}\right)^{(z+2-d)/(d-1)}, \tag{4.7}$$

for $T \to T_M$. The scaling functions ($\tilde{\rho}(\tilde{J})$) follows the same asymptotic behavior as $\rho(J)$, i.e., $\tilde{\rho}_{\pm}(x) \propto \tilde{J}^{(2+z-d)/(d-1)}$, as $x \to \infty$.

According to Eq. (4.5), if the values of T_M, ν and z are known, one may scale the quantities ρ and J by the following expressions:

$$\begin{aligned} \tilde{\rho} &= (E/J)|1 - T/T_M|^{-\nu(2-d+z)}, \\ \tilde{J} &= J|1 - T/T_M|^{-(d-1)\nu}, \end{aligned} \tag{4.8}$$

such that the ρ-vs-J isotherms in the critical regime of T_M can be "collapsed" into two universal functions $\tilde{\rho}_+(x)$ and $\tilde{\rho}_-(x)$ for the isotherms at temperatures above and below T_M, respectively. Here, $x = J/J_T = \tilde{J}/\tilde{J}_T$, with $\tilde{J}_T \equiv k_B T/(\Phi_0 \xi_0^{d-1})$.

In reality, T_M, ν and z values are unknown and therefore are treated as input parameters to a computer program which does the data transformation according to Eqs. (4.6) and (4.7) and displays the scaled isotherms. The T_M, ν and z values are obtained when scaled isotherms "collapse" into two universal curves. For a self-consistent check, the critical exponents ν and z should be independent of the magnitude and orientation of the applied magnetic fields. In addition, the scaling functions should be universal for all fields and angles, following the asymptotic behavior described above except for a non-universal coefficient.

In the case of frequency-dependent measurements of AC impedance, as long as the current density is much smaller than J_T, the amplitude and phase of the linear AC resistivity ($\rho_{ac} = |\rho_{ac}|e^{i\phi_\rho}$) near T_M can be expressed according to the following scaling relations (Fisher *et al.*, 1991; Yeh *et al.*, 1993a; Yeh *et al.*, 1992a; Reed *et al.*,

1993):

$$\begin{aligned} |\rho_{ac}| &\sim |1 - T/T_M|^{\nu(2-d+z)}\tilde{\rho}_{\pm}(\tilde{f}), \quad \tilde{f} = f|1 - T/T_M|^{-\nu z}, \\ \phi_\rho &= \tilde{\phi}_{\pm}(\tilde{f}). \end{aligned} \tag{4.9}$$

Similarly, defining

$$\begin{aligned} \tilde{\rho}_{ac} &= |\rho_{ac}||1 - T/T_M|^{-\nu(2-d+z)}, \\ \tilde{f} &= f|1 - T/T_M|^{-\nu z}, \end{aligned} \tag{4.10}$$

the amplitude and phase versus frequency curves can be scaled into the corresponding universal functions $\tilde{\rho}_{\pm}$ and $\tilde{\phi}_{\pm}$. Similar considerations for the asymptotic behavior of the scaling functions (Fisher *et al.*, 1991; Yeh *et al.*, 1993a; Yeh *et al.*, 1992a; Reed *et al.*, 1993) lead to $\tilde{\rho}_{ac}(\tilde{f}) \propto \tilde{f}^{(z+2-d)/z}$ as $\tilde{f} \to \infty$ or $T \to T_M$. In addition, as shown by Dorsey (1991), by inserting the phase and amplitude of the AC resistivity into the Kramers-Kronig relation,

$$\phi_\rho = -\mathcal{P}\int_{-\infty}^{+\infty} \frac{df'}{\pi} \frac{\ln|\rho(f')|}{f' - f}, \tag{4.11}$$

where $\mathcal{P}$ denotes a Cauchy principal-value integral, a frequency-independent critical phase is obtained as $\tilde{\phi}_c \equiv \phi_\rho(T_M) = \frac{\pi}{2}\left[1 - \frac{d-2}{z}\right]$.

The physical significance of a frequency-independent phase $\tilde{\phi}_c$ at T_M can be qualitatively understood as follows: Since both the real and imaginary parts of ρ follow the same asymptotic relation with the frequency at T_M, and since $\tilde{\phi} \equiv \tan^{-1}\left\{\frac{\mathrm{Im}[\rho(T_M)]}{\mathrm{Re}[\rho(T_M)]}\right\}$, $\mathrm{Re}[\rho(T_M)] = \text{constant} \cdot \tilde{f}^{(1-\frac{1}{z})}$, $\mathrm{Im}[\rho(T_M)] = \text{constant} \cdot \tilde{f}^{(1-\frac{1}{z})}$, we find that $\tilde{\phi}_c$ is independent of frequency.

4.2 Experimental Results & Data Analysis

4.2.1 Samples and Electrical Transport Measurements

Three samples have been studied to yield information about the role of point

defects. The samples were two similar $YBa_2Cu_3O_7$ single crystals originally from the same batch of crystal growth. Both crystals were dilutely twinned with an average twin boundary separation of $\sim 2\ \mu$m. One of these two as-grown crystals, studied with both DC and AC transport measurements in applied magnetic fields from 1 kOe to 90 kOe (Yeh *et al.*, 1993a; Reed *et al.*, 1993) and for different field orientations with the angle(θ) between the field and crystalline c-axis from 0° to 90°, is denoted as Sample # 1 (see also Table 4.1 and also Table 3.3). The other single crystal was used for 3.0 MeV protons irradiations. It was irradiated twice with a fluence of 5×10^{15}protons/cm^2 each. As discussed in Chapter 3, the defects created by 3-MeV protons were randomly distributed point defects with a volume density $\sim 1.1 \times 10^{19}$cm^{-3} for the fluence of 5×10^{15}protons/cm^2. Following each proton irradiation, DC transport measurements were carried out using the standard four-probe method in magnetic fields (H) ranging from 1 kOe to 90 kOe, with **H** perpendicular to the applied current density (**J**), and for **H** both parallel and perpendicular to the c-axis of the sample. We denote the sample after the first irradiation as Samples #2, and that after the second Sample #3, respectively. In addition, AC transport measurements are carried out on sample # 3. In the following, the Samples #1, #2 and #3 are also denoted as Samples A, B, and C, respectively. The zero-field transition temperatures (T_c's) for these three samples are shown in Table 4.1.

Table 4.1: The proton fluence f dependence of the zero-field transition temperature T_c, the zero-field critical exponents $\nu_{0||}$ ($\vec{H} \parallel c$) and $\nu_{0\perp}$ ($\vec{H} \perp c$), and the power a for the critical current density $J_x(T)$ (see text).

	f	T_c	ν_0		
Sample	$(protons/cm^2)$	(K)	$\nu_{0\|\|}$	$\nu_{0\perp}$	a
A (#1)	0	92.95 ± 0.05	0.65	0.65	0.62
B (#2)	$\sim 5 \times 10^{15}$	92.25 ± 0.05	0.63	0.64	0.58
C (#3)	$\sim 1 \times 10^{16}$	91.62 ± 0.05	0.62	0.63	0.67

4.2.2 E-vs-J Isotherms and Critical Scaling

The electric field (E) versus current density (J) isotherms are obtained from DC transport measurements in a constant applied magnetic field and at temperatures near the transition. Shown in Fig. 4.3 are the representative data taken at $H_{\|c} = 10$ kOe and $H_{\perp c} = 10$ kOe for Sample A. Figure 4.4 shows the data for $H_{\perp c} = 50$ kOe for Sample B and $H_{\|c} = 10$ kOe for Sample C.

We find that with the critical scaling analysis described earlier, all the E-vs-J isotherms within the critical regime can be "collapsed" into two universal curves $\tilde{\rho}_{\pm}$ with proper values of T_M, ν and z. The insets of figures 5.2 and 5.3 are the $\tilde{\rho}_{\pm}$ curves obtained from corresponding E-vs-J isotherms. For all the fields from $H = 1.0$ to 90 kOe and angles (θ) between the field and the sample c-axis from 0° and 90° and for all three samples, *universal* critical exponents are obtained with $\nu = 0.65 \pm 0.05$ and $z = 3.0 \pm 0.3$, consistent with the power-law dependence of the scaling function $\tilde{\rho} \propto \tilde{J}^{(z-1)/2}$ when $T \to T_M$ which yields $1.0 \pm 0.1 \approx (z-1)/2$. Furthermore, as demonstrated in Fig. 4.5, the universal functions $\tilde{\rho}_{\pm}$ are identical for different fields and different samples, except for a nonuniversal constant that provides information about the vortex correlation length $\xi_0(H)$ which will be discussed later. Consequently, the critical scaling behavior of the vortex transport properties in HTS samples with different densities of weak pinning defects is found to be universal, lending strong support for a true second-order phase transition.

The melting temperature $T_M(H)$ obtained from the above critical scaling analysis for different fields and different samples are plotted in the H-vs-T phase diagram (see Fig. 4.6). We note that all melting lines follow the same relation

$$H_M(T) = H_M(0)|1 - T/T_c|^{2\nu_0} \tag{4.12}$$

with the zero-field critical exponent $\nu_0 = 0.63 \pm 0.02$, consistent with a 3D XY model which asserts $\nu_0 = 2/3$. Interestingly, however, the high-field melting temperatures for both $H \parallel c$ and $H \perp c$ increase with the increasing disorder (see Fig. 4.6(a)) despite the decrease in T_c. When plotted in reduced temperatures (T/T_c) , as shown

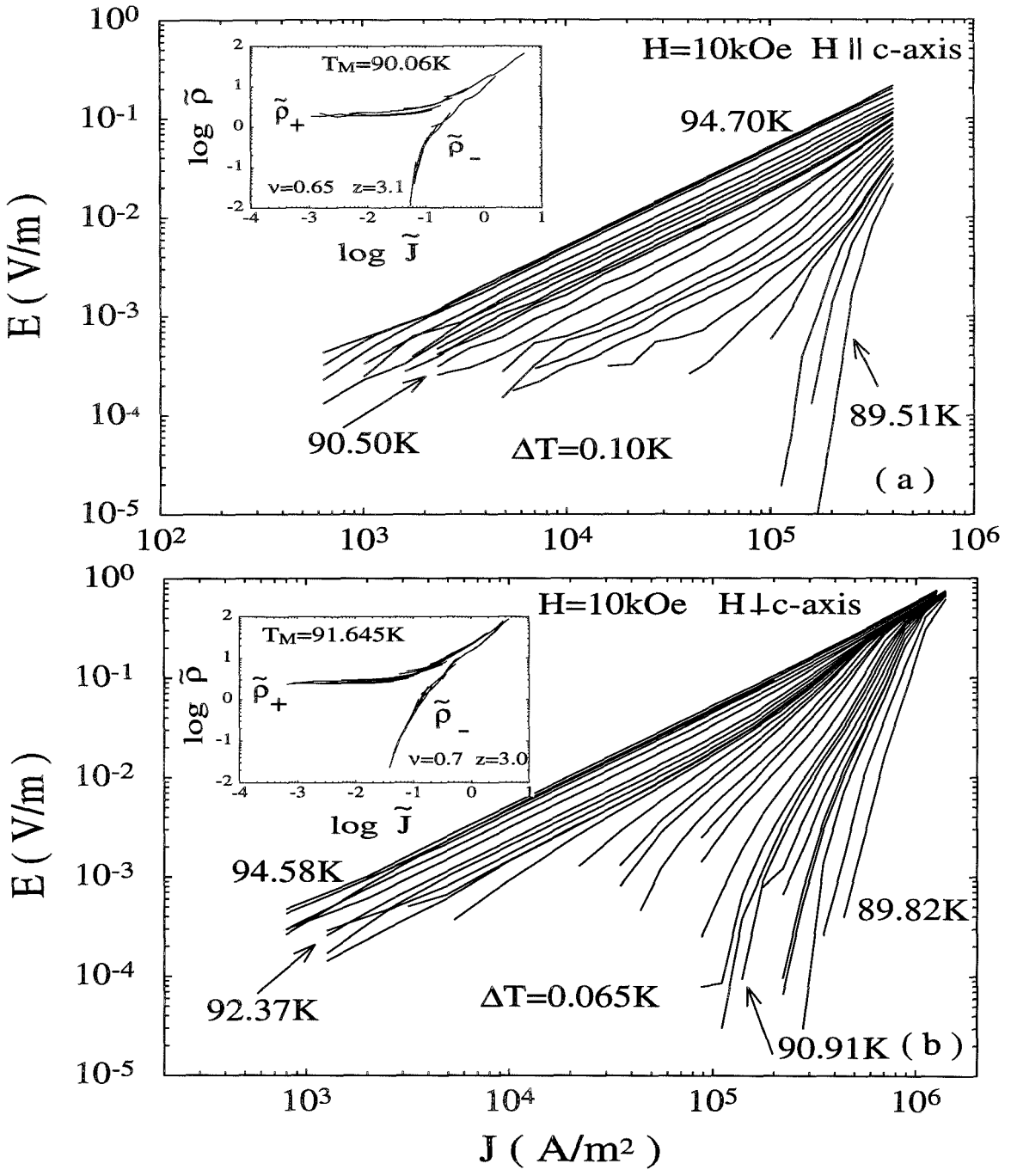

Figure 4.3: Representative electric field E vs current density J isotherms of the as-grown $YBa_2Cu_3O_7$ single crystal (Sample #1) for (a) $H_{\perp c} = 10$ kOe, and (b) $H_{\|c} = 10$ kOe. The insets are the universal functions $\tilde{\rho}_{\pm}(x)$ obtained from collapsing the isotherms with $J_\ell(T,H) < J < J_x(T,H)$ and T within the critical regime indicated by arrows. The parameters used for the collapsing are $\nu = 0.67$ and $z = 3.0$ and the $T_M(H)$ values indicated in the insets. δT is the averaged temperature increment of the isotherms in the critical regime.

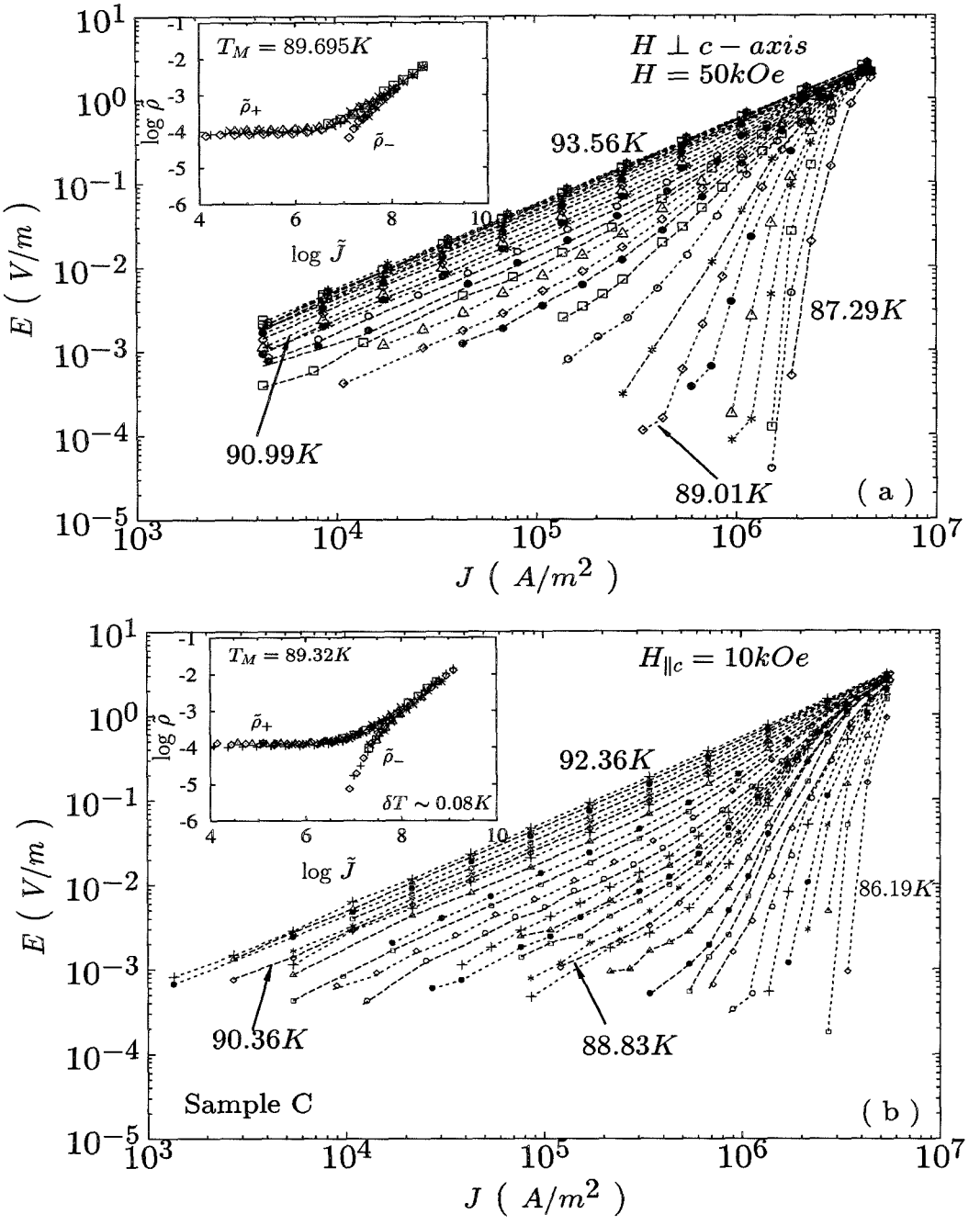

Figure 4.4: Representative electric field E vs current density J isotherms of proton irradiated $YBa_2Cu_3O_7$ single crystals (Samples B (#2), and C (#3)). (a) Sample B with $\mathbf{H} \perp \mathbf{c}$-axis and $H = 50$ kOe. (b) Sample C with $\mathbf{H} \parallel \mathbf{c}$-axis and $H = 10$ kOe. The insets are the universal functions $\tilde{\rho}_{\pm}(x)$ obtained from collapsing the isotherms with $J_\ell(T,H) < J < J_x(T,H)$ and T within the critical regime indicated by arrows. The parameters used for the collapsing are $\nu = 0.67$ and $z = 3.0$ and the $T_M(H)$ values indicated in the insets. δT is the averaged temperature increment of the isotherms in the critical regime.

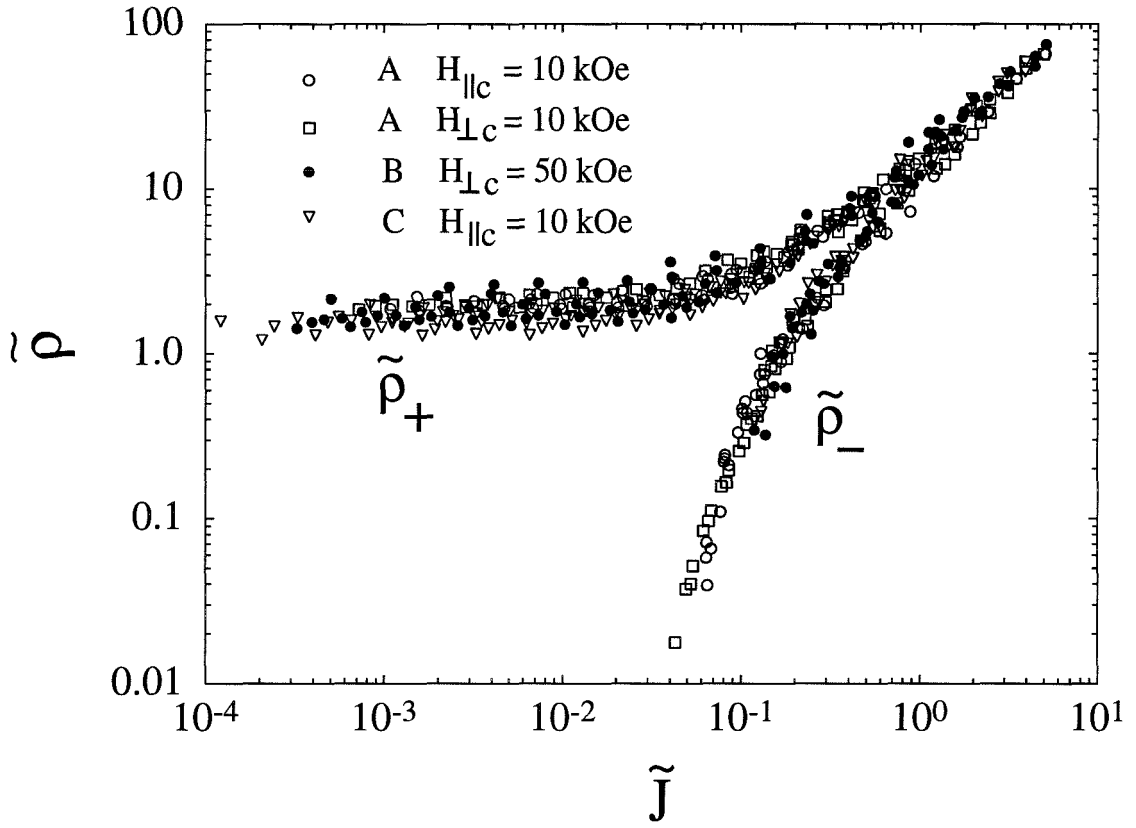

Figure 4.5: The scaled functions $\tilde{\rho}_{\pm}$ for all three Samples #1, #2 and #3 and for different magnetic fields plotted together.

in Fig. 4.6(b), the slopes of the melting lines increase with increasing disorder.

To verify the isotropic critical scaling behavior, various data sets taken at different θ values have been studied, yielding the same critical exponents as a function of θ. As shown in Fig. 4.7, the smooth increase of T_M with increasing θ results from the intrinsic anisotropy. The solid line is a theoretical fitting curve to the melting transition temperatures of an anisotropic superconductor, following the expression:

$$H_M(T,\theta) = \frac{H_M(T=0,\theta=0)|1-T/T_c|^{2\nu_0}}{\sqrt{cos^2\theta + \varepsilon^2 sin^2\theta}}. \tag{4.13}$$

All these results have proved that the vortex-glass transition is insensitive to

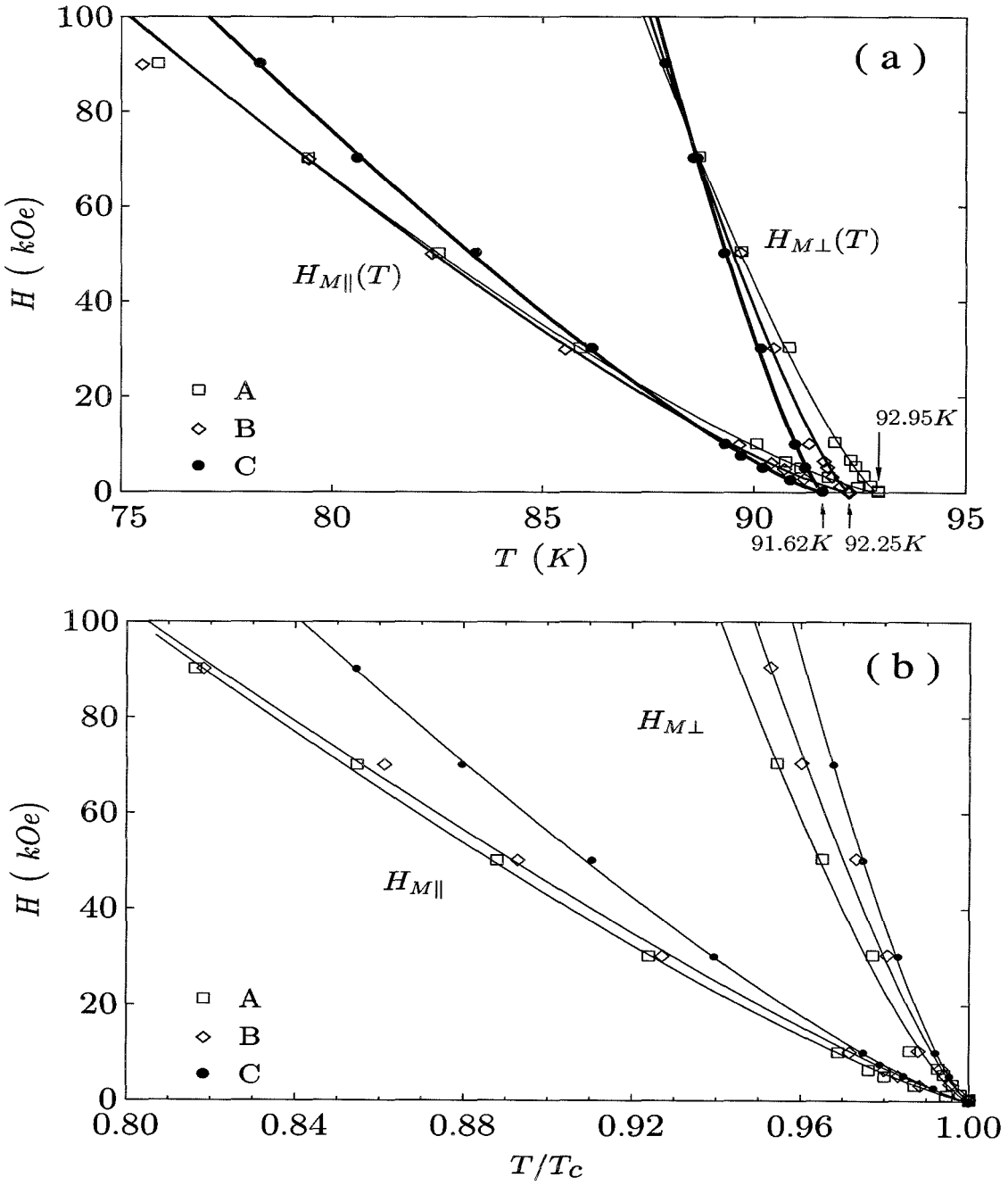

Figure 4.6: (a) The anisotropic vortex-solid melting transition lines for $\vec{H} \parallel$ c-axis ($H_{M\parallel}(T)$) and $\vec{H} \perp$ c-axis ($H_{M\perp}(T)$), and for Samples A, B, C. All solid lines satisfy the relation $H_M(T) = H_M(0)|1 - T/T_{c0}|^{2\nu_0}$ with ν_0 values given in Table 4.1. (b) The same $T_M(H)$ data plotted in the reduced temperature (T/T_c).

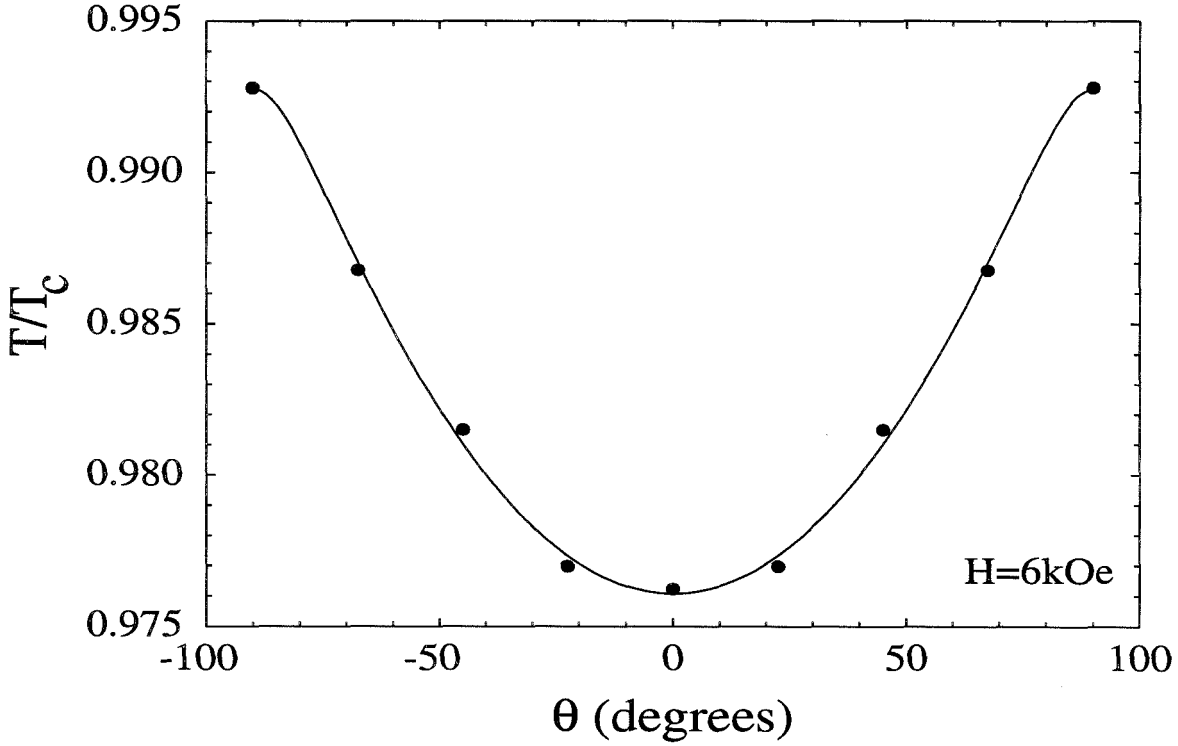

Figure 4.7: The vortex-solid melting transition temperature (T_M) as a function of the angle (θ) between the applied magnetic field and crystalline c-axis.

the density of randomly distributed weak-pinning point defects and that the vortex dissipation near the melting transition are governed by the same critical phenomena, independent of moderate variations in the density of point defects.

4.2.3 Critical Regime

As discussed earlier, critical phenomena can only be observed in the critical regime where the thermal fluctuations are dominant. We have shown in Chapter 2 that an estimate using the Ginzburg criterion yields a critical regime $\left(\frac{\Delta T}{T_M}\right) \approx 10^{-2}$ to 10^{-3} K in high-temperature superconductors, which is much larger than most conventional superconductors. The concept of restricting to the critical regime in the data analysis is essential for obtaining accurate critical exponents (see also Yeh et al. (1993a). For instance, the melting line $H_M(T)$ is below the mean-field upper critical field line $H_{c2}(T)$ in the phase diagram. The former corresponds to phase transitions associated

with the phase of the order parameter, and the latter with the amplitude of the order parameter. Since both lines converge to T_c in the low fields, the need for narrowing into the transition temperature $T_M(H)$ becomes even more important so that the corresponding critical phenomena can be revealed without being seriously influenced by the presence of another critical point $T_{c2}(H)$.

Empirically, the critical regime can be determined by the following method. After scaling functions are achieved with certain T_M, ν and z values, rescale the E-vs.-J isotherms are rescaled again with the same T_M and and critical exponents over a smaller temperature range. If the quality of the scaling function is worsened or no scaling can be observed, then the T_M, ν and z values have to be readjusted . Such process is repeated until consistent results are obtained. Then more isotherms at both higher and lower temperatures are included until the newly added isotherms no longer fall on the scaling functions. The temperature range within which consistent scaling behavior can be observed is then defined as the critical regime for that field. The critical regime obtained using this method for sample #1 is shown in Fig. 4.8 as the shaded regime. It ranges from 10^{-1} K to $\sim$ 2.5 K for magnetic fields from 1.0 kOe to 70 kOe.

4.2.4 Vortex Correlation Length Coefficient

Next, let's consider the asymptotic behavior discussed earlier in Section 4.1. From the scaling functions $\tilde{\rho}_{\pm}$ we can obtain the vortex correlation length coefficient $\xi_0(H)$. As shown in Fig. 4.9, if we assume that $\tilde{\rho}_+(x) \approx \tilde{\rho}_-(x) \approx \tilde{\rho}_0 x^{(z-1)/2}$ for $x \to \infty$ and $\tilde{\rho}_+(x) \approx \tilde{\rho}_0$ for $x \to 0$, where $\tilde{\rho}_0$ is a constant independent of T and J, and x is defined by $x \equiv \tilde{J}/\tilde{J}_T = J/J_T$, with $\tilde{J}_T = k_B T/(\xi_0^2 \Phi_0)$, we can obtain $\tilde{J}_T(T_M)$, and therefore ξ_0, directly from the universal function $\tilde{\rho}_+$ (Yeh *et al.*, 1993a; Yeh *et al.*, 1992a). The results of ξ_0 as a function of fields for all three samples are shown in Fig. 4.10. The ξ_0 values, within the order of a few hundreds of angstroms, increase with increasing H, consistent with a stronger intervortex correlation in higher magnetic fields.(Jiang *et al.*, 1993). In addition, ξ_0 decreases with increasing density of defects in fields

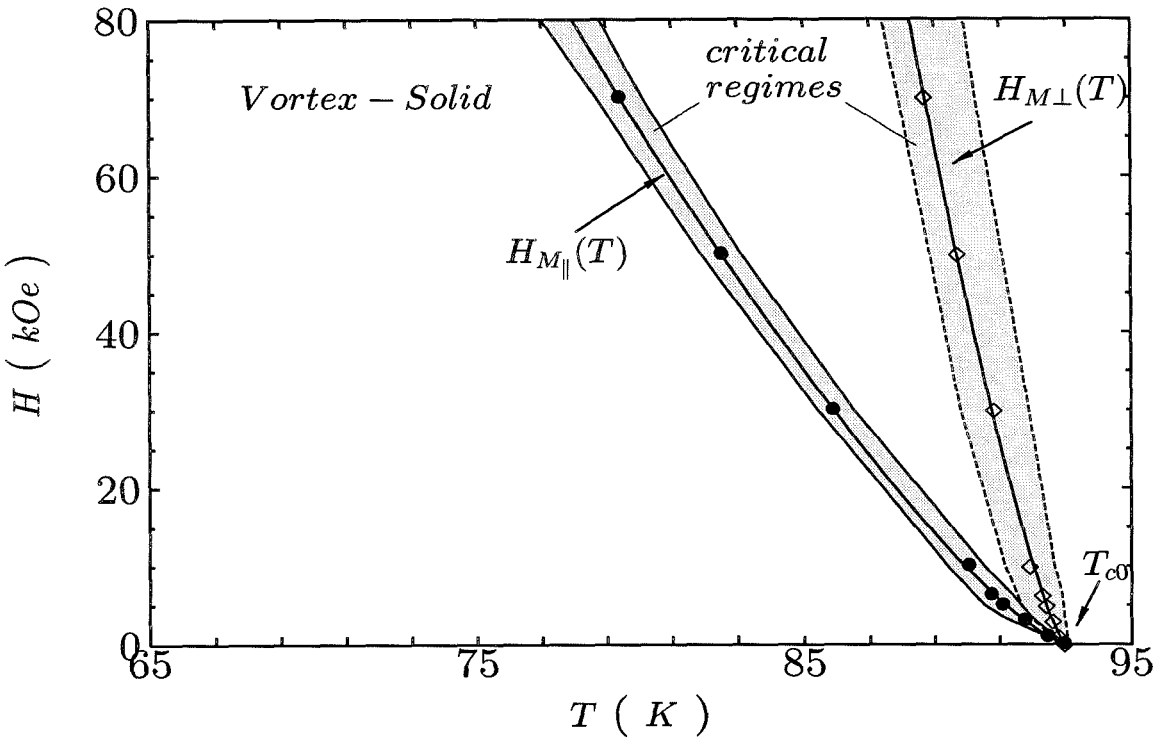

Figure 4.8: The critical regimes of the anisotropic vortex-solid melting transition lines for $\vec{H} \parallel$ c-axis ($H_{M\parallel}(T)$) and $\vec{H} \perp$ c-axis ($H_{M\perp}(T)$).

$H > 10\ kG$ for both $\mathbf{H} \parallel \mathbf{c}$ and $\mathbf{H} \perp \mathbf{c}$. The decrease of ξ_0 may be attributed to the smaller vortex dislocation loops in the presence of larger densities of point defects after proton irradiations. The inset of Fig. 4.10 shows that $\xi_0(H \perp c) \approx \xi_0(H \parallel c)$ is within the experimental error, consistent with our definition of one vortex correlation length for all the field orientations. In other words, we find that the evolving of the dislocation loop near the vortex-glass to vortex-liquid transition is isotropic.

4.2.5 Finite Size Effect

As mentioned before, the vortex correlation length ξ_v is a function of J when J is comparable to J_T. If a broad current range is used for measurements of the E-vs-J isotherms, the general expression for the vortex correlation length can be given as follows:

$$\xi_v = \xi_0(H)|1 - T/T_M|^{-\nu} f(x), x \equiv \frac{J}{J_T(T,H)}. \tag{4.14}$$

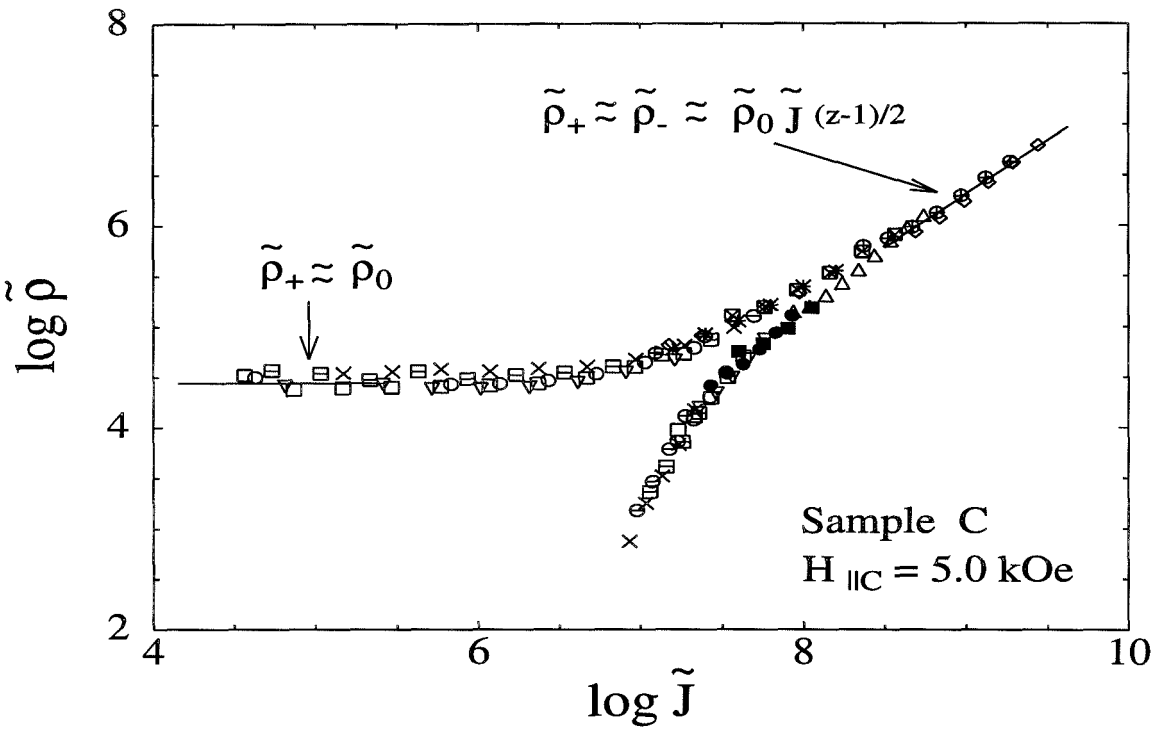

Figure 4.9: Illustration of how the vortex correlation length coefficient $\xi_0(H)$ values (see the text) are obtained experimentally from the critical scaling analysis.

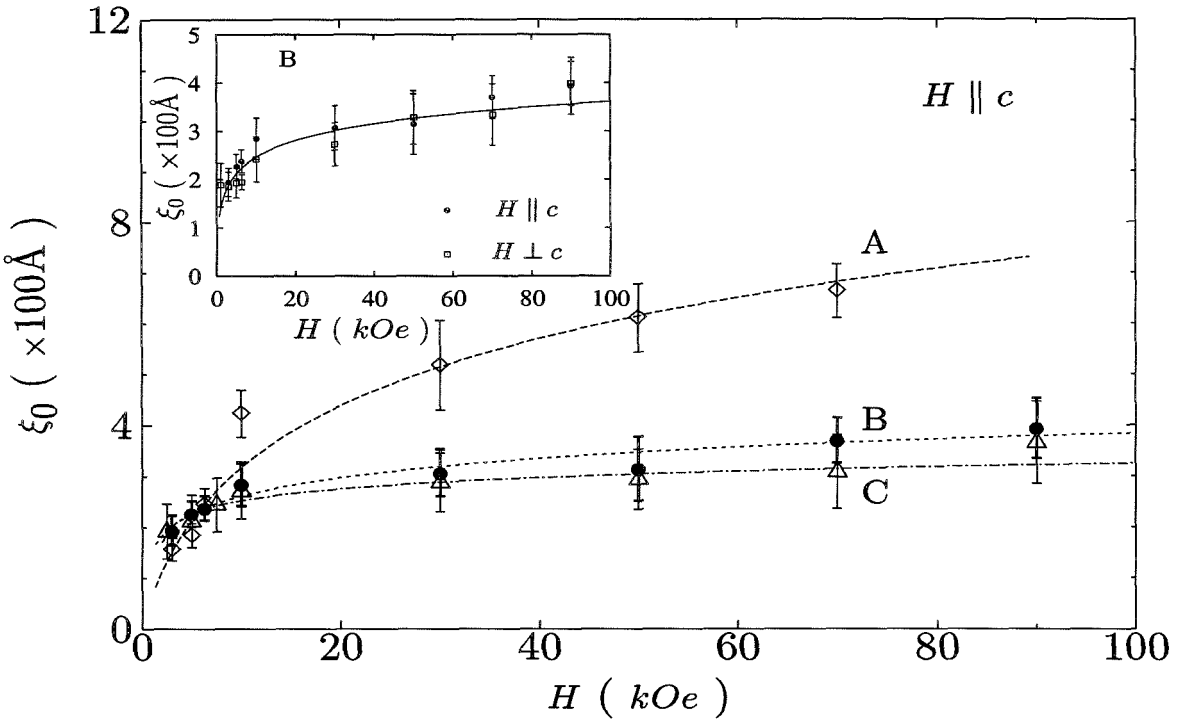

Figure 4.10: The correlation length (ξ_0) as a function of the magnetic field (H) for Samples A, B, C with **H** $\parallel$ **c**. The inset shows the ξ_0 values of Sample B for **H** $\parallel$ **c** and **H** $\perp$ **c**. The results for the other two samples are similar in that $\xi_0(H)$ values are the same for the two H orientations within the experimental error.

The functional form of the $f(x)$ satisfies two conditions: $f(x) \to 1$ for $x \to 0$ and $f(x) \to x^{-1/(d-1)}$ for $x \to \infty$, so that Eq. (4.14) reduces to $\xi_v = \xi_0|1 - T/T_M|^{-\nu}$ for $J << J_T$, and $\xi_v = [k_B T/(J\Phi_0)]^{1/(d-1)}$ for $J >> J_T$ (see (Yeh *et al.*, 1993a) and the references therein).

In twinned $YBa_2Cu_3O_7$ single crystals, as T approaches T_M, the growth of ξ_v will eventually be disrupted by the twin boundaries whenever $\xi_v \sim \ell$, where ℓ is a "vortex mean free path" comparable to the average twin boundary separation. Consequently, for constant T and H there is a characteristic current density $J_\ell(T, H)$ defined by the relation $\xi_v(T, H, J_\ell) = \ell$, such that for $J < J_\ell$ the vortex dislocation loops are pinned by the twin boundaries, and the critical scaling of the E-vs.-J isotherms breaks down. From Eqs. (4.14) and (4.4), we note that $J_\ell(T_M) = (k_B T_M)/(\ell^2 \Phi_0)$ is independent of the exact functional form of $f(x)$, and therefore ℓ can be determined if $J_\ell(T, H)$

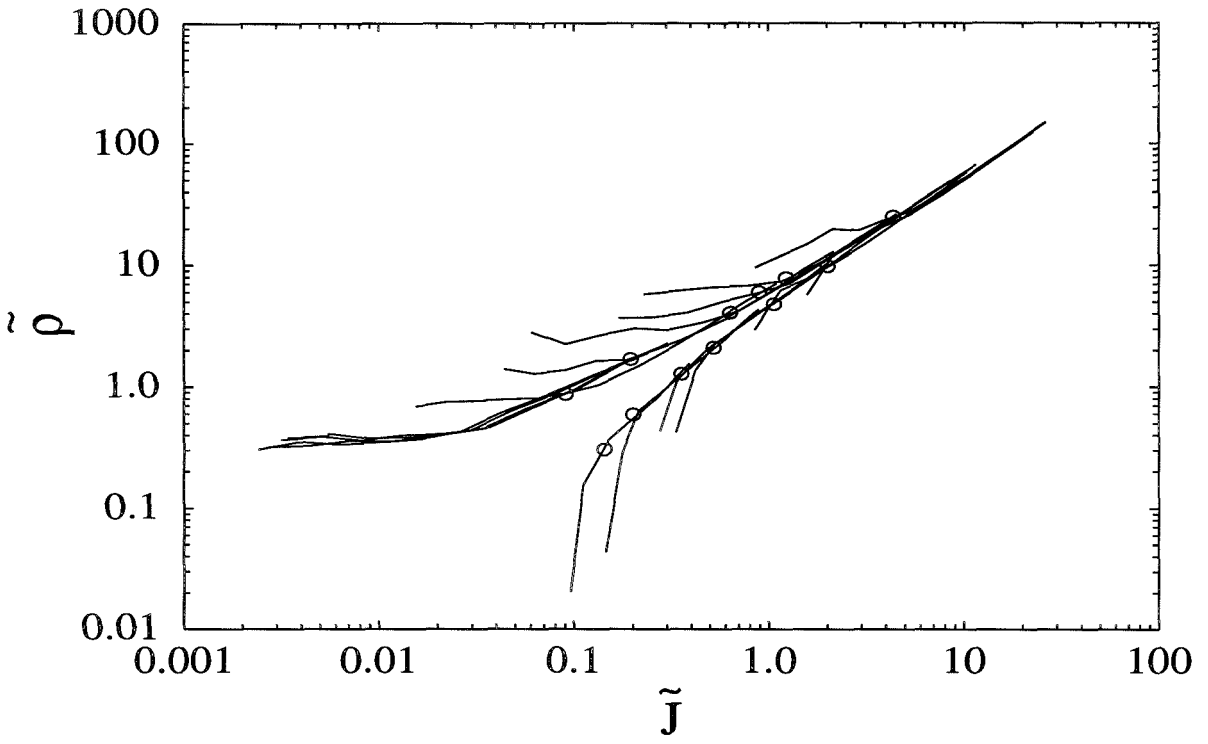

Figure 4.11: Illustration of how $J_\ell(T)$ values (see the text) are determined experimentally from the critical scaling analysis.

is known. Experimentally, the $J_\ell(T)$ values can be identified as the current density below which the scaled isotherm deviate from the universal scaling functions. Plotted in Fig. 4.10, are the $\tilde{\rho}$-vs.-$\tilde{J}$ data for Sample # 1. The circles indicate the J_ℓ values for each T. The obtained J_ℓ values are plotted in Fig. 4.12 for the J versus T diagram. Shown in Fig. 4.13 are the ℓ values as a function of field. We note that ℓ varies from 2.2 to 1.3 μm for the magnetic fields from 1 to 70 kOe, in agreement with the averaged twin boundary separation in the sample which is $\sim$ 2 μm. The slight decrease of ℓ with the increasing field may be attributed to the increasing vortex-pinning center interaction which reduces the vortex mean free path. Thus, the presence of J_ℓ is a natural consequence of the finite-size effect, not to be mistaken as the hint of another phase transition.

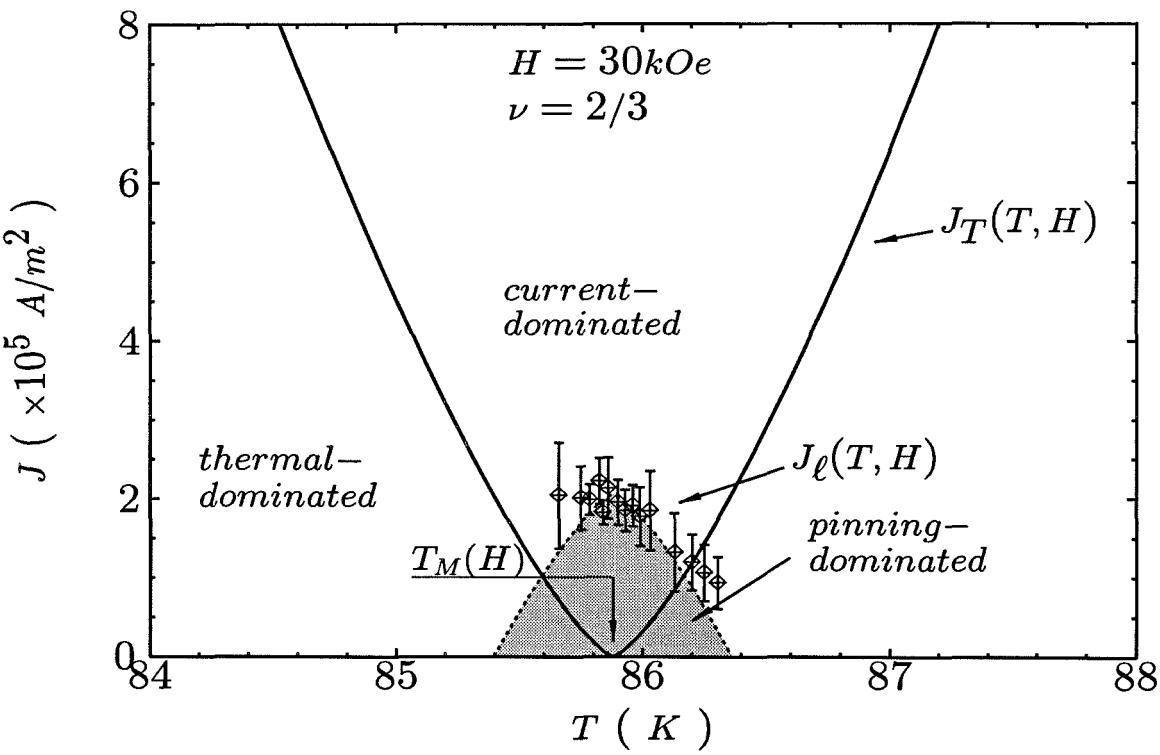

Figure 4.12: The current density (J) vs temperature (T) diagram for H = 30 kOe. The solid curve shows the characteristic current density $J_T(T, H)$ which separates the current-dominated regime from the thermal-dominated regime. The dashed curve shows the effective "depinning" current density $J_\ell(T, H)$. The data points are the experimental J_ℓ values obtained from analyzing the E-vs-J isotherms.

Another self-consistent way of demonstrating the pinning effects is to measure the

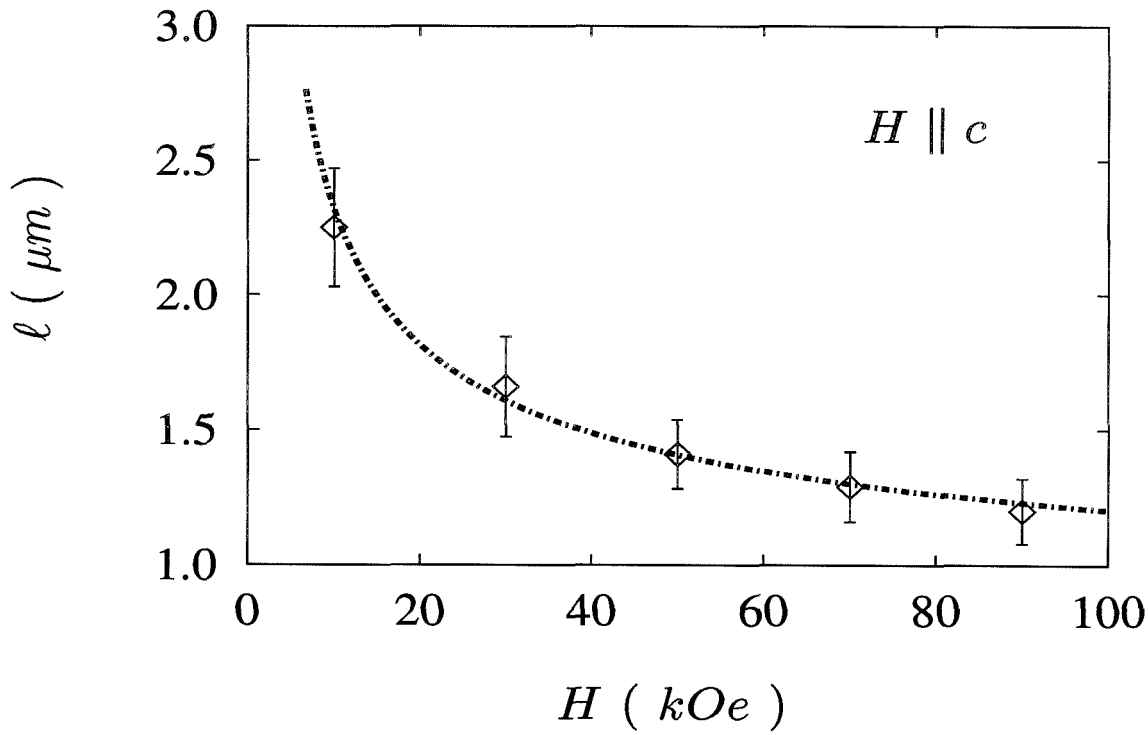

Figure 4.13: the vortex mean-free-path $\ell(H)$ obtained from Sample A and for **H** || **c**.

linear magnetoresistivity ρ versus T with a small current density $J << J_T$, and then to identify a temperature interval ΔT near T_M where the resistivity critical scaling relation (Eq. 4.5) breaks down. Here ΔT is obtained by asserting $\xi_v(T, H, J) = \ell$ at constant J and H, so that $\Delta T \equiv T_M(\xi_0/\ell)^{1/\nu}$. Note that ΔT increases with the increasing H (larger ξ_0) and the decreasing vortex mean free path (smaller ℓ). In Fig. 4.14, the second-order melting temperatures $T_M(H)$ for **H** || **c** are indicated by the arrows on the ρ-vs-T plot, so are the crossover temperature $T_x(H)$, defined as $T_x \equiv T_M + \Delta$. We find good agreement between the $T_x(H)$ values and the temperature where distinct changes in the resistivity occur. It should be noted that such resistivity "kink" near T_x is only visible for twinned crystals with a well defined vortex mean free path (ℓ). The "kink" disappears in inhomogeneous samples (such as epitaxial films) with a broad distribution of ℓ values, also in untwinned single crystals where ℓ is practically the size of the sample and $\ell >> \xi_0$, $\Delta T \rightarrow 0$.

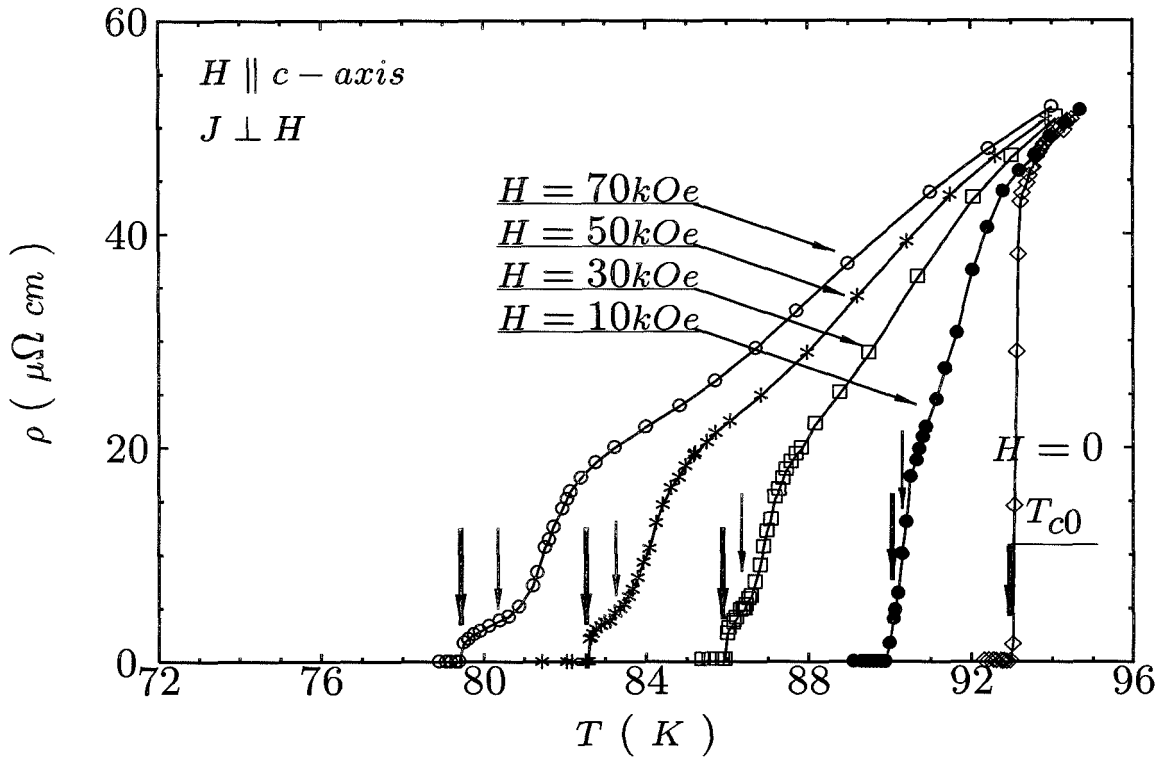

Figure 4.14: The linear ρ-vs-T curves at constant magnetic fields for **H** $\parallel$ **c**, and H = 0, 10, 30, 50, and 70 kOe. The melting temperatures T_M(H) obtained from the critical scaling analysis are indicated by the bold arrows, and the crossover temperatures $T_x(H)$ (see the text) are indicated by the light arrows.

4.2.6 Pinning Energy

The field dependence of the vortex mean free path ℓ in a dilutely twinned single crystal can be related to the twin boundary pinning range r_p by the expression $\ell(H) = L_t - r_p(H)$, where L_t is the average twin boundary separation and r_p is the twin boundary pinning range. The physical meaning of J_ℓ is associated with the work $(J_\ell \ell^2 \Phi_0)$ done on the vortex dislocation loop by the Lorentz force. In the steady state, the total thermal energy $k_B T$ of each dislocation loop is equal to the difference of the work done by the Lorentz force and by the pinning force on the dislocation loop, *i.e.*,

$$J_\ell \ell^2 \Phi_0 - W_p = k_B T. \tag{4.15}$$

Given a volume density n_p of randomly distributed point defects, it is known (Larkin

& Ovchinnikov, 1979) that the pinning energy W_p satisfies $W_p \propto n_p$ if the single-particle pinning dominates, and that $W_P \propto n_p^2$ if the collective-pinning dominates. In the limit of $n_p \to 0$, such as in the case of as-grown $YBa_2Cu_3O_7$ single crystals, we recover the result $J_\ell(T_M, H) = k_B T_M(H)/(\ell^2 \Phi_0)$ described in the previous section because $W_p \to 0$. The $\ell(H)$ values obtained from the data for sample # 1, shown in Fig. 4.13, decrease with the increasing magnetic field, consistent with the fact that L_t is constant and the twin-boundary pinning range $r_p(H)$ increases with the increasing density of vortices. In the case of proton-irradiated samples, we assume that the volume density of randomly distributed point defects is directly proportional to the proton fluence, such that the n_p value for Sample C is twice that of Sample B. Since $\ell(H)$ is independent of n_p, and since experimentally J_ℓ increases with the increasing n_p, it follows from Eq. (4.15) that the pinning energy W_p increases with the increasing n_p. Inserting the experimental values of $\ell(H)$, $T_M(H)$, and $J_\ell(T_M, H)$ into Eq. (4.15), we obtain $W_p(T_M, H)$ vs H data for samples # 2 and # 3, as shown in Fig. 4.15. Note that for each field, the ratio of the $W_p(T_M)$ values for the two samples is about the same as that of n_p's, consistent with $W_p \propto n_p$ and therefore single-particle pinning.

4.2.7 Flux-low Crossover Current Density

The flux-flow crossover current density $J_x(T)$ places an upper limit for the validity of the critical scaling relation in Eq. (4.5), so that for $J > J_x(T)$, the superconducting system is in the flux-flow regime with the ohmic vortex dissipation. Experimentally, J_x at a constant temperature can be obtained by identifying the current density of an E-vs-J isotherm above which the isotherm becomes ohmic. This flux-flow crossover behavior is observable for $H \perp c$. The results of the J_x-vs-T/T_c curves are given in Fig. 4.16 for all three samples.

There are two important features associated with the flux-flow crossover current densities. First, the fitting curves in Fig. 4.16 all follow the relation

$$J_x(T) = J_x(0)|1 - T/T_c|^a \tag{4.16}$$

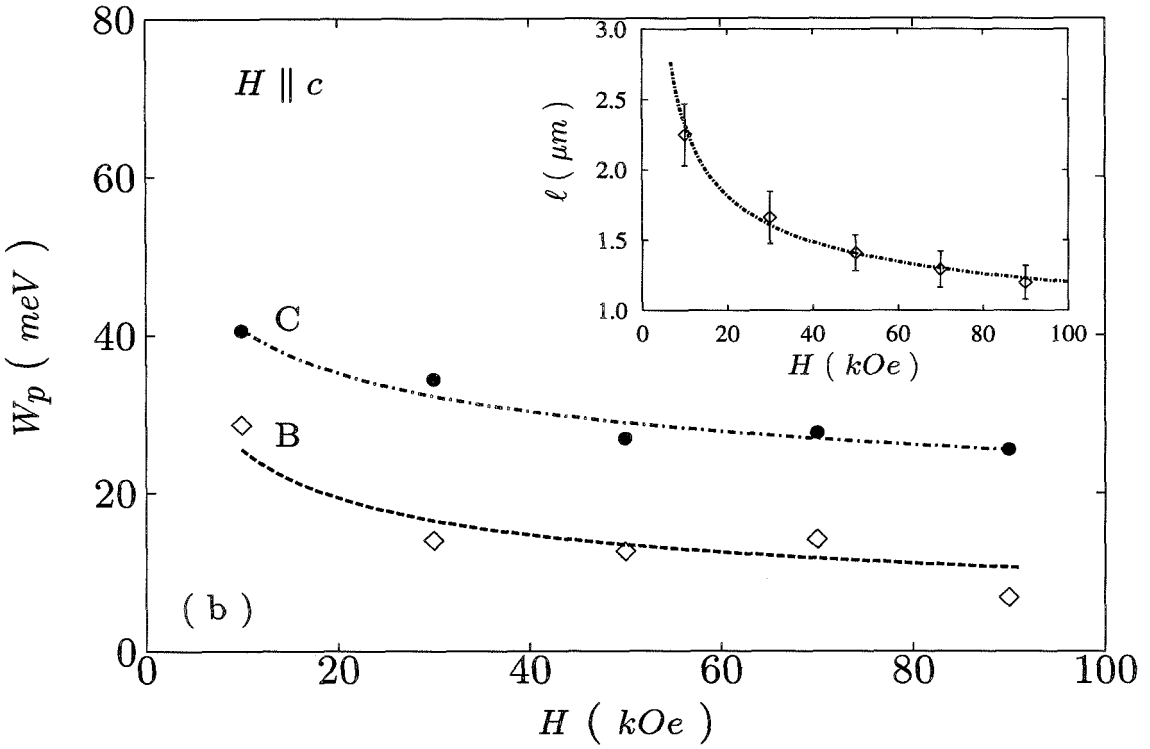

Figure 4.15: The pinning energy W_p as a function of the magnetic field H for Samples B and C. Note that $(W_p)_C \approx 2(W_p)_B$. The inset shows the vortex mean-free-path $\ell(H)$ obtained from Sample A and for **H** ∥ **c**.

where a is very close to ν_0 as shown in Table 4.1. Second, the magnitude of $J_x(0)$ is independent of H and is significantly enhanced for the irradiated samples.

One possible explanation for the magnitude and the temperature dependence of $J_x(T)$ is as follows. The flux-flow crossover current density can be related to the single vortex pinning energy (U_p) by the relation $U_p = J_x \Phi_0 r L$, where L is the length of a flux line, and r is the pinning range. Furthermore, U_p is approximately equal to the condensation energy $B_c^2 V_c/(2\mu_0)$, where B_c is the thermal dynamic critical field, μ_0 is the vacuum permeability, $V_c \sim \xi_s^3$ is the correlation volume per vortex in the flux-flow limit, and $\xi_s = \xi_s(0)|1 - T/T_c|^{-\nu_0}$ is the superconducting coherence length. Since $B_c^2 \approx \Phi_0^2/(8\pi^2\kappa^2\xi_s^4)$, where κ is the Ginzburg-Landau parameter, we find that

$$J_x(T) = \frac{\Phi_0}{16\mu_0\pi^2 r L \kappa^2 \xi_s(0)} \left[1 - \frac{T}{T_c}\right]^{\nu_0}. \tag{4.17}$$

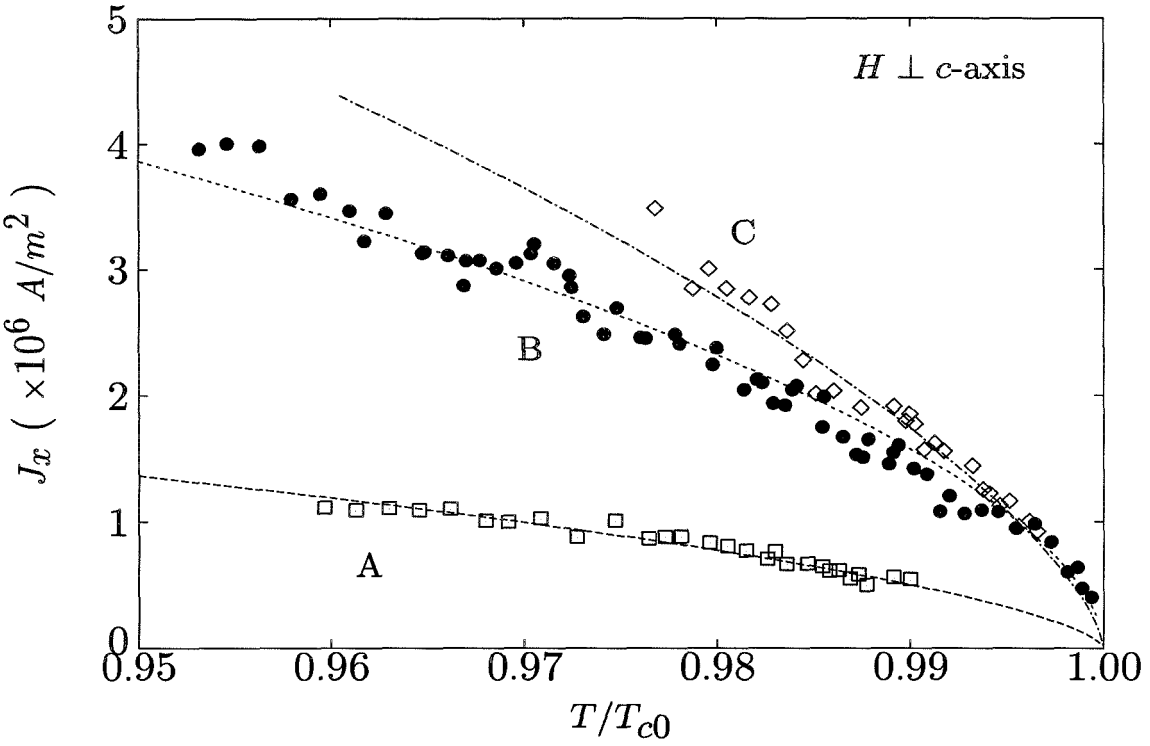

Figure 4.16: The flux-flow crossover current density (J_x) versus the reduced temperature (T/T_{c0}) for Samples A, B, C and **H** $\perp$ c-axis. Note that J_x is independent of the magnetic field.

Consequently, we have $a = \nu_0 \approx 2/3$, and J_x independent of H, consistent with the experimental observation, provided that r and L are only weakly dependent on the temperature and the magnetic field. (For instance, r could be the average size of a point defect and L could be the thickness of the sample.) In addition, since $J_x(0) \propto 1/\kappa^2$ from Eq. (4.17), and since $\kappa = \lambda_{eff}/\xi_s$, where λ_{eff} is the effective penetration depth, we find that for $\lambda_{eff} = \lambda_C = \sqrt{c_{44}/k_p}$, with λ_C being the Campbell penetration depth (Campbell, 1971), c_{44} the tilt modulus, and k_p the Labusch pinning force constant (Campbell & Evetts, 1972), κ decreases with the increasing pinning force constant k_p. Therefore $J_x(0) \propto k_p$, consistent with the observation of increasing J_x with the increasing strength and density of pinning.

By taking into consideration both $J_x(T)$ and $J_\ell(T)$, we obtain a typical J-vs-T diagram shown in Fig. 4.17 for $H = 30$ kOe. It should be noted that the experimental observation of J_x and J_ℓ depends on the experimental current density range relative

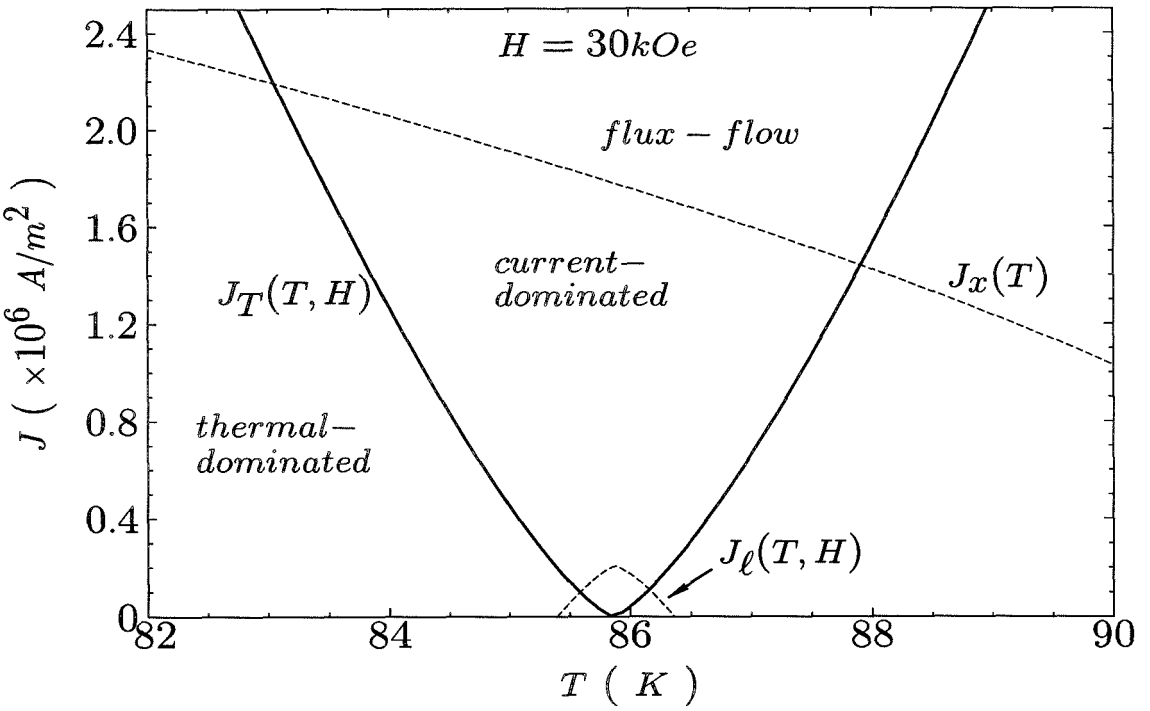

Figure 4.17: The J-vs-T diagram for $H = 30$ kOe showing the characteristic current density $J_T(T, H)$ (the solid line) which separates the current-dominated regime from the thermal-dominated regime. The dashed lines are the effective "depinning" current density $J_\ell(T, H)$ and the flux-flow crossover current density $J_x(T)$.

to the positions of J_x and J_ℓ. Our experimental current range is about the same for all three samples, but the positions of J_x and J_ℓ are sample dependent. For instance, within our experimental current range, the E-vs.-J characteristics for magnetic fields lower than 10 kOe are usually not affected by the finite size effect. As for the flux-flow crossover behavior, since it decreases as the temperature goes to T_c, it has only been observed for $H \perp \hat{c}$ when $T_M(H)$ values are much closer to T_c. Therefore, detailed analysis presented here is important to fully understand the physics embedded in the experimental data.

4.2.8 Ohmic Resistivity Versus Temperature

To further understand the effects of irradiation, we note that the Ohmic resistivity is generally higher in the irradiated samples, as shown by the resistivity versus

temperature curves in Fig. 4.18 for $\mathbf{H} \parallel \mathbf{c}$. The large normal resistivity in samples with more point defects is consistent with the decrease in the electron mean free path due to the increasing static disorder.

Another important effect of irradiation can be noted from the gradual disappearance of the "kink" in resistivity near the onset of vortex dissipation upon increasing the fluences of proton irradiation, as clearly shown in Figs. 4.18. This observation can be attributed to the large J_ℓ values in irradiated samples, because $J_\ell = k_B T_M/(\xi_0 \ell^2)$, and T_M is higher and ξ_0 is smaller in high fields with the increasing point defect density. Thus for the irradiated samples, a larger part of the current range falls into the pinning dominated regime shown in Figs. 4.12 and 4.17 where the current-voltage characteristics are linear. Therefore, the Ohmic resistivity can still be measured below T_M for the irradiated samples, and the ρ-vs-T data goes to zero smoothly.

4.2.9 AC transport results

In addition to the DC measurements, AC resistivity ($\rho_{ac} = |\rho_{ac}|e^{i\phi_\rho}$) isotherms as a function of frequency (f) from 100Hz to 2MHz were also measured on Sample #3 for H=3kOe and H=6kOe and with $H \parallel c$-axis. Shown in Fig. 4.19 are the representative $|\rho_{ac}|$-vs-f and ϕ_ρ-vs-f data for $H = 3.0$ kOe. By applying the scaling analysis outlined in Eqs. (4.9)-(4.11), consistent critical exponents $\nu \approx 2/3$ and $z \approx 3$ and the corresponding scaling functions (shown in the insets) were obtained. The critical phase obtained is $\phi(T_M) = 60° \pm 3°$, in good agreement with the critical scaling hypothesis which asserts that $\tilde{\phi}_c \equiv= \phi_\rho(T_M) = \frac{\pi}{2}(z-1)/z \approx \frac{\pi}{3}$ for $d = 3$ if $z \approx 3$. The fact that the same critical exponents ν and z, as well as universal scaling functions have been obtained for data taken at different magnetic fields and from different experimental techniques provides strong support for the existence of a true second-order phase transition.

It is worthwhile making a comparison between the time scale associated with the critical dynamics of the vortex-glass transition and our experimental time scales. As shown in the paper by Yeh et al. (1993a), from the universal functions $\tilde{\rho}_\pm$, we

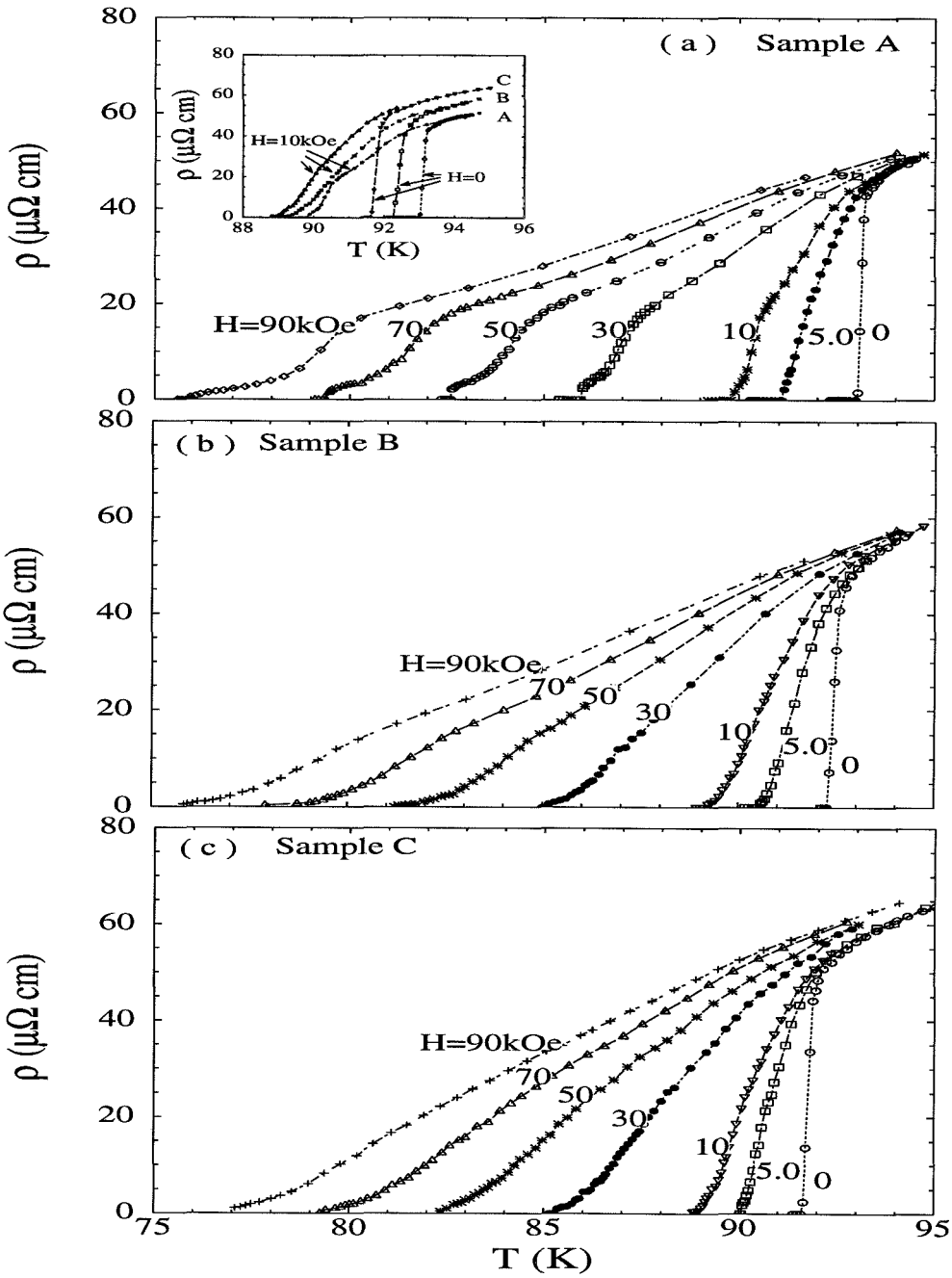

Figure 4.18: The resistivity (ρ) vs temperature (T) curves for Samples A, B, and C with $\mathbf{H} \parallel \mathbf{c}$ and $H = 0$, 5.0, 10, 30, 50, and 70 kOe.

can identify the coefficient f_c of the characteristic frequency $f_T = f_c|1 - (T/T_M)|^{\nu z}$ with a procedure similar to that used for obtaining ξ_0. It is found that $f_c \approx 10^{11}$ Hz for $H = 10$ kOe, and f_c varies slowly with H (Yeh *et al.*, 1993a). With our smallest temperature increment of $\Delta T = 0.02$ K, which indicates how close to the true transition temperature we can get, the smallest f_T (corresponding to the longest relaxation time) needed for our system to detect the critical fluctuations is about $f_T \sim |\Delta T/T_M|^{\nu z} \sim 5 \times 10^4$ Hz at $H = 10$ kOe where $T_M \approx 90$ K. Since our lowest measurement frequency is 100 Hz, our entire experimental frequency range has covered the complete critical dynamic time scales for the given temperature resolution.

4.3 Concluding Remarks and Discussions

In summary, we have investigated the critical phenomena of the vortex transport properties in 3-MeV-proton-irradiated Y-Ba-Cu-O single crystals. We find that the onset of vortex dissipation is consistent with a second-order vortex-solid melting transition, with universal critical exponents $\nu \approx 2/3$ and $z \approx 3$, independent of the density of point defects. On the other hand, variations in the point defect density have important effects on the pinning-related material parameters, as summarized below:

- The high-field melting transition temperature (T_M) increases with the increasing point defect density;
- The zero-field transition temperature T_c decreases with the increasing point defect density;
- The vortex correlation length ξ_0 decreases with the increasing point defect density;
- The flux-flow crossover current density J_x as a function of the reduced temperature (T/T_c) increases with increasing point disorder.

Despite these observations, there are several issues which are not clear at this point and need to be mentioned here. Although we have obtained a second-order

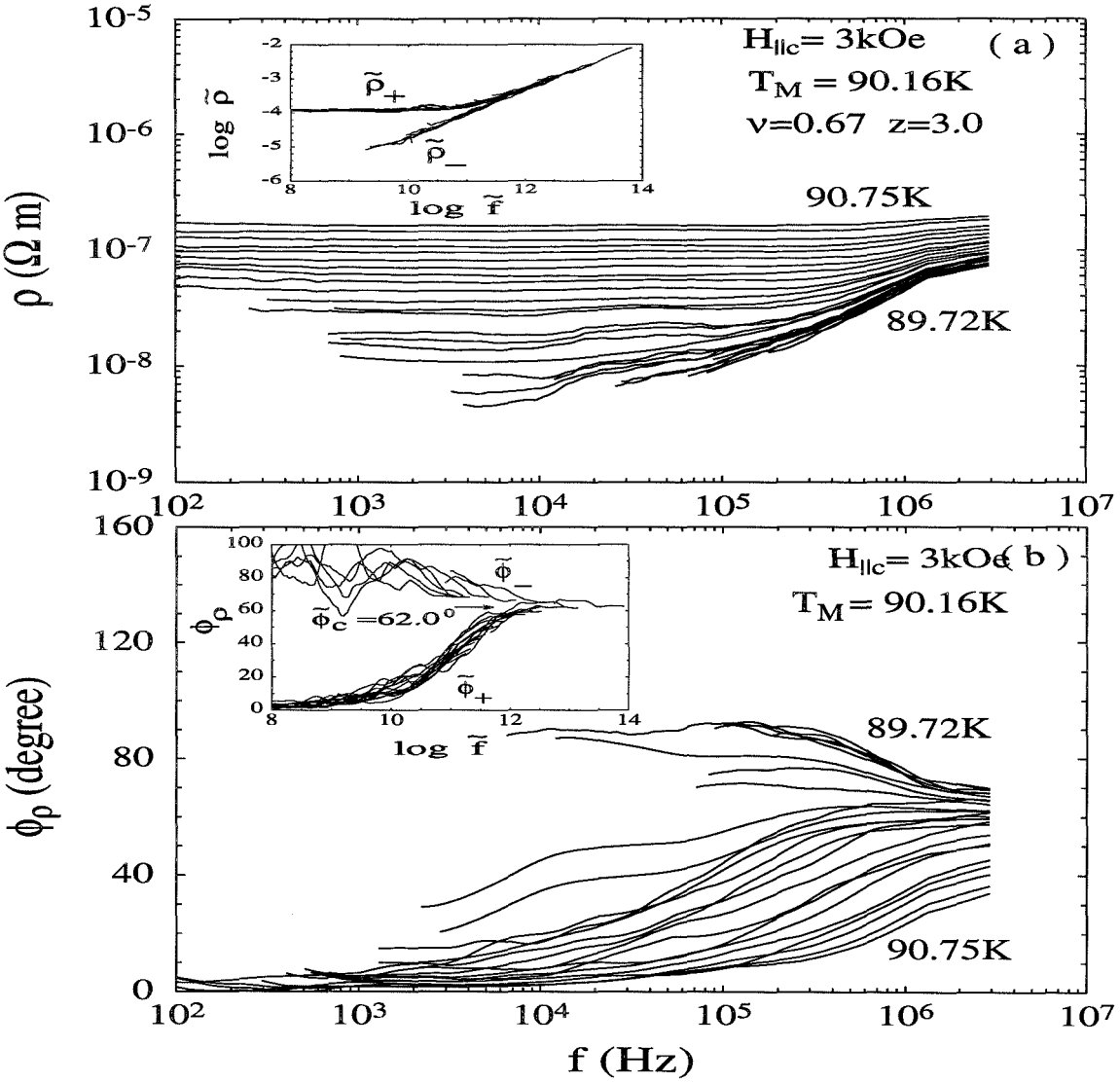

Figure 4.19: (a) Impedance (ρ_{ac} and (b) phase (ϕ) vs frequency (ω) isotherms for **H** $\|$ **c**-axis and H = 3.0 kOe. The insets are the universal functions (a) $\tilde{\rho}_{ac}$ vs $\tilde{f}$ and (b) $\tilde{\phi}$ vs $\tilde{f}$ obtained from "collapsing" the isotherms with values of ν, z, and T_M shown in the figure. The temperature increment ΔT between successive traces is 0.03 K, and the arrows indicate the critical regime.

vortex-solid to liquid melting transition line below $H_{c2}(T)$, this fact is by no means the proof for the same "vortex-glass" transition proposed by Fisher et al. (1991), because the latter model provides no prediction for the critical exponents except for a simple mean-field estimate which yields $\nu = 0.5$ and $z = 4.0$ (Dorsey *et al.*, 1992). Theses are different from our experimental results of $\nu \approx 2/3$ and $z \approx 3.0$. More rigorous theoretical calculations which incorporate both the thermal and disorder fluctuation effects are necessary for a meaningful comparison. The use of the phrase "vortex-glass" in the title of this chapter and in the following chapters is only meant to distinguish the second-order transition with an isotropic critical exponent from those with anisotropic static critical exponents due to other types of disorder.

Since most as-grown samples are twinned, two types of defects are important for vortex pinning: twin boundaries and point defects. A natural question to ask is which type of defects provides the dominant pinning mechanism for the observed vortex-solid phase. The fact that an isotropic static critical exponent ν can account for the critical phenomena for all field orientations indicates that the responsible static disorder in the vortex-solid state is spatially random and orientationally isotropic. Although on a macroscopic scale, the twin boundaries are randomly distributed in the *ab*-plane, and the average twin boundary separation is about 2 μm in our samples. This is much larger than the flux line separations for applied magnetic fields from 1.0 to 90 kOe. Therefore, our observations presented in this chapter seem to suggest that random point defects are the primary source of disorder determining the critical phenomena near the vortex-solid phase transition. However, to be more rigorous, it is necessary to study untwinned single crystals with random point defects only. As we shall see in Chapter 6, this issue is in fact rather complicated. Further experimental studies seem to suggest that the collective effects of both point defects and twin boundaries are responsible for the vortex-glass transition with isotropic exponents; any one type of disorder alone cannot account for all the experimental observations.

Finally, we emphasize again that this chapter focuses on the universality of vortex-glass transition upon moderately enhanced point disorder. However, since it involves similar techniques used by other research groups for the investigation of vortex-glass

transition, it is necessary to compare our results with those of others. As mentioned earlier, prior to our work, DC transport measurements had been carried out by Koch et al. (1989) and Gammel et al. (1991) and AC transport measurements by Olsson et al. (1991). The comparison of the approaches related to the AC transport measurements has been discussed by Reed et al. (1992; 1993) and in the Ph.D thesis by Reed (1995). Here we compare the critical scaling analysis of the DC resistivity.

The measurements by Koch et al. (1989) were performed on epitaxial thin films which usually contain a very high density screw dislocations. As have discussed by Yeh et al. (1993a), the lower current limit (J_ℓ) for observing critical scaling behavior due to the finite size effect in epitaxial films could become as high as $10^6 \sim 10^7$ A/m^2 (*cf.* their experimental current range is 10^5 to 10^9 A/m^2). However, finite size effect were not considered as a possible limiting factor in their studies. Another important issue as we have emphasized in the beginning of this chapter is that the critical scaling analysis is only applicable to data within the critical regime. However, in the studies by Koch et al. (1989), much broader temperature intervals, such as 11.8 K for $H = 40$ kOe with a temperature increment between successive E-vs.-J isotherm of 0.1 K, have been used in their so-called "critical scaling analysis". On the other hand, we have found that the critical regime for 50 kOe is less than 2.0 K (see Fig.4.8), which is consistent with the allowed temperature interval according to the Ginzburg criterion. As we have discussed earlier in section 4.2.3, when a broad temperature range is covered, the presence of the critical point T_{c2} associated with the upper critical field H_{c2} may affect the results of the critical exponents. In addition, a systematic error of 0.2 K exists in their transition temperatures, which could also affect the accuracy of the critical exponents. In Fig. 4.20, we compare the critical regime given by the Ginzzburg criterion with the temperature intervals involved in the scaling analyses by various groups. The severe inconsistency with the Ginzburg criterion in the "critical regimes" used by Koch et al. (1989) obviously imposes serious problems on their conclusions.

In addition to the issue of the critical regime, there are large discrepancies between the critical exponents obtained from DC and AC transport measurements on

similar samples in the work by Koch et al. (1989) and Olsson et al. (1991). Since the critical exponents for the same type of phase transition should be universal, their results indicate that either their scaling analysis lacks self-consistency, or the transport properties they studied may have been dominated by mechanisms other than critical fluctuations, as suggested by Coppersmith et al. (1990). To make a clear comparison between our results and others work, the values and the error corresponding bars in the critical exponents are plotted in Fig. 4.21. We note that the large errors in the critical exponents by Gammel et al. (1991) are possibly due to the fact that their sample used in the study is heavily twinned with an average twin boundary separation $\ell < 10^3$Å. Since their estimates for the transition temperatures are obtained from the Ohmic resistivity with very small current densities (10^2 to 10^4 A/m^2), and since the lower current limit imposed by the finite size effect is given by $J_\ell = (k_B T_M)/(\ell^2 \Phi_0) \approx 5 \times 10^7$ A/m^2 if $T_M = 74.0K$ for their $H = 60$ kOe data is assumed (see also the discussion by Yeh et al. (1993a)), we speculate that their data have been strongly limited by the finite size effect.

Furthermore, as listed in Table 4.2, our results are based on self-consistent analyses of a much larger amount of experimental data, in sharp contrast to the very limited experimental information by other groups. Based on the fact that our results carry much smaller errors and the fact that consistent results have been obtained for different magnetic fields, field orientations, samples and techniques, we conclude that our work has provided the most important evidence — the universality, for a true second-order phase transition. For more detailed discussions on various issues related to the vortex transport properties, please see the review article by (Farrell, 1994).

	This Work			Koch et al. (1989) Olsson et al. (1991)		Gammel et al. (1991)	
Experimental technique	DC transport	AC transport	AC susceptibility	DC & AC transport		DC & AC	
# of magnetic fields measured	9	9	6	4	1	5	0
# of samples measured	3 (2 w/ controlled defects)	2	1	1	1	1	0
# of magnetic field orientations	5	1	2	1	1	1	0
# of isotherms per field	~ 40	~ 80	~ 80	~ 20	~ 20	~ 15	0
Total isotherms	> 5000			~ 100		< 100	

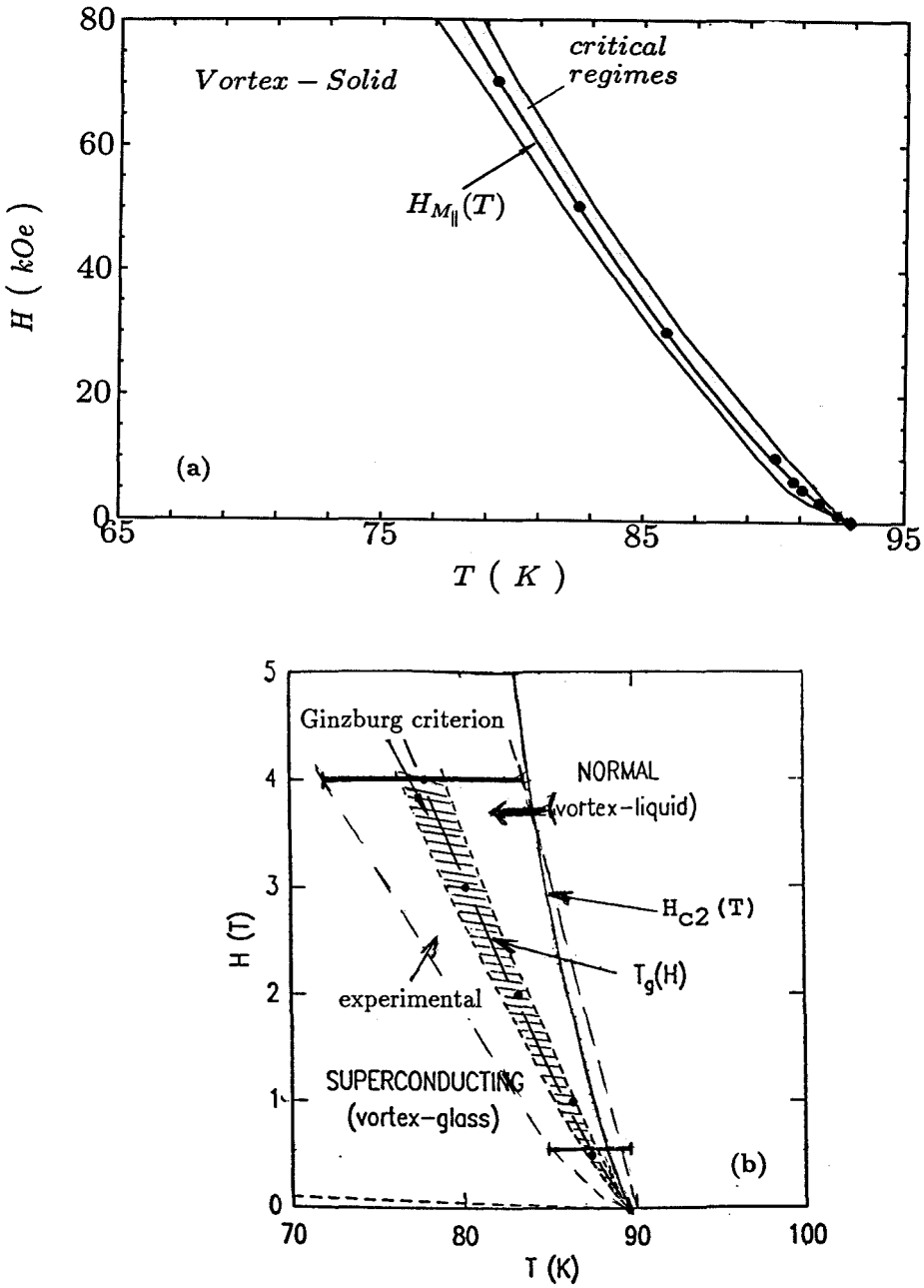

Figure 4.20: Comparison of the critical regime given by Ginzburg criterion with the experimental temperature intervals used by various research groups for their critical scaling analyses. (a). Our work. (b). Work by Koch et al. (1989)

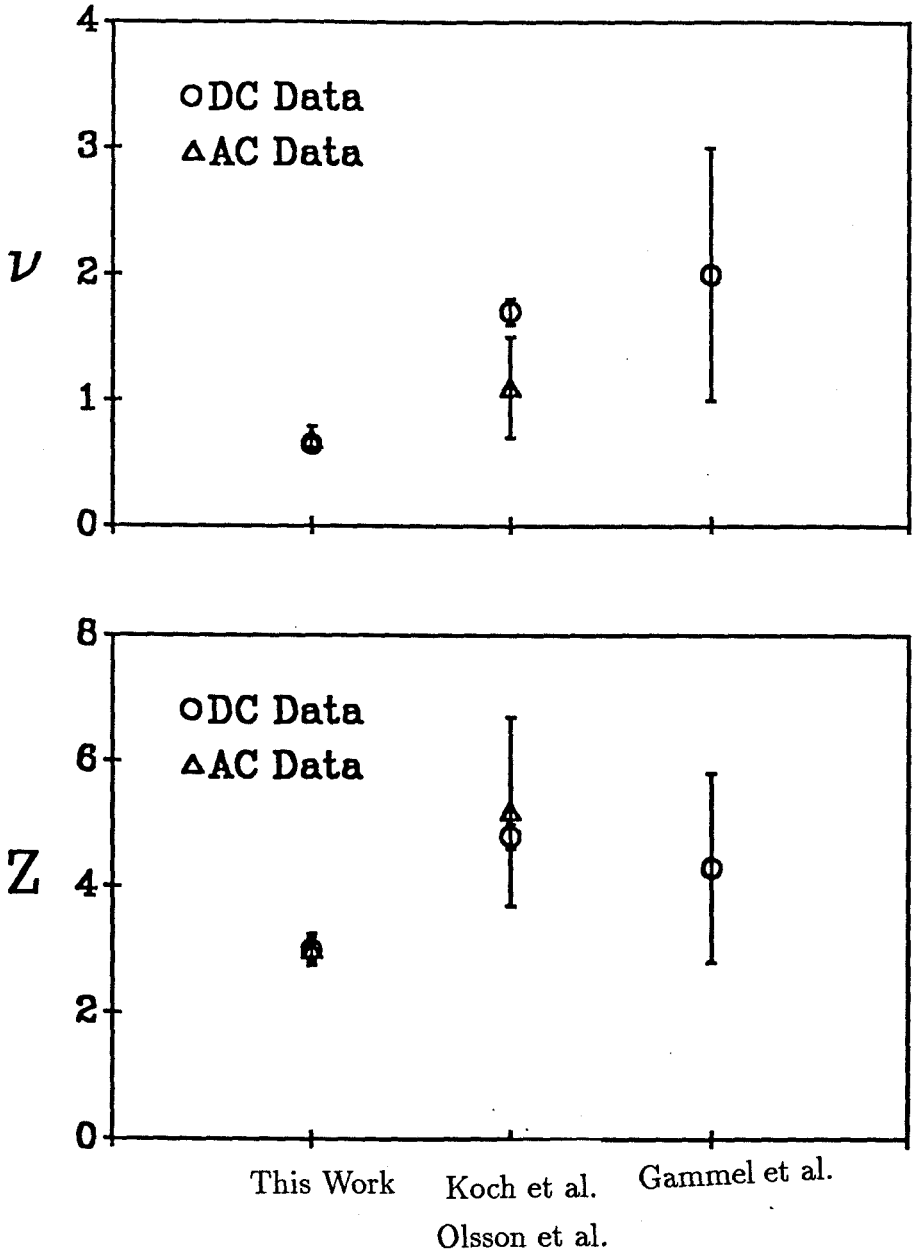

Figure 4.21: Comparison of the critical exponents and the corresponding error bars obtained experimentally by our group and other groups.

Chapter 5 Bose-Glass Transition in Twinned $YBa_2Cu_3O_7$ Single Crystals with Columnar Defects

As discussed in the previous chapter, a moderately increased amount of random point defects pinning does not affect the nature of the vortex phase transition. The enhancement of vortex pinning due to the addition of random point defects is also limited. From simple topological considerations, one can imagine much improved vortex pinning if cylindrically-shaped pinning sites, with a diameter comparable to the size of the superconducting coherence length and a length comparable to that of the flux lines, can be artificially created in the superconductors. The technique available for this purpose is the high-energy heavy ion irradiation which has been used to create amorphous columnar defects throughout the entire thickness of the sample. Over one order of magnitude enhancement in the critical current density of $YBa_2Cu_3O_7$ single crystals subject to heavy-ion irradiation has been first reported by Civale et al. (Civale *et al.*, 1991). However, simple measurements of the critical current densities alone do not provide insight into the nature of the vortex phases and phase transitions in the presence of columnar defects. It is the goal of this chapter to investigate these issues.

5.1 2D Boson Analogy

As illustrated in Fig.5.1, the columnar defects provide long pinning centers which interact with a vortex along its entire length. Nelson and Vinokur (Nelson & Vinokur, 1992) have shown that the vortex system in the presence of columnar defects can be mapped onto a two-dimensional interacting boson system.

Consider parallel columnar defects aligned with the c-axis of the sample, the trajectories of the flux lines can be described by $\{\mathbf{r_j}(z)\}$, with $\mathrm{r}_j(z) = (x_j(z), y_j(z))$

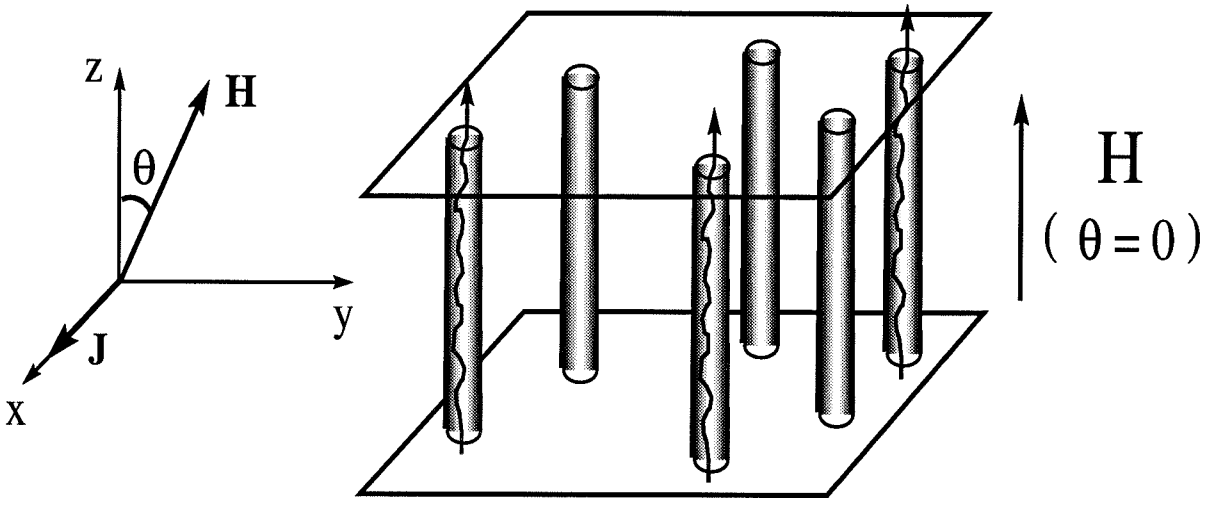

Figure 5.1: Illustration of vortices interacting with correlated columnar defects along the c-axis of a superconductor.

and the vortex system can be described by a simple model free energy $\mathcal{F}_N$ for N flux lines in an *isotropic* sample of thickness L (Nelson & Vinokur, 1992; Nelson & Seung, 1989),

$$\mathcal{F}_N = \frac{1}{2}\tilde{\varepsilon}_1 \sum_{i=1}^{N} \int_0^L \left|\frac{d\mathbf{r}_i(z)}{dz}\right|^2 dz + \frac{1}{2}\sum_{i\neq j}\sum_j \int_0^L V(|\mathbf{r}_i(z)-\mathbf{r}_j(z)|)dz + \sum_i \int_0^L U_D(\mathbf{r}_i(z))dz, \tag{5.1}$$

where $\tilde{\varepsilon}_1$ is the local tilt modulus, $V(|\mathbf{r}_i(z)-\mathbf{r}_j(z)|)$ is the interaction potential between flux lines, and $U_D(\mathbf{r}_j)$ represents a z-independent random pinning potential. The partition function is then

$$Z = \frac{1}{N!}\sum_P{}' \left[\prod_i \int_{\mathbf{r}_i(0)}^{\mathbf{r}_i(L)=P\mathbf{r}_i(0)} \mathcal{D}\mathbf{r}_i(z)\right] \exp(-\beta\mathcal{F}_N), \tag{5.2}$$

where $\beta = 1/(k_B T)$, and $\sum_P'$ means summing over all permutations.

Comparing Eqs.(5.1) and (5.2) with the following partition function of interact-

ing bosons in two dimensions with a random static potential U_D (Feynman, 1965; Feynman, 1972)

$$Z = \frac{1}{N!}\sum_P{}' \left[\prod_i \int_{\mathbf{r}_i(0)}^{P\mathbf{r}_i(0)} \mathcal{D}\mathbf{r}_i(t)\right] \exp\left(-\frac{1}{\hbar}\int_0^{\beta\hbar} \mathcal{F}(t)dt\right) \tag{5.3}$$

$$\text{and} \quad \mathcal{F}(t) = \frac{m}{2}\sum_i \left|\frac{d\mathbf{r}_i}{dt}\right|^2 + \sum_{i\neq j}\sum_i V(\mathbf{r}_i(t) - \mathbf{r}_j(t)) + \sum_i U_D(\mathbf{r}_i),$$

where $\mathbf{r} = (x, y)$, the two systems are isomorphic with the following analogies:

$2D-$boson	Vortices
$\hbar$	k_BT
$\hbar/(k_BT)$	L
m	$\tilde{\varepsilon}_1$
t	z

The phase transitions in 2D boson system at $T = 0$ have been well established (Fisher *et al.*, 1989). Note that by following the above analogy, $T = 0$ corresponds to an infinite sample thickness L in the vortex system. As illustrated in Fig.5.2, three phases are expected in the vortex system with columnar defects: the Bose-glass phase in which the vortices are localized at the vicinity of the columnar pins, the "superfluid" phase in which the flux lines are delocalized and hop freely from one columnar pin to another, and the "Mott insulator" phase (which does not mean an electrically insulating phase in the vortex system) when there is exactly one flux line localized on every one of the columnar pins. By definition, the "Mott insulator" can occur only when the number of vortices is the same as that of the columnar pins (n_{pin}), *i.e.*, when the applied field is the same as the matching field, B_ϕ, which is defined as $n_{pin}\Phi_0$. Furthermore, although this phase may exist at low temperatures and for $B = B_\varphi$, it could undergo a Mott-insulator to Bose-glass transition at a higher temperature (Fisher *et al.*, 1989), so that eventually all the high-temperature Bose-glass

to superfluid transitions for all magnetic fields may belong to the same universality class. The randomly distributed columnar defects also reduce the possibility of forming a Mott-insulator phase because the latter requires commensurate vortex-column registrations. We shall verify the nature of the vortex phase transition by considering magnetic fields ranging from below the matching field to above the matching field.

5.2 Critical Scaling Hypothesis for a Bose-Glass Transition

In the case that the density of vortices is smaller than that of the columnar defects (or, equivalently, if the applied magnetic field H is smaller than the "matching field" B_φ), it is argued that strong pinning of the artificially created columnar defects results in an equivalent "Bose localization" effect on vortices at low temperatures. At high temperatures, vortices could "hop" into neighboring empty columns via the formation of "superkinks" (Nelson & Vinokur, 1992; Nelson & Vinokur, 1993), thereby resulting in an entangled vortex liquid which resembles a superfluid state. On the other hand, if $B \geq B_\varphi$, a Bose-glass to superfluid transition can still take place via dislocated vortex "half-loops" (Fisher *et al.*, 1989), as shown in Fig.5.3. The theoretically well-defined Bose-glass transition differs from the vortex-glass transition for $YBa_2Cu_3O_7$ single crystals with random point defects in that the tilt modulus in the former is infinite. Furthermore, for columnar defects along the sample c axis, the Bose-glass transition temperature (T_{BG}) is predicted to decrease with the increasing angle (θ) between the applied magnetic field and c-axis, in sharp contrast to the increasing vortex-glass melting temperature (T_M) due to the sample anisotropy.

To find the Bose-glass to superfluid transition temperature (T_{BG}) and the corresponding critical exponents, we follow the discussion by Nelson and Vinokur that the transverse and longitudinal correlation lengths of vortex dislocations diverge at T_{BG}

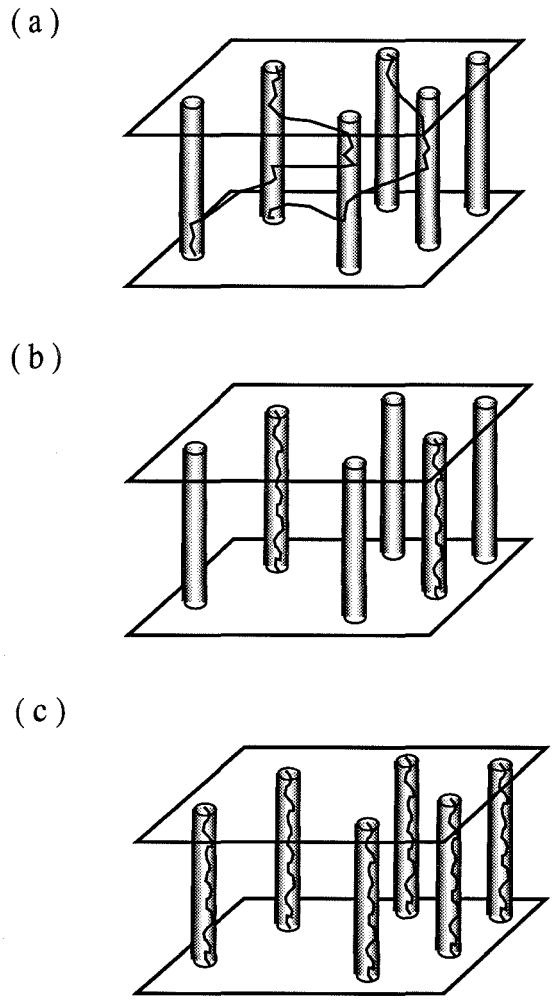

Figure 5.2: Schematic illustration of vortex interaction with the columnar defects in a superconductor. Following the 2D-boson analogy (see the text), there are three expected phases: (a) the vortex liquid phase; (b) the Bose-glass phase; and (c) the Mott insulator phase.

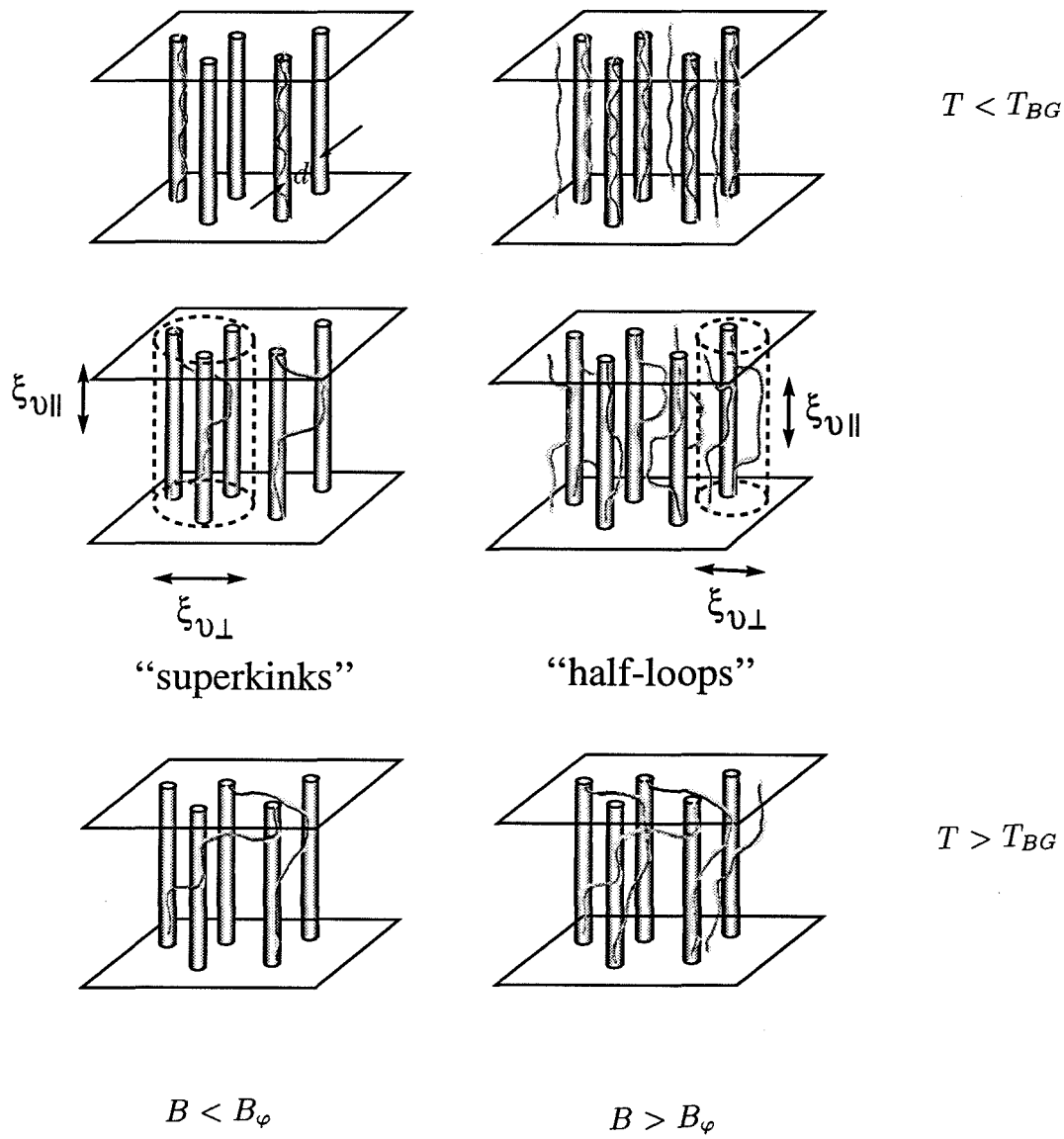

Figure 5.3: Schematic illustrations of Bose-glass to superfluid transitions for (a) $B < B_\varphi$ via dislocated vortex loops, and (b) $B > B_\varphi$ via dislocated vortex "half-loops".

with the following temperature dependence

$$\xi_\perp \sim |1 - T/T_{BG}|^{-\nu_\perp}, \quad \xi_{||} \sim |1 - T/T_{BG}|^{-\nu_{||}}, \tag{5.4}$$

where $\nu_\perp$ and $\nu_{||}$ are the transverse and longitudinal static exponent, respectively. The dynamic exponent z' may be defined by $\tau \sim \xi_\perp^{z'}$, where τ is the characteristic thermal relaxation time for the transverse vortex fluctuations. Assuming $\nu_{||} = \zeta\nu_\perp$ and a $(d'+1)$-dimensional phase transition with $d' = 2$, the superfluid density scales as

$$\rho_s \sim \xi_v^{2-d} \sim \frac{\xi_\perp^2}{\xi_\perp^2 \xi_{||}} \sim \xi_{||}^{-1}. \tag{5.5}$$

Note that Eq.(5.5) recovers the scaling relation $\rho_s \sim \xi_v^{2-d}$ for an isotropic correlation length $\xi_v(T,H) = \xi_0(H)\delta^{-\nu}$, if $\nu_\perp = \nu_{||} = \nu$, $\delta \equiv |1 - (T/T_M(H))|$ and $d = 3$. Since the frequency scales as $f \sim \xi_\perp^{-z'}$, the scaling relation for the resistivity becomes

$$\rho \sim i\frac{f}{\rho_s} \sim \frac{\xi_\perp^{-z'}}{\xi_{||}^{-1}} \sim \delta^{-\nu_\perp(\zeta - z')}, \quad \delta \equiv |1 - T/T_{BG}|. \tag{5.6}$$

In general, the critical scaling form for the AC resistivity ($\rho_{ac} = |\rho_{ac}|e^{i\phi_\rho}$) in an *isotropic* superconductor with columnar defects (anisotropic critical exponents) is given by

$$\rho_{ac}(f;T;H) = \delta^{\nu_\perp(z'-\zeta)}\tilde{\rho}(f\xi_\perp^{z'}; \delta\xi_\perp^{1/\nu_\perp}; h_\perp\xi_\perp\xi_{||}/\Phi_0), \tag{5.7}$$

where $h_\perp \approx Hsin\theta$, θ is the angle between the direction of the columnar defect and the magnetic field in an isotropic superconductor, and Φ_0 is th flux quantum. We have assumed that the induction $B \approx H$.

For a constant field H, and in the limit that $\theta << 90°$, Eq.(5.7) yields the following frequency-dependent scaling relations for $|\rho_{ac}|$ and ϕ_ρ:

$$\begin{aligned} |\rho_{ac}(f,T,H)| &\sim \delta^{\nu_\perp(z'-\zeta)}|\tilde{\rho}_\pm(\tilde{f})|, \\ \phi_\rho(f,T,H) &= \tilde{\phi}_\pm(\tilde{f}), \\ \tilde{f} &\equiv f|1 - T/T_{BG}|^{-\nu_\perp z'}, \end{aligned} \tag{5.8}$$

where $\tilde{\rho}_+(\tilde{\phi}_+)$ and $\tilde{\rho}_-(\tilde{\phi}_-)$ are the universal scaling functions for the amplitude (phase) at $T > T_{BG}$ and $T < T_{BG}$, respectively.

In the limit of $f \to 0$, Eq.(5.7) yields the following angular dependence of the ac resistivity:

$$|\rho_{ac}| \sim \delta^{\nu_\perp(z'-\zeta)}|\tilde{\rho}_\pm(\tilde{\Theta})|, \tag{5.9}$$

where $\tilde{\Theta} \equiv sin\theta|1 - T/T_{BG}|^{\nu_\perp(1+\zeta)}$.

5.3 Anisotropic to Isotropic Scaling Transformation

The scaling analysis outlined above assumes an isotropic sample system with the same effective mass along all principal crystalline axes. For HTS's, the intrinsic electronic anisotropy has to be accounted for in the critical scaling relations near the Bose-glass transition. Here, we adopt the anisotropic to isotropic scaling approach by Blatter et al. (Blatter *et al.*, 1992; Blatter *et al.*, 1994) which allows one to map results obtained for isotropic superconductors to anisotropic materials in a simple and direct way.

The scaling approach starts with the Gibbs free energy for an anisotropic superconductor (in the cgs units)

$$\mathcal{G} = \int d^3r \left[\alpha|\psi|^2 + \frac{\beta}{2}|\psi|^4 + \sum_{\mu=1}^{3} \frac{1}{2m_\mu}\left|\left(\frac{\hbar}{i}\frac{\partial}{\partial x_\mu} - \frac{2e}{c}A_\mu\right)\psi\right|^2 + \frac{B^2}{8\pi} - \frac{\mathbf{H}\cdot\mathbf{B}}{4\pi}\right], \tag{5.10}$$

where α and β are coefficients of the Ginzberg-Landau Hamiltonian, $\psi(\mathbf{r})$ is the order parameter, $\mathbf{A}$ is the vector potential, and $\mathbf{B} = \nabla \times \mathbf{A}$ is the external magnetic field and $\mathbf{H}$ is the microscopic magnetic field. The external field B is chosen to lie in the y-z plane and encloses an angle θ with the z axis (see Fig.5.1), and we also assume that $\mathbf{H} \approx \mathbf{B}$ for the field and temperature range of interest. This approximation generally holds well for these extreme type-II superconductors at moderate temperatures and for $B >> H_{c1}$. Here, the coordinate axes are chosen such that x-axis is along the

a-axis, y-axis along the b-axis, and z-axis along the c-axis of the sample. Since these oxide superconductors generally exhibit uniaxial symmetry, we choose $m_x = m_y = m$, $m_z = M$, and denote the mass anisotropy ratio by $\varepsilon^2 = m/M < 1$. It is worth noting that for untwinned $YBa_2Cu_3O_7$ single crystals, $m_a \neq m_b$. However, the difference is so small that $m_a \approx m_b << m_c$ is still a good approximation. Furthermore, for twinned single crystals, the difference between m_x and m_y can be completely removed.

To transform the anisotropic Ginzburg-Landau expression in Eq.(5.10) to an isotropic superconducting frame, we note that the anisotropic mass terms enter the gauge-invariant gradient term. Therefore, we consider the following rescaling of the coordinate axes

$$x = \tilde{x}, \quad y = \tilde{y}, \quad z = \varepsilon\tilde{z}, \tag{5.11}$$

(with "~" denoting the variables for the corresponding isotropic system), together with a rescaling of the vector potential

$$\mathbf{A} = (\tilde{A}_x, \tilde{A}_y, \tilde{A}_z/\varepsilon). \tag{5.12}$$

By using Eqs.(5.11) and (5.12), the anisotropy can be removed from the gradient term and reintroduced in the magnetic energy term, so that the Gibbs free energy becomes

$$\mathcal{G} = \int d^3r \left[\alpha|\psi|^2 + \frac{\beta}{2}|\psi|^4 + \frac{1}{2m}\left|\left(\frac{\hbar}{i}\tilde{\boldsymbol{\nabla}} - \frac{2e}{c}\tilde{A}\right)\psi\right|^2\right] + \mathcal{G}_m \tag{5.13}$$

where and the magnetic energy term $\mathcal{G}_m$ is defined as

$$\mathcal{G}_m = \frac{1}{8\pi}\int d^3r \left[\left(\frac{\tilde{B}_\perp^2}{\varepsilon^2} + \tilde{B}_z^2\right) - 2\left(\frac{\tilde{B}_\perp H_\perp}{\varepsilon} + \tilde{B}_z H_z\right)\right], \tag{5.14}$$

and the magnetic field satisfies the following rescaling relation $\mathbf{B} = (\tilde{B}_x/\varepsilon, \tilde{B}_y/\varepsilon, \tilde{B}_z)$.

In general, it is not possible to remove the anisotropy in both the gradient term and the magnetic energy term. But when the fluctuations in the magnetic field can be neglected, the anisotropy in $\mathcal{G}_m$ can also be removed by minimizing $\mathcal{G}_m$ with respect to

$\widetilde{\mathbf{B}}$. In the field range of interest, the intervortex spacing a is much smaller compared with the scale of fluctuations of the magnetic field λ and therefore the field can be considered as uniform.

Minimizing $\mathcal{G}_m$ gives

$$\widetilde{\mathbf{B}} = (\varepsilon H_x, \varepsilon H_y, H_z), \tag{5.15}$$

corresponding to $\mathbf{B} = \mathbf{H}$ in the original system. Thus Eq.(5.15) becomes $\widetilde{\mathbf{B}} = (\varepsilon B_x, \varepsilon B_y, B_z)$, or equivalently, $\widetilde{B} = \varepsilon_\theta B$, with ε_θ defined by the following relation

$$\varepsilon_\theta^2 = cos^2\theta + \varepsilon^2 sin^2\theta. \tag{5.16}$$

Based on this scaling approach, if we introduce columnar defects along the c-axis of an anisotropic superconductor, and then transform the system to an isotropic frame, we find that the transverse magnetic field component,

$$\frac{\widetilde{H}_\perp}{\widetilde{H}} = sin\tilde{\theta}, \tag{5.17}$$

which is a direct measure of the vortex fluctuations in the isotropic frame, can be related to the original sample coordinate (the anisotropic frame) by the following scaling transformation:

$$sin\tilde{\theta} \equiv \frac{\widetilde{H}_\perp}{\widetilde{H}} = \frac{\varepsilon sin\theta}{\sqrt{cos^2\theta + \varepsilon^2 sin^2\theta}}. \tag{5.18}$$

In the isotropic frame, the critical scaling behavior of $\widetilde{H}_\perp/\widetilde{H}$ follows that of $\tilde{\xi}_\perp$ and $\tilde{\xi}_{||}$ by the relation

$$\frac{\widetilde{H}_\perp}{\widetilde{H}} \sim \tilde{\xi}_\perp^{-1}\tilde{\xi}_{||}^{-1} \sim \delta^{\nu_\perp(1+\zeta)}, \tag{5.19}$$

where $\tilde{\xi}_\perp(=\xi_\perp)$ and $\tilde{\xi}_{||}(=\xi_{||}/\varepsilon)$ are the transverse and longitudinal correlation lengths in the isotropic frame. Consequently, the angular dependence of the ac resistivity in an anisotropic superconductor can be expressed by

$$|\rho_{ac}| \sim \delta^{\nu_\perp(z'-\zeta)}|\tilde{\rho}_\pm(\tilde{\Theta})|, \quad \tilde{\Theta} \equiv sin\tilde{\theta}\ \delta^{-\nu_\perp(1+\zeta)} \tag{5.20}$$

in the limit of $f \to 0$. As $T \to T_{BG}$, the scaling hypothesis yields the power-law dependence

$$\tilde{\rho}_{\pm} \propto \tilde{\Theta}^{(z'-\zeta)/(1+\zeta)}. \tag{5.21}$$

5.4 Experimental Results & Data Analysis

5.4.1 Sample and AC Transport Measurements

Despite its sound theoretical foundation, experimental verification of a Bose-Glass transition may be complicated by the presence of point defects or twin boundaries which could compete with the effect of columnar defects on vortices. It is therefore important to select superconducting single crystals with minimal defects and smaller anisotropies before creating columnar defects in them. The $YBa_2Cu_3O_7$ single crystal sample (# 4) with c-axis columnar defects was originally a dilutely twinned single crystal with an average twin boundary separation of $\sim 10\ \mu m$.

The sample (#4) used for the heavy-ion irradiation is a $YBa_2Cu_3O_7$ single crystal of dimensions $0.65 \times 0.50 \times 0.020$ mm^3. The information of 0.9 GeV Pb ion irradiation has been provided in Chapter 3. The fluence corresponds to a matching field $B_\varphi \approx 10$ kG and an averaging column separation ≈ 490 Å.

To study the frequency (f) dependent ac resistivity, four-probe ac transport measurements are carried out by using the technique described in Chapter 3 and the references therein. An HP4194 impedance analyzer is used to supply a uniform ac current to the entire thickness of the sample through a series 1 kΩ noninductive resistor. Since our sample resitance is only of the order of 10 mΩ even at room temperature, and our sample contact resistance is $<\sim 1\ \Omega$ at room temperature, the current in the circuit can be maintained as a nearly constant value determined by the 1 kΩ load resistor. As shown in the Ph.D. thesis by Reed ((1995)), the variations in the current due to slightly increased sample contact resistances at lower temperatures are usually small in our measurements. The resulting sample voltage is enhanced by an 80-dB low noise amplifier. Impedance versus frequency isotherms

are taken in various applied DC magnetic fields with the field direction tilted at an angle θ from 0° to 90° relative to the c-axis of the sample. Each isotherm consists of 400 frequencies from 10^2 to 2.5×10^6 Hz. The temperature stability for each isotherm is better than 10 mK. For three different magnetic fields $H = 3, 6, 15$ kOe, two below and one above the matching field $B_\varphi = 10$ KG, an average of 50 such isotherms are taken in each field and at a given angle. The angular dependence is investigated at $\theta = 0, 7.5°(9.4°), 15°, 22.5°, 30°, 45°, 60°, 75°$, and 90°.

5.4.2 $\theta \leq 30°$ — Bose-Glass Transition

Representative amplitude ($|\rho_{ac}|$) and phase(ϕ_ρ) of the ac resistivity versus frequency isotherms are shown in Figs. 5.4(a) and 5.5(a) for $H = 3.0$ kOe, $\theta = 7.5°$, and in Figs. 5.4(b) and 5.5(b) for $H = 6.0$ kOe, $\theta = 22.5°$. According to the scaling relations in Eq.(5.8), we may define $|\tilde{\rho}| \equiv |\rho_{ac}|\delta^{-a}$ and $\tilde{f} \equiv f\delta^{-b}$, where $a \equiv \nu_\perp(z' - \zeta)$ and $b \equiv \nu_\perp z'$. With these scaling relations, we find that $|\rho_{ac}(f)|$ and $\phi_\rho(f)$ isotherms for **all** data taken at $H < B_\varphi$ and $\theta \leq 30°$ can be simultaneously scaled into universal functions $\tilde{\rho}_\pm$ and $\tilde{\phi}_\pm$ with the **same** set of parameters $a = 1.1 \pm 0.1$ and $b = 2.2 \pm 0.2$, and with the $T_{BG}(H, \theta)$ value as a fitting parameter, as shown in the insets of Figs. 5.4(a)-(b) and 5.5(a)-(b). In addition, since scaling analysis asserts that $|\tilde{\rho}_\pm| \to \tilde{f}^{[1-(\zeta/z')]}$ and $\tilde{\phi}_\pm \to \phi_c = \frac{\pi}{2}(1 - \frac{\zeta}{z'})$ if $\tilde{f} \to \infty$, the data $|\tilde{\rho}_\pm| \sim \tilde{f}^{0.5}$ in the insets of Fig.5.4 and the phase $\phi_c = 45° \pm 5°$ in the insets of Fig.5.5 both confirm the finding that $(\zeta/z') = 1 - (a/b) \approx 0.5$. This demonstration of universality provides strong support for a second-order phase transition at T_{BG}.

The values of $T_{BG}(H, \theta)$ have been determined to within 30 mK accuracy from the above critical scaling analysis, and are shown in Fig.5.6 as a function of θ and for $H = 3$ and 6 kOe. We note that the drastic "cusp" feature at $\theta = 0$ is the signature of the Bose-glass transition (Nelson & Vinokur, 1992; Nelson & Vinokur, 1993; Hwa *et al.*, 1993), and is in sharp contrast to the smooth *increase* of the vortex-glass melting temperature (T_M) with increasing θ in as-grown and proton-irradiated $YBa_2Cu_3O_7$ single crystals (Reed *et al.*, 1993; Reed *et al.*, 1992; Yeh *et al.*, 1993a;

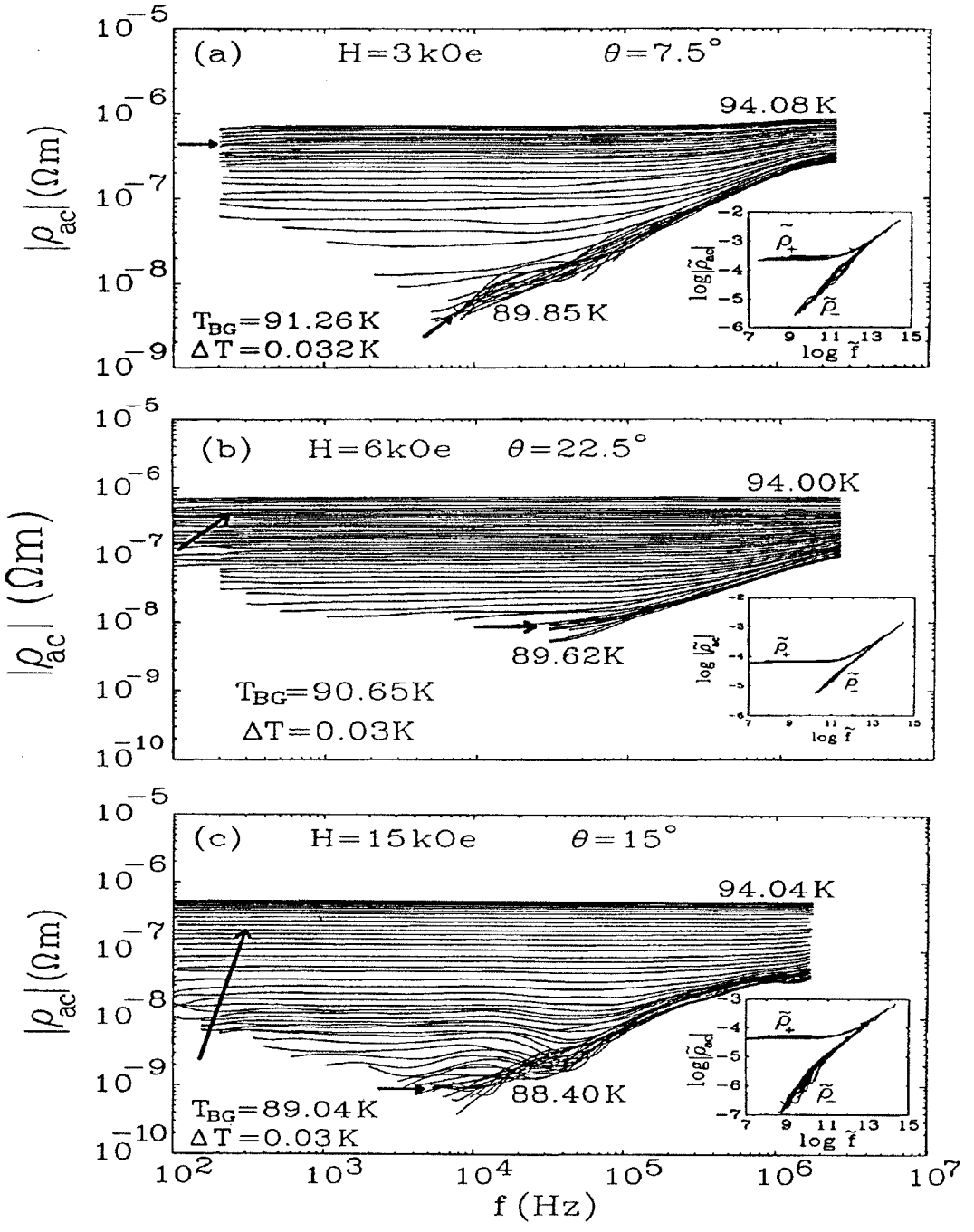

Figure 5.4: Amplitude of the AC resistivity $|\rho_{ac}|$ vs. frequency (f) isotherms taken at **(a)** $H = 3.0$ kOe, $\theta = 7.5°$; **(b)** $H = 6.0$ kOe, $\theta = 22.5°$; and **(c)** $H = 15.0$ kOe, $\theta = 15°$. The arrows indicate the isotherms in the critical regime which are scaled into universal functions $|\tilde{\rho}_{\pm}(\tilde{f})|$ in the insets by using Eq.(5.8). The temperature increment in the critical regime is $\Delta T \approx 0.03$ K. Note that the **same** critical exponents have been used for **all** data taken at $\theta \leq 30°$ to yield the same universal functions.

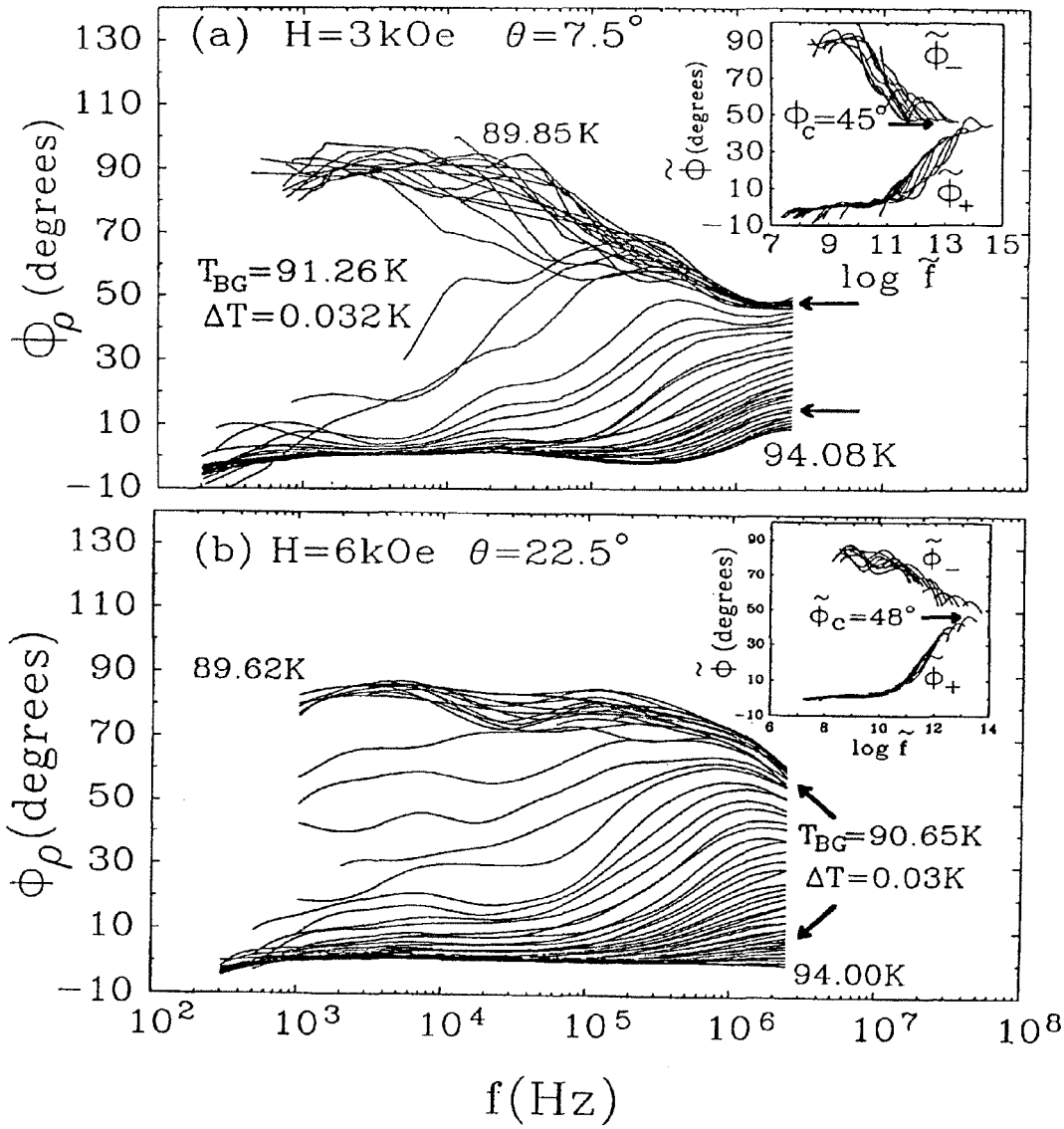

Figure 5.5: Phase of the AC resistivity ϕ_ρ vs. frequency (f) isotherms taken at **(a)** $H = 3.0$ kOe, $\theta = 7.5°$; and **(b)** $H = 6.0$ kOe, $\theta = 22.5°$. The arrows indicate the isotherms in the critical regime which are scaled into universal functions $|\tilde{\phi}_\pm(\tilde{f})|$ in the insets by using Eq.(5.8). The temperature increment in the critical regime is $\Delta T \approx 0.03$ K. Note that the **same** critical exponents have been used for **all** data taken at $\theta \leq 30°$ (including data for $H = 15$ kOe which is not shown) to yield the same universal functions.

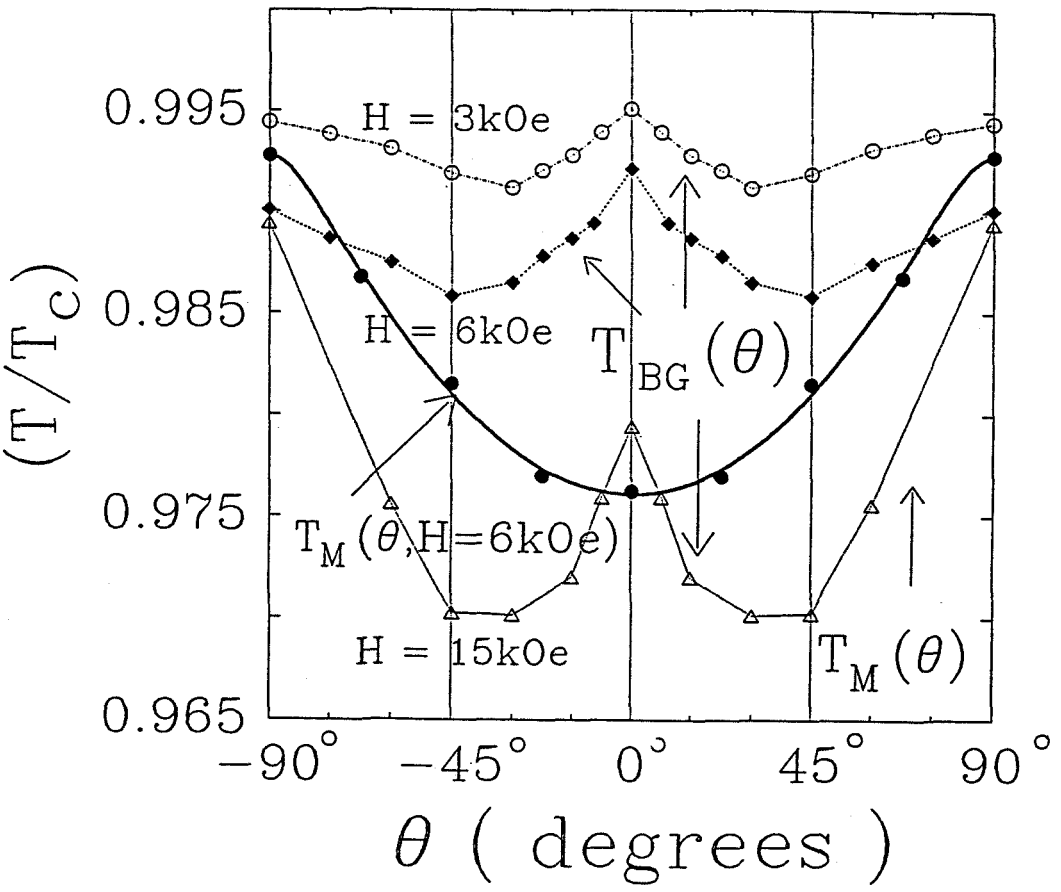

Figure 5.6: The reduced Bose-glass transition temperature (T_{BG}/T_c) for a $YBa_2Cu_3O_7$ single crystal with columnar defects (T_c = 91.77 K) and the reduced vortex glass temperature (T_M/T_c, thick solid line) for an as-grown $YBa_2Cu_3O_7$ single crystal (T_c = 92.95 K) are shown as functions of the angle (θ).

Although the ratio of $(\zeta/z') \approx 0.5$ has been obtained, additional information is still needed in order to find the values for $\nu_\perp$, ζ and z'. If the Bose-glass phase were *compressible* as has been suggested (Nelson & Vinokur, 1992; Nelson & Vinokur, 1993), so that the compression modulus $c_{11} \sim (\xi_\perp^{d'}/\xi_\parallel) \sim (\xi_\perp^{d'}/\xi_\perp^{\zeta})$ approaches a finite value at T_{BG}, the necessary condition would be $\zeta = d' = 2$ (Fisher *et al.*, 1989), yielding the exponents $\nu_\perp \approx 0.5$ and $z' \approx 4.0$ as reported previously (Yeh *et al.*, 1993b). However, the value $\nu_\perp \approx 0.5$ violates the theoretical constraint $\nu_\perp \geq (2/d') = 1$ (Fisher *et al.*, 1989; Chayes *et al.*, 1986), thereby implying that the assumption $\zeta = 2$ is incorrect. In fact, theoretical evidence shows that $\zeta \rightarrow 1$ can be realized in the limit of a long-range Bose interaction (Fisher & Grinstein, 1988). Since the

magnetic penetration depth ($\sim$ 1400Å at $T = 0$) in our sample is much larger than the separation of the columnar defects, it is not surprising that the vortex interaction is long-range and that ζ may differ from 2 even if $H < B_\varphi$. Recent numerical simulations (Lee *et al.*, 1993) have also shown evidences supportive of $\zeta \to 1$

The angular dependence of the AC resistivity described in Eq.(5.20) adds an additional scaling relation to determine the absolute values of ζ, $\nu_\perp$ and z'. Figure 5.7 shows the real part of the resistivity versus temperature curves taken at various angles for $H = 6$ kOe and $f \to 0$. We find that for $\theta \leq 30°$, the ρ_{ac}-vs.-T data at various angles near $T_{BG}(\theta)$ can be scaled into universal functions $\tilde{\rho}_\pm(\tilde{\Theta})$, as shown in the inset of Fig.5.7 for both $H = 3$ and 6 kOe. The power-law dependence $\tilde{\rho}_\pm \sim \tilde{\Theta}^{0.53}$ yields $(z' - \zeta)/(1 + \zeta) = 0.53 \pm 0.03$. Knowing that $(\zeta/z') = 0.50 \pm 0.03$ and $b \equiv \nu_\perp z' = 2.2 \pm 0.2$, we obtain $\zeta = 1.1 \pm 0.1$, $\nu_\perp = 1.0 \pm 0.1$, and $z' = 2.2 \pm 0.2$.

In the case of $H = 15$ kOe ($H > B_\varphi$) and $\theta \leq 30°$, the same scaling functions $|\tilde{\rho}_\pm|$ and $\tilde{\phi}_\rho$ can be obtained with the same set of exponents $\nu_\perp = 1.0$, $\zeta \approx 1.1$ and $z' \approx 2.2$, as shown in the insets of Fig.5.4(c). The angular dependence of the phase transition temperatures (which we also call T_{BG}) is also similar to that for $H < B_\varphi$ and $\theta \leq 30°$, as shown in Fig.5.6. Since an effective Bose-glass to superfluid transition is also possible for $H > B_\varphi$ via the dislocated vortex "half-loops" as described earlier, we speculate that the critical phenomena observed for both $H > B_\varphi$ and $H < B_\varphi$, and for $\theta \leq 30°$, are governed by the same type of phase transitions.

5.4.3 $\theta \geq 60°$ — Vortex-Glass Transition

Next, we consider the scaling behavior for $\theta \geq 60°$. For all three fields we find that neither $|\rho_{ac}(f)|$ nor $\phi_\rho(f)$ isotherms at $\theta \geq 60°$ can be scaled with the critical exponents derived from the low-angle ($\theta \leq 30°$) scaling analysis. Rather, different scaling functions $|\tilde{\rho}_\pm|$ and $\tilde{\phi}_\pm$ can be achieved for all data taken at $\theta \geq 60°$ by using a different set of exponents $\nu_\perp = \nu_\parallel = \nu \approx 2/3$ and $z = z' \approx 3$, which is consistent with the three-dimensional XY-model predicted by Nelson and Vinokur (1993) for $\theta \to 90°$ in systems with c-axis columnar defects. The difference between the scaling behavior

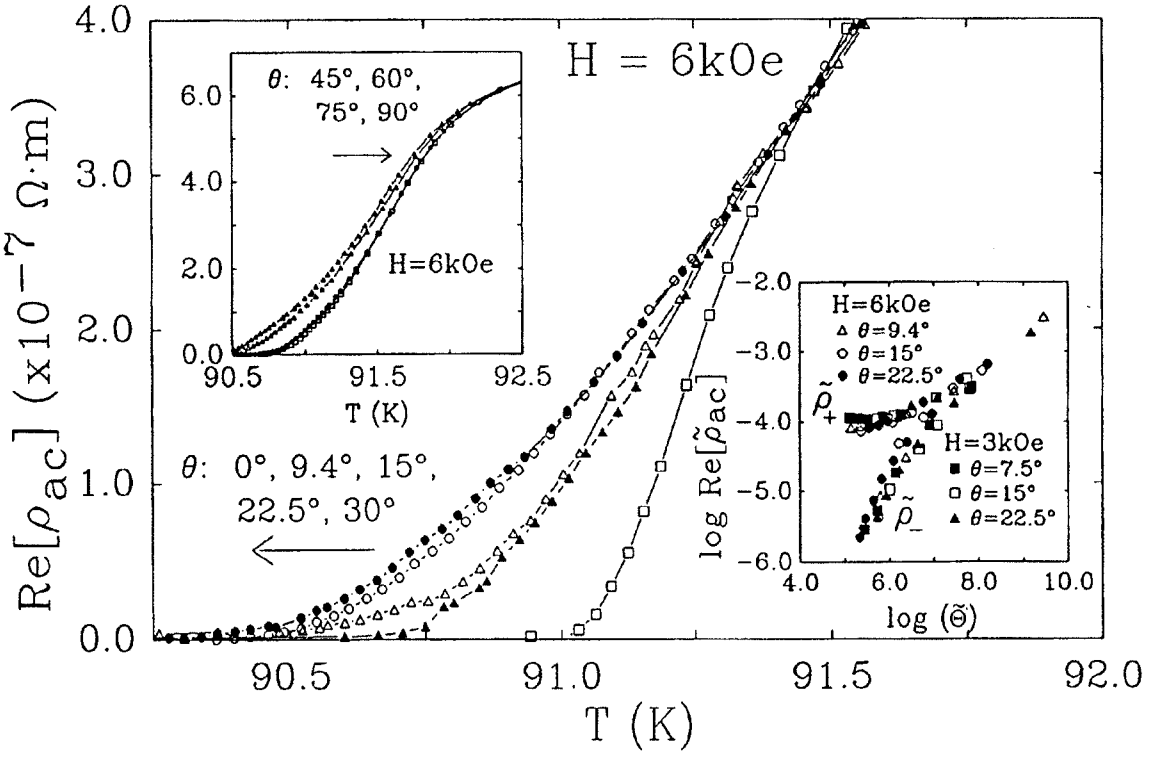

Figure 5.7: The angular dependence of the resistivity $\mathrm{Re}[\rho_{ac}]$ vs. temperature (T) curves at $H = 6.0$ kOe are shown for the $YBa_2Cu_3O_7$ single crystal with columnar defects and for $\theta \leq 30°$. The upper inset shows $\mathrm{Re}[\rho_{ac}]$-vs.-T for $\theta \geq 45°$. The lower inset shows that $\rho_{ac}(T,\theta)$ data near $T_{BG}(H,\theta)$ can be scaled into universal functions $\tilde{\rho}_{\pm}(\tilde{\Theta})$ by using Eq.(5.20).

for $\theta \leq 30°$ and that for $\theta \geq 60°$ can be further contrasted by considering the critical phases ϕ_c at the transition temperatures. We find that for $\theta \geq 60°$, the critical phase $\phi_c(T = T_M) = \frac{\pi}{2}(1 - \frac{1}{z}) \approx 60°$ is consistent with $z \approx 3.0$ for the XY model (Reed *et al.*, 1993; Reed *et al.*, 1992). In contrast, $\phi_c(T = T_{BG}) \approx 45°$ is found for **all** data taken at $\theta \leq 30°$, as shown in the insets of Figs. 5.5(a)-(b). Furthermore, the phase transition temperatures obtained for $\theta \geq 60°$ (see Fig.5.6) are found to **increase** with increasing θ, resembling the angular dependence in samples with point defects and in sharp contrast to the **decreasing** T_{BG} with increasing θ for data taken at $\theta \leq 30°$. It should be noted that for the data taken at an intermediate angle $\theta = 45°$ (between 30° and 60°), neither the Bose-glass nor the vortex-glass scaling relations are applicable.

The differences in the angular-dependent transition temperatures between the

data for $\theta \geq 60°$ and those for $\theta \leq 30°$ may be understood by the following argument. At sufficiently small angles, columnar defects become less efficient in confining vortices when the applied field is tilted away from the c axis, thereby resulting a decreasing transition temperature T_{BG} with increasing θ. On the other hand, at sufficiently high angles intrinsic electronic anisotropies in $YBa_2Cu_3O_7$ become dominant, giving rise to an increasing T_M with increasing θ.

5.4.4 The H-T Phase Diagram

The anisotropic phase transitions for the sample with columnar defects are delineated in the H vs. T phase diagram in Fig.5.8. For comparison, we also show the anisotropic vortex-glass melting lines ($H_{M||,\perp}(T)$) for $\theta = 0°$ and $90°$ in samples with random point defects. At $\theta \leq 30°$, the Bose-glass to superfluid transition line $H_{BG}(\theta, T)$ moves to lower temperatures with increasing θ. In contrast, the effective "vortex-glass" transition line at $\theta \geq 60°$ (see the inset of Fig.5.8) not only shifts towards higher temperatures with increasing θ, but even shows an abrupt change of slope at $\theta = 90°$ when $H > B_\varphi$.

Furthermore, both the Bose-glass transition lines and the vortex-glass transition lines are found to follow the empirical relation

$$H_{BG}(T,\theta) = H_{BG0,}(\theta)\left|1 - \frac{T}{T_c}\right|^{2\nu_0}, \tag{5.22}$$

$$H_M(T,\theta) = H_{M0}(\theta)\left|1 - \frac{T}{T_c}\right|^{2\nu_0'} \tag{5.23}$$

where T_c is the zero-field transition temperature and ν_0 and ν_0' are the zero-field critical exponents for Bose-glass and vortex-glass transitions, respectively. As discussed previously in Chapter 4, the ν_0' values for the vortex-glass transitions at all θ's yield $\nu_0 = 0.65 \pm 0.05$. On the other hand, for the Bose-glass transitions with $\theta \leq 30°$, we find that $\nu_0 = 0.5 \pm 0.05$.

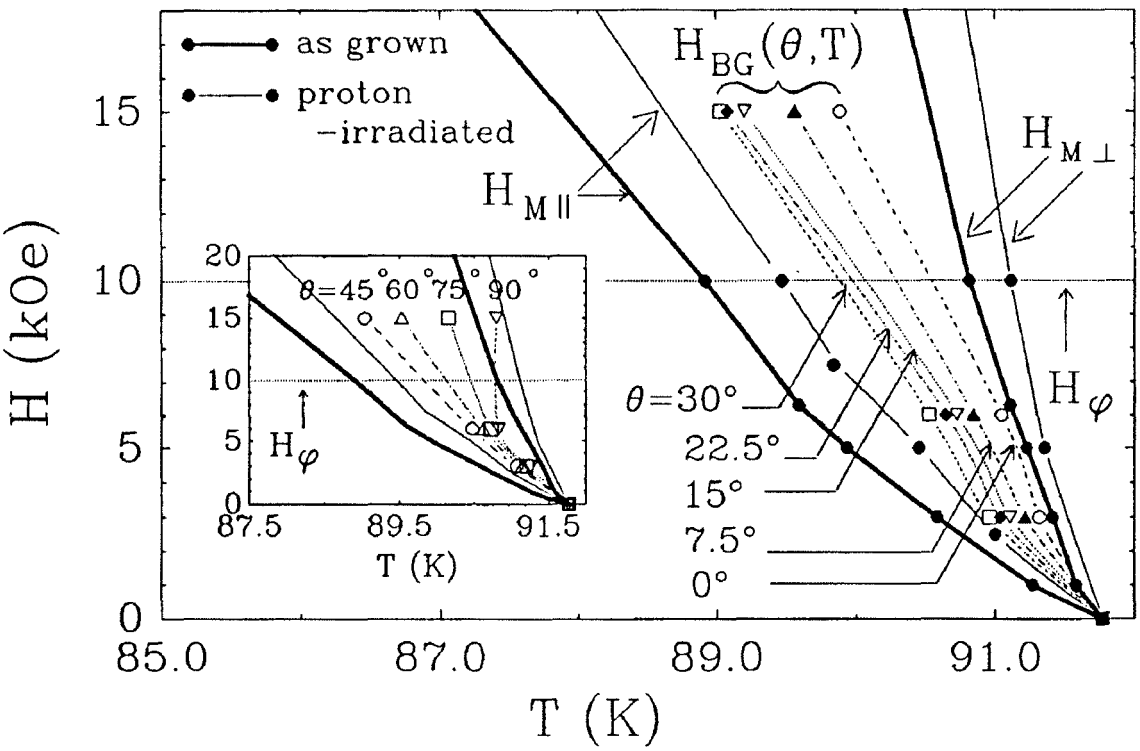

Figure 5.8: The low-angle ($\theta \leq 30°$) H-vs.-T vortex phase diagram for a $YBa_2Cu_3O_7$ single crystal with columnar defects ($T_c = 91.77$ K). The inset shows the high-angle ($\theta \geq 60°$) phase diagram. The thick solid lines denote the vortex-glass melting lines $H_{M\|}(T)$ and $H_{M\perp}(T)$ for an as-grown $YBa_2Cu_3O_7$ single crystal ($T_c = 92.95$ K), and the thin solid lines are those for a $YBa_2Cu_3O_7$ single crystal irradiated with 3 MeV protons($T_c = 91.62$ K). The data for all samples have been scaled to the same T_c for comparison.

5.5 Discussions

5.5.1 Anisotropic Vortex Phase Diagram

From the vortex anisotropic phase diagram shown in Fig.5.6, the angle beyond which the Bose-glass transition breaks down is approximately 30°, known as the accommodation angle (Nelson & Vinokur, 1993). To facilitate a better understanding of the effects of the transverse fields ($H_\perp = Hsin(\theta)$)) on the vortex phase transition, we first employ the scaling transformations described in section 5.3 to remove the intrinsic anisotropy in $YBa_2Cu_3O_7$ and plot the rescaled transition temperature ($\tilde{T}$) versus the effective angle ($\tilde{\theta}$) for the rescaled isotropic superconductor. As shown

earlier in Eq.(5.18), the rescaled angle $\tilde{\theta}$ is given by

$$sin\tilde{\theta} \equiv \frac{\widetilde{H}_{\perp}}{\widetilde{H}} = \frac{\varepsilon sin\theta}{\sqrt{cos^2\theta + \varepsilon^2 sin^2\theta}}.$$

The rescaled transition temperature ($\tilde{T}$) can be obtained by rewriting Eq.(5.22) for the rescaled isotropic superconductor for a fixed field $H_{BG}(T)$, i.e.,

$$H_{BG} = \widetilde{H}_{BG0}\left|1 - \frac{\tilde{T}}{T_c}\right|^{2\nu_0} = \varepsilon_\theta H_{BG0}(\theta)\left|1 - \frac{\tilde{T}}{T_c}\right|^{2\nu_0}. \tag{5.24}$$

Since $H_{BG}/H_{BG0}(\theta) = |1-(T/T_c)|^{2\nu_0}$, the rescaled transition temperature is therefore related to T and θ by the following expression:

$$\tilde{T} = T_c + \frac{T - T_c}{(\sqrt{cos^2\theta + \varepsilon^2 sin^2\theta})^{1/(2\nu_0)}}. \tag{5.25}$$

By replacing BG with VG and ν_0 with ν_0' in Eq.(5.25), we can obtain the rescaled vortex-glass transition temperatures. The resulting $\tilde{T}$-vs-$(\widetilde{H}_{\perp}/\widetilde{H})$ for the Bose-glass transition is plotted in Fig.5.9(a) for different fields. The resulting $\tilde{T}$-vs-$(\widetilde{H}_{\perp}/\widetilde{H})$ for the Vortex-glass transition in the as-grown twinned crystal (Sample #1) is plotted in Fig.5.9(b) for $H = 6.0$ kOe. We note that for all fields, the Bose-glass transition temperatures $\tilde{T}_{BG}(\tilde{\theta})$ follow the critical scaling relation:

$$[\tilde{T}_{BG}(0^\circ) - \tilde{T}_{BG}(\tilde{\theta})] \propto (sin\tilde{\theta})^{\frac{1}{\nu_\perp(1+\zeta)}}. \tag{5.26}$$

Using Eq.(5.26), we find that the theoretical fitting to the $\tilde{T}$-vs-$(sin\tilde{\theta})$ data is consistent with a power $\frac{1}{\nu_\perp(1+\zeta)} \approx 0.45$, once again confirming the self-consistency of our Bose-glass critical scaling analysis.

5.5.2 Critical Exponents for Bose-Glass Transition

One of our key results, $\zeta < d' = 2$, suggests that the compression modulus $c_{11} \sim \xi_\perp^{d'}/\xi_{||}$ diverges at T_{BG}, and that the Bose interaction is long ranged and the

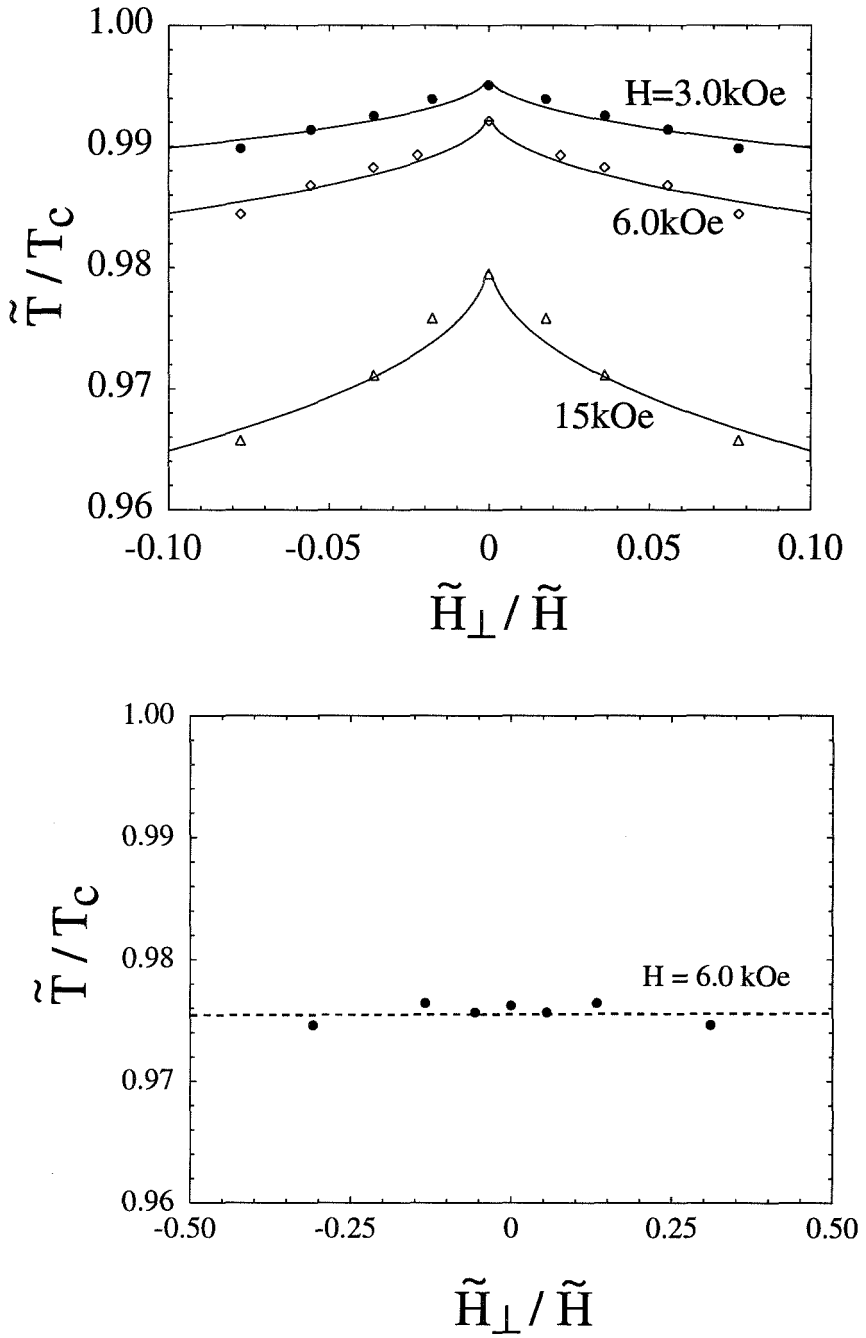

Figure 5.9: The scaled phase diagram $\tilde{T}$-vs.-$(\widetilde{H}_\perp/\widetilde{H})$ obtained (a) for the Bose-glass transitions by using Eqs. (5.18) and (5.25) for different magnetic fields H, where the solid lines are the fitting curves for the low angle data using Eq. (5.26) and a power $1/(\nu_\perp(1+\zeta)) \approx 0.45$, and (b) for the vortex-glass transitions (see Fig. 4.7 for the original anisotropic phase diagram) using the same approach.

Bose-glass incompressible. However, it is likely that ζ is a parameter dependent on both the density of columnar defects and the strength of the other types of defects. We speculate that a compressible Bose-glass transition with $\zeta = 2$ may be achieved in superconducting samples nearly free of point defects and twin boundaries and with columnar defects of separations greater than the magnetic penetration depth. However, due to the long magnetic penetration depth in all high-temperature superconductors, the requirement of column separations greater than 1400Å may cast additional complications due to the potential existence of other types of defects (e.g., oxygen vacancies) that may become more dominant because of their higher densities than the columnar defects.

It is worth noting another beautiful demonstration of the Bose-glass universality in a recent work (Reed *et al.*, 1995) on $YBa_2Cu_3O_7$ single crystals with c-axis columnar defects and $B_\phi = 10$ kG. That work involves a completely different experimental technique, the third-harmonic transmissivity. The critical scaling analysis on the data thus taken yields essentially identical critical exponents $\nu_\perp = 0.9 \pm 0.1$, $\nu_\parallel = 1.2 \pm 0.2$, and $z' = 2.3 \pm 0.3$ within experimental errors, once again supporting the universality of the Bose-glass transition in vortex systems with parallel columnar defects.

In summary, in this chapter we have demonstrated the experimental evidence of a second-order Bose-glass transition in $YBa_2Cu_3O_7$ single crystals with parallel columnar defects by showing **universal** critical scaling of frequency-dependent AC resistivity data from 10^2 to 2×10^6 Hz. The signature of the transition, that the Bose-glass transition temperature T_{BG} **decreases** with the increasing angle (θ) between the applied magnetic field and the c-axis, has been confirmed and is in sharp contrast to the smooth **increase** of the vortex-glass temperature (T_M). For $\theta \leq 30°$, the static and dynamic exponents $\nu_\perp \approx 1.0, \nu_\parallel \equiv \zeta\nu_\perp \approx 1.1$ and $z' \approx 2.2$ are found to be **independent** of the magnitude and orientation of the magnetic field. On the other hand, for $\theta \geq 60°$, the vortex phase transitions become consistent with the vortex-glass transitions. The different set of critical exponents distinguishes the Bose-glass transition from the universality class of the vortex-glass transition, and the diverging compression modulus at T_{BG} suggests an **incompressible** Bose glass with long-range

interaction at temperatures below T_{BG}.

Chapter 6 Vortex Transport Properties of Untwinned $YBa_2Cu_3O_7$ Single Crystals

The experimental investigations presented in the previous chapters have shown that large thermal and disorder fluctuations in high-temperature superconductors result in various universality classes of second-order vortex-solid to liquid transitions. Depending on the nature of the static disorder, such vortex phase transitions can be vortex-glass transitions for superconductors with random point defects and dilute twin boundaries, or Bose-glass transitions with correlated columnar defects. To further explore the interplay between vortex pinning and thermodynamic vortex phase transitions, it is necessary to study the vortex properties in the weak pinning limit of "clean" superconductors with minimal structural defects. In this chapter, we present our investigations on the vortex transport properties of untwinned $YBa_2Cu_3O_7$ single crystals.

One of the most important issues to be explored in clean type-II superconductors is the nature of the vortex-solid melting transition. Balents and Nelson have pointed out that renormalization group analysis for type-II superconductors which are free of pinning disorder yields a weak first-order melting transition due to the thermal fluctuations (Brezin *et al.*, 1985). Recent theoretical work using Monte Carlo simulations (Hetzel *et al.*, 1992) has also provided convincing evidence for a first-order vortex-solid melting transition in high-temperature superconductors free of pinning by demonstrating hysteretic behavior of the internal energy. However, the only nonequivocal experimental proof for a first-order phase transition relies on the observation of a discontinuous jump in relevant thermodynamic quantities such as the specific heat or magnetization at the transition temperature. Unfortunately, experimental measurements of these thermodynamic quantities were found to be technically very difficult because of the smallness (about one part in a million) of the vortex specific

heat relative to the contributions from electrons and phonons in the superconductor. In addition, recent state-of-the-art magnetization measurements on an untwinned $YBa_2Cu_3O_7$ single crystal by Farrell et al. (Farrell *et al.*, 1995) have also shown that the latent heat associated with a first-order vortex-solid melting transition, if exists, is at least two orders of magnitude smaller than that predicted by the Monte Carlo simulations.

Due to the extreme difficulties in the thermodynamic measurements, there have been other experimental attempts to resolve the order of the vortex-solid melting transition in "clean" high-temperature superconductors. For instance, the observation of resistive hysteresis (Safar *et al.*, 1992a; Safar *et al.*, 1992b; Kwok *et al.*, 1994a) in the vortex state of untwinned $YBa_2Cu_3O_7$ single crystals were initially viewed as the experimental evidence for the first-order transition. However, as the issue was further scrutinized, it became questionable whether a non-thermodynamic quantity such as the resistivity should follow the same hysteretic behavior as the internal energy. In this chapter, rather than trying to conclude whether the vortex-solid melting transition is first-order, we aim at understanding the physical origin of the resistive hysteresis in the vortex state. A current-induced non-equilibrium effect is proposed based on detailed investigations of the resistive hysteresis as a function of time, frequency, and magnetic field orientation. The experimental results suggest that the resistive hysteresis alone is neither a sufficient nor a necessary condition for a first-order phase transition. In addition, another current-induced phenomenon, the nonlinear resistive "peak effect" below the vortex-solid melting transition temperature, is also investigated extensively.

6.1 Sample, Experimental Setups and Techniques

Before going into details of our experimental investigations of the issues stated above, we first describe the sample characterizations and the experimental techniques.

The sample (#5) studied in this work is an untwinned $YBa_2Cu_3O_7$ single crystal with dimensions of 0.5mm $\times$ 0.5mm $\times$ 20μm. The high quality of the sample is manifested by the high superconducting transition temperature $T_c = 93.44 \pm 0.03$

K and the low normal-state a-axis resistivity $\rho_n = 25\mu\Omega$-cm at T_c. This sample is subsequently used for 3.0 MeV protons with a fluence of 1.5×10^{15} protons/cm^2, and we denote the sample after the irradiation as Sample #6. For more information on the comparison of these two samples with other samples investigated in the previous chapters, see Table 3.3.

The experimental techniques used in this investigation involve three types of electrical transport measurements performed with the use of a standard four-terminal method: the linear resistivity (ρ) as a function of the temperature (T), the AC impedance as a function of the applied current frequency (f) from 100 Hz to 1 MHz, and the DC current-voltage characteristics. Both AC and DC transport techniques have been given in Chapter 3. Described in this section are the lock-in technique and an improved temperature control technique for measuring the linear resistivity near the vortex-solid melting transition.

As demonstrated in the first observation of resistive hysteresis by Safar et al. (Safar *et al.*, 1992a; Safar *et al.*, 1992b), the hysteretic behavior occurs within a very narrow temperature range, no more than a few tens of millikelvins, near the vortex-solid melting transition temperature. In addition, the hysteretic behavior only appears with a very small applied current, giving rise to a typical voltage signal of a few tens of nanovolts for untwinned $YBa_2Cu_3O_7$ single crystals. Therefore, a voltage sensitivity of 1 nV and a temperature stability of 1 mK are essential in order to observe the resistive hysteretic behavior. Described below are the experimental setups and techniques used to achieve such voltage sensitivity and temperature stability.

6.1.1 Low-Frequency Resistivity Measurements

To achieve nanovolt sensitivity, the lock-in technique is used. As shown in Fig. 6.1 for the block diagram of the experimental set-up, two EG&G 5210 lock-in amplifiers are used. An AC current at 27 Hz supplied by one of the amplifiers is applied directly to the sample. A noninductive load resistor with a resistance of $R_L = 10$ kΩ (compared with the sample contact resistances of $\sim 0.1\ \Omega$ at room temperature) is

connected in series with the sample to ensure a constant current. The sample voltage signal ($\tilde{V}_s$) is measured by the same lock-in amplifier phase referenced to the drive current. The voltage signal of the load resistor ($\tilde{V}_L$) is measured by the other lock-in amplifier with the same reference frequency to yield the applied current to the sample. The sample resistance is therefore

$$R = \frac{Re[\tilde{V}_s]}{(Re[\tilde{V}_L]/R_L)}, \tag{6.1}$$

where "Re" refers to the real part signal.

To obtain the best sensitivity, voltage signals are measured using differential input connections with a floating ($1k\Omega$) ground, and the electrical connections are all made via BNC coaxial cables. In addition, the current and voltage coaxial cables are twisted in pairs to minimize any possible loops which may result in magnetic noise pickups. Cautions in electrical shieldings are taken to eliminate ground loops. However, even with all these efforts, noises of a few tens of nanovolts or larger still exist particularly during the day time. After adding a TOPAZ power conditioner to the power line, these random noises were greatly suppressed and a voltage resolution of $\sim 2nV$ was achieved, which is essentially to the instrumental limit (with a quoted voltage resolution of $\sim 10nV$) of the lock-in amplifiers.

6.1.2 Temperature Control with Millikelvin Resolutions

For most of the experiments discussed in the previous chapters, a temperature stability of $\pm$10mK at temperatures around 90 K is sufficient and can be achieved with the commercial LakeShore temperature controllers DRC-91 and DRC-93C, provided that proper designs for the cryogenic insert are made as discussed in Chapter 3.

However, to achieve the required stability of $\sim$1 mK for measurements on untwinned $YBa_2Cu_3O_7$ single crystals, additional modifications to the sample stage are needed. As shown in Fig. 6.2, on a sapphire substrate, the sample and a carbon-glass resistance temperature sensor are mounted next to each other (about 2 mm apart) to minimize the temperature gradient between the sample and the sensor. A ring heater

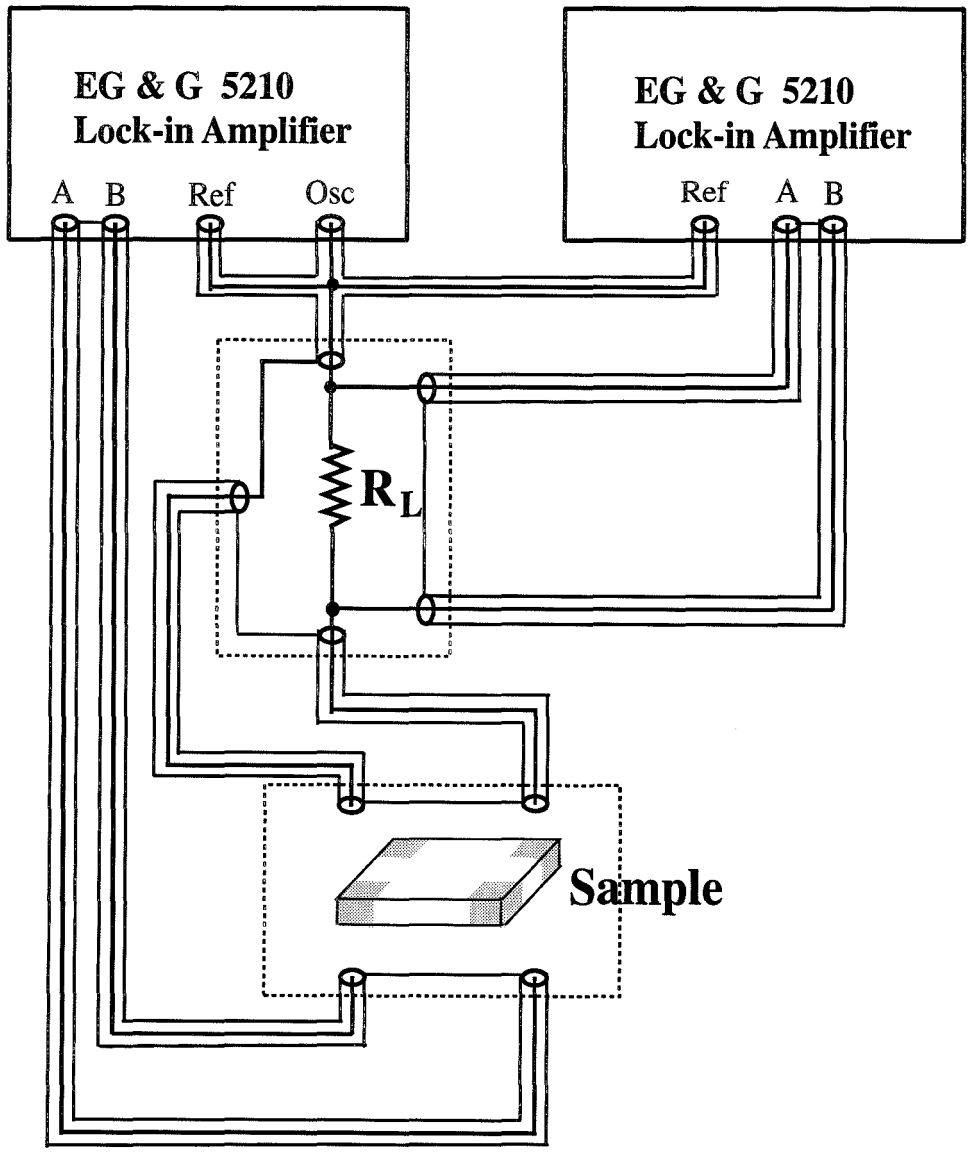

Figure 6.1: The block diagram of the experimental setup for low-frequency resistivity measurements using the lock-in technique.

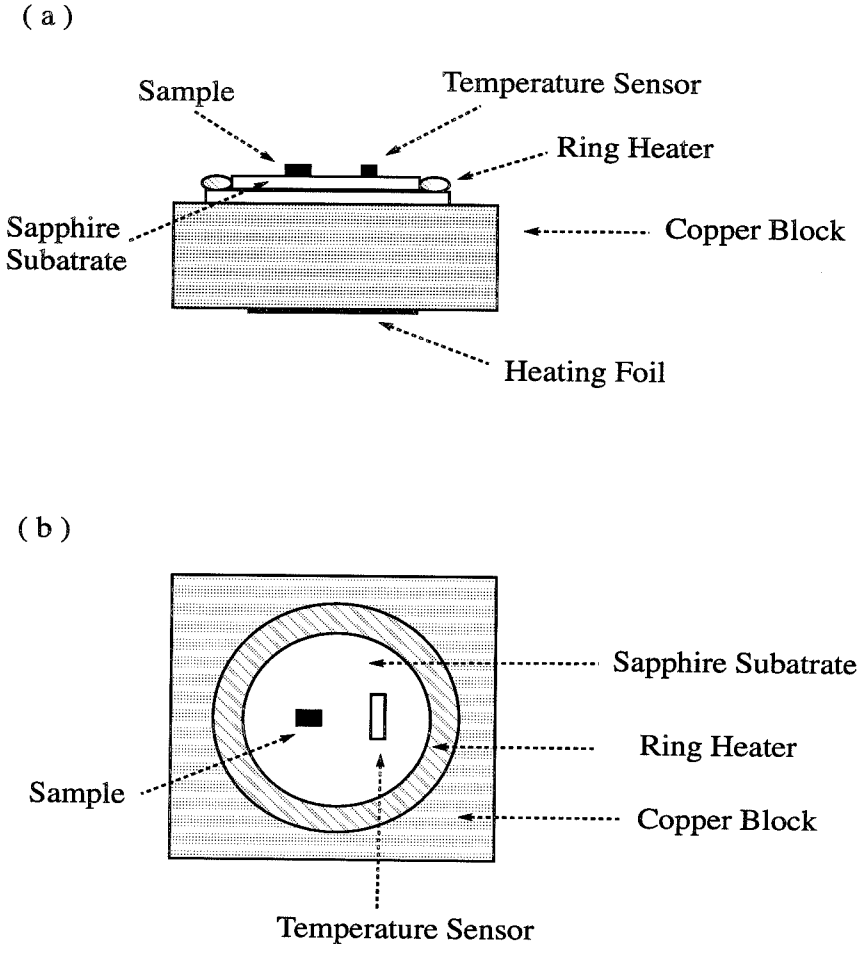

Figure 6.2: The sample stage specially designed for achieving mK temperature stability. (a) The side view; (b) The top view.

made of a twisted heating wire is varnished to the edge of the sapphire for uniform heating. The sapphire is in good thermal contact with a copper block to which a constant heating power is supplied through the heating foil. About one inch of each electrical lead to either the sensor or the sample is varnished to the copper block for proper heat sinking.

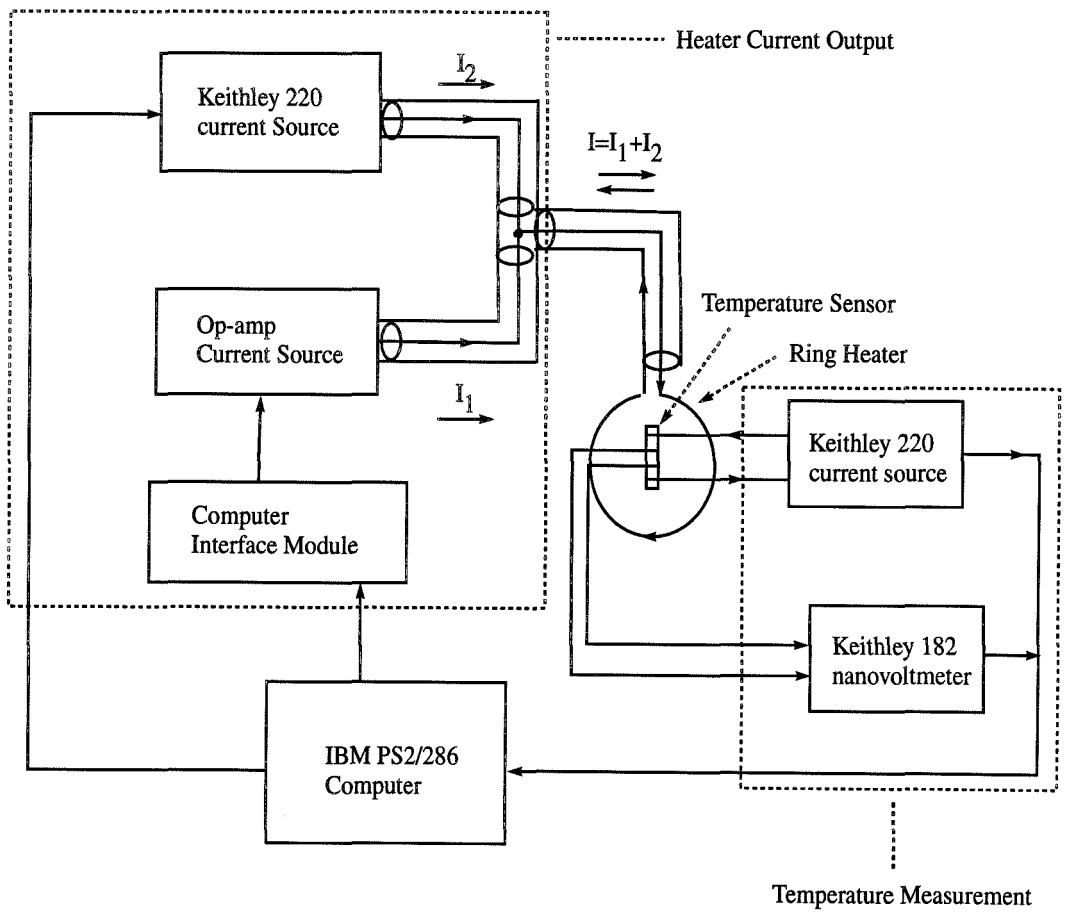

Figure 6.3: The block diagram of the experimental setup for temperature measurements. Two current sources are used to achieve a resolution of 0.2 μA in the total current output to the ring heater.

In addition to an improved design for the sample stage, the following two conditions have to be satisfied to achieve millikelvin stability for the temperature range of interest $(80-100K)$: The carbon-glass sensor resistance has to be measured to an accuracy of $10^{-4}\Omega$, and the current passing through the ring heater has to be adjustable with an accuracy of $10^{-7}A$. Since the commercial LakeShore DRC temperature con-

trollers do not have sufficient resolutions in either the sensor resistance measurement or the heater current output, different electronic instruments are used as shown in Fig. 6.3. The sensor resistance is measured via the standard four-point method as shown by the "Temperature Measurement" block in Fig. 6.3. With a Keithley 220 current source and a Keithley 182 nanovoltmeter, an accuracy in the sensor resistance reading, $\sim 2 \times 10^{-5}\Omega$, is achieved. In addition, the offset of the carbon-glass sensor resistance in magnetic fields has been calibrated using a capacitance sensor. The output current to the ring heater is supplied by a home-made op-amp current source and a Keithley 220 current source, as shown by the "Heater Current Output" block in Fig. 6.3. Two current sources are used, one for the coarse control of the temperature and the other for the fine tuning. The electronics layout of the op-amp current source used for fine-tuning the temperature is shown in Fig. 6.4. The input voltage (V_{in}) is provided by an analog signal from the computer interface module and the output current in the ideal case is $I_{out} = kV_{in}$, where $k = (R_2/R_3) \times R_1$. The actual coefficient k with the load resistor of the ring heater is obtained by measuring the current-voltage characteristics of the op-amp current source. The current output (I_1) of the op-amp current source is adjustable within a few tens of microamperes on a scale of a few tens of milliamperes. When a smaller variation in the total current is necessary, I_2 is added to I_1 which has a resolution of $0.2\mu A$ on the scale of $200\mu A$.

The central unit of the above experimental setup is the computer, which performs the temperature control by reading the sample temperature (T), comparing T with the set point temperature T_{setpt} and calculating the output heating power based on the idea of conventional proportional-integral (PI) control:

$$u(t) = g\Delta e(t) + \tau \int_0^t \Delta e(t')dt', \tag{6.2}$$

where $u(t)$ is the heater power output at time t, g and τ are the controller gain and reset, respectively, and $\Delta e(t)$ is the difference between the set point temperature T_{setpt} and the actual sample temperature T at time t, i.e., $\Delta e(t) = T_{setpt} - T(t)$. In reality, the sample temperatures are measured at a series of sampling times $t_1, t_2, \cdots, t_n, \cdots$

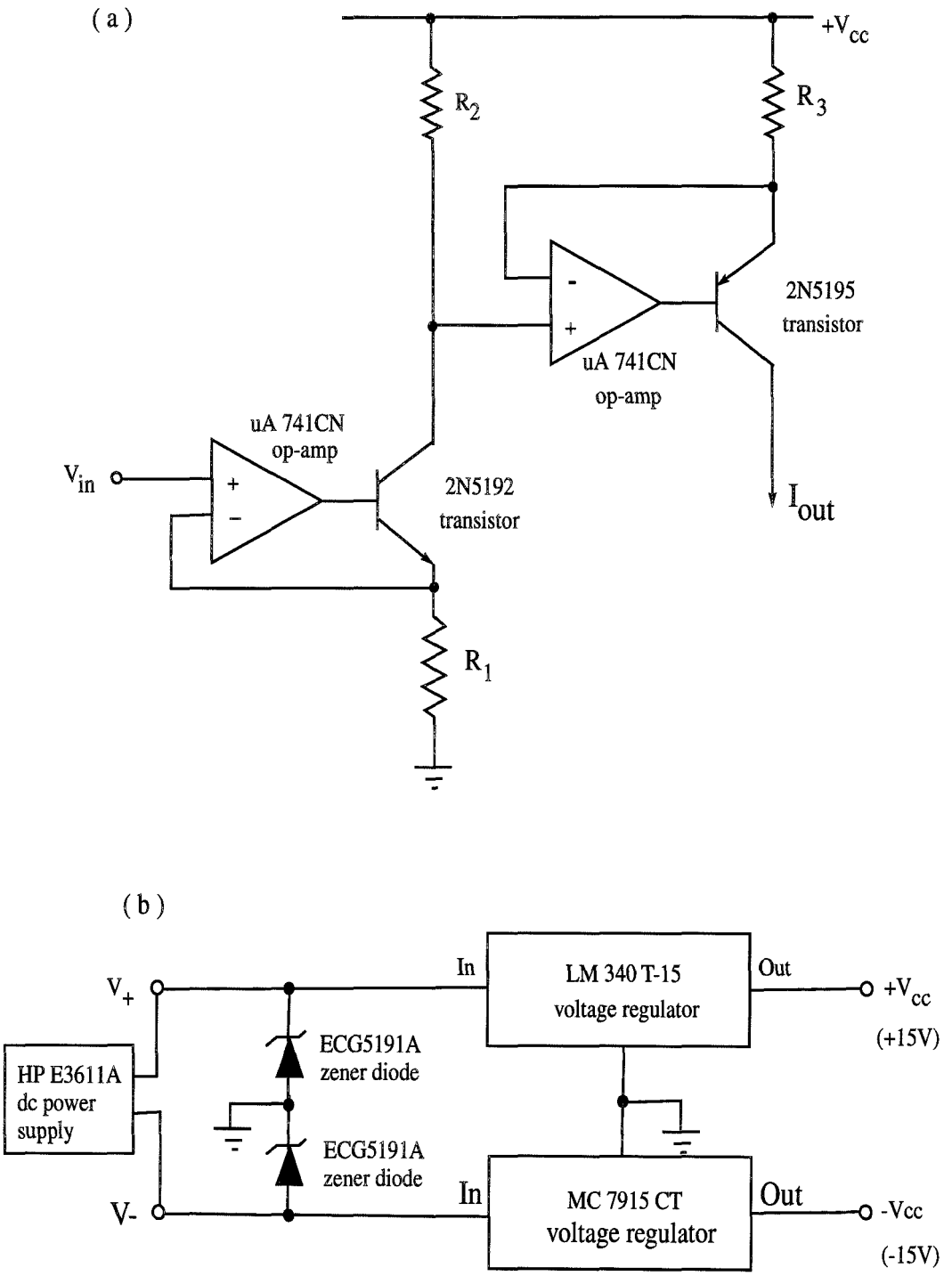

Figure 6.4: The electronics layout for (a) the op-amp current source, and (b) its power supply.

with a time interval Δt between two consecutive times. Converting Eq.(6.2) into its discrete form, we obtain

$$u_n = g\Delta e_n + \tau' \sum_{i=0}^{n} \Delta e_n, \tag{6.3}$$

where $\Delta e_n = T_{setpt} - T(t_n)$ and $\tau' = \tau \Delta t$. Similarly, the heater power at t_{n-1} is

$$u_{n-1} = g\Delta e_{n-1} + \tau' \sum_{i=0}^{n-1} \Delta e_{n-1}. \tag{6.4}$$

From Eqs.(6.3) and (6.4), an iteration relation between u_n and u_{n-1} can be expressed as

$$u_n = u_{n-1} + g(\Delta e_n - \Delta e_{n-1}) + \tau' \Delta e_n, \tag{6.5}$$

which yields the relation for the total current output I_n:

$$I_n^2 = I_{n-1}^2 + \mathcal{G}(\Delta e_n - \Delta e_{n-1}) + \mathcal{T}\Delta e_n, \tag{6.6}$$

because the heating power u_n is proportional to the square of the total current output at t_n, $I_n = I_{1n} + I_{2n}$ to the heater, with I_{1n} and I_{2n} being the current outputs of the coarse and fine controls at t_n. Here, $\mathcal{G}$ and $\mathcal{T}$ are the normalized gain and reset with the unit of A^2/K, and their values are obtained from trial-and-error. For simplicity, I_{1n} and I_{2n} are calculated with the following rules:

- if $I_n - I_{n-1} < 100\mu A$, $I_{2n} = I_n - I_{n-1}$, $I_{1n} = I_{1,n-1}$;
- otherwise, $I_{2n} = I_n - I_{1n} = I_n - k(V_{in})_n$.

Typical values of k, $\mathcal{G}$, $\mathcal{T}$ and the voltage supply $V_{+-} = V_+ - V_-$ are listed in Table 6.1.

This control process results in a temperature stability better than ± 1.0 mK over a time scale of approximately two to three minutes, as shown in Fig. 6.5. A possible constant offset between the set point and the real temperature has been considered in the computer program, so that the performance of the temperature control is not affected as long as the real temperature is stable within the experimental time scale.

Table 6.1: Experimental Parameters (k, $\mathcal{G}$, $\mathcal{T}$ and V_{+-}) for the Temperature Control

k (Ω)	$\mathcal{G}$ (A^2/K)	$\mathcal{T}$ (A^2/K)	V_{+-} (V)
1.070	2.0×10^{-5}	1.0×10^{-5}	31.5

6.2 Resistive Hysteresis in the Vortex State of Untwinned $YBa_2Cu_3O_7$ Single Crystals

Let us now return to the issue regarding whether it is justified to interpret the resistive hysteresis as an experimental evidence for a first-order vortex-solid melting transition. Figure 6.6 shows the resistive hysteresis data taken by Safar et al. (Safar *et al.*, 1992a) on an untwinned $YBa_2Cu_3O_7$ single crystal at $H = 60$ kOe. The hysteretic behavior had been once regarded as the evidence for a first-order vortex-solid melting transition. However, if the resistive hysteresis were indeed associated with the occurrence of a first-order phase transition, one would expect partial hysteresis loops upon partial heating and cooling cycles, due to the presence of a finite latent heat and a finite solidification time. Furthermore, if the temperature width of the hysteresis $\Delta T_{\ell p}$ were indeed proportional to the latent heat as suggested (Geshkenbein *et al.*, 1993), one would expect $\Delta T_{\ell p}$ in anisotropic $YBa_2Cu_3O_7$ single crystals to increase with increasing angle (θ) between the applied magnetic field and the crystalline c-axis, because the melting temperature (T_M) and therefore the latent heat increases with θ. However, none of these crucial tests had been conducted prior to our work (Jiang *et al.*, 1994). In the following, we shall see that the experimental results contradict the properties expected for a first-order related hysteretic behavior.

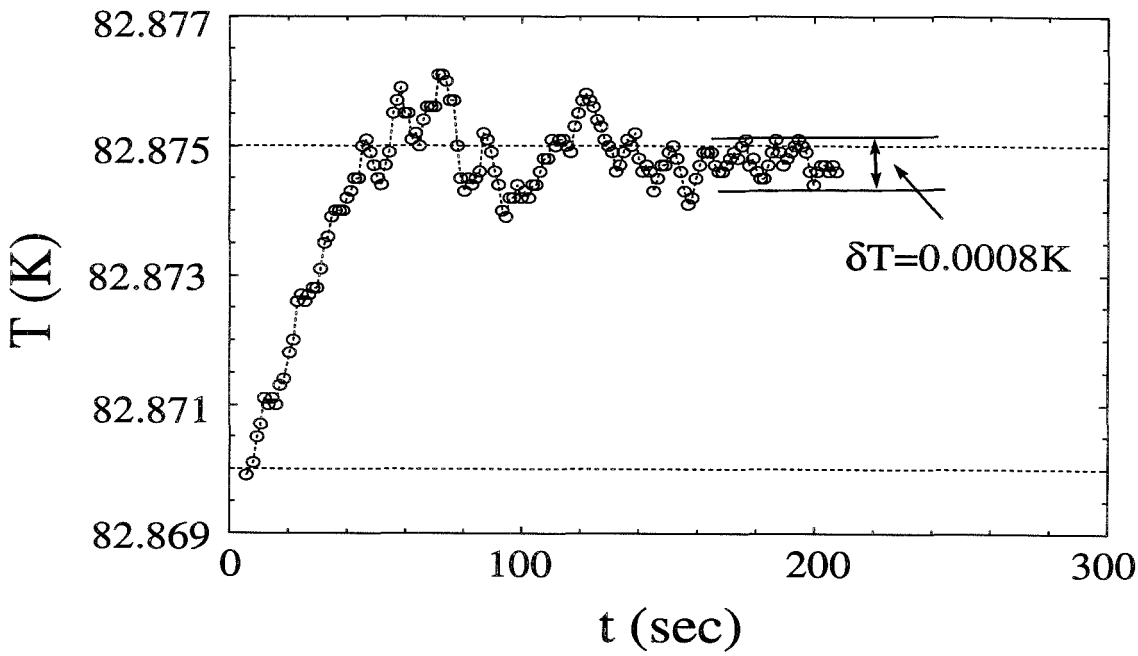

Figure 6.5: The temperature (T) of the sample as a function of time (t).

6.2.1 Experimental Results and Discussions

As mentioned in the previous section, three types of electrical transport measurements have been conducted for this investigation. The first measurement is that of the linear resistivity (ρ) as a function of the temperature (T) by using the lock-in technique with four different current densities of 0.27, 2.70, 9.99 and 16.55 A/cm^2 at 27 Hz. The voltage resolution for these measurements is $\sim$ 2 nV, and the temperature stability is within $\pm$1 mK, as detailed in the previous section. The second experiment involves measuring isotherms of the AC impedance as a function of the applied current frequency (f), from 100 Hz to 1 MHz. The third experiment measures DC current-voltage characteristics. All measurements are performed in applied magnetic fields (H) from 1 to 90 kOe and for angles (θ) from 0° to 90°. The applied current density $\vec{J}$ is always transverse to $\vec{H}$ and $\vec{J} \perp \hat{c}$.

Hysteresis behavior is observed in the ρ-vs.-T measurements of our sample for $H \geq 10$ kOe and $\theta < 90°$. Shown in Figs.6.7(a) and 6.7(b) are the representative data taken at $H = 50$ and 70 kOe and for $\theta = 0°$. At each constant magnetic

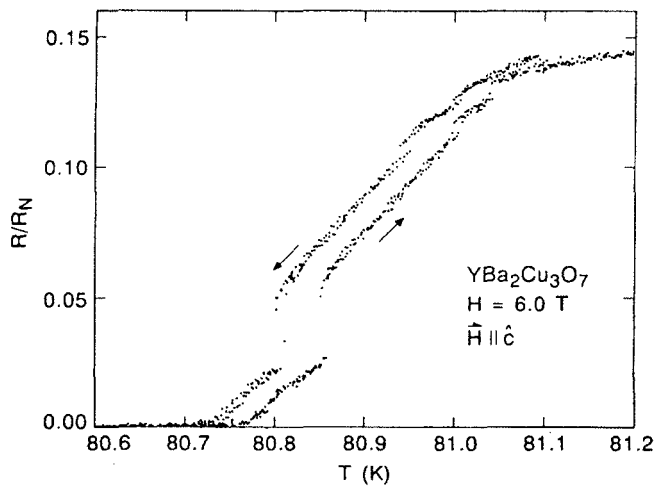

Figure 6.6: Hysteresis behavior observed by Safar et al. in normalized linear resistance (R/R_N) versus temperature T for $H = 60$ kOe, near the vortex-solid melting transition of an untwinned $YBa_2Cu_3O_7$ single crystal. (After reference (Safar *et al.*, 1992a).)

field, the temperature is ramped in steps of 5 mK. At each step, the temperature is monitored for $\sim$ 3 min to ensure the temperature stability before the data is taken. The hysteresis width $\Delta T_{\ell p}$ for a given H and θ is defined as the temperature width at the top of the resistive loop. The magnetic field dependence of $\Delta T_{\ell p}$ for $\vec{H} \parallel \hat{c}$ is shown in the inset of Fig. 6.7(b). A peak in $\Delta T_{\ell p}$ is found at $\sim$ 70 kOe, consistent with previous reports by Safar et al. (1992a; 1992b). However, we notice that the hysteretic behavior in our system appears to be more pronounced than that reported by Safar et al. (Safar *et al.*, 1992a).

Metastability and Time Dependence

To investigate whether the resistive hysteresis is directly associated with the latent heat of a first-order melting transition, consider a hysteresis loop $A \rightarrow B \rightarrow C' \rightarrow A' \rightarrow B' \rightarrow C \rightarrow A$ arising from superheating and supercooling vortices so that the bulk melting temperature T_M is between T_A and T_B, as shown schematically in the inset of Fig. 6.8. If the hysteresis width is comparable to the latent heat and is due to superheating or supercooling, as suggested by Hetzel et al. (1992) and Geshkenbein

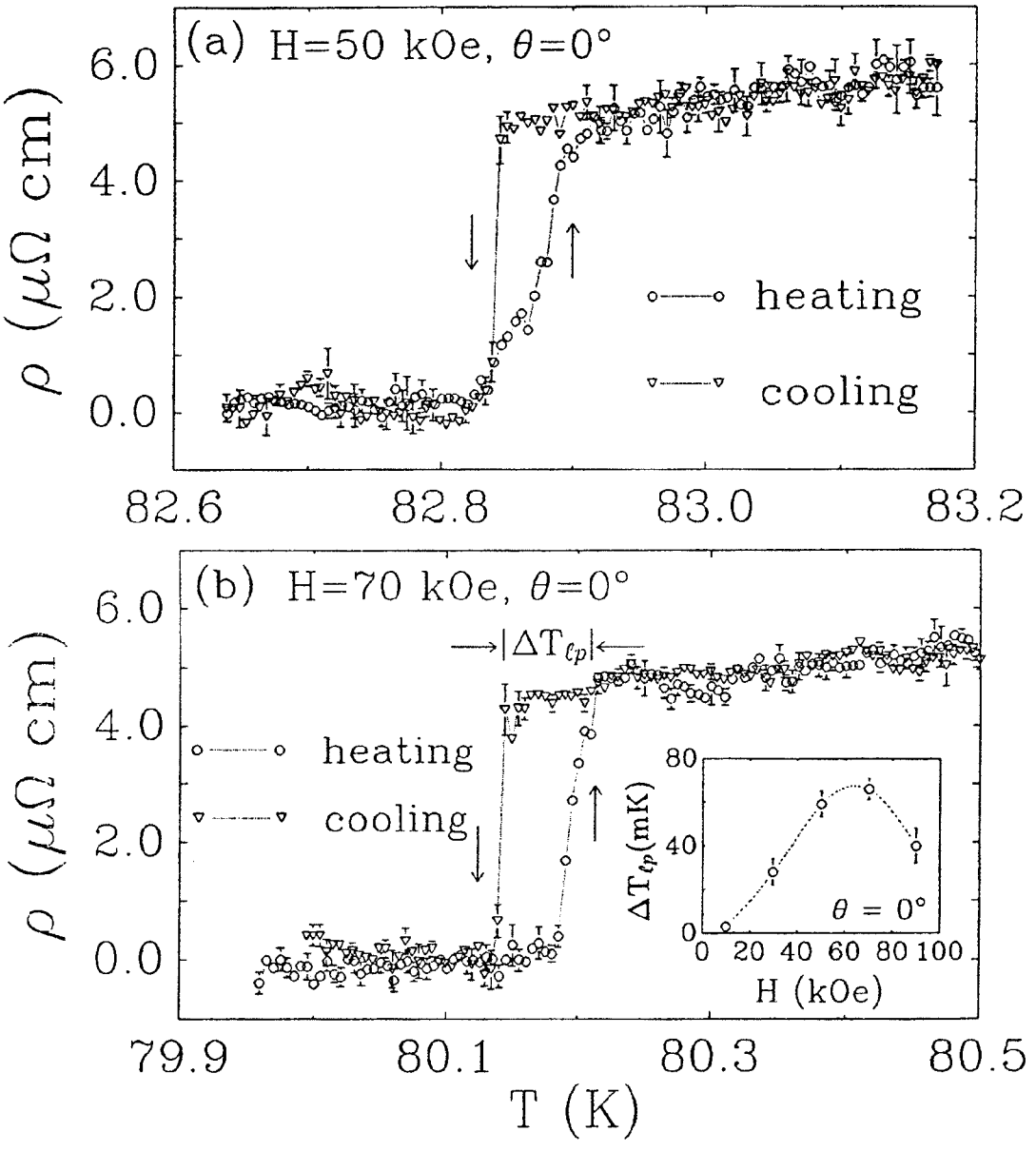

Figure 6.7: Representative data of the resistive hysteresis ρ as a function of temperature T. **(a)** $H = 50$ kOe and $\theta = 0°$. (b) $H = 70$ kOe and $\theta = 0°$. The inset shows the temperature width of the hysteresis $\Delta T_{\ell p}$ as a function of the magnetic field H.

et al., (1993), then a partial heating and cooling cycle which follows the history of $A \rightarrow B \rightarrow C \rightarrow A$ would result in a subloop indicated by the dashed line. The reason is during the cooling process from T_B to T_A, the liquid regions have to dissipate excess latent heat before complete solidification. Therefore the resistivity would not immediately reduce to that of the heating process $A \rightarrow B$. Similarly, for a partial cooling and heating cycle following the history of $A' \rightarrow B' \rightarrow C' \rightarrow A'$, a subloop indicated by the dashed line is expected, because once some liquid regions solidified, they would not melt immediately upon the heating process $B' \rightarrow C'$. However, our experimental data for all H and θ do not show any evidence of subloops, as exemplified in Fig. 6.8 for $H = 50$ kOe and $\theta = 0°$.

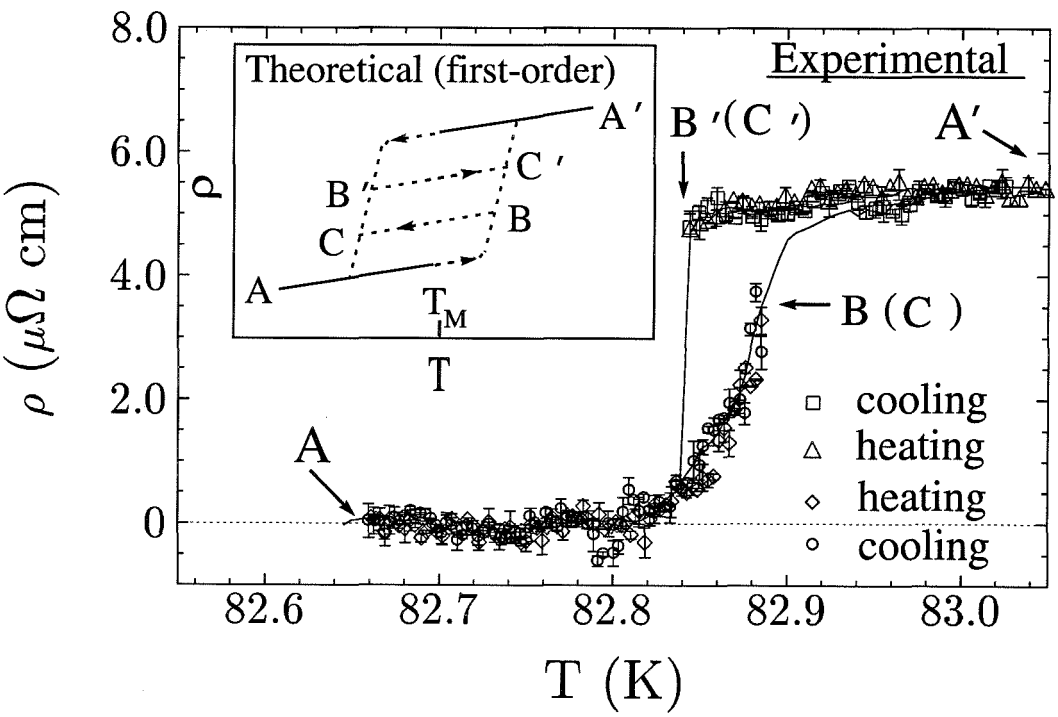

Figure 6.8: History and time-dependence of the resistivity hysteresis. The solid curves are the experimental data given in Fig. 6.7(a), and the data points shown are taken for partial heating and cooling cycles. The inset is a schematic hysteresis and the corresponding subloops based on the assumption of a first-order phase transition.

Next we consider the time dependence of the hysteresis. If the hysteresis is associated with the conventional superheating and supercooling, when the system is

warmed up from T_A to T_B and kept at T_B for a sufficiently long time, a larger area of the vortex-solid melts, so that the resistivity at T_B increases with increasing time. Similarly, if one follows the supercooling curve $A' \rightarrow B'$ and keeps the system at $T_{B'}$ for a long time, the resistivity decreases with increasing time because larger regions of the liquid solidify. Similar time-dependent resistivity is also expected for a "first-order glass transition" in systems with a broad distribution of metastable states (Geshkenbein *et al.*, 1993), because the longer vortices stay in the glass state, the lower-energy metastable states they fall into, giving rise to smaller resistivity with increasing time. However, all experimental data taken at T_B and $T_{B'}$ for various scans and with wait times ranging from 1 to 10^3 sec show no visible changes in the resistivity. The lack of time-dependence again suggests that the hysteresis is not directly related to the latent heat. It is worth noting that a weakly time-dependent *c-axis* resistive hysteresis has been reported previously (Charalambous *et al.*, 1993) on a *twinned* $YBa_2Cu_3O_7$ single crystal with a different experimental configuration of $\vec{J} \parallel \hat{c}$ and $\vec{H} \parallel ab$-plane. The difference in the samples (a twinned crystal by Charalambous et al. (1993) vs. an untwinned crystal in this work), as well as the complications involved in the c-axis conduction of the anisotropic superconducting system, make it difficult to directly compare the observation by Charalambous et al. (1993) with those described in this work.

One possible explanation for the absence of subloops and time dependence could be that the hysteresis width is not directly proportional to the latent heat and the latent heat associated with the first-order vortex-solid melting may be so small that its effect is hard to be observed experimentally. In that case, the resistive hysteresis could be due to effectively overheating the vortex-liquid with an applied current during the cooling cycle, so that vortices "supercooled" to a temperature below the first-order melting transition temperature, as suggested by Koshelov and Vinokur ((Koshelov & Vinokur, 1994). However, this assumption would have led to a hysteresis width independent of the orientation of the applied field (Vinokur, private communications), which is inconsistent with the distinct angular dependence of the hysteresis observed in our experiments which is detailed below. Thus, to our knowledge, none of the

theoretical works by Hetzel et al. (1992), Geshkenbein et al. (1993) and Koshelov and Vinokur (1994) can conclusively address the issue of first-order phase transtions in a clean vortex system.

Angular Dependence

In addition to investigating the subloops and time dependence, it is also important to understand the anisotropic behavior of the resistive hysteresis. According to the first-order glass transition model (Geshkenbein *et al.*, 1993), the latent heat absorbed during the melting process is proportional to T_M. Since T_M increases with increasing θ in $YBa_2Cu_3O_7$ single crystals, one expects $\Delta T_{\ell p}$ to also increase with θ if $\Delta T_{\ell p}$ is proportional to the latent heat. However, as shown in Fig. 6.9, $\Delta T_{\ell p} \to 0$ as $\theta \to 90°$, contrary to the expected increasing $\Delta T_{\ell p}(\theta)$. Such angular dependence cannot be straightforwardly explained by the first-order melting model.

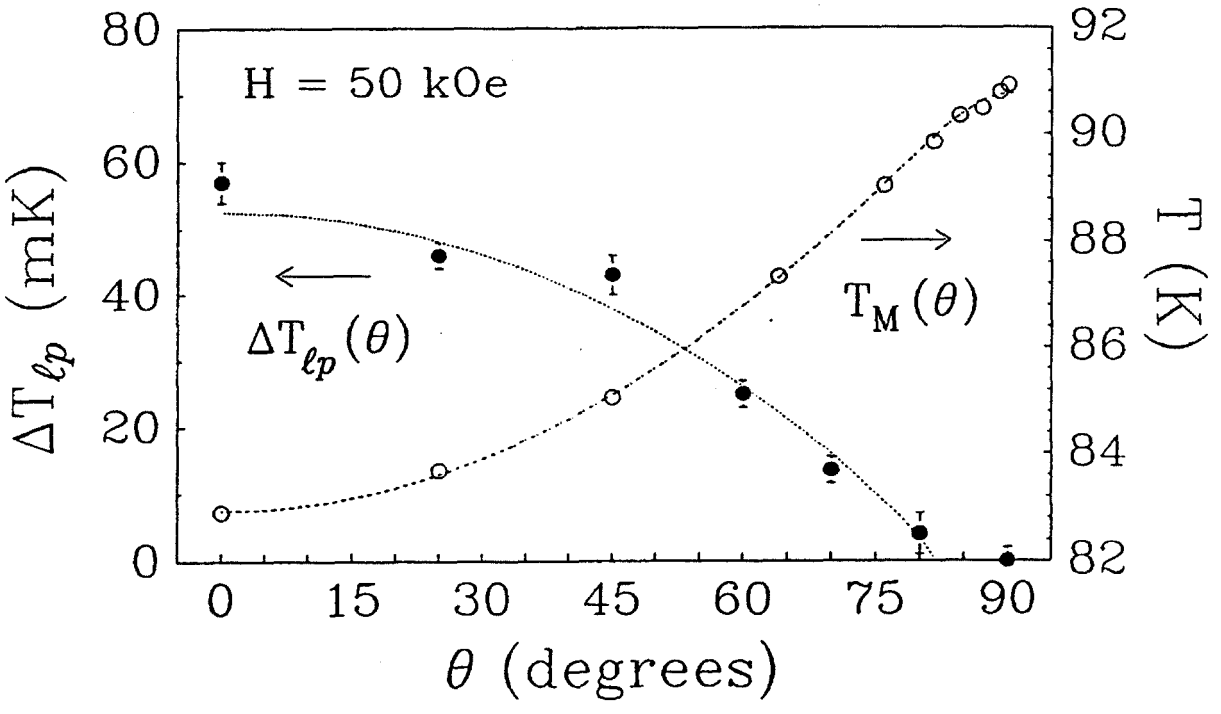

Figure 6.9: The angular dependence of the resistive hysteresis width $\Delta T_{\ell p}(\theta)$ and the melting temperature $T_M(\theta)$ for $H = 50$ kOe. The dotted line is the theoretical fitting for the angular dependent $\Delta T_{\ell p}(\theta)$ by using Eq.(6.9), and the dashed line is the fitting for the angular dependent $T_M(\theta)$ by using Eq.(6.10).

Frequency Dependence

To find out whether pinning is responsible for the above experimental observation, we perform frequency dependent measurements of $\Delta T_{\ell p}$ by applying AC transport currents to the sample. Figure 6.10 shows $\Delta T_{\ell p}$-vs.-f data for $\theta = 0°$ and $H = 50$ and 70 kOe. We note that the data does not follow the typical frequency dependence for a vortex energy barrier $U \sim k_B T \ln[1/(2\pi f \tau)]$, if $\Delta T_{\ell p} \propto U$ is assumed, and τ is a characteristic relaxation time (van der Beek *et al.*, 1993). Instead, $\Delta T_{\ell p}$ is nearly independent of the frequency up to $f \approx 3 \times 10^4$ Hz and then decreases rapidly until $f \sim 10^6$ Hz.

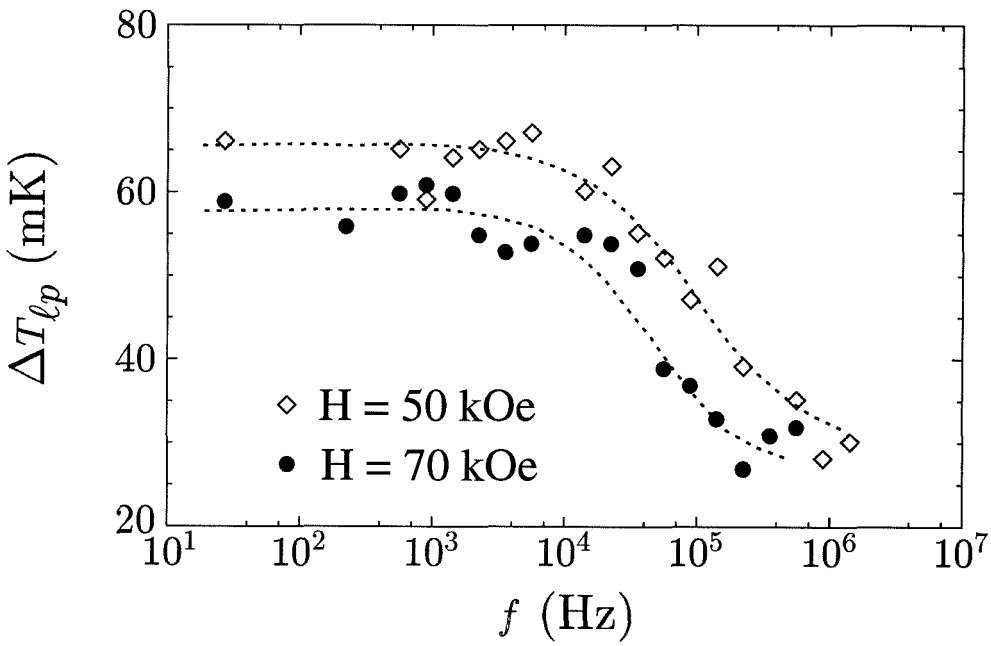

Figure 6.10: The frequency dependence of the hysteresis width $\Delta T_{\ell p}(f)$ for $\theta = 0°$, $H = 50$ and 70 kOe.

Current Voltage Characteristics for H$\|$ c−axis

Another important issue to be addressed is the sharpness of the resistive transition. We find that although the resistive transition for $\theta = 0°$ and $H \geq 10$ kOe is always very sharp, typically within $< 10^{-1}$ K, the linear resistivity near the onset becomes more gradual with increasing θ. In particular, for data taken at $\theta = 90°$ and for all

fields, the onset of resistivity is such that the current-voltage characteristics follow the critical scaling behavior for a second-order XY-like transition (Yeh *et al.*, 1993a; Reed *et al.*, 1993), consistent with recent experimental observation (Kwok *et al.*, 1994b) and the theoretical interpretation of a smectic crystal to vortex-liquid transition near $\theta \approx 90°$ (Balents & Nelson, 1994).

6.2.2 Possible Origin of the Hysteresis—Current-Induced Non-Equilibrium Effect

In view of all the experimental results given above, we propose a current-induced non-equilibrium effect as a possible scenario for the occurrence of resistive hysteresis. Suppose that the untwinned samples are nearly free of defects so that the pinning potential (U_p) is less significant than the elastic energy near the vortex-solid melting temperature T_M. As the sample is cooled down from the vortex-liquid state and a current is applied for resistive measurements, vortices are continuously driven by the Lorentz force until the local shear elastic modulus c_{66} becomes finite. The shear energy per flux line below T_M can be expressed by $U_s = c_{66}\xi_s^2 L_c$ (Geshkenbein *et al.*, 1993), where c_{66} is the shear modulus, ξ_s the superconducting coherence length, and L_c the longitudinal vortex correlation length. We note that $c_{66} = 0$ at T_M, although the total elastic energy is still finite due to the finite tilt energy ($c_{44} \neq 0$). This definition is different from the conventional one (Brandt, 1977) which asserts $c_{66} \neq 0$ until $H_{c2}(T)$, so that the presence of a vortex-liquid state is implicitly neglected. Since vortices are moving with an initial velocity v upon cooling, where $v \propto J$ is the flux-flow velocity, the onset of finite c_{66} would not be sufficient to impede the vortex motion immediately. Thus, the system "supercools" until U_s exceeds the work (W) done by the Lorentz force. That is,

$$U_s = c_{66}\xi_s^2 L_c \approx W = (J - J_c)\Phi_0 \xi_s L_c \qquad \text{at } T = (T_M - \Delta T_{\ell p}), \tag{6.7}$$

where Φ_0 is the flux quantum, and J_c is the critical current density. Once $U_s \geq W$, the

resistivity begins to drop precipitously. On the other hand, if the system is warmed up from the vortex-solid state, the initial vortex velocity is smaller than the flux-flow velocity, so that the resistivity (which is proportional to v) increases smoothly and stays below that of the cooling curve until $U_s \to 0$.

Field and Angular Dependence

To test our scenario quantitatively, consider the following expression for the shear modulus

$$c_{66}(T \leq T_M, H) = c_{66}^0(H)\,[1 - (T/T_M(H))]^{\nu_s}\,, \tag{6.8}$$

where $\nu_s > 0$ so that $c_{66} = 0$ at T_M, and $c_{66}^0(H)$ as well as ν_s are to be determined empirically. Thus, $\Delta T_{\ell p}$ can be derived from Eqs.(6.7) and (6.8), which yields:

$$\Delta T_{\ell p}(H,\theta) = T_M(H,\theta)\left\{\frac{[J - J_c(\theta)]\Phi_0}{c_{66}^0(H,\theta)\xi_s}\right\}^{1/\nu_s}. \tag{6.9}$$

To obtain the angular dependent quantities $T_M(H,\theta)$, $\xi_s(T_M(H,\theta))$ and $c_{66}^0(H,\theta)$, let us first consider the empirical relation $H_M(T) = H_M^0|1 - (T/T_c)|^{2\nu_0}$. Combining this temperature dependence with the anisotropic property $H_M(\theta) = \varepsilon_\theta^{-1} H_M(0°)$ (Blatter *et al.*, 1994), we obtain

$$T_M(H,\theta) = T_c[1 - (H\varepsilon_\theta/H_M^0)^{1/(2\nu_0)}]. \tag{6.10}$$

Here $\varepsilon_\theta \equiv \sqrt{\cos^2\theta + \varepsilon^2 \sin^2\theta}$ and $\varepsilon^{-2} \approx 60$ is the mass anisotropy ratio (Beck *et al.*, 1992). Similarly, since $\xi_s^2(T) = \xi_s^2(0)|1 - (T/T_c)|^{-1}$, we can employ Eq. 6.10 to yield the angular dependence for ξ_s:

$$\xi_s(T_M(H,\theta)) = \xi_s(0)\left(\frac{H\varepsilon_\theta}{H_M^0}\right)^{-1/(4\nu_0)}. \tag{6.11}$$

The angular dependence of c_{66}^0 is given by the hard-axis shear modulus of the vortex-

lattice (Kogan & Campbell, 1989; Blatter *et al.*, 1992; Blatter *et al.*, 1994)

$$c_{66}^{0}(H,\theta) = \varepsilon_{\theta}^{-1} c_{66}^{0}(H,0°), \tag{6.12}$$

because $\vec{J} \perp \vec{H}$ and $\vec{J} \perp \hat{c}$ for all θ so that the Lorentz force is always along the hard axis. By inputting Eqs. (6.10) to (6.12) into Eq. (6.9) and using the approximation $J_c(\theta) = \varepsilon_{\theta}^{-1} J_c(0°)$, Eq. (6.9) can be expressed for $\theta = 0°$ as the following:

$$\Delta T_{\ell p}(H,0°) = T_M(H,0°) \left\{ \frac{[J - J_c(0°)]\Phi_0}{c_{66}^{0}(H,0°)\xi_s(T_M(H,0°))} \right\}^{1/\nu_s}. \tag{6.13}$$

For a constant field H_1, Eq. (6.9) yields:

$$\Delta T_{\ell p}(H_1,\theta) = T_M(H_1,\theta) \left\{ \frac{[J - J_c(0°)/\varepsilon_\theta)]\Phi_0}{(c_{66}^{0}(H_1)/\varepsilon_\theta)\xi_s(T_M(H_1,\theta))} \right\}^{1/\nu_s}. \tag{6.14}$$

By simultaneously applying Eqs.(6.13) and (6.14) to the $\Delta T_{\ell p}$-vs.-H data for $\theta = 0°$, and the $\Delta T_{\ell p}$-vs.-θ data for $H = 50$ kOe, we obtain the fitting parameter $\nu_s \approx 1.3$ and an empirical functional form for $c_{66}^{0}(H,0°)$ shown in the inset of Fig. 6.11 which satisfies both the field and angular dependence of $\Delta T_{\ell p}$. The resulting curves of $\Delta T_{\ell p}(\theta = 0°)$-vs.-$H$ and $\Delta T_{\ell p}(H = 50\text{kOe})$-vs.-$\theta$ are shown by the solid line in Fig. 6.11 and the dotted curve in Fig. 6.9, respectively. Both semi-empirical fittings are in good agreement with our data. We note that for $H \leq 70$ kG, $\Delta T_{\ell p}$ increases with H, indicating a decreasing $c_{66}^{0}(H,0°)$ which is consistent with a decreasing superconducting order parameter and therefore smaller elasticity (Brandt, 1977). However, our observation of decreasing $\Delta T_{\ell p}$ for $H > 70$ kG and the report by Safar et al. (1992a; 1992b) of $\Delta T_{\ell p} \to 0$ at $H >\sim 100$ kG suggest an increase in either c_{66}^{0} or J_c above $H \sim 100$ kG. This finding may be attributed to the increasing importance of pinning when the flux line separation in higher fields becomes comparable to the average distance between point defects (Safar *et al.*, 1992a; Safar *et al.*, 1992b). However, this issue still awaits further theoretical investigations.

The input parameters for the fitting curves in Figs. 6.9 and 6.11 are summa-

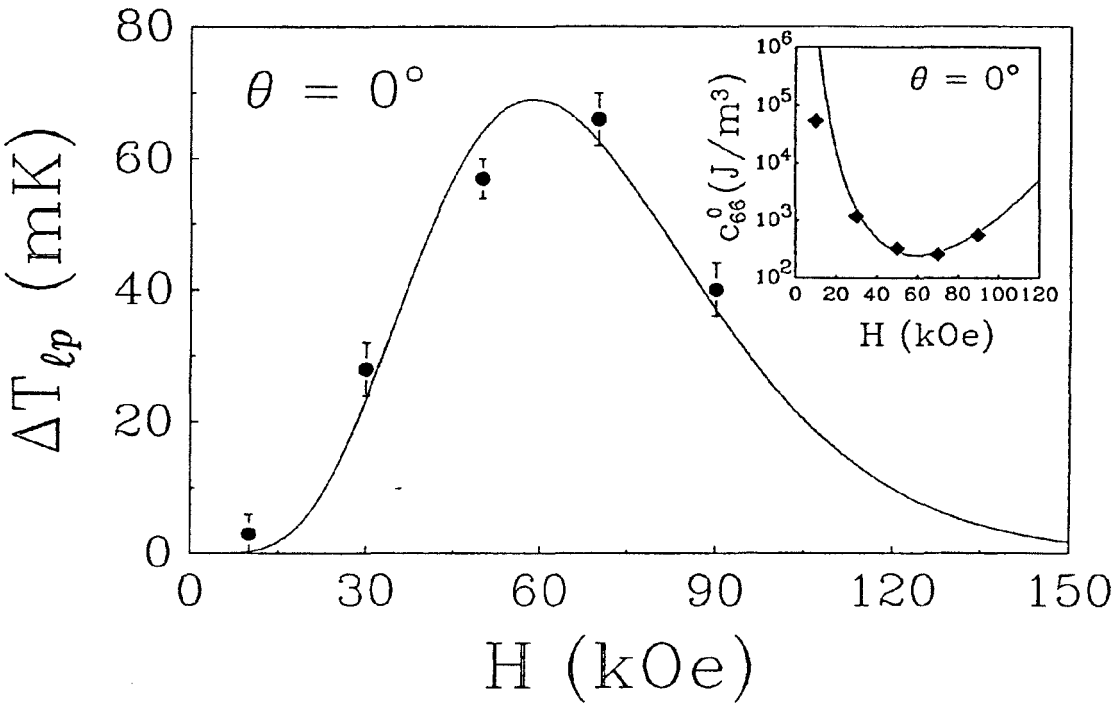

Figure 6.11: The theoretical fitting for the $\Delta T_{\ell p}(H, 0°)$-vs.-H data with the use of Eq.(6.9) is represented by the solid line. The inset shows the fitting curve of $c_{66}^0(H, 0°)$-vs.-H.

rized in Table 6.2, where H_M^0 and ν_0 are obtained from fitting the melting transition temperatures (T_M) as a function of the magnetic field, $\xi_s(0) = 20\text{Å}$ is the typical value for the superconducting coherence length in the ab-plane for $YBa_2Cu_3O_7$, and $J_c(0^{circ}) = 0.2J$ with $J = 0.27$ A/cm^2 the applied current density is an approximation for a weak pinning system.

Current Dependence

Another stringent test for our model is to consider the current dependence of $\Delta T_{\ell p}$. If the applied current density is too high, vortex motion occurs well below the thermodynamic melting temperature T_M. Therefore the condition $U_s \approx W$ in Eq.(6.7) cannot be satisfied near T_M, the resistive transition broadens and hysteresis vanishes. On the other hand, if the applied current density is so small that $(J - J_c)\Phi_0 \ll c_{66}^0 \xi_s$, then $\Delta T_{\ell p} \to 0$ according to Eq.(6.9). It is therefore not surprising that the anisotropic

Table 6.2: Input parameters used for obtaining $c_{66}^0(H, 0°)$ and ν_s.

H_M^0 (Tesla)	ν_0	ξ_0 (Å)	$J_c(0°)/J$
50	0.7	20	0.2

hysteresis width $\Delta T_{\ell p}$ decreases rapidly when $\theta \to 90°$, because both $c_{66}^0(\theta)$ and $J_c(\theta)$ increase substantially. Another corollary of our model is that for comparable values of $(J - J_c)\Phi_0$ and $(c_{66}^0 \xi_s)$, the cooling branch of the resistivity would move slightly towards lower temperatures with increasing J, because vortices had to "supercool" more to compensate for the larger driving force of the currents. This argument predicts an increase in $\Delta T_{\ell p}$ with a small increase of J according to Eq.(6.9), and is confirmed by the data in Fig. 6.12 for three different current densities $J = 0.27$, 2.70 and 9.99 A/cm^2 and for $H = 70$ kG. Similar results for $H = 50$ kG and $J = 0.27$, 9.99, 16.55 A/cm^2 are also shown in the inset of Fig. 6.12. We note that for both magnetic fields, the heating branches broaden with increasing J, in contrast to the nearly constant width of the cooling branches. Furthermore, the temperatures where the heating curves begin to increase rapidly remain the same for all current densities, whereas those for the cooling curves *decrease* with increasing J. Thus, $\Delta T_{\ell p}$ increases with J, qualitatively consistent with Eq.(6.9) and the report by Kwok et al. (1994a) as shown in Fig. 6.13.

Since it appears that an opposite current dependence was reported by Safar et al. (1992a) and Charalambous et al. (1993), this issue requires further discussions. Let us first compare the data by different research groups. In the studies by Safar et al., no hysteresis data with currents between 5 μA and 1 mA has ever been shown. As shown in Fig. 6.6, their data at 1 μA for $H = 60$ kOe shows a maximum hysteresis width which is no more than a half of the widths observed in our data for either $H = 50$

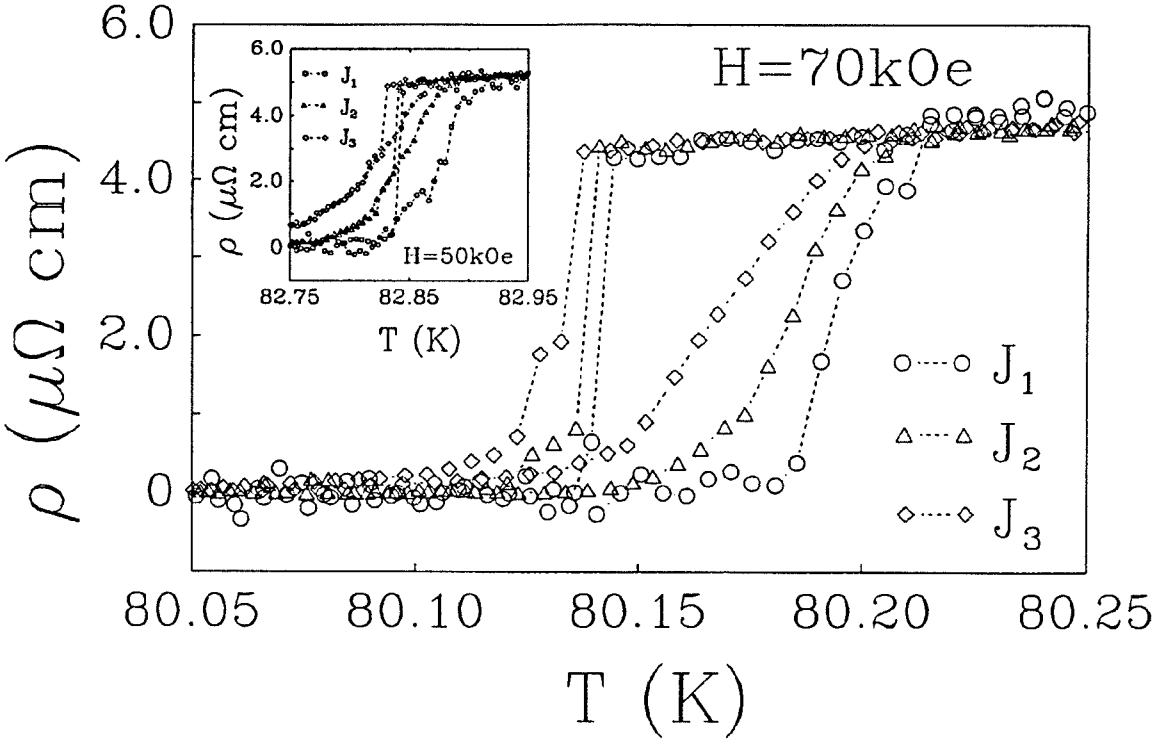

Figure 6.12: The current dependence of the resistive hysteresis for $H = 70$ kOe and $\theta = 0°$ is shown for three different current densities $J_1 = 0.27$ A/cm^2, $J_2 = 2.70$ A/cm^2 and $J_3 = 9.99$ A/cm^2. The inset shows similar results for $H = 50$ kOe, $\theta = 0°$ and $J = J_1$, J_3, $J_4(= 16.55$ A/cm^2).

kOe or $H = 70$ kOe. In addition, the shape of the hysteresis loop in Fig. 6.6, similar to that obtained by Charalambous et al. (1993), is very different from ours shown in Fig. 6.7 and that by Kwok et al. shown in Fig. 6.13. The broadness of the transition in the data by Safar et al. is indicative of the presence of large scale inhomogeneities in the sample. In fact, we note that the current density used by Safar et al. (1992a) (~ 0.015 A/cm^2) is the lowest, comparing to our lowest current density of 0.27A/cm^2 and that of 1A/cm^2 used in the studies by Kwok et al. (1994a). If we consider the finite size effect associated with the sample thickness ($\ell \sim 0.020$ mm), and noting that the thickness is comparable for our sample and the sample used by Safar et al. (1992a), the current density below which surface pinning prevails can be given (see Chapter 3) by $J_\ell(T_M) = (k_B T_M/(\ell^2 \Phi_0) \sim 0.13$ A/cm^2 at a melting temperature of 80 K. Therefore, the broadness of the transition shown in Fig. 6.6 by Safar et al. may

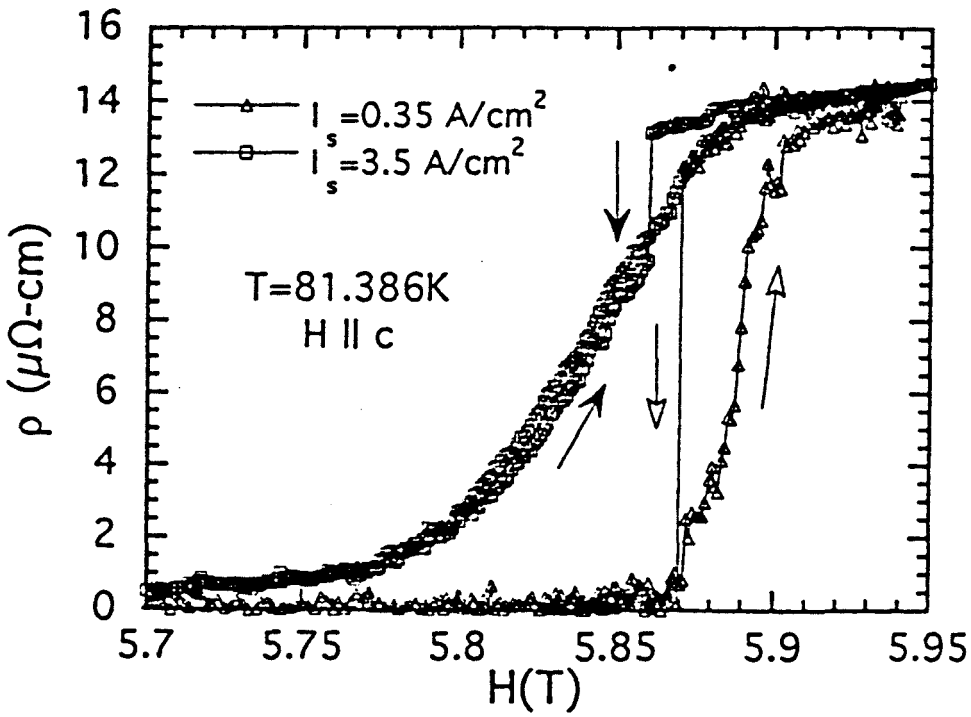

Figure 6.13: The current dependence of the hysteresis width in resistivity versus field data by Kwok et al. (1994a).

have been the result of inhomogeneities on the scale of the sample thickness. Note also that the smallest dimension of the sample used by Kwok et al. (1994a) is much larger (0.08 mm). Therefore their data shall not be affected by the finite size effect.

Next, let us consider the current effect. As shown from both our data and that by Kwok et al. (see Fig. 6.13), with increasing current, the heating curve becomes broadened but the temperatures (or the fields) at which the resistance drops abruptly upon cooling shift to lower temperatures in our experiment and to lower fields in the work by Kwok et al. (1994a). In addition, the broadening of the heating curve is more significant than the increase of the hysteresis width at the top of the transition. With an overall broad transition ("background" of the sharp transition part) to start with in the work by Safar et al. (1992a) (see Fig. 6.6), it is very likely that the observed "decreasing" hysteresis width with the increasing current is only an artifact due to the broadening of the background. The same explanation can be applied to the observation by Charalambous et al. (1993).

Our scenario of current-induced nonequilibrium effect may also be applicable to the frequency dependence of $\Delta T_{\ell p}(f)$ in Fig. 6.10, because c_{66} becomes effectively "stiffer" with the increasing frequency of the AC current, so that $\Delta T_{\ell p}$ decreases. However, quantitative understanding of the frequency dependence requires better knowledge of the dispersion relation for $c_{66}(f)$. Finally, we notice the importance of small J_c, small ξ_s and high T_M for the occurrence of resistive hysteresis. The latter two conditions are unique features of high-temperature superconductors, and the first is unique for weak-pinning samples such as untwinned $YBa_2Cu_3O_7$ single crystals.

6.2.3 Discussions

Although the proposed current-induced non-equilibrium effect can successfully explain qualitatively the magnetic field, current, frequency and angular dependence of the resistive hysteresis in untwinned $YBa_2Cu_3O_7$ single crystals, it is important to realize that this model does not distinguish whether the vortex-solid melting transition is first or second-order. The only conclusions we can draw from the investigations are that vortices are weakly pinned, and that the resistive hysteresis occurs below the thermodynamic melting temperature. The hysteresis itself is neither a sufficient nor a necessary condition for a first-order melting transition, and its width is not directly related to the latent heat. Although the weak pinning and sharp resistive transition in the vortex state of untwinned $YBa_2Cu_3O_7$ single crystals are very suggestive of a first-order melting transition, this issue can only be unambiguously settled with measurements of thermodynamic quantities such as specific heat or magnetization.

Finally, we notice that our interpretation for the resistive hysteresis is qualitatively consistent with recently developed theory by Koshelov and Vinokur (1994). According to this theory, the presence of an applied current could enhance the effective temperature of vortices, and therefore upon cooling, the melting occurs at a lower temperature. However, as stated earlier, this model cannot account for the angular and frequency dependence of our data. Consequently, more quantitative comparisons await further investigations.

6.3 Nonlinear Resistive Peak Effect due to Vortex-Solid Softening in Untwinned $YBa_2Cu_3O_7$ Single Crystals

In addition to the resistive hysteresis which has been attributed to an current-induced non-equilibrium effect in the weak pinning limit, another current-induced phenomena, the "peak effect", is observed in the same untwinned $YBa_2Cu_3O_7$ single crystal. The "peak effect" refers to a peak feature in the critical current density (J_c) as a function of the temperature or magnetic field (DeSorbo, 1964; Pippard, 1969; Wstrördenweber *et al.*, 1986). Unlike the resistive hysteresis which was only recently observed in high-temperature superconducting $YBa_2Cu_3O_7$ untwinned single crystals, this peak effect has been of interest in the research of type-II superconductors since 1964. In conventional superconductors such as niobium (DeSorbo, 1964) and Nb_3Ge films (Wstrördenweber *et al.*, 1986), the peak effect has been observed just below the upper critical field H_{c2}, and has been attributed to the softening of the elastic moduli of the vortex lattice first by Pippard (Pippard, 1969) and then generalized by Larkin and Ovchinnikov (Larkin & Ovchinnikov, 1979). Recently similar peak effects have been reported in both conventional superconductors such as 2H-$NbSe_2$ single crystals (Bhattacharya & Higgins, 1993) and high-temperature superconductors such as $YBa_2Cu_3O_7$ single crystals with very few twin boundaries (Ling & Budnick, 1991; Kwok *et al.*, 1994c) or completely untwinned (D'Anna *et al.*, 1994). One common factor among all these superconductors is that they are all extremely type-II superconductors with a large Ginzburg-Landau parameter $\kappa \gg 1$. In addition, it is believed that all these observations occur just below the vortex-solid melting temperature T_M, which is sufficiently away from the upper critical field line (Larkin *et al.*, 1994). These results suggest that in extreme type-II superconductors, the shear modulus c_{66} goes to zero at T_M (Nelson & Seung, 1989; Jiang *et al.*, 1995; Larkin *et al.*, 1994) due to the rapid softening of the vortex lattice. In this section, quantitative analysis the nonlinear resistive peak effect will be given based on the

transport measurements of untwinned $YBa_2Cu_3O_7$ single crystals.

6.3.1 Experimental Observations

The peak effect is mostly investigated by various DC transport measurements. The DC current-voltage characteristics are measured using a standard four-terminal method. The measurements are performed in applied magnetic fields (H) from 1 to 90 kOe and for angles (θ) from 0° to 90°. The applied current density $\vec{J}$ is always transverse to $\vec{H}$ and $\vec{J} \parallel \hat{a}$. The resistivity defined as $\rho \equiv E/J$ is obtained from the electric field versus current density (E-vs.-J) isotherms. Illustrated in Fig. 6.14 are the temperature-dependent resistivity curves near the vortex solid melting transition for different applied currents. For $J <\sim 15\text{A/cm}^2$, the ρ-vs.-T curves exhibit hysteretic behavior upon cooling and heating, as reported in the previous sections. However, for current densities $J >\sim 15$ A/cm^2, the hysteretic behavior disappears, and a resistive peak occurs and becomes more pronounced with increasing J until $J \sim 240\text{A/cm}^2$. We note that a "dip" in the resistivity occurs at temperatures lower than the thermodynamic vortex-solid melting temperature T_M, which corresponds to the occurrence of a peak in the critical current density. The nonlinear vortex response near the peak region is further illustrated by the current-voltage characteristics shown in Fig. 6.15 for the E-vs.-J isotherms taken with $H = 50$ kOe and $\vec{H} \parallel \hat{c}$. We note that the temperature interval within which the current-dependent resistive peaks occur (see Fig. 6.14)) corresponds to the occurrence of nonlinear E-vs.-J isotherms in Fig. 6.15. A summary of our measurements which exhibit the resistive peak effect is given in Table 6.3. We note that for field along the c-axis, the peak effect always exists if $H \leq 90$ kOe. On the other hand, for field in ab plane the peak effect can be observed only if 10 kOe $\geq H \leq 90$ kOe.

6.3.2 Quantitative Analysis of E-vs-J Characteristics

To attain a better understanding of the E-vs.-J characteristics, we notice the curvature of the nonlinear E-vs-J isotherms at low temperatures is suggestive of a

Table 6.3: Summary of "Peak Effect" Data

H(kOe)	θ	Peak Effect
1.0	0°	yes
1.0	90°	no
3.0	0°	yes
3.0	90°	no
5.0	0°	yes
5.0	90°	no
6.0	0°	yes
6.0	10°	yes
6.0	45°	yes
6.0	90°	no
10.0	0°	yes
10.0	90°	yes
50.0	0°	yes
50.0	90°	yes
90.0	0°	yes
90.0	90°	no

vanishing resistivity as $J \rightarrow 0$. Such nonlinearity is consistent with the bundle-hopping resistivity of vortices proposed by the collective flux-creep model (Blatter *et al.*, 1994; Feigel'man *et al.*, 1989),

$$\rho(T,J) = \rho_0(T) exp\left[-\left(\frac{J_0(T)}{J}\right)^{\mu}\right], \tag{6.15}$$

where J_0 is a characteristic current density, and μ is a positive exponent. Applying Eq.(6.15) to our data, we find that the resistivity agrees well with the collective flux-creep model with a fixed μ value and two temperature dependent fitting parameters $\rho_0(T)$ and $J_0(T)$. As a demonstration, three representative E-vs-J fitting curves are plotted as solid lines in Fig. 6.16 together with the original data points. In addition, the solid lines in Fig. 6.14 are also fitting curves to the $\rho(T,J)$-vs-T data with Eq.(6.15). The μ values are found to be increasing with the increasing field, as shown in the inset of Fig. 6.16 for the results for both $\vec{H} \parallel \hat{c}$ and $\vec{H} \perp \hat{c}$. This increase of μ is consistent with the collective flux creep model as the vortex bundles become smaller in higher fields. In fact, all the μ values obtained experimentally fall between the theoretical values 7/9 for large vortex bundles hopping and 5/2 for small vortex bundles hopping (Blatter *et al.*, 1994).

In addition to the physical significance of the μ-values, we note that $\lim_{J \gg J_0} \rho \rightarrow \rho_0(T)$ according to Eq.(6.15), and the fitting result of ρ_0 has a similar but much weaker temperature dependence than that of ρ. The characteristic current density $J_0(T)$ shows a distinct peak at the dip of the resistivity, and therefore is analogous to the behavior of the critical current density J_c (Kwok *et al.*, 1994c). To make a direct comparison between J_0 and J_c, we employ the common criterion $E(J_c) = 10\mu\mathrm{V/cm}$ for deriving J_c. The resulting temperature dependence of the $J_c(T)$ curves are consistent with that of $J_0(T)$, although we believe that J_0 is a more intrinsic quantity.

6.3.3 Vortex Dissipations Near the Peak Region

It is worthwhile comparing the temperature dependence of the current-independent quantities $\rho_0(T)$ and $J_0(T)$ (or $J_c(T)$). As shown in Fig. 6.17, the characteristic cur-

rent dencity $J_0(T)$ first decreases with the increasing temperature, then begins a sharp upturn at the onset of a "viscoelastic motion temperature" T_{ve} where $\rho(T)$ is at locat maximum values, reaching a peak value at the "fluctuation temperature" T_{fl} where both $\rho_0(T)$ and $\rho(T)$ dip to a local minimum, and finally decreases rapidly to zero at approxiamtely the htermodynamic temperature T_M that has been defined previously with the resistive hysteresis studies ((Jiang *et al.*, 1995)) in the small current limit ($J < 10$ A/cm^2.

Noting the correlation between the $\rho_0(T)$ and $J_0(T)$ curves as shown in Fig. 6.17, the theoretical understanding of the vortex-softening near the peak of $J_c(T \rightarrow T_M^-)$ (Larkin & Ovchinnikov, 1979; Pippard, 1969), and the fact that resistive peak effects only occur if the condition $J >\sim J_c(T)$ holds for the temperature range of interest, we propose the following phenomenological explanation for the observed resistive peak effect. Following the ρ-vs.-T and J_0-vs.-T curves in Fig. 6.17, we note that for $T < T_{ve}$, the presence of an external current density exceeding J_c gives rise to finite dissipation due to the plastic vortex motion at low temperatues. As $T \rightarrow T_{ve}$, vortex bundles with the size of the Larkin domian ((Larkin & Ovchinnikov, 1979)) becom depinned, and the resistivity $\rho(T)$ reaches a maximum. The assertion of complete depinning of vortex bundles for $J >> J_0$ is consistent with the fact that $\rho_0(T \leq T_{ve}) \approx$ constant due to the plastic motion of all vortex bundles at $T \leq T_{ve}$, as shown in Fig. 6.17(a). However, the moving vortex bundles with short-range crystalline correlations become increasingly softened due to the thermal effects. Therefore the rapidly decreasing c_{66} results in softened vortex bundles which no longer move like a rigid body, and the effective mobility for the vortex motion becaomes smaller with increasing temperature for $T < T_{ve}$. Such a "viscoelastic" motion of vortex bundles gives rise to an increase in the effective viscoelasticity and the critical current density $J_c(T)$, and therefore in this temperature region resistivity decreases with the increasing temperature.

With further increase of the temperature, thermal fluctuations become more and more important, and the root-mean-square amplitude of vortex lattice vibrations $\sqrt{\langle u^2 \rangle}$ becomes so large that the softened mobile vortex bundles begin to break apart, and resistivity rises rapidly at $T > T_{lf}$. Eventually at T_M, $\sqrt{\langle u^2 \rangle}$ exceeds the Linde-

mann criterion $c_L a_0$, where c_L and a_0 are the Lindemann constant and vortex lattice constant, respectively. At this temperature T_M a vortex-solid melting transition takes place, the resistivitycontinues to rise until the phase fluctuation effects associated with the melting transition subside and resistivity becomes current-independent at a temperature T_{lin} slightly above T_M.

By plotting in the H-vs-T diagram (see Fig. 6.18) all the characteristic temperatures T_{ve}, T_{fl} and T_{lin} for different fields, together with the thermodynamic vortex-solid melting transition line $H_M(T)$, we find that all three lines $H_{ve}(T)$, $H_{fl}(T)$, and $H_{lin}(T)$ merge to the thermodynamic melting line $H_M(T)$ in high fields, although in the low field limit the peak effect is found to occur at temperatures more than 0.5 K away from T_M. Furthermore, we note that $H_{ve}(T)$ and $H_{fl}(T)$ lines are below $H_M(T)$, whereas $H_{lin}(T)$ is above $H_M(T)$.

6.3.4 Quantitative Analysis of the Resistive Peak Effect

In order to perform quantitative analysis of the the rsistive peak effecs, we consider the quantity $\rho_0(T)$, $\lim_{J \gg J_c} \rho(T) \rightarrow \rho_0(T)$. Assuming that the saturated resistivity for $\rho_0(T \leq T_{ve})$ is proportional to the average mobility of the vortex bundles, we compare $\rho_0(T_{ve})$ with the flux-flow resistivity ρ_{ff} at the same temperature which corresponds to the complete coherent motion of all vortices if the vortex system is without either short-range elasticity or pinning. We may therefore define a parameter α_r which is the ration of the mobility of viscoelastic vortex bundles to that of the coherent-motion vortices:

$$\alpha_r = \frac{\rho_0(T_{ve})}{\rho_{ff}(T_{ve})}, \tag{6.16}$$

where ρ_{ff} is the flux-flow resistivity defined by Bardeen-Stephen model,

$$\rho_{ff}(T, \theta) = \frac{B\rho_n(T_c)}{B_{c2}(T, \theta)}, \tag{6.17}$$

with $\rho_n(T_c)$ being the normal resistivity at T_c, and $B_{c2}(T, \theta)$ defined in (Blatter *et al.*,

1994)

$$B_{c2}(T,\theta) = B_{c2}^{\|c}(0)|1 - T/T_c|/\varepsilon_\theta, \tag{6.18}$$

where $\varepsilon_\theta = \sqrt{\cos^2\theta + \varepsilon^2 \sin^2\theta}$, and ε^2 is the anisotropic factor. By using the empirical values for $\rho_0(T_{ve})$ and $\rho_n(T_c) = 25.0\mu\Omega cm$, as well as $B_{c2}(0) \approx 50\ Tesla$, and $\varepsilon^2 \approx 1/60$ (Beck *et al.*, 1992), the α_r values are obtained for different fields and angles as shown in Figs.6.19(a) and 6.19(b), respectively. The field dependence is found to be $\alpha_r \propto B^{-1/4}$. Furthermore, as shown in the inset of Fig. 6.19(b), an empirical relation

$$\alpha_r B^{1/4} = (\alpha_0 + \alpha_1/\varepsilon_\theta), \tag{6.19}$$

with $\alpha_0 = 0.22$ and $\alpha_1 = 0.084$, is found to be applicable to all the α_r values. The θ-independent contribution from α_0 may be attributed to the point-defect-like, isotropic pinning sites such as oxygen vacancies, whereas the angular-dependent contribution from the term $\alpha_1/\varepsilon_\theta$ follows the same angular dependence as some of the intrinsic anisotropic properties such as the hard-axis shear modulus c_{66}^h and the upper critical field $H_{c2}(\theta)$ (Kogan & Campbell, 1989; Blatter *et al.*, 1994). Consequently, the second contribution in Eq.(6.19) may be related to the intrinsic pinning due to the layered structure of $YBa_2Cu_3O_7$, or to the sample surfaces which can also contribute to the anisotropic pinning mechanism.

6.3.5 Effects of 3.0 MeV Proton Irradiation

The same sample is subsequently irradiated by 3.0 MeV protons with a fluence of 5×10^{15} protons/cm^2. After proton irradiation, neither peak effect at high currents (see Fig. 6.20) nor hysteresis at low currents is observed in the resistivity as a function of temperature. The corresponding E-vs.-J isotherms as shown in the inset for the representative data taken at $H_{\|c} = 50$ kOe, and are found to be mostly ohmic for the entire temperature range. It seems that a large density of point defects may have provided such strong disorder that the shear modulus is significantly hardened and the phase transition widely broadened so that the critical current peak effect due

to softening of the vortex-solid never occurs. Furthermore, the large disorder may have resulted in an effectively frozen vortex-liquid at low temperatures, and therefore ohmic resistivity is observed over the entire temperature range of interest.

6.3.6 Concluding Remarks

To summarize our studies of the nonlinear resistive peak effect in an as-grown untwinned $YBa_2Cu_3O_7$ single crystal, we have shown that the current-voltage characteristics in the temperature range where the peak effect occurs are consistent with the collective flux-creep theory. The nonlinear resistive peak effect (which appears only if $J > J_c$) is closely correlated with the peak effect in the critical current density near the vortex-solid melting transition. With the increasing temperature, the resistive peak can be described in terms of a plastic vortex motion at lower temperatures, followed by a maximum vortex dissipation due to thermally depinning of vortices, and then a decrease in dissipation due to the viscoelastic motion of softened vortex bundles, and finally a rapid rise in the dissipation when thermal fluctuations become so large that the vortex lattice eventually undergoes a melting transition. By comparing our results with various previous reports of similar observations in samples different from ours, we conclude that the peak effect in J_c is a general phenomenon in both conventional type-II and high-temperature superconductors when the vortex-solid becomes significantly softened before its melting transition. The only difference in the studies of this nearly defect-free untwinned single crystal is that the pinning mechanisms at low temperatures are attributed to two possible origins, one is the bulk pinning due to either the dilute random point disorder or the intrinsic layered structure of the superconductor, and the other is the surface pinning due to the sample boundaries.

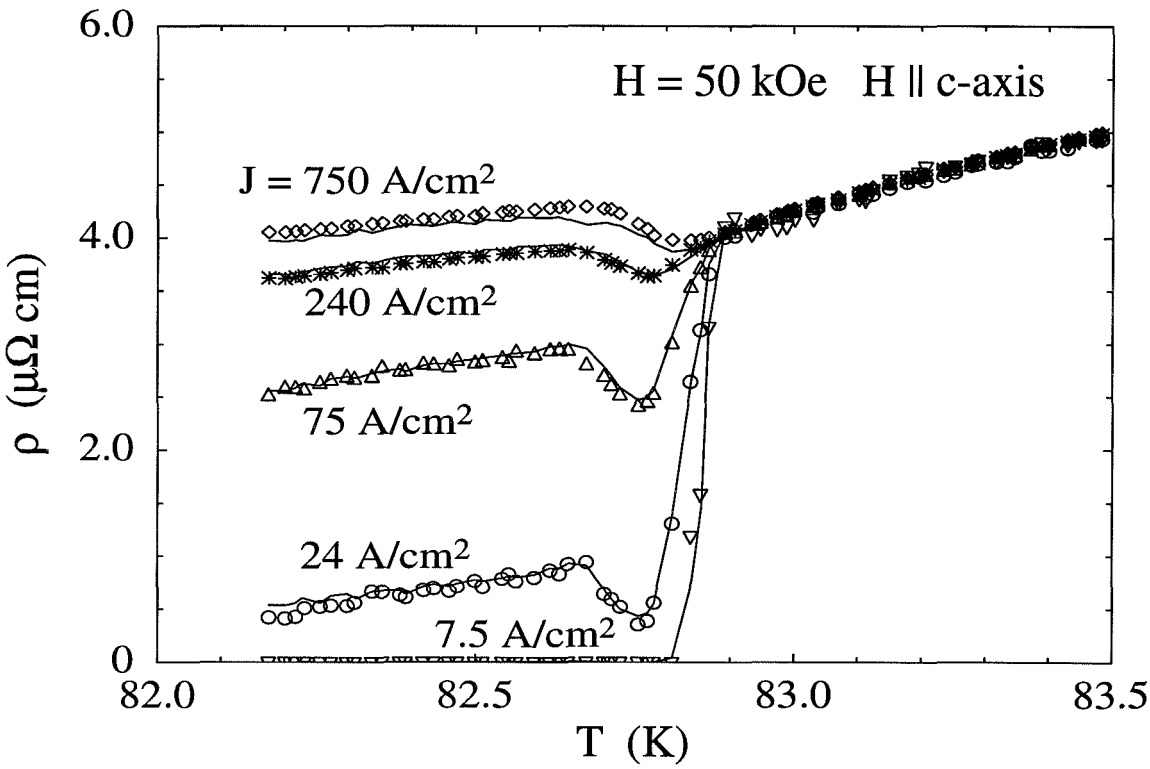

Figure 6.14: Nonlinear resistivity ρ versus temperature T curves of the as-grown untwinned $YBa_2Cu_3O_7$ single crystal taken at different current densities and for $H =$ 50 kOe, and $\vec{H} \parallel \hat{c}$.

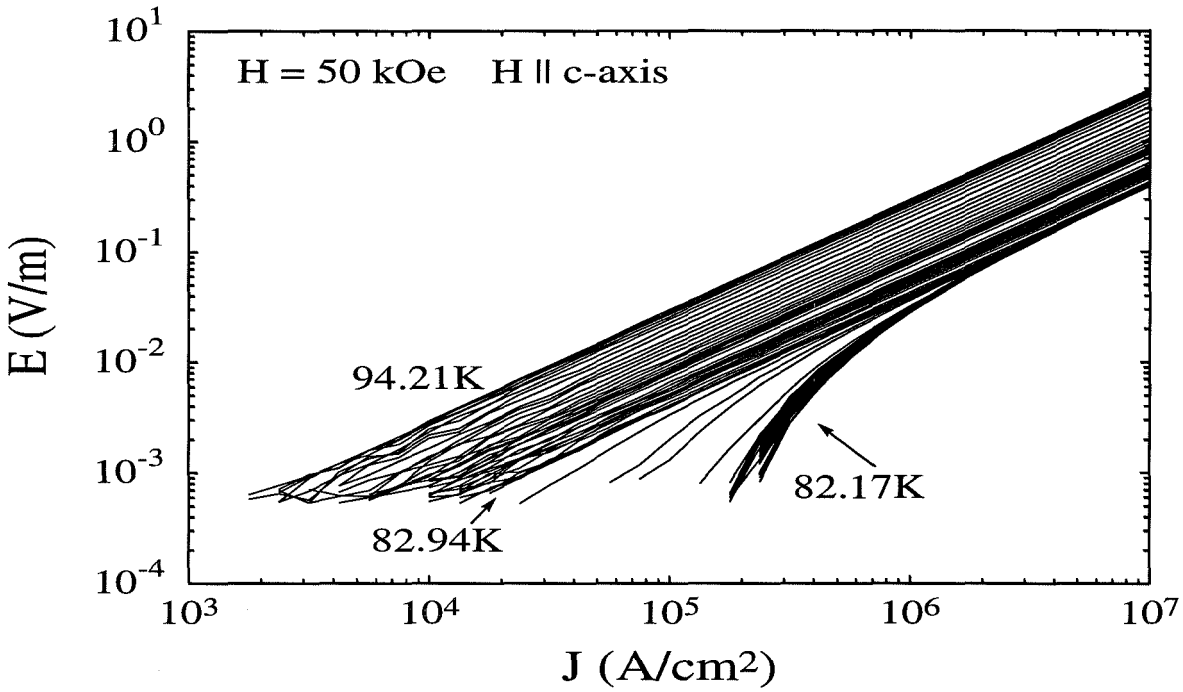

Figure 6.15: A representative set of electric field (E) versus current density (J) isotherms on the sample for $H = 50$ kOe and $\vec{H} \parallel \hat{c}$.

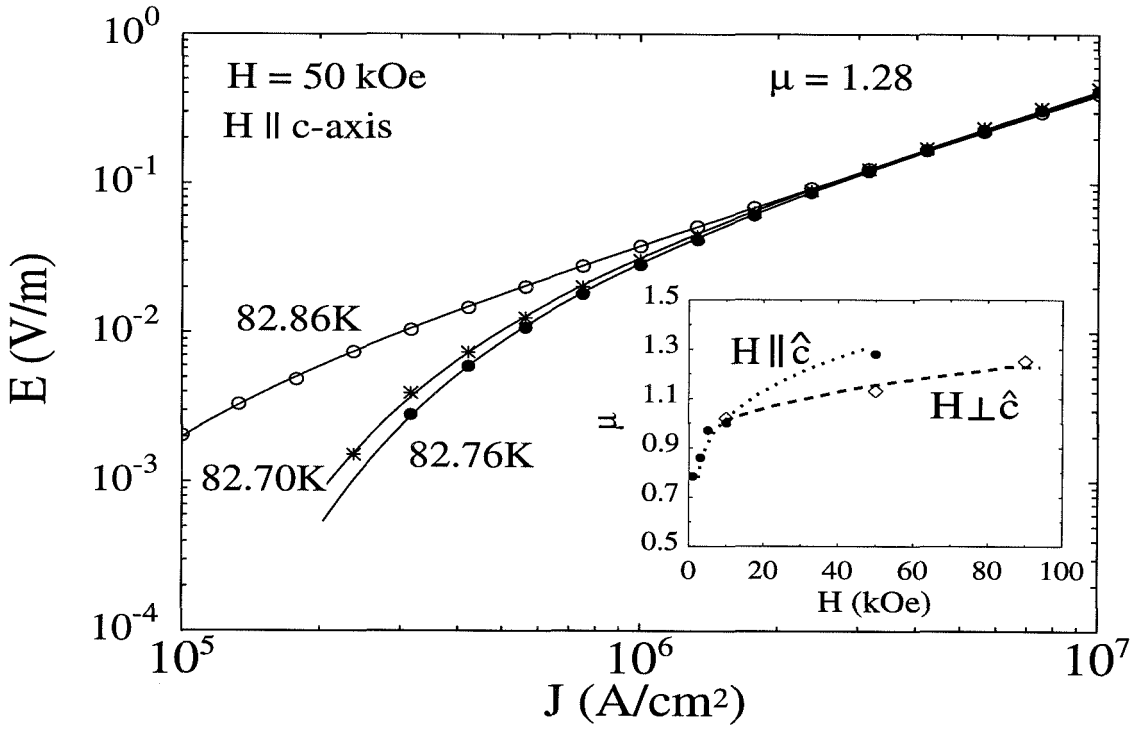

Figure 6.16: Representative theoretical fitting curves (solid lines) on the E-vs.-J isotherms with the use of the collective flux-creep model in Eq.(6.15) and a fitting parameter $\mu = 1.28$. The inset shows the μ values for different magnetic fields and orientations. We note that the range of μ values is between $\mu = 5/2$ in high fields for small bundle pinning, and $\mu = 7/9$ in low fields for large bundle pinning.

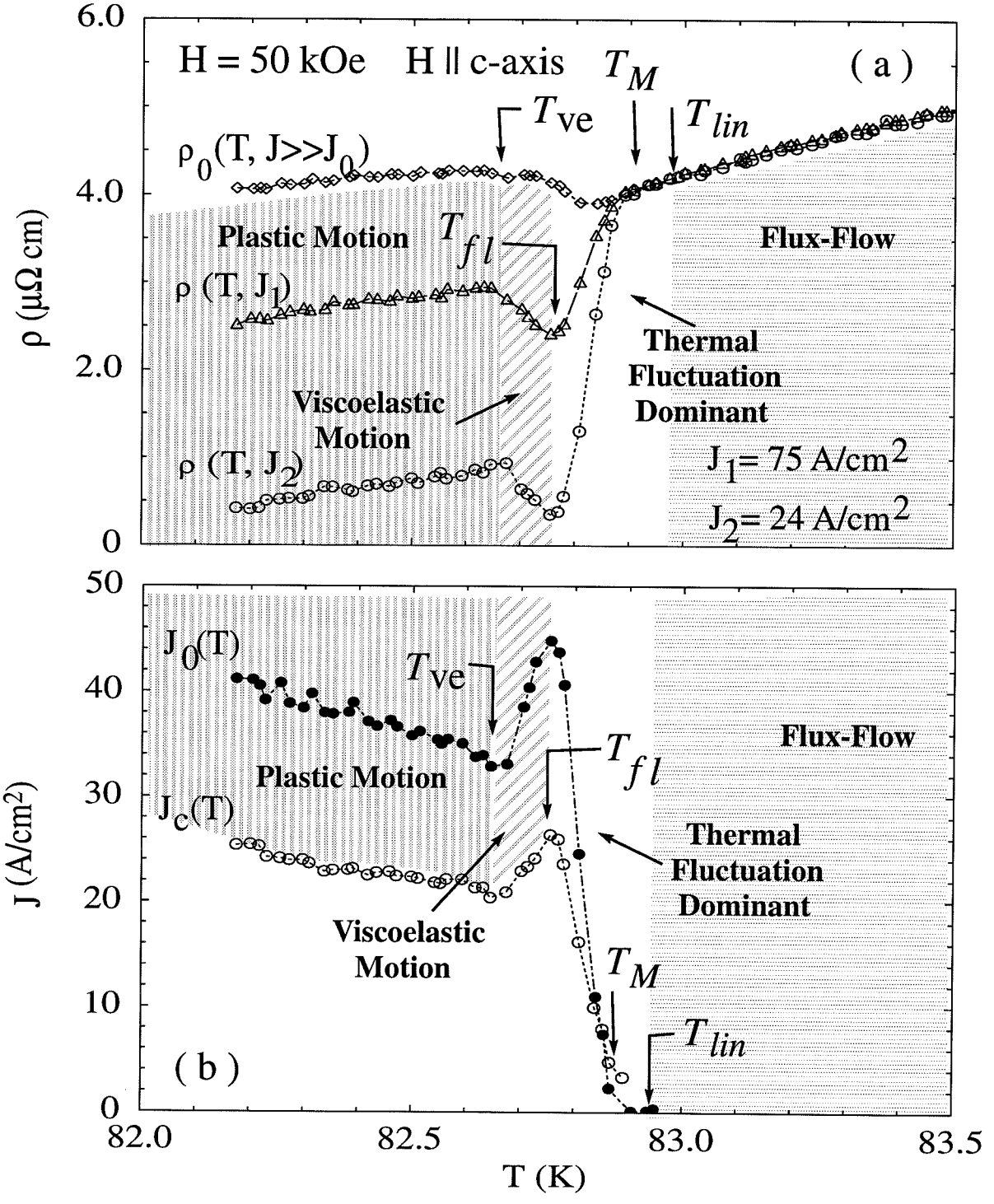

Figure 6.17: Representative data of **(a)** ρ_0-vs.-T and $\rho(J = 75A/cm^2)$-vs-T curves for $H = 50$ kOe and $\vec{H} \parallel \hat{c}$ is compared with **(b)** the corresponding $J_0(T)$ and $J_c(T)$ data. Note the strong correlations between the peak feature in $\rho_0(T)$ and those in $J_0(T)$ and $J_c(T)$. Various vortex regimes are as indicated.

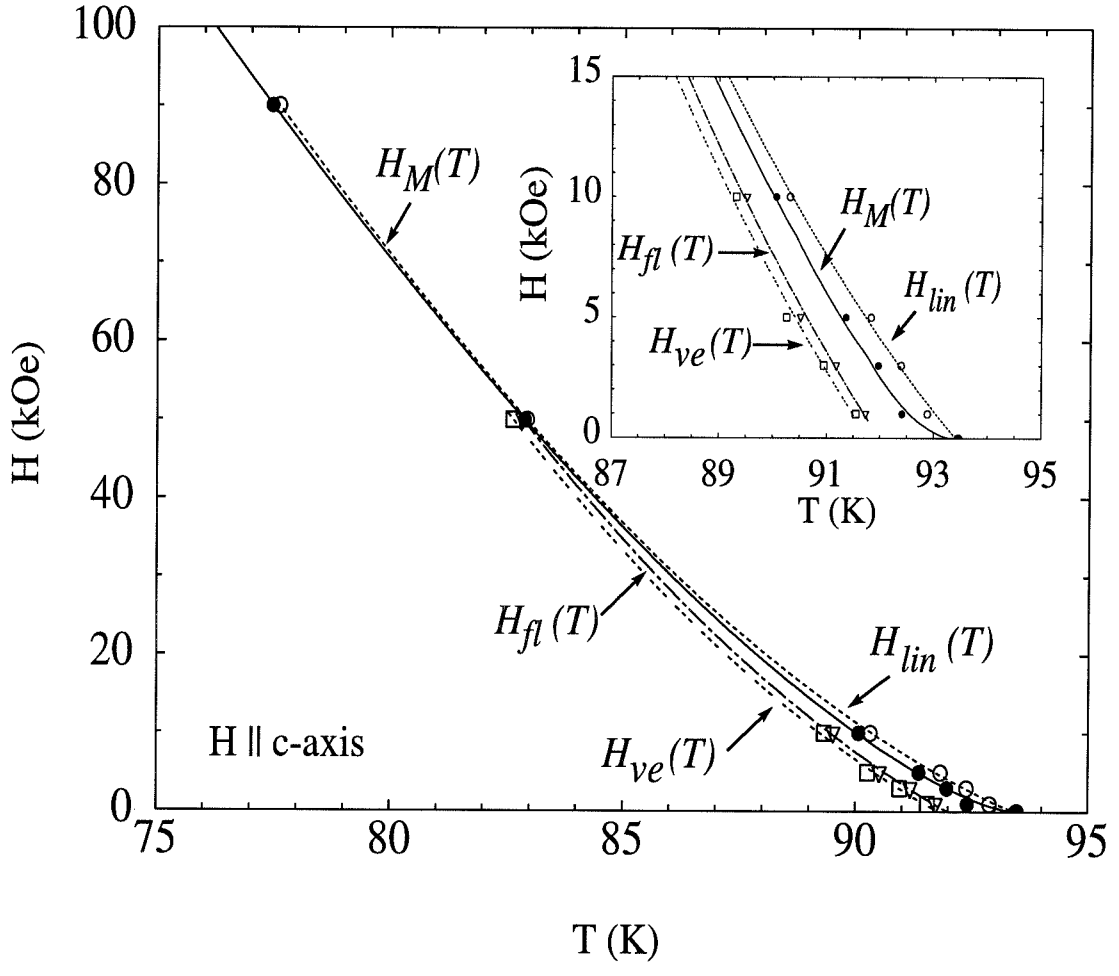

Figure 6.18: The H-vs.-T vortex phase diagram showing the thermodynamic phase transition line $H_M(T)$ and various other crossover lines $H_{dp}(T)$, $H_{pl}(T)$ and $H_{lin}(T)$. The inset shows a close-up look at the phase diagram in the lower field limit, with various vortex regimes as indicated.

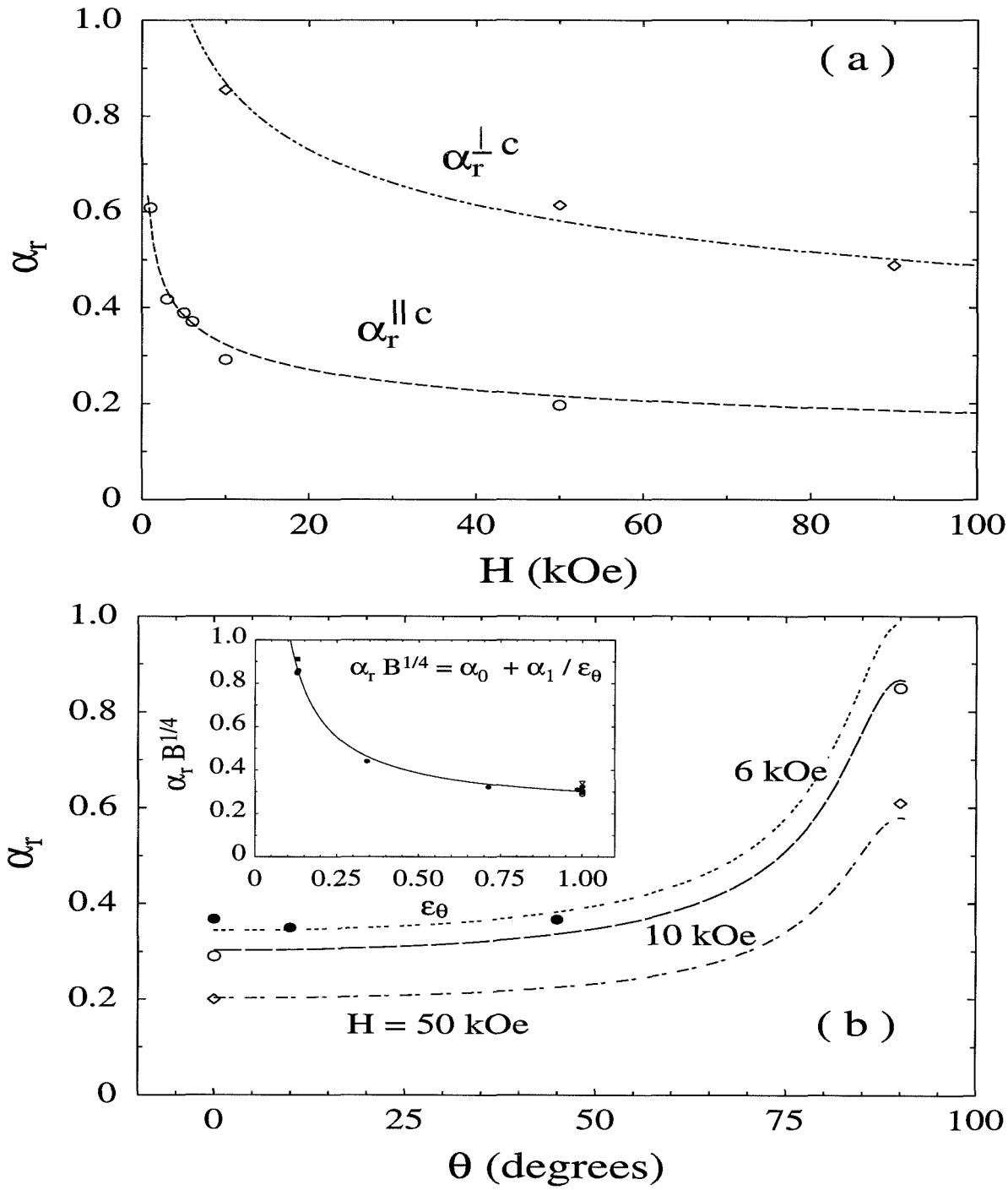

Figure 6.19: **(a)** The magnetic field dependence of α_r, defined as the ratio of the pinned vortices relative to the total vortices, is shown for both $\vec{H} \parallel \hat{c}$ and $\vec{H} \perp \hat{c}$. **(b)** The angular dependence of $\alpha_r(\theta)$ is shown for various magnetic fields. The inset demonstrates the empirical relation $\alpha_r B^{1/4} = \alpha_0 + \alpha_1/\varepsilon_\theta$ that accounts for all data taken at different H and θ values.

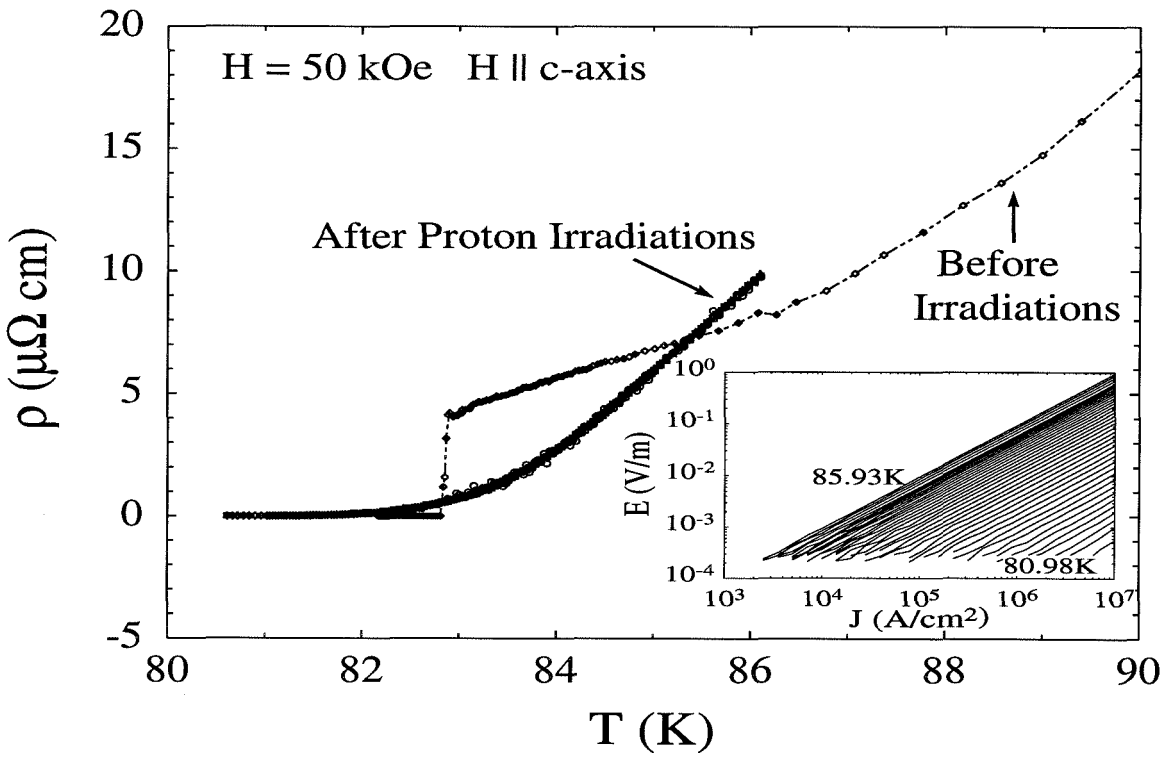

Figure 6.20: Comparison of the ohmic ρ versus T curves of the untwinned $YBa_2Cu_3O_7$ single crystal before (with $J = 7.5$ A/cm^2) and after (with J from 1.4 to 708 A/cm^2) 3 MeV proton irradiation. Note that the nearly complete ohmic behavior after irradiation, shown in the inset, is in sharp contrast to the significant nonlinear E-vs.-J isotherms before irradiation.

Chapter 7 Conclusions

This thesis has focused on investigating the effects of static disorder on the vortex phases of high-temperature superconducting $YBa_2Cu_3O_7$ single crystals. By studying the critical phenomena near the vortex-solid to liquid phase transition, we are able to obtain critical exponents and universal scaling functions for different vortex phase transitions associated with different types of disorder. In addition, novel current-induced vortex properties in nearly defect-free samples near the vortex-solid to liquid melting transition are also studied quantitatively. This work has therefore provided new understandings for the interplay of vortex pinning and vortex dynamics in high-temperature superconductors.

The experimental investigations have focused on the vortex transport properties near the vortex-solid to liquid transition. A self-consistent critical scaling analysis has been applied to the critical behavior in both DC and AC resistivity. Samples containing different types of static disorder, such as point defects, columnar defects and twin boundaries, have been investigated in Chapters 4 to 6.

Since most as-grown $YBa_2Cu_3O_7$ single crystals contain mostly point defects and twin boundaries, controlled point defects have been created by 3.0 MeV proton irradiation on as-grown samples with dilutely twinned boundaries. By comparing both the DC and AC transport properties in samples with different point defect densities, we have shown in Chapter 4 that the critical exponents and scaling functions associated with the second-order vortex-glass transition are invariant under moderately increased random point disorder. However, variations in the point defect density have important effects on the pinning-related material parameters. For instance, the high-field melting transition temperature (T_M) increases with the increasing point defect density; the zero-field transition temperature T_c decreases with the increasing point defect density; the zero-temperature vortex correlation length ξ_0 decreases with the increasing point defect density; and the flux-flow crossover current density J_x as a

function of the reduced temperature (T/T_c) increases with the increasing point disorder. In addition, in an effort of studying the critical behavior of DC resistivity, we have emphasized the importance of considering the critical regime and the appropriate current range within probing the vortex critical phenomena, because the limitations of the finite size effect at low currents and the flux-flow crossover at high currents impose additional complications to the critical analysis. Further investigations in Chapter 6 on the vortex transport properties in samples with similar point defect densities but without twin boundaries, together with the results in Chapter 4, have suggested that the presence of a second-order vortex-glass transition is the result of collective effects provided by both the random point defects and the twin boundaries.

Another type of controlled disorder that has been studied extensively in Chapter 5 is the correlated columnar defects created by 0.9 GeV Pb ion irradiations. This type of disorder results in very different vortex pinning effects because of the following general features: The average diameter of the columnar defects is comparable to the vortex core size at low temperatures; the defects extend throughout the entire thickness of the sample, thereby providing very efficient pinning; and the parallel columnar defects break the symmetry of the vortex system, giving rise to anisotropic static critical exponents. The experimental evidence of a second-order Bose-glass transition in $YBa_2Cu_3O_7$ single crystals with parallel columnar defects has been manifested by the **universal** critical scaling of frequency-dependent AC resistivity data from 10^2 to 2×10^6 Hz. The signature of the transition, that the Bose-glass transition temperature T_{BG} **decreases** with the increasing angle (θ) between the applied magnetic field and the c-axis, has also been confirmed and is in sharp contrast to the smooth **increase** of the vortex-glass temperature (T_M). For magnetic fields aligned sufficiently close to the parallel columns, $\theta \leq 30°$, the static and dynamic exponents ($\nu_\perp \approx 1.0, \nu_\parallel \equiv \zeta\nu_\perp \approx 1.1$ and $z' \approx 2.2$) are found to be **independent** of the magnitude and orientation of the magnetic field. On the other hand, for $\theta \geq 60°$, the vortex phase transition become consistent with the vortex-glass transitions. The different set of critical exponents ($\nu_\perp, \nu_\parallel$, and z') distinguishes the Bose-glass transition from the universality class

of the vortex-glass transition. In addition, the diverging compression modulus at T_{BG} suggests an **incompressible** Bose-glass with long-range vortex interactions at temperatures below T_{BG}.

The effects of the intrinsic mass anisotropy of $YBa_2Cu_3O_7$ on the vortex phase transitions have been studied in all samples, and anisotropic vortex phase diagrams have been obtained. As discussed in Chapter 5, by applying an anisotropic to isotropic scaling transformation to remove the intrinsic sample anisotropy, we are able to obtain the rescaled vortex phase diagrams which demonstrate the distinct differences among different universality classes of vortex phase transitions: An angular independent vortex-glass transition is obtained in the rescaled isotropic frame. On the other hand, the "cusp" feature (a sharp decrease in the transition temperature upon increasing the tilt of the magnetic field, relative to the columns) remains in the rescaled Bose-glass transition temperature versus angle phase diagram.

The interplay of vortex pinning and thermodynamic vortex phase transitions has been further studied in the weak pinning limit by investigating the vortex transport properties of an untwinned $YBa_2Cu_3O_7$ single crystal. Two novel phenomena have been observed near the vortex-solid to liquid melting transition. One is the resistive hysteretic behavior near the melting transition. The other is the resistive "peak effect" slightly below the melting transition. These two phenomena have also been observed by other research groups. However, prior to our work, the resistive hysteresis had been commonly interpreted as the experimental evidence for a first-order vortex-solid melting transition, and the peak effect was only qualitatively described as a precursor of the vortex-solid, melting transition in a system with few twin boundaries. Our detailed and quantitative investigations presented in Chapter 6 have clarified that both phenomena are current-induced effects in the weak pinning limit. In particular, the resistive hysteresis occurs near the vortex-solid melting transition temperature (T_M) if the applied current density is sufficiently small and is attributed to an excess momentum of the vortices due to the applied current that makes the solidification process of the vortex system more difficult. On the other hand, the resistive peak effect is the result of the softening of vortex lattice at temperatures below T_M when the shear

modulus c_{66} becomes very small but still finite. As a softened vortex-solid becomes more adaptable to the local disorder, vortices become more strongly pinned, giving rise to a peak in the critical current density. The peak effect in the critical current density also results in a nonlinear resistive peak, and the current-voltage characteristics in the temperature range where the peak effect occurs have been quantitatively described in terms of the vortex bundle hopping resistivity $\rho = \rho_0 \exp[-(J_0/J)^{\mu}]$, with the μ value corresponding to the increasing vortex bundle size in an increasing magnetic field. We therefore conclude that the nonlinear vortex dissipation below the thermodynamic melting transition temperature is consistent with the collective flux-creep theory. The corresponding pinning mechanisms at low temperatures are also inferred from the experimental data.

A Controlled Defects Due to 3.0 MeV Proton Irradiation

Among various means of creating defects in a solid, irradiation has been widely used for material modifications because the concentration, distribution and nature of the defects produced by irradiation can be controlled. The defect concentration is proportional to the dose of irradiation, and the nature and distribution of defects is a function of the species and energy of the irradiating particles. In addition, the impurities contained in the material, which may be capable of trapping the defects originally produced by the irradiation, are also important in determining the final defect structure in the material. The slow-down process of an energetic particle in a known material can be well modeled. In the following, the mechanism of defect creation, the characteristics and density of defects created by 3.0 MeV protons are given. For more comprehensive descriptions for the collision theory and defect creations, see, for example, references (Bourgoin & Lannoo, 1983; Chu *et al.*, 1978).

When light ions such as protons pass through a solid, the energetic particles lose their energy primarily through inelastic collisions with atomic electrons. Such an energy loss mechanism is called "electronic-energy loss." The energetic particles can also transfer energy to the nuclei of the solid through small angle elastic scattering events. This energy loss mechanism is called "nuclear energy loss." In the case of 3.0 MeV proton irradiation, defect creations are mainly due to the nuclear energy loss. When the energy transferred to the target nucleus is large enough, the nucleus will be knocked out of its lattice position, which results in a pair of atomic size defects: one void and the other interstitial. The primary scattering mechanism between the protons and target nuclei can be described by the well-known Rutherford scattering theory. A brief description of this theory is given below.

A.1 Rutherford Scattering

Rutherford scattering describes the elastic collisions between charged particles under a Coulomb interaction. Let E and m be the kinetic energy and mass of an incident particle. When a collision occurs between the incident particle and an atom (of mass M) of a solid, the kinetic energy T transferred to this atom depends directly on the deflecting angle θ of the incident particle (see Fig.A.1). For an elastic collision with the incident particle at a nonrelativistic energy, the conservations of kinetic energy and momentum yields the following relation between T and θ:

$$\frac{T}{E} = 2\frac{M}{m}\frac{1-\eta(\theta)}{(1+M/m)^2}, \tag{A.1}$$

where $\eta(\theta)$ is given by

$$cos\theta = \frac{1+(M/m)\eta}{\sqrt{1+2(M/m)\eta+(M/m)^2}}. \tag{A.2}$$

The maximum energy (T_{max}) transferring to the atom occurs when $\theta = 0$, i.e., for $\eta(\theta) = -1$:

$$T_{max} = \frac{4Mm}{(M+m)^2}E. \tag{A.3}$$

The interaction between the charged incident particles and the nuclei of the solid can be represented by a Coulomb potential (Rutherford scattering). The differential scattering cross section $d\sigma$, i.e., the cross section for scattering in the solid angle (θ, $\theta + d\theta$) is directly related to the impact parameter (see Fig.A.1):

$$d\sigma = 2\pi b db. \tag{A.4}$$

The relation between T and b can be obtained by assuming that T is small enough

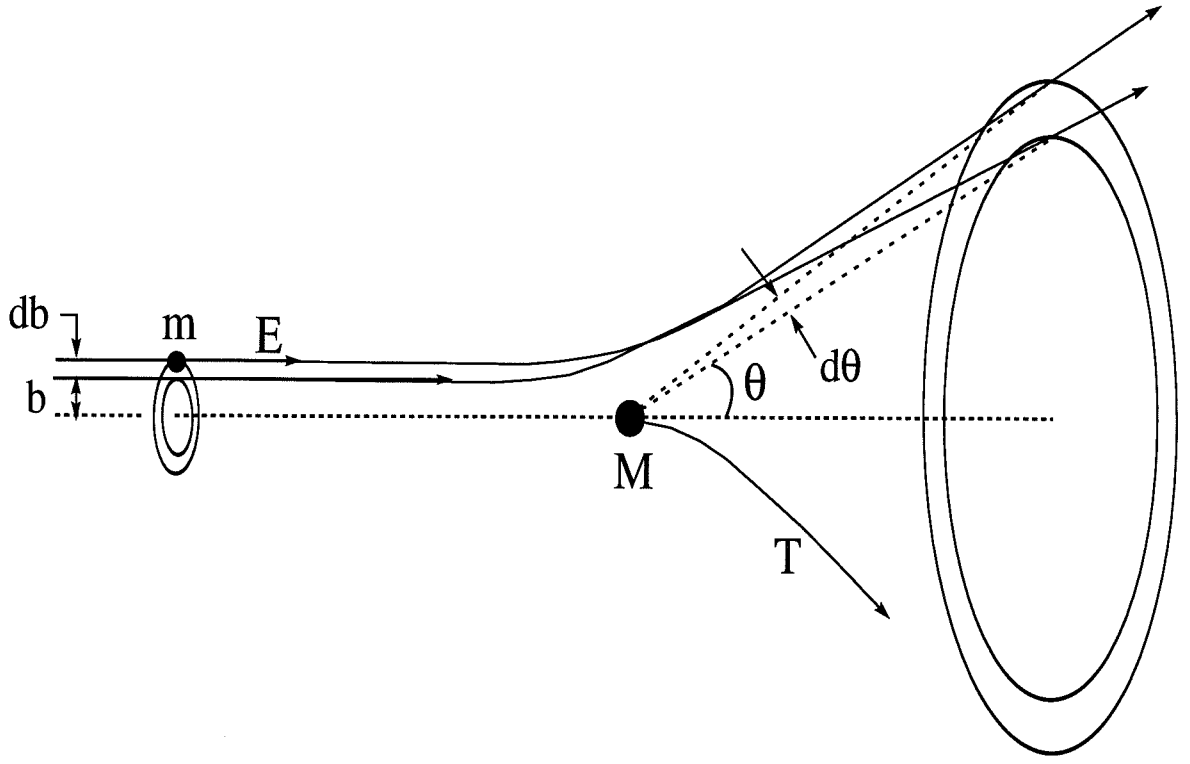

Figure A.1: Rutherford scattering.

to leave the velocity of the incident particle unchanged:

$$T = \frac{M}{m}\frac{Z_1 Z_2 e^4}{E}\frac{1}{b^2}. \tag{A.5}$$

The resulting differential scattering cross section

$$d\sigma = 2\pi b \frac{db}{dT} dT \tag{A.6}$$

is given by the Rutherford formula

$$d\sigma = \frac{a}{T^2} dT, \qquad a \equiv \frac{\pi Z_1 Z_2 e^4}{E}\frac{M}{m}. \tag{A.7}$$

A.2 The Range and Energy Loss of the Incident Ions

Next, we want to know how far a 3.0 MeV proton can travel in a presumably infinitely thick $YBa_2Cu_3O_7$ sample and how much energy it loses by passing through a real sample.

The traveling range of the incident ions is related to the total stopping power contributed by all the elements in the solid:

$$R = \int_0^{E_0} \left[\sum_i p_i (\frac{1}{\rho} \frac{dE}{dx})_i \right]^{-1} dE, \tag{A.8}$$

where p_i is the percentage composition of the ith element,

$$p_i = \frac{A_i n_i}{\sum_i A_i n_i}, \tag{A.9}$$

with n_i the atomic composition of ith element, A_i the atomic weight for the ith element, and $(\frac{1}{\rho}\frac{dE}{dx})_i$ the stopping power of the ith element. The range R can be calculated by the numerical program TRIM (Biersack & Ziegler, 1989) which utilizes Monte Carlo simulations based on the collision theory described above. The results are found to agree very well with the experimental data. As shown in the Table A.1, the range of a 3 MeV proton in $YBa_2Cu_3O_7$ is $\sim 46\mu$m. For our samples of typical thickness of 20μm, the protons can all pass through. The approximate energy loss of protons in the sample can be obtained in the following simple manner. We know that a 3.0MeV proton, after passing through the sample, is able to penetrate through another $46 - 20 = 26\mu$m depth of $YBa_2Cu_3O_7$ material. The initial energy required for a range of 26μm can be found in Table A.1 as approximately $2.1 MeV$. Therefore, the energy loss of a 3.0 MeV proton in a sample of thickness 20μm is simply $3.0 - 2.1 = 0.9$ MeV.

A.3 The Creation of Defects

With the collision theory given above, we are ready to calculate the point defect density created by 3.0 MeV protons when they pass through a $YBa_2Cu_3O_7$ single crystal.

The minimum energy E_d required to displace an atom from its lattice site is called the threshold energy. The total cross section for the displacement of an atom in the solid is

$$\sigma = \int_{E_d}^{T_{max}} d\sigma(E,T). \tag{A.10}$$

Using Eq.(A.7),

$$\sigma = a(\frac{1}{E_d} - \frac{1}{T_{max}}) \quad a \equiv \frac{\pi Z_1 Z_2 e^4}{E}\frac{M}{m}. \tag{A.11}$$

A primary knocked-on atom, to which the energy T has been transferred from the incident energetic particle, can in turn displace other atoms when T is large enough. This process is called the secondary displacement. Here, for simplicity, we only consider the primary displacements. The number of defects (n_D) created by each 3.0 MeV proton in an $YBa_2Cu_3O_7$ single crystal can be estimated by

$$n_D = 2 \times \sum_i \sigma_i N_i t, \tag{A.12}$$

where i indicates each types of atom, N_i is the number density of each types of atom, i.e.,

$$N_i = A_v \frac{\rho n_i}{\sum_i A_i n_i} \tag{A.13}$$

with A_v the Avogadro number, and t is the thickness of the sample. The factor of 2 is from the fact that one displacement creates a pair of defects: one void and the other interstitial. The density of defects for a fluence of Φ is given by

$$N_D = \frac{\Phi \times n_D}{t}. \tag{A.14}$$

Assuming that the threshold displacement energy is $\sim$ 20 eV, same for all the atoms,

and that the average ion energy in the sample is about 2.5 MeV, we get $n_D \sim 4.7$ defects/proton. Therefore, for a fluence of 5×10^{15} protons/cm^2 and a sample of 20 μm thick, N_D is approximately 4×10^{19} defects/cm^3.

Table A.1: Results of traveling range (R) and energy losses calculated by using TRIM for 3.0 MeV protons in $YBa_2Cu_3O_7$.

Ion Energy	dE/dx Elec.	dE/dx Nuclear	Projected Range	Longitudinal Straggling	Lateral Straggling
100.00 keV	1.996E+02	3.608E-01	5364 A	949 A	1588 A
110.00 keV	1.993E+02	3.367E-01	5839 A	977 A	1660 A
120.00 keV	1.982E+02	3.159E-01	6317 A	1004 A	1731 A
130.00 keV	1.967E+02	2.975E-01	6801 A	1029 A	1799 A
140.00 keV	1.946E+02	2.815E-01	7290 A	1054 A	1867 A
150.00 keV	1.923E+02	2.674E-01	7786 A	1079 A	1934 A
160.00 keV	1.898E+02	2.548E-01	8290 A	1103 A	2000 A
170.00 keV	1.871E+02	2.434E-01	8801 A	1127 A	2066 A
180.00 keV	1.843E+02	2.331E-01	9321 A	1150 A	2132 A
200.00 keV	1.785E+02	2.145E-01	1.04 um	1202 A	2265 A
220.00 keV	1.728E+02	1.994E-01	1.15 um	1253 A	2399 A
240.00 keV	1.671E+02	1.864E-01	1.26 um	1304 A	2535 A
260.00 keV	1.618E+02	1.752E-01	1.38 um	1356 A	2673 A
280.00 keV	1.567E+02	1.654E-01	1.50 um	1409 A	2814 A
300.00 keV	1.518E+02	1.567E-01	1.63 um	1462 A	2959 A
330.00 keV	1.451E+02	1.454E-01	1.83 um	1552 A	3181 A
360.00 keV	1.391E+02	1.357E-01	2.03 um	1643 A	3411 A
400.00 keV	1.318E+02	1.248E-01	2.32 um	1780 A	3729 A
450.00 keV	1.240E+02	1.136E-01	2.71 um	1971 A	4147 A
500.00 keV	1.172E+02	1.043E-01	3.11 um	2166 A	4586 A
550.00 keV	1.114E+02	9.660E-02	3.54 um	2366 A	5045 A
600.00 keV	1.062E+02	9.002E-02	4.00 um	2571 A	5524 A
650.00 keV	1.017E+02	8.434E-02	4.47 um	2780 A	6022 A
700.00 keV	9.761E+01	7.939E-02	4.96 um	2993 A	6539 A
800.00 keV	9.063E+01	7.115E-02	6.01 um	3583 A	7624 A
900.00 keV	8.481E+01	6.457E-02	7.13 um	4170 A	8775 A
1.00 MeV	7.987E+01	5.918E-02	8.33 um	4758 A	9988 A
1.10 MeV	7.560E+01	5.467E-02	9.60 um	5352 A	1.13 um
1.20 MeV	7.186E+01	5.085E-02	10.94 um	5954 A	1.26 um
1.30 MeV	6.855E+01	4.756E-02	12.35 um	6563 A	1.40 um
1.40 MeV	6.559E+01	4.470E-02	13.82 um	7182 A	1.54 um
1.50 MeV	6.292E+01	4.218E-02	15.36 um	7810 A	1.69 um
1.60 MeV	6.050E+01	3.996E-02	16.96 um	8448 A	1.84 um
1.70 MeV	5.829E+01	3.797E-02	18.62 um	9097 A	2.00 um
1.80 MeV	5.627E+01	3.618E-02	20.35 um	9756 A	2.17 um
2.00 MeV	5.268E+01	3.309E-02	23.98 um	1.17 um	2.51 um
2.20 MeV	4.959E+01	3.052E-02	27.85 um	1.35 um	2.87 um
2.40 MeV	4.690E+01	2.835E-02	31.96 um	1.54 um	3.24 um
2.60 MeV	4.452E+01	2.648E-02	36.29 um	1.73 um	3.64 um
2.80 MeV	4.241E+01	2.485E-02	40.85 um	1.92 um	4.05 um
3.00 MeV	4.052E+01	2.343E-02	45.62 um	2.11 um	4.48 um
3.30 MeV	3.802E+01	2.159E-02	53.19 um	2.48 um	5.15 um
3.60 MeV	3.586E+01	2.004E-02	61.24 um	2.85 um	5.86 um
4.00 MeV	3.338E+01	1.830E-02	72.70 um	3.43 um	6.86 um
4.50 MeV	3.077E+01	1.653E-02	88.16 um	4.26 um	8.20 um
5.00 MeV	2.860E+01	1.509E-02	104.87 um	5.07 um	9.63 um
5.50 MeV	2.675E+01	1.389E-02	122.79 um	5.88 um	11.15 um
6.00 MeV	2.515E+01	1.288E-02	141.91 um	6.70 um	12.76 um
6.50 MeV	2.376E+01	1.202E-02	162.19 um	7.52 um	14.46 um
7.00 MeV	2.253E+01	1.126E-02	183.63 um	8.36 um	16.23 um
8.00 MeV	2.046E+01	1.003E-02	229.83 um	11.07 um	20.04 um
9.00 MeV	1.878E+01	9.044E-03	280.45 um	13.67 um	24.16 um
10.00 MeV	1.739E+01	8.246E-03	335.36 um	16.23 um	28.60 um

Multiply Stopping by	for Stopping Units
1.0000E-01	eV / Angstrom
1.0000E+00	keV / micron
1.0000E+00	MeV / mm
1.5291E-03	keV / (ug/cm2)
1.5291E-03	MeV / (mg/cm2)
1.5291E+00	keV / (mg/cm2)
1.3012E-01	eV / (1E15 atoms/cm2)
1.0575E-01	L.S.S. reduced units

References

Abrikosov, A. A., 1957. *Zh. Eksperim. i Teor. Fiz.*, **32**, 1442. [Soviet Phys.-JEPT, **5**, 1174 (1957)].

Anderson, P. W., 1962. *Phys. Rev. Lett.*, **9**, 302.

Anderson, P. W., & Kim, Y. B., 1964. *Rev. of Mod. Phys.*, **36**, 39.

Balents, L., & Nelson, D. R., 1994. *Phys. Rev. Lett.*, 2613.

Bardeen, J., & Stephen, M. J., 1965. *Phys. Rev.*, **140**, 1197.

Bardeen, J., Cooper, L. N., & Schrieffer, J. R., 1957. *Phys. Rev.*, **108**, 1175.

Beck, R. G., Farrell, D. E., Rice, J. P., GInzberg, D. M., & Kogan, V. G., 1992. *Phys. Rev. Lett.*, **68**, 1594.

Bednorz, J. G., & Muller, K. A., 1986. *Phys. Rev. B*, **64**, 189.

Beno, M. A., Soderholm, L., & II, D. W. Capone, 1987. *Appl. Phys. Lett.*, **51**, 57.

Bhattacharya, S., & Higgins, M. J., 1993. *Phys. Rev. Lett.*, **70**, 2617.

Biersack, J. P., & Ziegler, J. F., 1989. A Monte Carlo simulation program for calculating stopping power, projected range, etc. for energetic ions in solids.

Blatter, G., Geshkenbein, V. B., & Larkin, A. I., 1992. *Phys. Rev. Lett.*, **68**, 875.

Blatter, G., Feigel'man, M. V., Geshkenbein, V. B., Larkin, A. I., & Vinokur, V. M., 1994. *Rev. Mod. Phys.*, **66**, 1125.

Bourgoin, J., & Lannoo, M., 1983. *Point Defects in Semiconductors II.* Berlin Heidelberg New York: Springer-Verlag.

Brandt, E. H., 1977. *J. Low Temp. Phys*, **26**, 709, 735.

Brandt, E. H., 1986. *Phys. Rev. B*, **34**, 6514.

Brandt, E. H., 1991. *Int. J. Mod. Phys. B*, **5**, 751.

Brezin, E., Nelson, D. R., & Thiaville, A., 1985. *Phys. Rev. B*, **31**, 7124.

Campbell, A.M., 1971. *J. Phys. C*, **4**, 3186.

Campbell, A.M., & Evetts, J.E., 1972. *Adv. Phys.*, **21**, 199.

Charalambous, M., Chaussy, J., Lejay, P., & Vinokur, V., 1993. *Phys. Rev. Lett.*, **71**, 436.

Chayes, J. T., Chayes, L., Fisher, D. S., & Spencer, T., 1986. *Phys. Rev. Lett.*, **57**, 2999.

Chew, W., Riley, A. L., Rascoe, D. L., Hunt, B. D., Foote, M. C., Cooley, T. W., & Bajuk, L. J., 1991. *IEEE Transactions on Microwave Theory and Techniques*, **39**, 1455.

Chu, W. K., Mayer, J. W., & Nicolet, M. A., 1978. *Backscattering Spectroscopy.* New York: Academic Press.

Civale, L., Marwick, A. D., McElfresh, M. W., Malozemoff, A. P., & Holtzberg, F., 1990. *Phys. Rev. Lett.*, **65**, 1164.

Civale, L., Marwick, A. D., , Worthington, T. K., Kirk, M. A., Thompson, J. R., L.Krusin-Elbaun, Sun, Y., Clem, J. R., & Holtaberg, F., 1991. *Phys. Rev. Lett.*, **67**, 648.

Coppersmith, S.Ñ. Inui, M. & Littlewood, P.B̃. 1990. *Phys. Rev. Lett.*, **64**, 2585.

D'Anna, Indenbom, M. V., Andre, M. O., Benoit, W., & Walker, E., 1994. *Europhys. Lett*, **25**, 225.

DeSorbo, W., 1964. *Rev. Mod. Phys.*, **36**, 90.

Dorsey, A. T., 1991. *Phys. Rev. B*, **43**, 7575.

Dorsey, A. T., Huang, M., & Fisher, M. P. A., 1992. *Phys. Rev. B*, **45**, 523.

Farrell, D. E., 1994. *Page 7 of:* Ginsberg, D. M. (ed), *Physical Properties of High Temperature Superconductors.* Singerpore NewJersey London HongKong: World Scientific.

Farrell, D. E., Kwok, W. K., Welp, U., Fredrich, J., & Crabtree, G. W., 1995. Preprint.

Feigel'man, M. V., Geshkenbein, V. B., Larkin, A. I., & Vinokur, V. M., 1989. *Phys. Rev. Lett.*, **63**, 2303.

Feynman, R. P., 1965. *Quantum Mechanics and Path Integrals.* New York: McGill-Hill.

Feynman, R. P., 1972. *Statistical Mechanics.* Reading: W. A. Benjamin, Inc., Advanced Book Program.

Fisher, D. S., Fisher, M. P. A., & Huse, D., 1991. *Phys. Rev. B*, **43**, 130.

Fisher, M. E., Barber, M. N., & Jasnow, D., 1973. *Phys. Rev. A*, **8**, 1111.

Fisher, M. P. A., & Grinstein, G., 1988. *Phys. Rev. Lett.*, **60**, 208.

Fisher, M. P. A., Weichman, P. B., Grinstein, G., & Fisher, D. S., 1989. *Phys. Rev. B*, **40**, 546.

Fleischer, R. L., Price, P. B., & Walker, R. M., 1975. *Nuclear Tracks in Solids.* Berkeley: University of California Press.

Gammel, P. L., Schneemeyer, L. F., & Bishop, D. J., 1991. *Phys. Rev. Lett.*, **66**, 953.

Geshkenbein, V. B., Ioffe, L. B., & Larkin, A. L., 1993. *Phys. Rev. B*, **48**, 9917.

Giapintzakis, Ginzberg, D. M., & Han, P. D., 1989. **77**, 155.

Ginzburg, V. L., 1950. *Fiz. Tverd. Tela*, **2**, 2031. [Sov. Phys. Solid State *2*, 1824 (1961)].

Ginzburg, V. L., & Landau, L. D., 1950. *Zh. Eksp. Teor. Fiz.*, **20**, 1064.

Gor'kov, L. P., 1958. *Zh. Eksp. Teor. Fiz.*, **34**, 735. [Sov. Phys.-JETP *7*, 505 (1958)].

Gor'kov, L. P., 1959. *Zh. Eksp. Teor. Fiz.*, **36**, 1918. [Sov. Phys.-JETP *9*, 1364 (1958)].

Gupta, A., Sun, J. Z., & Tsuei, C. C., 1994. *Science*, **265**, 1075.

Hardy, V., Groult, D., Hervieu, M., Provost, J., Raveau, B., & Bouffard, S., 1991. **54**, 472.

Hetzel, R. E., Sudbo, A., & Huse, D. A., 1992. *Phys. Rev. Lett.*, **69**, 518.

Huebener, R. P., 1979. *Magnetic Flux Structures in Superconductors.* Berlin Heidelberg New York: Springer-Verlag.

Hwa, T., Nelson, D. R., & Vinokur, V. M., 1993. *Phys. Rev. B*, **48**, 1167.

Jiang, W., Yeh, N.-C., Reed, D. S., Kriplani, U., Tombrello, T. A., Rice, A. P., & Holtzberg, F., 1992. *Page 789 of:* et al., D. T. Shaw (ed), *Layered Superconductors: Fabrication, Properties, and Applications.* Pittsburgh: Material Research Society.

Jiang, W., Yeh, N.-C., Reed, D. S., Kriplani, U., Tombrello, T. A., Rice, A. P., & Holtzberg, F., 1993. *Phys. Rev. B*, **47**, 8038.

Jiang, W., Yeh, N.-C., Reed, D. S., Kriplani, U., Beam, D. A., Konczykowski, M., Tombrello, T. A., & Holtzberg, F., 1994. *Phys. Rev. Lett.*, **72**, 550.

Jiang, W., Yeh, N.-C., Reed, D. S., Kriplani, U., & Holtzberg, F., 1995. *Phys. Rev. Lett.*, **74**, 1438.

Kaiser, D. L., Holtzberg, F., Chisholm, M. F., & Worthington, T. K., 1987. **85**, 593.

Kaiser, D. L., Gayle, F.W., Roth, R.S., & Swartzendruber, L.J., 1989. **4**, 745.

Koch, R. H., Foglietti, V., Gallagher, W. J., Koren, G., GUpta, A., & Fisher, M. P. A., 1989. *Phys. Rev. Lett.*, **63**, 1511.

Kogan, V. G., & Campbell, L. J., 1989. *Phys. Rev. Lett.*, **62**, 1552.

Konczykowski, M., 1991. *Physica A*, **168**, 291.

Konczykowski, M., Ruller-Albeque, F., Yacoby, E. R., Shaulov, A., Yeshurun, Y., & Lejay, P., 1991. *Phys. Rev. B*, **44**, 7167.

Koshelov, A. E., & Vinokur, V. M., 1994. *Phys. Rev. Lett.*, **73**, 3580.

Kwok, W. K., Fendrich, J., Fleshler, S., Welp, U., Downey, J., & Crabtree, G. W., 1994a. *Phys. Rev. Lett.*, **72**, 1092.

Kwok, W. K., Fendrich, J., Welp, U., Fleshler, S., Downey, J., & Crabtree, G. W., 1994b. *Phys. Rev. Lett.*, **72**, 1088.

Kwok, W. K., Fendrich, J. A., Vanderbeek, C. J., & Crabtree, G. W., 1994c. *Phys. Rev. Lett.*, **73**, 2614.

Larkin, A. I., & Ovchinnikov, Yu. N., 1979. **34**, 409.

Larkin, A. I., Marchetti, M. C., & Vinokur, V. M., 1994. preprint.

Lee, K. H., Stroud, D., & Girvin, S. M., 1993. *Phys. Rev. B*, **48**, 1233.

Ling, X., & Budnick, J. I. 1991. *Page 377 of:* Hein, R. A., Francavilla, T. L., & Liebenberg, D. H. (eds), *Magnetic Susceptibility of Superconductors and Other Spin Systems.*

Lobb, C. J., 1987. *Phys. Rev. B*, **36**, 3930.

Marchetti, M. C., & Nelson, D. R., 1990. *Phys. Rev. B*, **41**, 1910.

Martin, S., Fiory, A. T., Fleming, R. M., Schneemeyer, L. F., & Waszczak, J. V., 1988. *Phys. Rev. Lett.*, **60**, 2194.

Muller, K. A., Takashige, M., & Bednorz, J. G., 1987. *Phys. Rev. Lett.*, **58**, 1143.

Nelson, D. R., & Halperin, B. I., 1978. *Phys. Rev. B*, **19**, 2457.

Nelson, D. R., & Seung, H. S., 1989. *Phys. Rev. B*, **39**, 9153.

Nelson, D. R., & Vinokur, V. M., 1992. *Phys. Rev. Lett.*, **68**, 2398.

Nelson, D. R., & Vinokur, V. M., 1993. *Phys. Rev. B*, **48**, 13060.

Olsson, H. K., Koch, R. H., Eidelloth, W., & Rodertazzi, R. P., 1991. *Phys. Rev. Lett.*, **66**, 2261.

Pippard, A. B., 1969. *Philos. Mag.*, **19**, 217.

Raider, S. I. (ed), 1988. *Low Temperature Superconductors and High Temperature Superconductors.* 10 South Main St., Pennington, NJ08534-2896: The Electrochemical Soceity, Inc.

Reed, D. S. 1995. Ph.D. thesis, California Institute of Technology.

Reed, D. S., Yeh, N.-C., Jiang, W., Kriplani, U., & Holtzberg, F., 1992. *Page 413 of: Layered Superconductors: Fabrication, Properties, and Applications.* Pittsburgh: Material Research Society.

Reed, D. S., Yeh, N.-C., Jiang, W., Kriplani, U., & Holtzberg, F., 1993. *Phys. Rev. B*, **47**, 6150.

Reed, D. S., Yeh, N.-C., Jiang, W., Kriplani, U., Beam, D. A., & Holtzberg, F., 1994. *Phys. Rev. B*, **49**, 4384.

Reed, D. S., Yeh, N.-C., Konczykowski, M., & Samoilov, A. V., 1995. *Phys. Rev. B*, June. In press.

Rice, J. P., & Ginzberg, D. M., 1991. *J. Crys. Growth*, **109**, 432.

Richard, P. (ed), 1980. *Methods of Experimental Physics, V.17.* New York: Academic Press.

Safar, H., Gammel, P. L., Huse, D. A., Bishop, D. J., Rice, J. P., & Ginsberg, D. M., 1992a. *Phys. Rev. Lett.*, **69**, 824.

Safar, H., Safar, H., Gammel, P. L., Huse, D. A., Bishop, D. J., Lee, W. C., Giapintzakis, J., & Ginsberg, D. M., 1992b. *Phys. Rev. Lett.*, **70**, 3800.

Schmid, H., Burkhardt, E., Sun, B. N., & Rivera, J. P., 1989. **157**, 555.

Subramanian, M. A., Calabrese, J. C., Torardi, C. C., Gopalakrishnan, J., Askew, T. R., Flippen, R. B., Morrissey, K. J., Chowdhry, U., & Sleight, A. W., 1988. **332**, 420.

Tsuei, C. C., Gupta, A., & Trafas, G., 1994. **263**, 1259.

van der Beek, C. J., Geshkenbein, V. B., & Vinokur, V. M., 1993. *Phys. Rev. B*, **48**, 3393.

van Dover, R. B., Gyorgy, E. M., Schneemeyer, L. F., Mitchell, J. W., Rao, K. V., Puzniak, R., & Waszczak, J. V., 1989. **342**, 55.

Vasquez, R. P., Foote, M. C., Bajuk, L., & Hunt, B. D., 1991. **57**, 317.

Vichery, H., Rullier-Albenque, F., Pascard, H., Konczykowski, M., Kormann, R., Favrot, D., & Collin, G., 1989. **159**, 697.

Welp, U., Kwok, W. K., Crabtree, G. W., Vandervoort, K. G., & Liu, J. Z., 1989a. *Phys. Rev. Lett.*, **62**, 1908.

Welp, U., Grimsditch, M., You, H., , Kwok, W. K., Fang, M. M., , Crabtree, G. W., & Liu, J. Z., 1989b. **161**, 1.

Wstrördenweber, R., Kes, P. H., & Tsuei, C. C., 1986. *Phys. Rev. B*, **33**, 3172.

Wu, M. K., Ashburn, J. R., Torng, C. J., Hor, P. H., Meng, R. L., Gao, L., Huang, Z. H., Wang, Y. Q., & Chu, C. W., 1987. *Phys. Rev. Lett.*, **58**, 908.

Yeh, N.-C., Jiang, W., Reed, D. S., Kriplani, U., & Holtzberg, F., 1992a. *Page 169 of:* et al., D. T. Shaw (ed), *Layered Superconductors: Fabrication, Properties, and Applications.* Pittsburgh: Material Research Society.

Yeh, N.-C., Reed, D. S., Jiang, W., Kriplani, U., Holtzberg, F., Gupta, A., Hunt, B.D., Vasquez, R.P., Foote, M.C., & Bajuk, L., 1992b. *Phys. Rev. B*, **45**, 5654.

Yeh, N.-C., Jiang, W., Reed, D. S., Kriplani, U., & Holtzberg, F., 1993a. *Phys. Rev. B*, **47**, 6146.

Yeh, N.-C., Jiang, W., Reed, D. S., Kriplani, U., Holtzberg, F., Konczykowsi, M., Tsuei, C. C., & Chi, C. C., 1993b. *Physica A*, **200**, 374.

Yeh, N.-C., Reed, D. S., Jiang, W., Kriplani, U., Konczykowski, M., & Holtzberg, F., 1994. *Physica C*, **235**, 2659.

Yeshurun, Y., & Malozemoff, A. P., 1988. *ibid*, **60**, 2202.